Arindam Biswas · Amit Banerjee ·
Aritra Acharyya · Hiroshi Inokawa ·
Jintendra Nath Roy *Editors*

Emerging Trends in Terahertz Solid-State Physics and Devices

Sources, Detectors, Advanced Materials, and Light-matter Interactions

Emerging Trends in Terahertz Solid-State Physics and Devices

Arindam Biswas · Amit Banerjee ·
Aritra Acharyya · Hiroshi Inokawa ·
Jintendra Nath Roy
Editors

Emerging Trends in Terahertz Solid-State Physics and Devices

Sources, Detectors, Advanced Materials, and Light-matter Interactions

Editors
Arindam Biswas
School of Mines and Metallurgy
Kazi Nazrul University
Asansol, West Bengal, India

Aritra Acharyya
Department of Electronics
and Communication
Cooch Behar Government
Engineering College
Cooch Behar, West Bengal, India

Jintendra Nath Roy
Department of Physics
Kazi Nazrul University
Asansol, West Bengal, India

Amit Banerjee
Department of Electrical
and Computer Engineering
National University of Singapore
Singapore, Singapore

Hiroshi Inokawa
Research Institute of Electronics
Shizuoka University
Shizuoka, Japan

ISBN 978-981-15-3234-4 ISBN 978-981-15-3235-1 (eBook)
https://doi.org/10.1007/978-981-15-3235-1

© Springer Nature Singapore Pte Ltd. 2020
This work is subject to copyright. All rights are reserved by the Publisher, whether the whole or part of the material is concerned, specifically the rights of translation, reprinting, reuse of illustrations, recitation, broadcasting, reproduction on microfilms or in any other physical way, and transmission or information storage and retrieval, electronic adaptation, computer software, or by similar or dissimilar methodology now known or hereafter developed.
The use of general descriptive names, registered names, trademarks, service marks, etc. in this publication does not imply, even in the absence of a specific statement, that such names are exempt from the relevant protective laws and regulations and therefore free for general use.
The publisher, the authors and the editors are safe to assume that the advice and information in this book are believed to be true and accurate at the date of publication. Neither the publisher nor the authors or the editors give a warranty, expressed or implied, with respect to the material contained herein or for any errors or omissions that may have been made. The publisher remains neutral with regard to jurisdictional claims in published maps and institutional affiliations.

This Springer imprint is published by the registered company Springer Nature Singapore Pte Ltd.
The registered company address is: 152 Beach Road, #21-01/04 Gateway East, Singapore 189721, Singapore

Preface

General interest in photonics research has been increasing significantly because of their enormous and promising application prospects in the advancement of human civilization. Photonics is regarded as one of the key technologies with applications ranging from light sources, optical communications, imaging, detectors and sensors, optical data storage and displays, medical optics and biophotonics, photovoltaics, plasmonics technology, etc. The importance of photonics was marked by the United Nations endorsing 2015 as the International Year of Light. Photonics is collectively combined with micro- and nanoelectronics, biotechnology or nanotechnology. Hence, the development of new photonic technologies needs the fundamental understanding of light–matter interactions, implementation of new concepts using novel materials with tailored properties, multidisciplinary research combining photonics modeling with long-term strategic aim on final applications. Study on these devices considering the compatibility and ease of fabrication with currently available technologies and scope of further miniaturization is of enormous importance. This also leads to an increasing interest for terahertz (THz) technology in the past decade in the efforts to harness the power of the thermal radiation in the region from 300 GHz to 3 THz (wavelength: 100 μm to 1 mm) and comes with some uniquely attractive qualities with enormous application possibilities. This book deals with the emerging applications in terahertz solid-state physics and devices, including sources, detectors, advanced materials, and light–matter interactions with theoretical, methodological, well-established, and validated empirical examples. The title covers a very vast audience from basic science to engineering and technology experts and learners. This could eventually work as a textbook for engineering and biomedical students or science masters programs and for researchers. This title also serves common public interest by presenting new methods to improve the quality of life in general, with a better integration into society.

Asansol, India — Arindam Biswas
Singapore — Amit Banerjee
Cooch Behar, India — Aritra Acharyya
Shizuoka, Japan — Hiroshi Inokawa
Asansol, India — Jintendra Nath Roy

Contents

THz Bandpass Filter Design Using Metamaterial-Based Defected 1D Photonic Crystal Structure 1
Arpan Deyasi and Angsuman Sarkar

Terahertz Radiators Based on Silicon Carbide Avalanche Transit Time Sources—Part I: Large-Signal Characteristics 23
S. J. Mukhopadhyay, P. Mukherjee, A. Acharyya and M. Mitra

Terahertz Radiators Based on Silicon Carbide Avalanche Transit Time Sources—Part II: Avalanche Noise Characteristics 37
S. J. Mukhopadhyay, P. Mukherjee, A. Acharyya and M. Mitra

RF Performance of Ultra-wide Bandgap HEMTs 49
Rajan Singh, T. R. Lenka, D. Panda, R. T. Velpula, B. Jain, H. Q. T. Bui and H. P. T. Nguyen

Potentiality of Impact Avalanche Transit Time Diode as Terahertz Source Based on Group IV and III–V Semiconducting Materials 65
Girish Chandra Ghivela, S. J. Mukhopadhyay, Joydeep Sengupta and M. Mitra

Analysis of InN-Based Surrounded Gate Tunnel Field-Effect Transistor for Terahertz Applications 77
Ritam Dutta and Nitai Paitya

On the Quantum Capacitance of Quantum Wire Field-Effect Transistors of Compound Semiconductors 85
A. H. Seikh, N. Alharthi, P. K. Bose and K. P. Ghatak

Heterostructure Devices for THz Signal Recognition 107
Amit Bhattacharyya, Manash Chanda and Debashis De

Data Transmission with Terahertz Communication Systems 121
Mohammed El Ghzaoui and Sudipta Das

Advances in Terahertz Imaging 143
Arijit Saha

Terahertz Emission Mechanisms in III–V Semiconductors: The Influence of Isoelectronic Dopants 169
Rajeev N. Kini and C. P. Vaisakh

Group III—Nitrides and Other Semiconductors for Terahertz Detector 189
Bijit Choudhuri and Aniruddha Mondal

About the Editors

Dr. Arindam Biswas Assistant Professor, School of Mines and Metallurgy, Kazi Nazrul University, Asansol, Burdwan, West Bengal, 713340, India.

He was born in West Bengal, India in 1984. He received M.Tech. degree in Radio Physics and Electronics from University of Calcutta, India in 2010 and Ph.D. from NIT Durgapur in 2013. He was a Post-Doctoral Researcher at Pusan National University, South Korea with prestigious BK21PLUS Fellowship, Republic of Korea. He got Visiting Professor at Research Institute of Electronics, Shizouka University, Japan. He has been selected for IE(I) Young Engineer Award: 2019–2020 in Electronics and Telecommunication Engineering discipline, Institute of Engineers, India. Dr. Biswas has 10 years' of experience in teaching research and administration. Presently Dr. Biswas is working as an Assistant Professor in School of Mines and Metallurgy at Kazi Nazrul University, Asansol, West Bengal, India. He has 48 technical paper in different journals and 30 conference proceedings and six books, one edited volume and one book chapter with international repute. Dr. Biswas received research grant from Science and Engineering Research Board, Govt of India, under Early Career Research Scheme for research in Terahertz based GaN Source. He also received Research Grant from Centre of Biomedical Engineering, Tokoyo Medical and Dental University in association with RIE, Shizouka University, Japan for study of biomedical THz Imaging based on WBG semiconductor IMPATT Source. Presently Dr. Biswas is serving as an Associate Editor

of Cluster Computing, Springer (SCI Indexed) and as a guest editor of Nanoscience and Nanotechnology-Asia (Scopus Indexed), Recent Patent in Material Science (Scopus Indexed), Benthamscience Publisher. Dr. Biswas has produced four Ph.D. students in different topics of applied optics and high frequency semiconductor device. He has organized and chaired difference International Conferences in India and abroad. His research interest is in carrier transport in low dimensional system and electronic device, non-linear optical communication, THz Semiconductor Source. Dr. Biswas acted as reviewer for reputed journals, and member of the Institute of Engineers (India) and Regular Fellow of Optical Society of India (India).
e-mail: mailarindambiswas@yahoo.co.in

Dr. Amit Banerjee Scientist, Microelectronic Technologies and Devices, Department of Electrical and Computer Engineering, National University of Singapore, 21 Lower Kent Ridge Rd, Singapore, 119077, Singapore.

He joined the Advanced Device Research Division, Research Institute of Electronics, National University Corporation, Japan as a Scientific Researcher in 2016 and was also part of the Innovative Photonics Evolution Research Center (iPERC) at Hamamatsu, Japan. He later joined the Microelectronic Technologies & Devices, Department of Electrical and Computer Engineering of the prestigious National University of Singapore, as Scientist in 2017. Currently Amit is member of 30+ international advisory boards, technical program committees in various countries, acted as panel editor, reviewer for reputed journals and scientific book volumes, member of Japan Society of Applied Physics, Indian Physical Society; External Adviser, Bioelectronics and Biomedical Technologies, Ocuro Science and Technology (Biomed-startup); Adviser and Lead Contributor: Semiconductor Devices and Process Technologies, EDGE196, Entrepreneur Development Global Ecosystem; Adviser, EntrepreneursFace, Singapore, Global Venture Capital and Entrepreneurs Network, Singapore; Technical Adviser to ULVAC Technologies; among various others. Amit has co-authored several scientific papers, edited books, presented in several international conferences as

plenary and keynote speakers, received awards including young physicist award and honorary life-membership from Indian Physical Society, award by the Metrology Society of India (MSI), Indian Institute of Chemical Engineers (IIChE), award by Department of Atomic Energy (DAE), his work on nanodiamonds, was also awarded and featured as a key scientific article contributing to excellence in engineering, scientific and industrial research, by Advances in Engineering, USA; recently their work related to on-chip integrable terahertz detectors was awarded by Quality in Research (QiR), Indonesia along with Prof. Hiroshi Inokawa, RIE, Japan. Alongside the pursuit of research and administrative ambitions, Amit is keenly engaged in consulting futuristic technologies for business firms, educational ventures and universities. Amit received Ph.D. degree in Semiconductor Technology from Energy Research Unit, Indian Association for the Cultivation of Science (DST, Government of India), and extensively worked on design and development of high vacuum plasma CVD reactors, which are used in industrial manufacturing of solar cells, coatings and TFTs. He also developed low cost high vacuum MW-PECVD units, and conceived the process for cost effective commercial grade antireflection coatings (ARC) synthesis for solar cells by nanocrytalline diamonds. His current work is on Terahertz Technology, including THz sensors and sources, design, fabrication, aiming at biomedical imaging applications. His recent work on antenna-coupled microbolometer arrays, are compatible with the state-of-the-art medium-scale semiconductor device fabrication processes, and technologically competitive with commercial viability as on-chip integrable detector arrays for terahertz imaging.

e-mail: amitbanerjee.nus@gmail.com; eleami@nus.edu.sg

Dr. Aritra Acharyya Assistant Professor, Department of Electronics and Communication Engineering, Cooch Behar Government Engineering College, Harinchawra, Ghughumari, West Bengal, 736170, India.

He was born in 1986. He received B.E. and M.Tech. degrees from IIEST, Shibpur, India, and Institute of Radio Physics and Electronics, University of Calcutta, India, in the years 2007 and 2010 respectively. Finally he obtained Ph.D. degree from Institute of Radio Physics and Electronics, University of Calcutta, in the year 2016. He is currently working as an Assistant Professor of Electronics and Communication Engineering Department at Cooch Behar Government Engineering College, West Bengal. His research interests are high frequency semiconductor devices. He has already published more than 115 research papers in peer reviewed journals and conference proceedings.

e-mail: ari_besu@yahoo.co.in

Dr. Hiroshi Inokawa Professor, Research Institute of Electronics, Shizuoka University, 3-5-1 Johoku, Naka-ku, Hamamatsu 432-8011, Japan.

He received B.S., M.S., and Ph.D. degrees in electrical engineering from Kyoto University, Japan in 1980, 1982 and 1985, respectively. In 1985, he joined the Atsugi Electrical Communications Laboratories, Nippon Telegraph and Telephone Corporation (NTT), Kanagawa, Japan. Since then, he has been engaged in the research and development of scaled-down CMOS devices and silicon single-electron devices. During the course of his research, he invented the basic structure of FinFET in 1989 and single-electron multiple-valued logic in 2001, and received IEEE International Symposium on Multiple-Valued Logic (ISMVL) Outstanding Contributed Paper Awards in 2004 and 2006, Director's Award of NTT Basic Research Laboratories in 2004, 28th JSAP Award for the Best Original Paper in 2006, etc. In 2006, he became a professor of the Research Institute of Electronics, Shizuoka University, Hamamatsu, Japan, where he

has been studying nanodevices for advanced circuits and systems. His recent work on SOI MOSFET single-photon detector was introduced by IEEE Photonics Journal in 2012 as a Breakthrough in Photonics. Prof. Inokawa is a member of the Institute of Electrical and Electronics Engineers (IEEE), the Japan Society of Applied Physics (JSAP), the Institute of Electronics, Information and Communication Engineers of Japan (IEICE), and the Institute of Electrical Engineers of Japan (IEEJ). He has served as a JSAP board member of representative in 2001–2003, an editor of JJAP in 2007–2013, the chair of the IEEJ survey committee of silicon nanosystem integration technology in 2009–2011, an advisory committee member of NICT Japan Trust International Research Cooperation Program in 2006–2009, a researcher of National Institute of Science and Technology Policy (NISTEP) in 2002–present, etc.
e-mail: inokawa.hiroshi@shizuoka.ac.jp

Dr. Jintendra Nath Roy Professor and Dean (Science), Department of Physics, Kazi Nazrul University, C H Kalla, Asansol, West Bengal, India.

He received M.Sc. and Ph.D. degree in Physics from Vidyasagar University, India. He had joint research program at Department of Electrical and Computer Engineering, Light wave Communications Research Group, Xanthi-Greece. Professor Roy received International Sardar Patel Award from Sardar Vallabhbhai Patel Foundation for significant contribution in physical science. Dr. Roy has 20 years of experience in teaching research and administration. Presently Dr. is working as a Professor and Dean (science) in Department of Physics at Kazi Nazrul University, Asansol, West Bengal, India. He has already published more than 123 research papers in peer reviewed journals and conference proceedings. Dr. Roy received research grant from AICTE, Govt of India, under FRS Scheme for research in “Designing of an all-optical conversion scheme from binary to its Modified Trinary Number”. Dr. Roy is member of

many International Advisory Committees, Technical Program Committees in various countries, acted as Panel Editor, Reviewer for reputed journals. Professor Roy has produced nine Ph.D. students in different topics of Applied optics and photonics, linear & nonlinear optical material, laser. His current research interest is in Terahertz Optical Asymmetric Demultiplexer (TOAD) based switch in Computing, Communication and Control.
e-mail: jnroys@yahoo.co.in

THz Bandpass Filter Design Using Metamaterial-Based Defected 1D Photonic Crystal Structure

Arpan Deyasi and Angsuman Sarkar

Abstract In the present chapter, bandpass filter in THz spectra is designed using defected one-dimensional structure where the central wavelength is chosen at 1550 nm. Double negative index materials, i.e. metamaterials are considered for filter design which is already a proved candidate for providing better SNR in planar antenna than the known positive index materials; intentionally pint defects are considered within the structure which improves the amount in ripple in passband and makes the guard bands sharper compared with defect-free ideal structure. Along with normal incidence, oblique incidences are also taken into account within a limited range of incidence angle for estimation of filter properties where both TM and TE modes of propagations are analysed. Result speaks in favour of paired nanorod structure for gradual variation of bandwidth, however, for higher operating frequency range; nanofishnet with elliptic void is favoured.

Keywords Metamaterial · Bandpass filter · Photonic crystal · THz spectrum · Oblique incidence · Defected structure

1 Introduction

Progress in applied physics related to the field of optoelectronic devices and systems is rapidly replaced by all-photonic counterparts, precisely due to the characteristic of lower noise, higher operating speed [1, 2], lower attenuation loss, coherency and large bandwidth [3, 4]. The physical realization of photonic integrated circuit becomes possible due to the fabrication of photonic crystal undoubtedly can be termed as the building block of optical devices [5]. This structure has the unique

A. Deyasi (✉)
Department of Electronics and Communication Engineering, RCC Institute of Information Technology, Kolkata 700015, India
e-mail: deyasi_arpan@yahoo.co.in

A. Sarkar (✉)
Department of Electronics and Communication Engineering, Kalyani Govt. Engineering College, Nadia 741235, India
e-mail: angsumansarkar@ieee.org

© Springer Nature Singapore Pte Ltd. 2020

A. Biswas et al. (eds.), *Emerging Trends in Terahertz Solid-State Physics and Devices*,
https://doi.org/10.1007/978-981-15-3235-1_1

property of rejecting the unwanted wavelength band of propagating e.m wave, due to the formation of multiple forbidden regions, and also allows the desired spectra [6]. This unique feature leads to several new photonic devices in the form of transmitter [7], receiver [8], waveguide [9], sensor [10], fibre [11], along with realization of non-linear effect [12] and quantum information processing [13]. Though two-dimensional [14] or three-dimensional photonic crystals [15] are experimentally realizable, most of the devices, as of now, are made using one-dimensional structure [16–18]; henceforth, it is customary to investigate the optical properties offered by this structure in further details. The properties of the devices are critically dependent on the material composition [19] as well as dimensions of different layers [20], incident angles [21] and mode of propagations [22]. In the next paragraph, we will briefly explain the role of different materials used so far to fabricate devices and the importance of negative index materials in this context.

Semiconductor heterostructures are recently being considered as a suitable composition for making photonic crystal [23], though dielectric combinations are favoured because of less fabrication cost. Very recently, metamaterials or negative refractive index materials are also considered to visualize the same [24], owing to their established quality performance in antenna engineering [25], where they exhibited improved SNR performance. Henceforth, it becomes the duty of design engineers to check the performance of single negative index or double negative index material-based optical devices, under the light of Bragg grating [26]. A few results are recently reported [27, 28], which forces the workers for further investigation, as the outcome is positive. Therefore, research is directed towards LHM-based photonic crystal investigation, and computation of bandwidth becomes the first step of that analysis.

2 Objective

In the present chapter, the design of optical bandpass filter with one-dimensional metamaterial–air-based photonic crystal has been studied for transmissivity characteristics of optical filter. Generally, two different metamaterials with refractive index -4 and -0.3 have been introduced in photonic crystal in air [29]. The former is the nanofishnet structure having shape of the internal void as elliptical in nature, and the latter is termed as paired nanorod. Both the materials are well-established and already physically realizable; henceforth, they can safely be considered for analysis purpose. Our aim is to study and compare the defected photonic crystal structure with the ideal photonic crystal and also study that how the transmission property of optical filter varies due to change in the angle of incidence, metamaterial length and air thickness. Transmission properties have been analysed due to the variation of these parameters for TE and TM mode, along with bandwidth variation [30]. From this observation, we can select the photonic filter with which the refractive index is better for practical application and for practical designing of optical bandpass filter

defected photonic crystal up to which the value of defect density can be accepted so that it will not affect the proper filtering action.

3 Mathematical Formulation

Computation of optical bandwidth for photonic filter is a combination of multiple measures, where in the initial step, transmission profile is calculated in given spectra, and then, bandwidth can be estimated considering the wavelength difference between two subsequent notches. In this section, we have shown a detailed computation procedure.

At first, we consider the normal incidence of e.m wave propagation. Furthermore, the oblique incidence is considered. The well-known transfer matrix approach is applicable for both type of polarized incident waves, namely TE polarization, and TM polarization of light is shown in details in Sect. 3.1, whereas for the unit section, it is simplified and presented in Sect. 3.2. From the definition, TE-polarized wave is also called as *s*-polarized wave; where electric field vector of the propagating wave is parallel to the stack layers of the structure. TM-polarized light is popularly known as *p*-polarized wave; where magnetic field vector is exactly parallel to the same stack layers, i.e. the electric field is now perpendicular. Therefore, the problem can now be reformulated as the investigation of characteristics and performance of electromagnetic field when we consider its propagation through the perpendicular direction of a multiple stack layer where all the layers are made by different (two in this case in alternative mode) dielectric media with different refractive indices. The solution is simple and can easily be derived from Maxwell's equations by decoupling it in two independent formats in the two media under consideration and therefore use of suitable boundary conditions in the terms of electric and magnetic fields at the interface. Here, we may consider both tangential as well as transverse solutions, though tangential components are extremely crucial and their continuity property will determine the final solution.

3.1 Transmission and Reflection Coefficients for Polarized Wave Incidence

We consider propagation of transverse wave along the z-direction in a liner medium where 'n' is the refractive index. Here for generalization, we can presume that 'n' is homogeneous in X–Y plane, but its property should have a dependence along the field direction, i.e. in this case, it is dependent on Z. Therefore, the wave equation may be formulated in the following form:

$$\frac{\partial^2 E}{\partial z^2} = -\kappa_0^2 n^2 E \tag{3.1}$$

where κ_0 is the propagation vector, as characteristics of the medium. The general solution of the electric field Eq. (3.1) is given by:

$$E = A_1 \exp(i\kappa z) + A_2 \exp(-i\kappa z) \quad (3.2)$$

Similar procedure can be adopted for the magnetic field, which will provide almost same solution using the Maxwell equation as

$$B = A_1 n \exp(i\kappa z) - A_2 n \exp(-i\kappa z) \quad (3.3)$$

Now replace the single medium by two media with refractive indices 'n_1' and 'n_2' which have a common interface. We consider the propagation as from the left ($z = 0$) between these two media (all are assumed as semi-infinite), and therefore, we can get the amplitude of reflection coefficient from the equality of tangential components of magnetic and electric fields [from Eqs. (3.2) and (3.3)] which is put in Eq. (3.4)

$$r \equiv \frac{A_2^{m1}}{A_1^{m1}} = \frac{n_1 - n_2}{n_1 + n_2} \quad (3.4)$$

as well as the amplitude transmission coefficient

$$t \equiv \frac{A_1^{m2}}{A_1^{m1}} = \frac{2n_1}{n_1 + n_2} \quad (3.5)$$

where 'm_1' and 'm_2' are the medium 1 and medium 2, respectively. Reflectivity from Eq. (3.4) can be calculated as

$$R = |r|^2 \quad (3.6)$$

Transmissivity from Eq. (3.5) can be put into the form

$$T = \frac{n_2}{n_1}|t|^2 \quad (3.7)$$

For stack type of multiple layer structures, we can directly put the boundary conditions in the Maxwell equations at each interface. This will provide decoupled algebraic equations which are very easy to solve. In the present problem, if we adopt this procedure, we will get two equations per interface. In order to solve the set of algebraic equations, transfer matrix method is adopted, and this will provide the meaningful solutions through a number of equations. This is described in the subsequent steps as follows:

Let us introduce the vector

$$\vec{\psi}(z) = \begin{bmatrix} E(z) \\ B(z) \end{bmatrix} = \begin{bmatrix} E(z) \\ -\frac{i}{\kappa_0} \frac{\partial E(z)}{\partial z} \end{bmatrix} \tag{3.8}$$

where $E(z)$, $B(z)$ have the usual significances, i.e. field components along Z-directions. The important factor while solving Eq. (3.8) is that the wave function $\vec{\psi}(z)$ is continuous throughout the structure, even the refractive index can change.

From the definition of transfer matrix at the interface between two arbitrary layers, $\hat{T}_M$ along the layer of dimension 'l' is:

$$\widehat{T}_M \vec{\psi}|_{z=0} = \vec{\psi}|_{z=l} \tag{3.9}$$

where $\widehat{T}_M$ is a 2×2 matrix. Now we have to verify the amplitudes of field components through substitution into Eq. (3.9) as defined in Eqs. (3.2) and (3.3) assuming the fact that 'n' is considered as consistent and identical throughout the layer, then

$$\widehat{T}_M = \begin{bmatrix} \cos \kappa l & \frac{i}{n} \sin \kappa l \\ in \sin \kappa l & \cos \kappa l \end{bmatrix} \tag{3.10}$$

Henceforth, final transfer matrix can be calculated from the knowledge of transfer matrices obtained at individual interfaces assumed as composed of 'm' layers

$$\widehat{T} = \prod_{j=1}^{j=m} \widehat{T}_j \tag{3.11}$$

where $\widehat{T}_j$ is the transfer matrix across jth layer. Let us consider that 't_s' and 'r_s' are the amplitudes of transmission and reflection coefficients of that structure containing 'm' layers. We further consider that n_{left} and n_{right} are the refractive indices of those two semi-infinite media before and after the structure. Therefore, the continuity equation becomes

$$\widehat{T} \begin{bmatrix} 1 + r_s \\ n_{\text{left}} - n_{\text{left}} r_s \end{bmatrix} = \begin{bmatrix} t_s \\ n_{\text{right}} t_s \end{bmatrix}. \tag{3.12}$$

With a few mathematical steps, we can obtain r_s and t_s as

$$r_s = \frac{n_{\text{right}} t_{11} + n_{\text{left}} n_{\text{right}} t_{12} - t_{21} - n_{\text{left}} t_{22}}{t_{21} - n_{\text{left}} t_{22} - n_{\text{right}} t_{11} + n_{\text{left}} n_{\text{right}} t_{12}} \tag{3.13}$$

$$t_s = 2 n_{\text{left}} \frac{t_{12} t_{21} - t_{11} t_{22}}{t_{21} - + n_{\text{left}} n_{\text{right}} t_{12} - n_{\text{left}} t_{22} - n_{\text{right}} t_{11}} \tag{3.14}$$

Using Eqs. (3.6) and (3.7), we can finally calculate the desired properties

$$R = |r_{\mathrm{s}}|^2 \tag{3.15}$$

$$T = |t_{\mathrm{s}}|^2 \frac{n_{\mathrm{right}}}{n_{\mathrm{left}}} \tag{3.16}$$

If we consider the structure as symmetrical w.r.t incident and propagation of e.m wave and also w.r.t refractive indices of the interfaces, i.e. $n_{\mathrm{left}} = n_{\mathrm{right}} \equiv n$ (this situation is analogous to the cavity-embedded quantum well), then the boundary conditions lead to:

$$\begin{gathered} \widehat{T}\begin{bmatrix} 1 + r_{\mathrm{s}} \\ n - nr_{\mathrm{s}} \end{bmatrix} = \begin{bmatrix} t_{\mathrm{s}} \\ nt_{\mathrm{s}} \end{bmatrix} \\ T\begin{bmatrix} t_{\mathrm{s}} \\ -nt_{\mathrm{s}} \end{bmatrix} = \begin{bmatrix} 1 + r_{\mathrm{s}} \\ -n + nr_{\mathrm{s}} \end{bmatrix} \end{gathered} \tag{3.17}$$

Solution of Eq. (3.17) leads to the actual composite transfer matrix

$$\widehat{T} = \frac{1}{2t}\begin{bmatrix} t_{\mathrm{s}}^2 - r_{\mathrm{s}}^2 + 1 & -\frac{(1+r_{\mathrm{s}})^2 - t_{\mathrm{s}}^2}{n} \\ n\left((r_{\mathrm{s}} - 1)^2 - t_{\mathrm{s}}^2\right) & t_{\mathrm{s}}^2 - r_{\mathrm{s}}^2 + 1 \end{bmatrix} \tag{3.18}$$

Now we have to introduce independently both the polarization conditions. First we will insert the condition for TE mode for which boundary conditions of field components will be modified with the following substitutions:

$$k_z = k\cos\theta$$

$$n \to n\cos\theta \tag{3.19}$$

where 'θ' is angle of propagation.

Similarly, we can proceed for *TM* polarization, following the Born and Wolf approximation, substitutions become

$$k_z = k\cos\theta$$

$$n \to \frac{\cos\theta}{n} \tag{3.20}$$

Introducing suitable suffixes considering propagation from left to right, Eqs. (3.18) and (3.19) can be reformulated as for TE polarization

$$n_{\mathrm{left}} \to n_{\mathrm{left}} \cos\theta_{\mathrm{left}}$$

$$n_{\mathrm{right}} \to n_{\mathrm{right}} \cos\theta_{\mathrm{right}} \tag{3.21}$$

and for *TM* polarization

$$n_{\text{left}} \rightarrow \frac{\cos\theta_{\text{left}}}{n_{\text{left}}}$$
$$n_{\text{right}} \rightarrow \frac{\cos\theta_{\text{right}}}{n_{\text{right}}} \tag{3.22}$$

3.2 Eigenmodes for Planar Photonic Structure

Formulation of Sect. 3.1 can now be extended for a multilayer/stack structure which is obviously planar in nature. The structure is characterized by $\hat{T}$ which is nothing but the product of all the transfer matrices as computed in each individual interfaces including the two ends as depicted in Eq. (3.11). Photonic eigenmodes for this structure can be computed using the conservation of energy principle which satisfies the Maxwell equations with boundary conditions: incidence of any e.m wave is prohibited from both the sides, $z \rightarrow -\infty$ and $z \rightarrow +\infty$. This tunes the expression of electric field of the eigenmode at $z \rightarrow -\infty$ as

$$\vec{E}_0 \mathrm{e}^{ik_x x + ik_y y + ik_z z} \tag{3.23}$$

For TE polarization, we define the Cartesian system in such a way that the field vectors can be defined in the following manner:

$$\vec{E} = \begin{pmatrix} 0 & E_y & 0 \end{pmatrix} \tag{3.24}$$

$$\vec{B} = \begin{pmatrix} B_x & 0 & B_z \end{pmatrix} \tag{3.25}$$

The transfer matrix under that polarization concerned $\hat{T}_{\text{TE}}$ can be correlated with the existing field vectors $\begin{pmatrix} E_y \\ B_x \end{pmatrix}$ at both the boundaries, so that

$$\widehat{T}_{\text{TE}} \begin{pmatrix} E_y^{\text{left}} \\ B_x^{\text{left}} \end{pmatrix} = \begin{pmatrix} E_y^{\text{right}} \\ B_x^{\text{right}} \end{pmatrix} \tag{3.26}$$

Substitution of the electric field in Eq. (3.2) yields

$$\frac{\kappa_z}{\kappa_0} E_y = B_x \tag{3.27}$$

where $\kappa_0 = \frac{\omega}{c}$.

Therefore, we can modify Eq. (3.26) as

$$\hat{T}_{\mathrm{TE}}\begin{pmatrix} 1 \\ \frac{\kappa_z^{\mathrm{left}}}{\kappa_0} \end{pmatrix} = A\begin{pmatrix} 1 \\ \frac{\kappa_z^{\mathrm{right}}}{\kappa_0} \end{pmatrix} \tag{3.28}$$

where κ_z^{left} and $\kappa_z^{\mathrm{right}}$ are wave vectors along Z-axis.

The transcendental equation for the eigenmodes of the structure:

$$t_{11}^{\mathrm{TE}}\frac{\kappa_z^{\mathrm{right}}}{\kappa_0} + t_{12}^{TE}\frac{\kappa_z^{\mathrm{left}}\kappa_z^{\mathrm{right}}}{\kappa_0^2} - t_{21}^{\mathrm{TE}} - \frac{\kappa_z^{\mathrm{left}}}{\kappa_0}t_{22}^{\mathrm{TE}} = 0 \tag{3.29}$$

where t_{ij} have usual meanings as matrix elements of $\hat{T}_{\mathrm{TE}}$. Solution of Eq. (3.29) leads to complex values of frequencies. Henceforth, we have to consider only those values as real solutions which consist of positive real values and zero imaginary values. So solution numbers will be limited, and they can only carry the practical aspects.

Similar procedure can be taken for TM mode also. Again, we have to choose respective Cartesian system along with existing field components as given by

$$\vec{E} = \begin{pmatrix} E_x & 0 & E_z \end{pmatrix} \tag{3.30}$$

$$\vec{B} = \begin{pmatrix} 0 & B_y & 0 \end{pmatrix} \tag{3.31}$$

The transfer matrix under that polarization concerned $\hat{T}_{\mathrm{TM}}$ can be correlated with the existing field vectors $\begin{pmatrix} B_y \\ -E_x \end{pmatrix}$ at both the boundaries

$$\hat{T}_{\mathrm{TM}}\begin{pmatrix} B_y^{\mathrm{left}} \\ -E_x^{\mathrm{left}} \end{pmatrix} = \begin{pmatrix} B_y^{\mathrm{right}} \\ -E_x^{\mathrm{right}} \end{pmatrix} \tag{3.32}$$

The Maxwell equation gives

$$-\frac{\kappa_z}{n^2\kappa_0}B_y = E_x \tag{3.33}$$

Therefore, modifying (3.32) as

$$\hat{T}_{\mathrm{TM}}\begin{pmatrix} 1 \\ \frac{\kappa_z^{\mathrm{left}}}{n_{\mathrm{left}}^2\kappa_0} \end{pmatrix} = A\begin{pmatrix} 1 \\ \frac{\kappa_z^{\mathrm{right}}}{n_{\mathrm{right}}^2\kappa_0} \end{pmatrix} \tag{3.34}$$

Corresponding transcendental equation is

$$t_{11}^{\mathrm{TM}}\frac{\kappa_z^{\mathrm{right}}}{n_{\mathrm{right}}^2\kappa_0}+t_{12}^{\mathrm{TM}}\frac{\kappa_z^{\mathrm{left}}\kappa_z^{\mathrm{right}}}{n_{\mathrm{left}}^2 n_{\mathrm{right}}^2\kappa_0^2}-t_{21}^{\mathrm{TM}}-\frac{\kappa_z^{\mathrm{left}}}{n_{\mathrm{left}}^2\kappa_0}t_{22}^{\mathrm{TM}}=0 \tag{3.35}$$

Progressing towards the condition of normal incidence, we find that both Eqs. (3.29) and (3.35) are identical. This also ensures the validity of our mathematical formulation.

Using appropriate transformations, both equations can be reduced to

$$t_{11}n_{\mathrm{right}}+n_{\mathrm{left}}t_{22}-t_{12}n_{\mathrm{right}}n_{\mathrm{left}}-t_{21}=0 \tag{3.36}$$

The condition for convergence for reflection and transmission coefficients assuming both the refractive indices at left and right boundaries may be written as

$$|r_{\mathrm{s}}|^2+\frac{n_{\mathrm{right}}}{n_{\mathrm{left}}}|t_{\mathrm{s}}|^2\le 1 \tag{3.37}$$

Now we will consider the unit cell for calculation for reflection and transmission coefficients.

3.3 Transmission Coefficient

We have now considered the smallest unit of one-dimensional photonic crystal structure, where propagating waves can be represented in generalized form

$$p_j=t_{ji}p_i+r_{ij}q_j \tag{3.38}$$

$$q_i=t_{ij}q_j+r_{ji}p_i \tag{3.39}$$

where t_{ij} and r_{ij} are transmissivity and reflectivity in passing from layer i to layer j (Fig. 1).

From the coupled wave equations, transfer matrix at the interface for ideal (defect-free) structure can be obtained as [31]

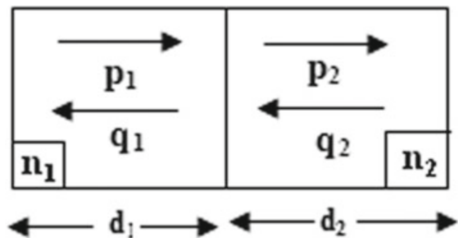

Fig. 1 Unit block of one-dimensional photonic crystal

$$M_{i,j}^{\mathrm{T}} = \frac{1}{t}\begin{pmatrix} 1 & r_{ji,ij} \\ r_{ji,ij} & 1 \end{pmatrix} \tag{3.40}$$

If we now consider the phase factor of the field components, then propagation matrix is given by

$$P_{i,j} = \begin{pmatrix} \mathrm{e}^{jk_{i,j}d_{i,j}} & 0 \\ 0 & -\mathrm{e}^{jk_{i,j}d_{i,j}} \end{pmatrix} \tag{3.41}$$

where 'd_j' is the length of propagation in jth layer, and 'k_j' is the wave vector in that layer.

With this consideration, transfer matrix for that simplest cell is

$$M = M_i^{\mathrm{T}} P_i M_j^{\mathrm{T}} P_j \tag{3.42}$$

Assuming the medium is periodic where the Bragg condition can now be applied, composed of 'C' simplest cells, total transfer matrix becomes

$$M_{\mathrm{tot}} = M_C \tag{3.43}$$

Therefore, the transmissivity is given by

$$T = \frac{1}{M_{11}^2(\mathrm{tot})} \tag{3.44}$$

In the presence of defect, Eq. (3.42) can be modified as [32]

$$P_{i,j}\big|_f = \begin{pmatrix} \exp[jk_{i,j}d_{i,j}]d_f & 0 \\ 0 & -\exp[jk_{i,j}d_{i,j}]d_f \end{pmatrix} \tag{3.45}$$

where 'd_f' is the point defect density. Using the same procedure as mentioned above, the transmission coefficient is again computed. From the knowledge of transmission coefficient, bandwidth of the structure is obtained as the difference between two consecutive notches which creates a passband.

4 Results and Discussions

Based on the formulation described in Sect. 3, we have calculated transmission coefficient for different material systems, and corresponding optical bandwidth is achieved. For simulation purpose, we have considered two metamaterials independently, namely paired nanorod ($n = -0.3$) and nanofishnet structure with elliptic void ($n = -4$). Using Eq. 3.45 and assuming defect density within the limited range,

transmissivity of both the structures are calculated and graphically characterized as a function of wavelength, where the central wavelength of passband is chosen as 1550 nm, for the purpose of implementing the device in optical communication. Results are computed in the presence of defect under oblique incidence and compared with the condition of the ideal structure, i.e. the defect is absent.

Figure 2 shows the transmittance profile in both ideal structure (structure without defect) and the defected one under TE mode of propagation [33]. From the plot, it can be concluded that the amount of ripple in the passband is less for the higher negative index materials, which is suitable for filter application. However, sharp notch in guard band is present for the other material system, and henceforth, a trade-off is required.

Effect of incidence angle is also computed for transmissivity analysis. From Fig. 3, it is seen that with increase in incidence angle, a significant amount of redshift is observed for paired nanorod structure, whereas the shift is negligible for the fishnet structure. Layer dimension also has a significant influence on filter characteristics, as already reported [29]. In this case, though bandwidth remains the same, overall a redshift of the spectrum is observed. Bandwidth can be tuned by changing the width of air. This is shown in Fig. 4.

Once transmissivity is calculated, the next step is to get the bandwidth around 1550 nm for the same defected structure. Here, we consider elliptical void structure. In Fig. 5a, it is disclosed that the bandwidth is remain fixed for metamaterial length up to 2.3 μm (which ranges from 2.29 to 2.34 μm). A sharp change of bandwidth at 2.3 μm, where bandwidth is increased to 0.04 μm, and again, it is varied at 2.32 μm, results in the change of bandwidth at 0.0408 μm. In Fig. 5b, it is observed

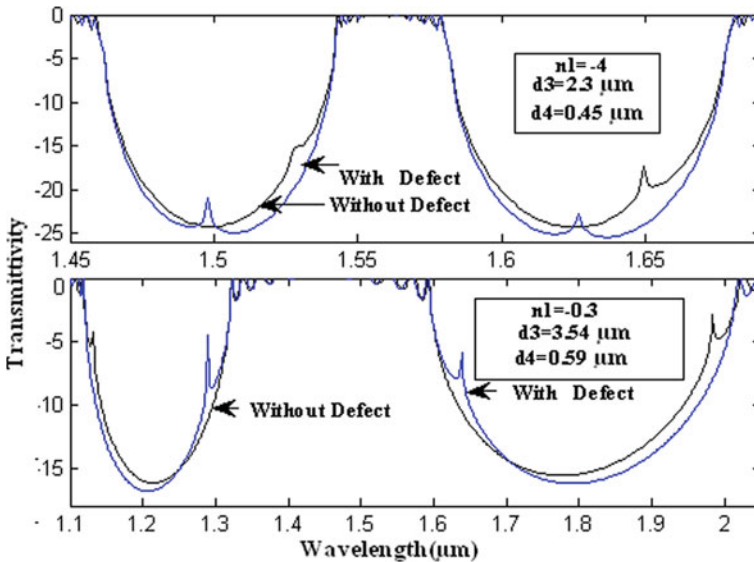

Fig. 2 Transmissivity with wavelength for TE mode for defected structure with different incident angles and for different refractive indices of metamaterials [33]

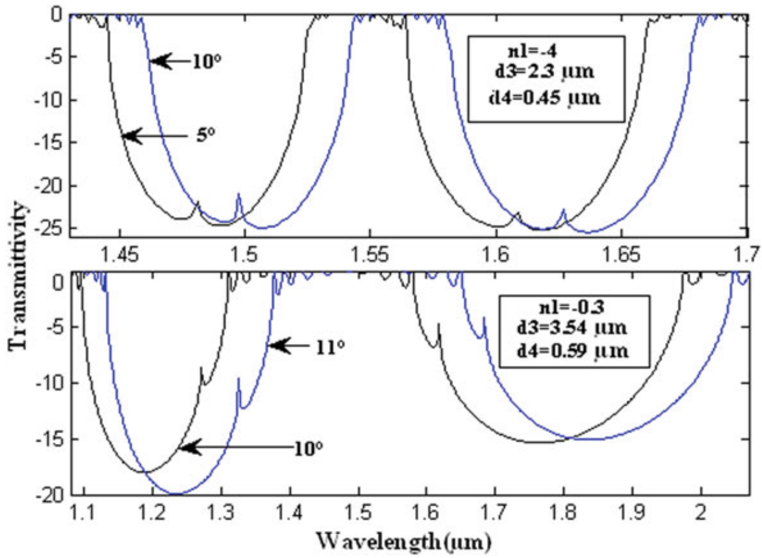

Fig. 3 Transmissivity with wavelength for TM mode for defected structure with different incident angles and for different refractive indices of metamaterials [33]

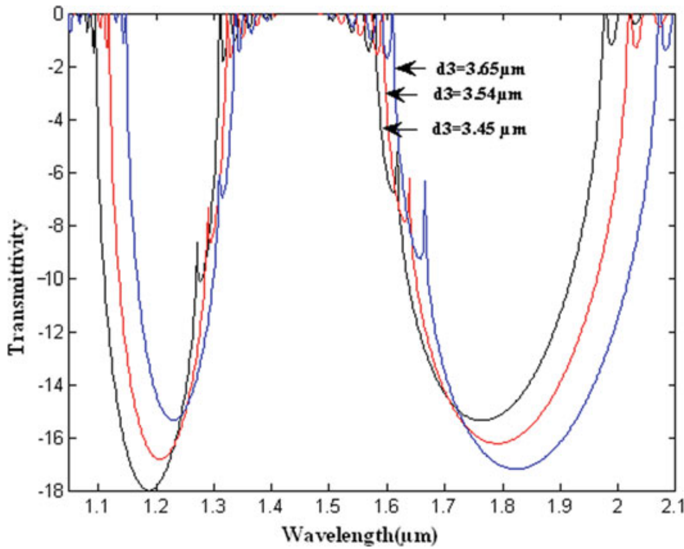

Fig. 4 Transmissivity with wavelength for TM mode for the defected structure with different propagation lengths of metamaterial [32]

that with slow increase variation in the air thickness, bandwidth is increased, and a sharp increase is seen from 0.50 μm air thickness which results in the variation of bandwidth (about 0.06 μm). It is almost continuous in nature.

In Fig. 6a, it is seen that the bandwidth is almost unchanged for the variation of metamaterial length (it is varied in a small range from 2.28 to 2.34 μm) except for a sharp change of bandwidth at 2.285 μm. At this point, bandwidth is increased to 0.04 μm. Again when metamaterial length becomes 2.33 μm, bandwidth rises upto 0.0408 μm. In Fig. 6b, it is observed that with the increase in variation of the air thickness, bandwidth is increased, and a sharp increase is seen from 0.55 μm air thickness which results in the variation of bandwidth (about 0.06 μm).

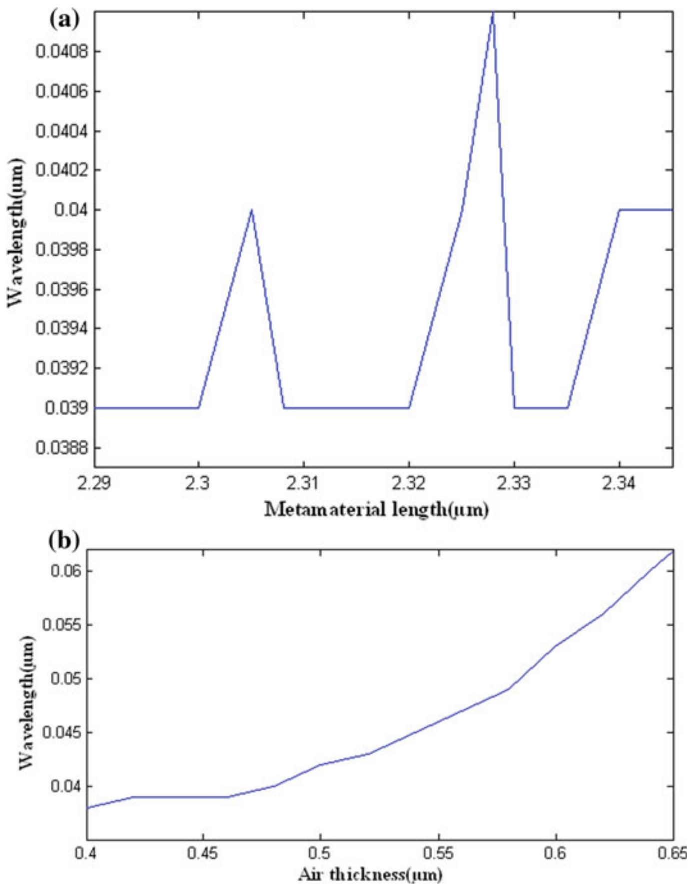

Fig. 5 **a** Bandwidth with length of metamaterial for normal incidence of EM wave for defected structure considering nanofishnet structure having elliptical void [34]. **b** Bandwidth with air thickness for normal incidence of EM wave for defected structure considering nanofishnet structure having elliptical void [34]

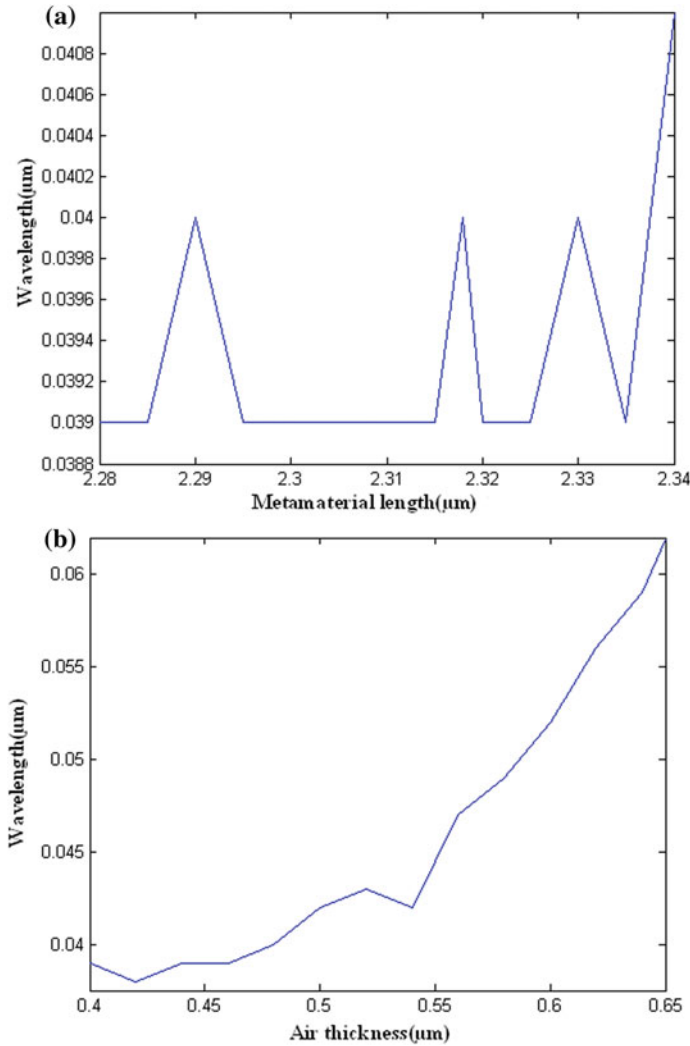

Fig. 6 **a** Bandwidth with length of metamaterial for oblique incidence (5° incident angle) under TE mode for defected structure considering nanofishnet structure having elliptical void. **b** Bandwidth with air thickness for oblique incidence (5° incident angle) under TE mode for defected structure considering nanofishnet structure having elliptical void

In Fig. 7a, keeping air thickness and metamaterial length fixed angle of incidence is varied (its variation is in the range from 0° to 11.5°). A change in bandwidth is noticed by means of increasing the incident angle at the interface (interface w.r.t air and material) which ranges from 9.5° to 11.5°. In Fig. 7b, the same process is maintained (i.e. keeping air thickness and metamaterial length fixed), and the angle of incidence is varied (it ranges from 0° to 11.5°). The bandwidth is changed

accordingly, and a notch is found at 1 m, where it shows its increasing wave of bandwidth up to 0.04 μm, and decreases at 8° (angle of incidence).

Similar results are obtained for paired nanorod structure, but from the characteristic point-of-view, minute but significant differences are observed. In Fig. 8a, optical bandwidth is drawn by changing angle of occurrence at the primary interface. It is

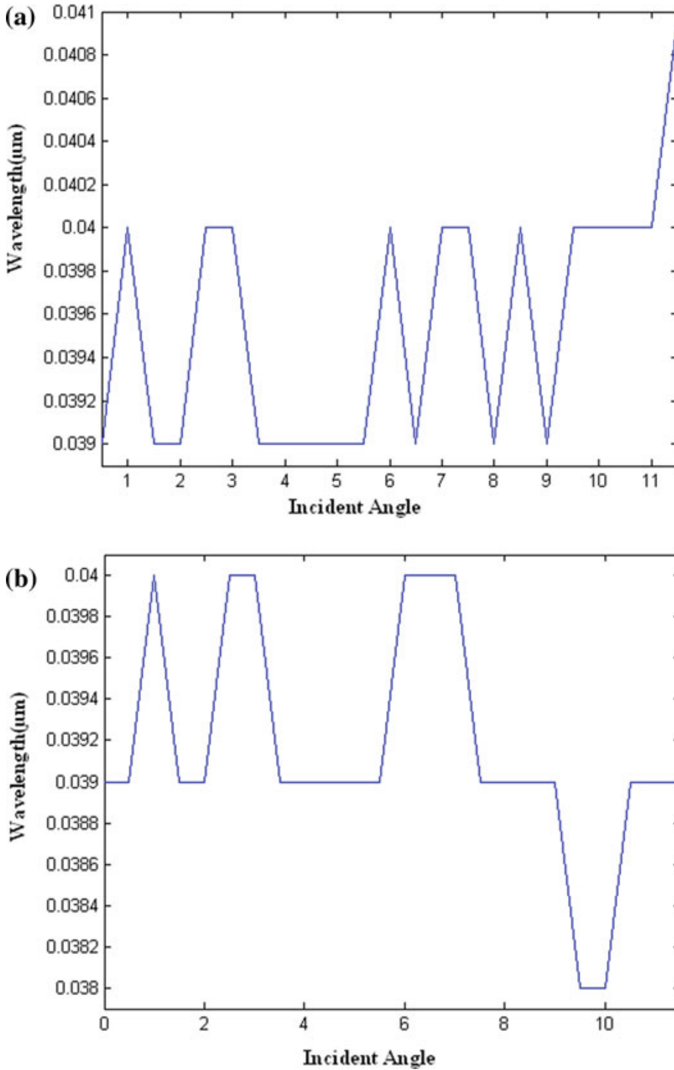

Fig. 7 **a** Bandwidth with incident angle under TE mode for defected structure considering nanofishnet structure having elliptical void. **b** Bandwidth with air thickness for oblique incidence (5° incident angle) under TE mode for defected structure considering nanofishnet structure having elliptical void

seen that the bandwidth is gradually increased for the increased variation of metamaterial length (its range is from 0.0318 to 0.33 μm). In Fig. 8b, it is observed that with slow increase variation in the air thickness, bandwidth is increased and almost forms a ramp structure (about 0.81 μm).

In Fig. 9a, it is seen that the bandwidth is monotonously increasing for the increasing variation of metamaterial length (its range is from 3.5 to 3.56 μm) except for

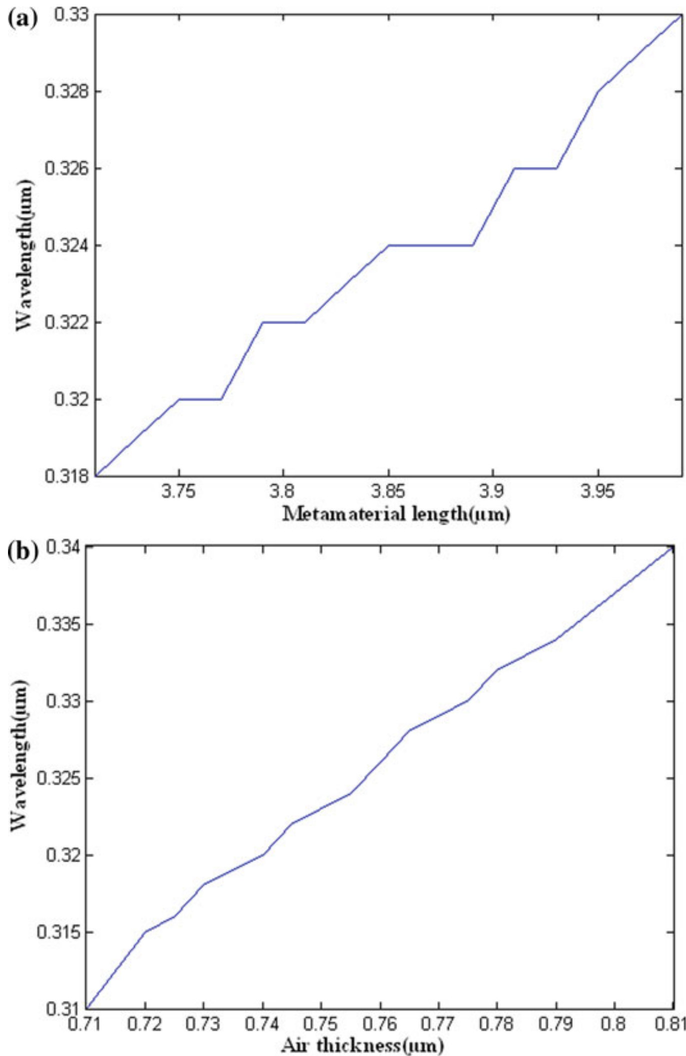

Fig. 8 **a** Bandwidth with length of metamaterial for normal incidence for defected structure considering paired nanorod. **b** Bandwidth with air thickness for normal incidence for defected structure considering paired nanorod

a sharp decrease in bandwidth at 3.56 μm. In Fig. 9b, it is observed that with slow increase variation in the air thickness, bandwidth is increased (about 0.63 μm).

In Fig. 10a, keeping air thickness and metamaterial length fixed angle of incidence is varied (its variation is in the range from 9° to 13°). Here, the bandwidth is changed with the increase in angle of incidence which ranges from 9° to 13° and almost forms a ramp structure. In Fig. 10b, here the same process is maintained (i.e. keeping air

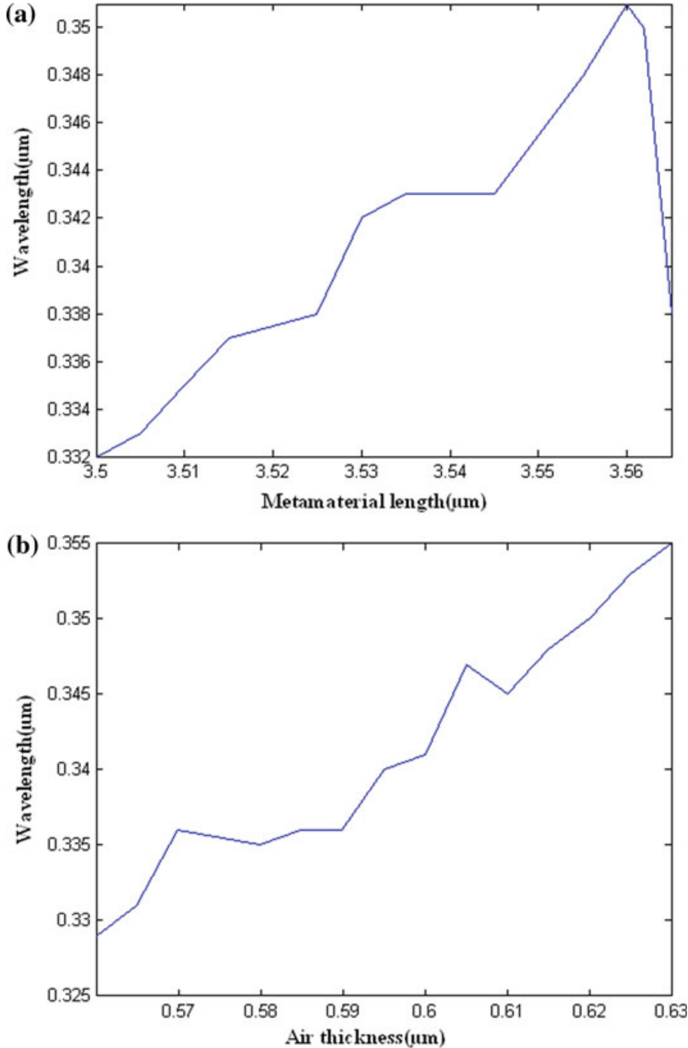

Fig. 9 **a** Bandwidth with length of metamaterial for oblique incidence (10° incident angle) TE mode for defected structure considering paired nanorod. **b** Bandwidth with air thickness for oblique incidence (10° incident angle) TE mode for defected structure considering paired nanorod

thickness and metamaterial length fixed), and the angle of incidence is varied (it ranges from 9° to 13°). The bandwidth is changed accordingly and forms a parabolic structure.

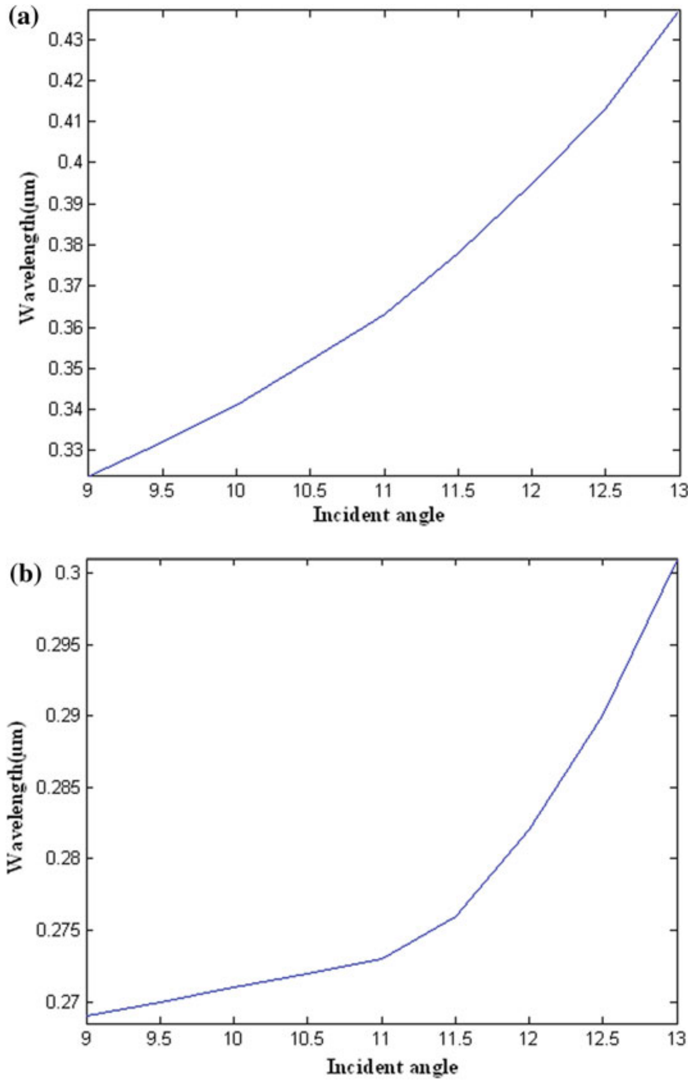

Fig. 10 **a** Bandwidth with incidence angle for TE mode for defected structure considering paired nanorod. **b** Bandwidth with incidence angle for TM mode for defected structure considering paired nanorod

5 Conclusion

Henceforth, all possible bandwidth variations are illustrated in this section for both TE and TM mode of propagations, where 1550 nm is considered as the central wavelength for the filter design. From the results, it can very easily be concluded that THz bandwidth can be obtained for 1D PhC-based filter, where the nanometric change in layer dimensions at the time of fabrication leads to the fluctuation in bandwidth. Moreover, the change of incidence angle also changes the bandwidth. Henceforth, simulation findings are extremely crucial for determining the optical properties before making the photonic integrated circuits. Results also speak about the range of incidence angle required for making the filter under operating condition, for both TE and TM modes. A comparative study suggests that paired nanorod provides a continuous monotonic increment of bandwidth with the change of incidence angle for both the modes, which is not possible once nanofishnet structure is considered. However, the nanofishnet structure provides a higher frequency of operation which is beyond to 10^{15} Hz. Hence, the compromization is required depending on the application requirement.

References

1. X. Lu, L. Hong, K. Sengupta, CMOS optical PUFs using noise-immune process-sensitive photonic crystals incorporating passive variations for robustness. IEEE J. Solid-State Circ. **53**(9), 2709–2721 (2018)
2. X. Zhang, H. Zhang, H. Li, The OAM transmission fiber based on circular photonic crystal fiber structure. in *16th International Conference on Optical Communications and Networks* (2017)
3. S. Olyaee, F. Taghipour, A new design of photonic crystal fiber with ultra-flattened dispersion to simultaneously minimize the dispersion and confinement loss. J. Phys. Conf. Ser. 3rd Int. Photon. OptoElectron. Meet. **276**, 012080 (2011)
4. R. Ahmad, M. Komanec, D. Suslov, S. Zvanovec, Modified octagonal photonic crystal fiber for residual dispersion compensation over telecommunication bands. Radioengineering **27**(1), 10–14 (2018)
5. J.S. Jensen, O. Sigmund, Topology optimization of building blocks for photonic integrated circuits. in *6th World Congresses of Structural and Multidisciplinary Optimization* (2005)
6. D. Mao, Z. Ouyang, J.C. Wang, A photonic-crystal polarizer integrated with the functions of narrow bandpass and narrow transmission angle filtering. Appl. Phys. B **90**, 127–131 (2008)
7. Y. Xu, J. Lin, R. Dubé-Demers, S. LaRochelle, L. Rusch, W. Shi, A single-laser flexible-grid WDM silicon photonic transmitter using microring modulators. in *Optical Fiber Communication Conference, OSA Technical Digest, paper W1I.3* (2018)
8. K. Nozaki, S. Matsuo, T. Fujii, K. Takeda, E. Kuramochi, A. Shinya, M. Notomi, Forward-biased photonic crystal photodetector towards amplifier-free bias-free receiver. in *Conference on Lasers and Electro-Optics, OSA Technical Digest*, *paper STh4N.1* (2017)
9. S. Saravi, T. Pertsch, F. Setzpfandt, Photonic crystal waveguides as integrated sources of counter propagating factorizable photon pairs. in *Conference on Lasers and Electro-Optics: OSA Technical Digest* (2018), p. FTh1G.2
10. T.W. Lu, C.C. Wu, P.T. Lee, 1D photonic crystal strain sensors. ACS Photon. **5**(7), 2767–2772 (2018)

11. R.M. Gerosa, P.G. Vianna, S.H. Domingues, C.J.S. de Matos, Reduced graphene oxide coated photonic crystal fiber for all-fiber laser mode locking. in *Conference on Lasers and Electro-Optics: OSA Technical Digest* (2019), p. STu4L.2
12. U.A. Laudyn, K.A. Rutkowska, R.T. Rutkowski, M.A. Karpierz, T.R. Woliński, J. Wójcik, Nonlinear effects in photonic crystal fibers filled with nematic liquid crystals. Cent. Eur. J. Phys. **6**(3), 612–618 (2008)
13. J.C. Norman, D. Jung, Y. Wan, J.E. Bowers, Perspective: the future of quantum dot photonic integrated circuits. APL Photon. **3**, 030901 (2018)
14. H. Chen, R. Lou, Y. Chen, L. Chen, J. Lu, Q. Dong, Photonic crystal materials and their application in biomedicine. Drug Deliv. **24**(1), 775–780 (2017)
15. E. Armstronga, C. O'Dwyer, Artificial opal photonic crystals and inverse opal structures—fundamentals and applications from optics to energy storage. J. Mater. Chem. C **3**, 6109–6143 (2015)
16. J. Zhao, X. Li, L. Zhong, G. Chen, Calculation of photonic band-gap of one dimensional photonic crystal. J. Phys: Conf. Ser. **183**(1), 012018 (2009)
17. S. Prakash, G. Sharma, G.C. Yadav, V. Singh, Photonic band gap alteration in $LiNbO_3$-SiO_2 based 1D periodic multilayered structure via plate wave. Silicon **11**, 1–7 (2018)
18. T. Yuan, T. Feng, Y. Xu, Manipulation of transmission by engineered disorder in one-dimensional photonic crystals. Opt. Expr. **27**, 6483–6494 (2019)
19. H. Hardhienata, A.I. Aziz, D. Rahmawati, H. Alatas, Transmission characteristics of a 1D Photonic crystal sandwiched by two graphene layers. J. Phys. Conf. Ser. **1057**, 012003 (2018)
20. A. Deyasi, S. Banerji, S. Bose, A. Halder, Analytical computation of band structure of 1D photonic crystal under normal incidence of electromagnetic wave. in *Lecture Notes in Electrical Engineering: Computational Advancement in Communication Circuits and Systems, Part 6: Advances in Devices and Circuit (Chap. 36)*, vol. 335 (2014), pp. 331–338
21. D. Devashish, S.B. Hasan, J.J.W. van der Vegt, W.L. Vos, Reflectivity calculated for a three-dimensional silicon photonic band gap crystal with finite support. Phys. Rev. B **95**, 155141 (2017)
22. F. Meng, Y. Li, S. Li, H. Lin, B. Jia, X. Huang, Achieving large band gaps in 2D symmetric and asymmetric photonic crystals. J. Lightw. Technol. **35**(9), 1670–1676 (2017)
23. F. Pommereau, M. Attali, R. Brenot, C. Cuisin, E. Derouin, O. Drisse, G.H. Duan, J. Landreau, L.L. Gouezigou, O.L. Gouezigou, F. Lelarge, F. Poingt, B. Rousseau, Technologies and applications of two-dimensional InP-based photonic crystals. in *IEEE International Conference on Indium Phosphide and Related Materials Conference Proceedings* (2006)
24. N.R. Ramanujam, K.S.J. Wilson, P. Mahalakshmi, S. Taya, Analysis of photonic band gap in photonic crystal with epsilon negative and double negative materials. Optik **183**, 203–210 (2019)
25. K.R. Jha, G. Singh, Analysis and design of terahertz microstrip antenna on photonic bandgap material. J. Comput. Electron. **11**(4), 364–373 (2012)
26. J. Čtyroký, J.G. Wangüemert-Pérez, P. Kwiecien, I. Richter, J. Litvik, J.H. Schmid, Í. Molina-Fernández, A. Ortega-Moñux, M. Dado, P. Cheben, Design of narrowband Bragg spectral filters in subwavelength grating metamaterial waveguides. Opt. Express **26**(1), 179–194 (2018)
27. Z. Jiao, R. Ning, Y. Xu, J. Bao, Tunable angle absorption of hyperbolic metamaterials based on plasma photonic crystals. Phys. Plasmas **23**, 063301 (2016)
28. I. Al-Naib, W. Withayachumnankul, J. Infr. Millim. Terahertz Waves **38**(9), 1031–1033 (2017)
29. S. Ghosh, R. Dutta, V. Shaw, A. Deyasi, Improved noise rejection in metamaterial based defected photonic crystal structure. in *Springer Proceedings in Physics: Advances in Optical Science and Engineering (Chap. 62)* (2017), pp. 507–512
30. A. Deyasi, A. Sarkar, Variation of optical bandwidth in defected ternary photonic crystal under different polarisation conditions. Int. J. Nanopart. **10**(1–2), 27–34 (2018)
31. A. Maity, B. Chottopadhyay, U. Banerjee, A. Deyasi, Novel band-pass filter design using photonic multiple quantum well structure with p-polarized incident wave at 1550 nm. J. Elect. Dev. **17**, 1400–1405 (2013)

32. P. Biswas, A. Deyasi, Computing transmissivity of one-dimensional defected photonic crystal under polarized incidence for band-pass filter applications. J. Electr. Dev. **21**, 1816–1822 (2015)
33. A. Deyasi, S. Ghosh, R. Dutta, V. Shaw, Comparative analysis of filter performance in DNG material based photonic crystal structure. in *Advancement of Computer Communication and Information Technology* (2016), pp. 181–184
34. A. Deyasi, A. Sarkar, Computing optical bandwidth of bandpass filter using metamaterial-based defected 1D PhC. AIP Conf. Proc. **2072**, 020003 (2019)

Terahertz Radiators Based on Silicon Carbide Avalanche Transit Time Sources—Part I: Large-Signal Characteristics

S. J. Mukhopadhyay, P. Mukherjee, A. Acharyya and M. Mitra

Abstract The static and high-frequency simulations have been performed to explore the potency of avalanche transit time (ATT) oscillators based upon wide bandgap (WBG) semiconducting substances like 3C-SiC and type-IIb diamond (C) as millimeter-wave (mm-wave) and terahertz (THz) wave generators; characteristics of those sources have been compared with the DDR IMPATTs on the basis of traditional substance, i.e., Si. A non-sinusoidal voltage excited (NSVE) large-signal simulation procedure has been employed here to scrutinize the static and large-signal features of the sources. The simulation studies show that the DDR 3C-SiC IMPATTs possess better RF power delivery capability from 140 GHz to 1.0 THz as compared to the diamond IMPATTs, whereas the diamond IMPATT source is a better option for RF power generation at 94 GHz due to its better power generation capability at lower mm-wave frequencies. However, IMPATT sources based on both 3C-SiC and diamond are much powerful in comparison with mm-wave and THz IMPATT sources based on Si.

Keywords 3C-SiC · Diamond · IMPATT · Millimeter-wave · Si · Terahertz

1 Introduction

This is widely recognized that impact avalanche transit time (IMPATT) devices proved the capacity of generating sufficient power at microwave, millimeter-wave, and terahertz frequency bands [1–6]. Researchers had to choose THz frequency domain because of overcrowd in lower frequency bands for communication. The

S. J. Mukhopadhyay · M. Mitra
Department of ETC, IIEST, Shibpur, Howrah, West Bengal 711103, India

P. Mukherjee
Department of Electrical Engineering, Cooch Bihar Government Engineering College, Cooch Behar, West Bengal 736170, India

A. Acharyya (✉)
Department of Electronics and Communication Engineering, Cooch Bihar Government Engineering College, Cooch Behar, West Bengal 736170, India
e-mail: ari_besu@yahoo.co.in

© Springer Nature Singapore Pte Ltd. 2020
A. Biswas et al. (eds.), *Emerging Trends in Terahertz Solid-State Physics and Devices*,
https://doi.org/10.1007/978-981-15-3235-1_2

THz frequency band has enormous necessity like imaging [7], spectrum analysis [8], nano-electronic [9], inspection services [10, 11], drug industry [12, 13], space research [14], etc. Despite enormous application probability of THz frequency band, this area is yet to be utilized because of unavailability of potential solid-state sources that may produce, identify terahertz frequencies. In the last part of the twentieth century, when the development of IMPATT devices gained its momentum then basically fabrication was done by using germanium (Ge) and silicon (Si) as semiconducting substance. But at present, Ge IMPATTs are no longer in existence. Due to very fast development of Si process technology, single-drift and double-drift region (i.e., SDR and DDR) Si IMPATTs have received appreciable attention due to capacity of producing greater RF power with considerable conversion efficiency at mm-wave frequencies [15–18].

Recently, wide bandgap (WBG) materials like SiC and diamond IMPATT sources exhibited the capacity of producing high mm-wave and terahertz power [19–22]. The group IV-IV compound material SiC has different polytypes forms like 2H-SiC, 4H-SiC, 6H-SiC, and 3C-SiC; fabrication of 4H-SiC IMPATT source has already been reported [21]. However, very low RF power output (in the order of milli-watts) was reported from 4H-SiC IMPATT source at microwave frequencies [21]. Simulations reveal that the 4H-SiC IMPATTs possess the capacity of generating high mm-wave power (~watts) with significantly high efficiency [19, 20, 22]. One major problem of 4H-SiC IMPATT devices is its high series resistance. This high series resistance problem can be eliminated by replacing 4H-SiC with 3C-SiC since the mobility of electrons and holes in 3C-SiC are higher than those of 4H-SiC. Thus, authors have taken 3C-SiC-based IMPATTs for operation at high-frequency regime.

Type-IIb diamond being very inspiring WBG material and researchers have preferred it for best quality features. In the year 1976, it was termed as carbon and afterward it was synthesized in 1954. The favorable mechanical and thermal properties of diamond coupled with the development of its growth technique made great interest to utilize this substance to fabricate high-power-high-frequency semiconductor devices. Devices which are diamond-based like MESFET, IMPATT diode, and BJT have been reported by Trew et al. in 1991 as useful sources of microwave power [23]. Diamond-based IMPATTs can also be developed as potential high-power mm-wave [24] and THz sources.

As far as this chapter is concerned, the results of a co-relative research among Si, 3C-SiC, and type-IIb diamond-based IMPATT sources operating at various mm-waves, and THz frequency bands have been presented. This comparative study is very much important in order to discover the potency of 3C-SiC IMPATT as a suitable solid-state source at the specified frequency bands.

2 Substance Parameters and Design Strategy

The electric field (ξ) dependences of ionization rate ($\alpha_{n,p}$) and drift velocity ($v_{n,p}$) of electrons and holes in Si, 3C-SiC, and diamond are expressed as

$$\alpha_{n,p}(\xi) = A_{n,p} \exp\left(-\frac{B_{n,p}}{\xi}\right) \text{ and } v_{n,p}(\xi) = v_{\text{sn,sp}}\left[1 - \exp\left(-\frac{\mu_{n,p}\xi}{v_{\text{sn,sp}}}\right)\right] \quad (1)$$

where $A_{n,p}, B_{n,p}$ are of ionization coefficients, and v_{sn}, v_{sp} are saturation drift velocities of electrons and holes, respectively. Important material parameters of Si, 3C-SiC, and diamond have been drawn from various published reports [25–31].

Operating frequency of IMPATT device depends upon carrier transit time (τ_T). Double-drift region (DDR) IMPATT diode having n^+-n-p-p^+ structure, initially designed for a definite frequency (f_d) from the transit time formula, is focused by Sze et al. [32]. Then, the design parameters are optimized via the large-signal simulation technique based on NSVE model [33]. The design parameters of Si, 3C-SiC, and diamond are listed in Table 1.

Table 1 Design parameters

Base material	Design frequency, f_d (GHz)	n-layer thickness, W_n (nm)	p-layer thickness, W_p (nm)	n-layer doping concentration, N_D ($\times10^{23}$ m^{-3})	p-layer doping concentration, N_A ($\times10^{23}$ m^{-3})	n^+- and p^+-layer doping concentrations, N_{Sub} ($\times10^{26}$ m^{-3})
Si	94	400.0	380.0	1.20	1.25	1.00
	140	280.0	245.0	1.80	2.10	1.00
	220	180.0	160.0	3.95	4.59	1.00
	300	132.0	112.0	6.00	7.30	1.00
	500	72.0	70.0	15.0	16.2	1.00
3C-SiC	94	410.0	410.0	2.50	2.50	1.00
	140	300.0	300.0	5.00	5.00	1.00
	220	200.0	200.0	8.00	8.00	1.00
	300	160.0	160.0	11.00	11.00	1.00
	500	103.0	103.0	16.50	16.50	1.00
	1000	57.0	57.0	23.50	22.50	1.00
Type-IIb diamond	94	780.0	780.0	0.460	0.530	1.00
	140	530.0	530.0	0.810	0.870	1.00
	220	320.0	320.0	1.350	1.490	1.00
	300	220.0	220.0	2.050	2.220	1.00
	500	120.0	120.0	3.750	4.100	1.00
	1000	52.0	52.0	9.500	10.00	1.00
	1500	30.0	30.0	36.00	37.00	1.00

3 NSVE Large-Signal Model

The small-signal simulation of an IMPATT oscillator provides some preliminary idea regarding the high-frequency performance of the source. Most popular and reliable small-signal model for IMPATT oscillators was formulated by Gummel et al. in the year 1967 [34]. After the pioneer work of Gummel et al. [34], several researchers and research groups have adopted their small-signal model for predicting the high-frequency performance of microwave, mm-wave, and THz IMPATT sources based on different semiconductor materials [35–38]. However, the small-signal simulation models are actually based on different simplified assumptions; out of those, one of the most important assumptions is that voltage modulation factor must be very small, around less than 5%, which is untrue for practical free-running IMPATT oscillators. Due to this unrealistic assumption, small-signal simulation fails to provide accurate information regarding the conversion efficiency and power output from IMPATT oscillators. The most realistic and very close to practical results can be achieved by performing large-signal simulation of IMPATT oscillators.

Several researchers had developed large-signal simulation models for IMPATT oscillators during 1968, 1969 [39, 40]. Most significant work was carried out by Gupta et al. [41] in the year 1973; they had proposed a current excited large-signal model for IMPATTs capable of predicting conversion efficiency and power output of IMPATT sources with very good accuracy. In the year 2013, Acharyya et al. proposed a NSVE large-signal model for IMPATT oscillators [42]; and later, they had investigated the influences of band-to-band tunneling, parasitic series resistance, skin effect, junction temperature, optical illumination, magnetic field, etc., on the large-signal characteristics of IMPATT sources based on different semiconductor materials as well as some potential heterostructures [33, 42–49]. Comparison with suitable experimental data available in literature has been used to validate NSVE large-signal simulation method [1, 5, 16, 17, 50–52].

The NSVE large-signal simulation provides complete time-domain as well as frequency-domain information if the free-running IMPATT sources are based on any semiconductor material or heterostructure. The one-dimensional (1-D) model of the DDR IMPATT device and its equivalent circuit of the diode embedded in resonant cavity are shown in Figs. 1 and 2, respectively. Suitable quantum corrections have been integrated in the said model for considering the effects of quantum tunneling, quantum confinement, etc., for simulating THz IMPATT diodes having very narrow

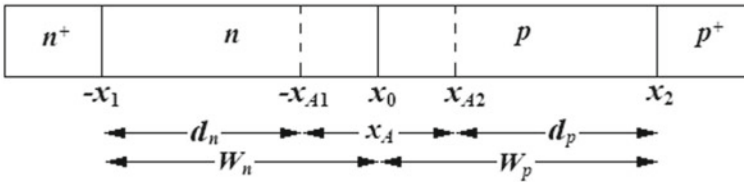

Fig. 1 1-D model for DDR IMPATT structure [42]

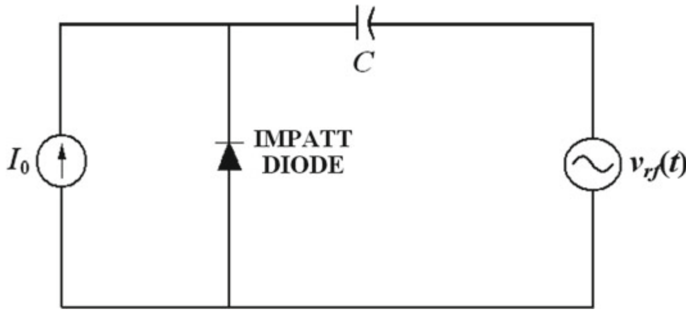

Fig. 2 Equivalent circuit for the voltage-driven IMPATT diode embedded in a resonant cavity under free oscillating condition [42]

dimensions [53, 54]. Examples of some large-signal simulation results of some popular semiconductor material-based IMPATT sources have been illustrated in Figs. 3,

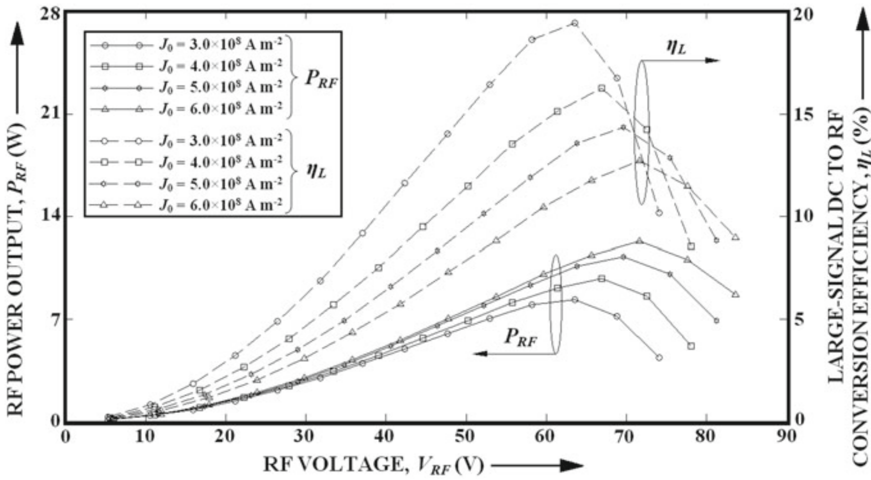

Fig. 3 Power output (P_{RF}) and conversion efficiency (η_L) of 94 GHz diamond IMPATT source versus RF voltage (V_{RF}) plots for different bias current densities (J_0) [55]

4 and 5 [43, 48, 55, 56].

4 Observations and Discussion

Primarily, the DC simulation is performed by obtaining the simultaneous solution device by imposing suitable boundary conditions at the n^+-n and p^+-p interfaces by using finite difference method (FDM), keeping voltage modulation factor equal to

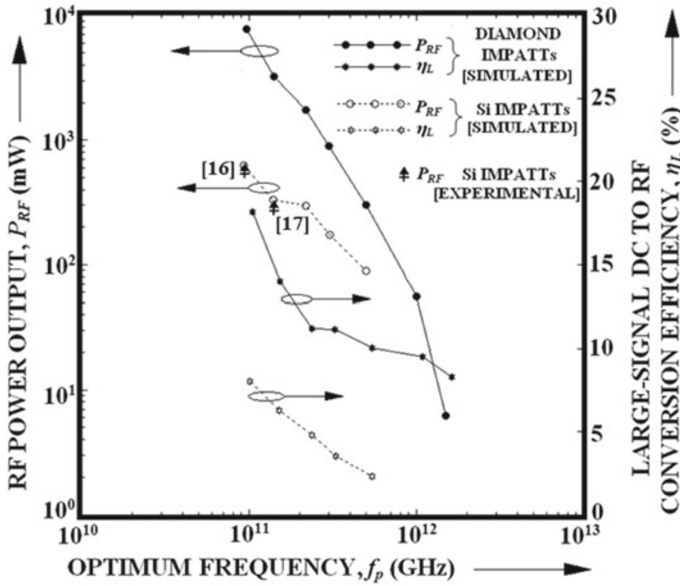

Fig. 4 Power output and conversion efficiency of Si and diamond IMPATT sources versus optimum frequency (f_p) plots [56]

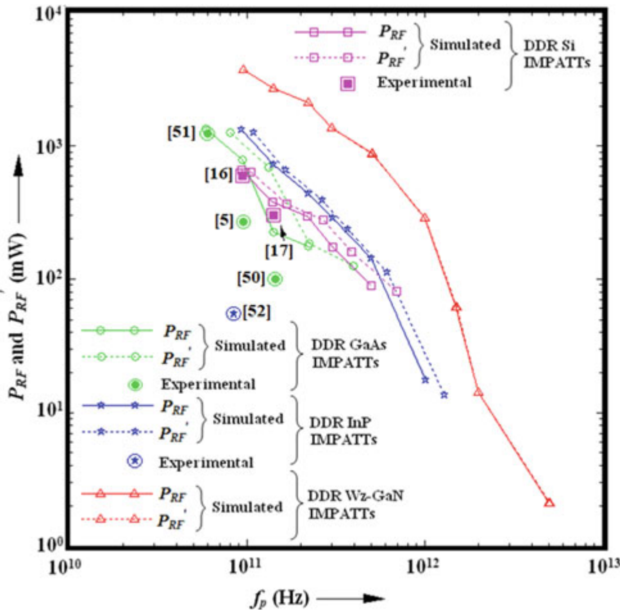

Fig. 5 Power output of GaAs, InP, Si, and Wz-GaN IMPATTs versus optimum frequency plots [43, 48]

zero. The changes of peak electric field (ξ_p), breakdown voltage (V_B), avalanche zone voltage (V_A), and avalanche layer width (x_A) of Si, 3C-SiC, and type-IIb diamond DDR IMPATTs versus operating frequency plots are shown in Figs. 6, 7 and 8, respectively. It is observed that ξ_p increases while V_B, V_A, and x_A decrease with operating frequency. It can be observed from Figs. 6 and 7 that the peak electric fields are minimum in 3C-SiC IMPATTs, while the breakdown voltages of those are largest among all. However, the IMPATT diodes based on 3C-SiC possess much broader avalanche zone beyond 140 GHz which indicates greater noise level of 3C-SiC-based source.

Significant large-signal parameters like optimum frequency (f_p), avalanche resonance frequency (f_a), peak negative conductance (G_p), susceptance (B_p), power output (P_{RF}), and efficiency (η_L) are acquired from large-signal simulation. The G_p and B_p versus f_p are illustrated in Figs. 9a, b, respectively. Highest magnitudes of G_p in 3C-SiC-based IMPATTs indicate the higher power delivery capability of those as compared to diamond and Si IMPATTs, which is reflected in Fig. 10a. At 94 GHz, diamond IMPATT delivers highest RF power. But the frequencies above 140 GHz, 3C-SiC-based IMPATTs are more suitable for the production of RF output power as per graph plotted in Fig. 10a. However, the DC to RF conversion efficiency of 3C-SiC IMPATTs is observed to be significantly low (much lower than the diamond and Si IMPATTs) due to their large bias current requirements. The bias current density (J_0), f_p, f_a and junction diameter (D_j) of the diodes are shown in Table 2.

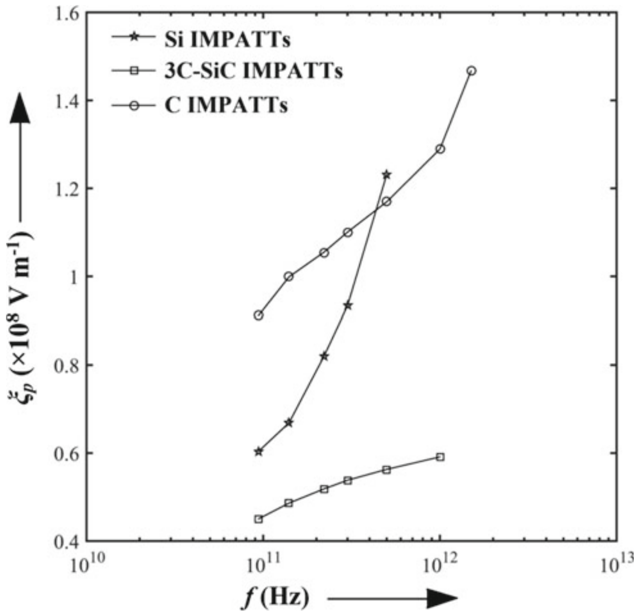

Fig. 6 Variations of peak electric field at metallurgical junction of Si, 3C-SiC, and type-IIb diamond-based IMPATT diodes with operating frequency

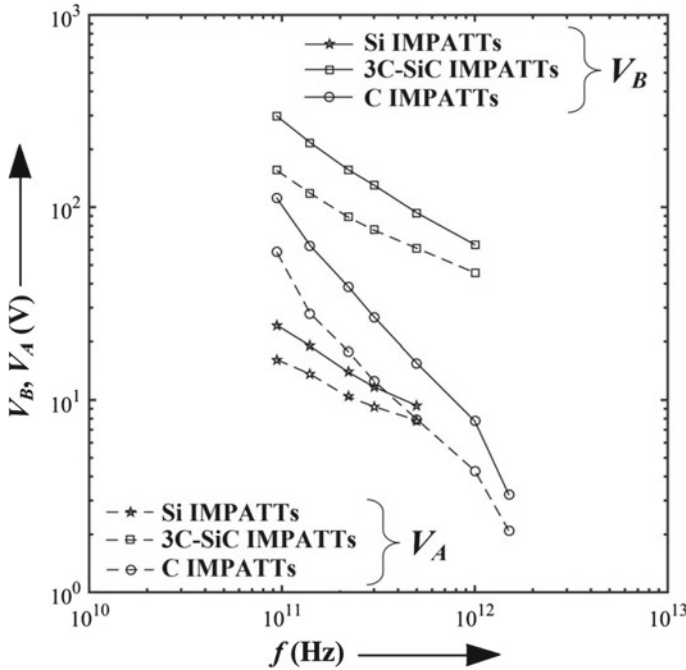

Fig. 7 Changes of V_B, V_A, and x_A of DDR IMPATT diodes based on Si, 3C-SiC, and diamond versus operating frequency plots

Experimentally measured power output of Si IMPATT sources are 600 and 300 mW at 94 and 140 GHz, respectively [16, 17], which are very close to the simulation results. This comparison with experimental results validates the simulation method highlighted herein. So far, at mm-wave or THz frequency band, experimental study on the 3C-SiC and diamond-based IMPATT devices are not available; that is why comparison could not be made with the simulation results.

5 Conclusion

The static and large-signal analysis have been carried out and presented here in order to focus the potentialities of DDR IMPATT sources based on WBG semiconductors like 3C-SiC and type-IIb diamond (C) as mm-wave and THz frequency radiators. High-frequency characteristics of those sources have been compared with the DDR IMPATTs based on the conventional semiconductor substance, i.e., Si. The simulation studies show that the DDR 3C-SiC IMPATTs possess better RF power delivery capability from 140 GHz to 1.0 THz as compared to the diamond IMPATTs, whereas the diamond IMPATT source is a better option for RF power generation at 94 GHz

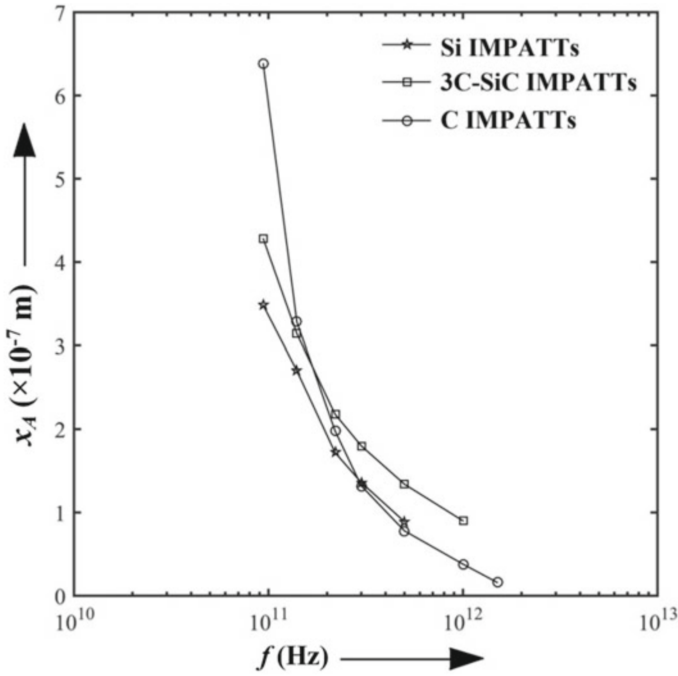

Fig. 8 Variations of avalanche zone width of Si, 3C-SiC, and diamond-based IMPATT diodes with operating frequency

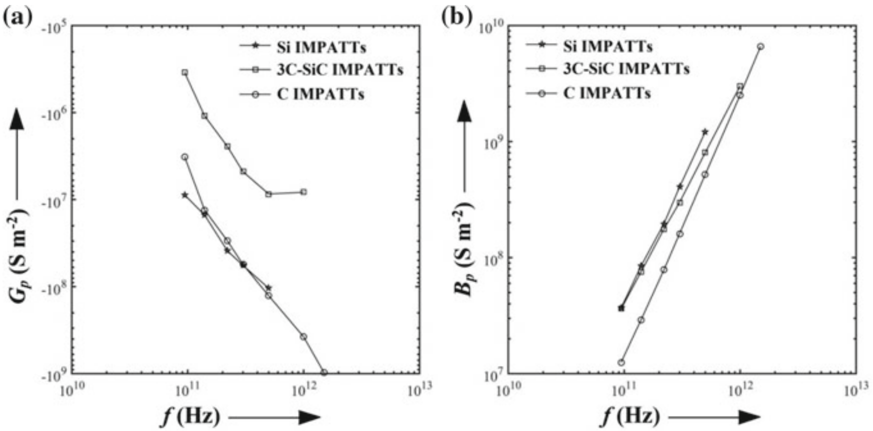

Fig. 9 Changes of **a** G_p and **b** B_p of Si, 3C-SiC, and diamond-based IMPATT sources versus operating frequency plots

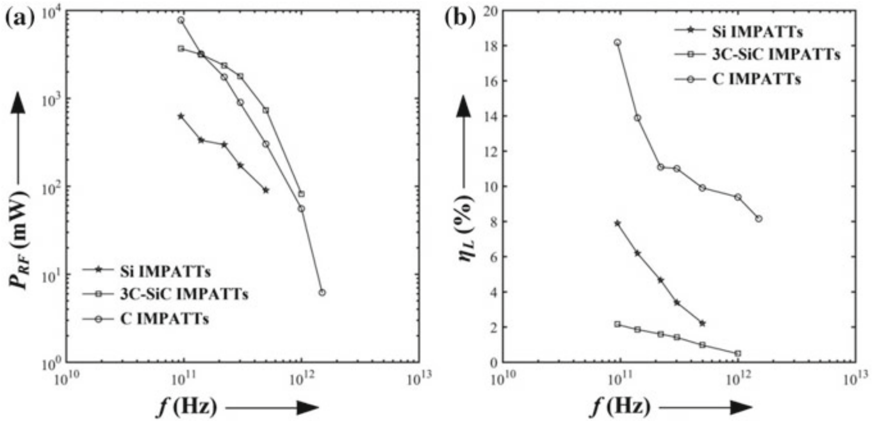

Fig. 10 Changes of **a** P_{RF} and **b** η_L of Si, 3C-SiC, and diamond-based IMPATT sources versus operating frequency plots

Table 2 Some important parameters of mm-wave and THz DDR Si, 3C-SiC, and type-IIb diamond IMPATTs

Base material	Parameter	Design frequency, f_d (GHz)						
		94	140	220	300	500	1000	1500
Si	J_0 ($\times 10^8$ A m^{-2})	3.40	5.80	14.50	24.50	55.00	–	–
	f_p (GHz)	93.0	139.5	218.5	301.5	501.5	–	–
	f_a (GHz)	52.0	70.9	111.5	141.3	196.7	–	–
	D_j (μm)	35.0	25.0	20.0	15.0	10.0	–	–
3C-SiC	J_0 ($\times 10^8$ A m^{-2})	6.00	16.00	30.00	55.00	104.00	135.00	–
	f_p (GHz)	94.40	146.20	226.30	308.80	529.50	1078.20	–
	f_a (GHz)	17.40	31	47.30	67.60	101.20	129.800	–
	D_j (μm)	35.0	25.0	20.0	15.0	10.0	5.0	–
Type-IIb diamond	J_0 ($\times 10^8$ A m^{-2})	4.00	7.50	13.00	17.00	25.00	39.00	48.00
	f_p (GHz)	95.6	140.0	218.0	301.0	502.0	1002.0	1501.0
	f_a (GHz)	49.5	99.0	144.5	192.1	283.9	469.0	704.4
	D_j (μm)	35.0	25.0	20.0	15.0	10.0	5.0	2.5

due to its better power generation capability at lower mm-wave frequencies. However, IMPATT sources based on both 3C-SiC and diamond are much powerful in comparison with mm-wave and THz Si IMPATTs.

Acknowledgements The authors deeply feel and acknowledge the help and spontaneous support rendered by the authority of IIEST, Shibpur, West Bengal, by making a suitable arrangement to perform the research work smoothly.

References

1. T.A. Midford, R.L. Bernick, Millimeter wave CW IMPATT diodes and oscillators. IEEE Trans. Microw. Theory Tech. **27**, 483–492 (1979)
2. R.E. Goldwasser, F.E. Rosztoczy, High efficiency GaAs low-hig-low IMPATTs. Appl. Phys. Lett. **25**, 92 (1974)
3. W.W. Gray, L. Kikushima, N.P. Morentc, R.J. Wagner, Applying IMPATT power sources to modern microwave systems. IEEE J. Solid-State Circ. **4**, 409–413 (1969)
4. Y. Chang, J.M. Hellum, J.A. Paul, K.P. Weller, Millimeter-wave IMPATT sources for communication applications. in *IEEE MTT-S International Microwave Symposium Digest* (1977), pp. 216–219
5. H. Eisele, Selective etching technology for 94 GHz, GaAs IMPATT diodes on diamond heat sinks. Solid State Electron. **32**(3), 253–257 (1989)
6. H. Eisele, GaAs W-band IMPATT diode for very low noise oscillations. Electron. Lett. **26**(2), 109–110 (1990)
7. W.L. Chan, J. Deibel, D.M. Mittleman, Imaging with terahertz radiation. Rep. Prog. Phys. **70**, 1325–1379 (2007)
8. D. Grischkowsky, S. Keiding, M. Exter, C. Fattinger, Far-infrared time-domain spectroscopy with terahertz beams of dielectrics and semiconductors. J. Opt. Soc. Am. B **7**, 2006–2015 (1990)
9. C. Debus, P.H. Bolivar, Frequency selective surfaces for high sensitivity terahertz sensing. Appl. Phys. Lett. **91**, 184102 (2007)
10. T. Yasui, T. Yasuda, K. Sawanaka, T. Araki, Terahertz paintmeter for noncontact monitoring of thickness and drying progress in paint film. Appl. Opt. **44**, 6849–6856 (2005)
11. C.D. Stoik, M.J. Bohn, J.L. Blackshire, Nondestructive evaluation of aircraft composites using transmissive terahertz time domain spectroscopy. Opt. Expr. **16**, 17039–17051 (2008)
12. A.J. Fitzgerald, B.E. Cole, P.F. Taday, Nondestructive analysis of tablet coating thicknesses using terahertz pulsed imaging. J. Pharm. Sci. **94**, 177–183 (2005)
13. P.H. Siegel, Terahertz technology in biology and medicine. IEEE Trans. Microw. Theory Tech. **52**, 2438–2447 (2004)
14. P.H. Siegel, THz instruments for space. IEEE Trans. Antenn. Propag. **55**, 2957–2965 (2007)
15. C. Dalle, P. Rolland, G. Lieti, Flat doping profile double-drift silicon IMPATT for reliable CW high power high-efficiency generation in the 94-GHz window. IEEE Trans. Electr. Dev. **37**, 227–236 (1990)
16. J.F. Luy, A. Casel, W. Behr, E. Kasper, A 90-GHz double-drift IMPATT diode made with Si MBE. IEEE Trans. Electr. Dev. **34**, 1084–1089 (1987)
17. M. Wollitzer, J. Buchler, F. Schafflr, J.F. Luy, D-band Si-IMPATT diodes with 300 mW CW output power at 140 GHz. Electron. Lett. **32**, 122–123 (1996)
18. D. Ghoshal, Measurement of electrical resistance of silicon single drift region IMPATT diode based on the study of the device and mounting circuit at threshold condition. J. Electron Dev. **11**, 625–631 (2011)
19. M. Mukherjee, S. Banerjee, J.P. Banerjee, Dynamic characteristics of III–V and IV–IV semiconductor based transit time devices in the terahertz regime: a comparative analysis. Terahertz Sci. Tech. **3**, 98–109 (2010)
20. M. Mukherjee, N. Mazumder, S.K. Roy, Prospects of 4H-SiC double drift region IMPATT device as a photo-sensitive high-power source at 0.7 terahertz frequency regime. Act. Passive Electron. Compon. **2009**, 1–9 (2009)

21. K.V. Vassilevski, K. Zekentes, A.V. Zorenko, L.P. Romanov, Experimental determination of electron drift velocity in 4H-SiC p^+-n-n^+ avalanche diodes. IEEE Electron Dev. Lett. **21**, 485–487 (2000)
22. A. Acharyya, J.P. Banerjee, Potentiality of IMPATT devices as terahertz source: an avalanche response time based approach to determine the upper cut-off frequency limits. IETE J. Res. **59**(2), 118–127 (2013)
23. R.J. Trew, J.B. Yan, P.M. Mock, The potentiality of diamond and SiC electronic devices for microwave and millimeter-wave power applications. Proc. IEEE **79**(5), 598–620 (1991)
24. P.M. Mock, R.J. Trew, RF performance characteristics of double-drift MM-wave diamond IMPATT diodes. *in Proceedings of IEEE/Cornell Conference Advanced Concepts in High-Speed Semiconductor Devices and Circuits* (1989), pp. 383–389
25. W.N. Grant, Electron and hole ionization rates in epitaxial silicon. Solid State Electron. **16**, 1189–1203 (1973)
26. R. Mickevicius, J.H. Zhao, Monte carlo study of electron transport in SiC. J. Appl. Phys. **83**, 3161–3167 (1998)
27. E.A. Konorova, Y.A. Kuznetsov, V.F. Sergienko, S.D. Tkachenko, A.K. Tsikunov, A.V. Spitsyn, Y.Z. Danyushevski, Impact ionization in semiconductor structures made of ion-implanted diamond. Sov. Phys. Semicond **17**, 146 (1983)
28. C. Canali, G. Ottaviani, A.A. Quaranta, Drift velocity of electrons and holes and associated anisotropic effects in silicon. J. Phys. Chem. Solids **32**, 1707–1720 (1971)
29. D.K. Ferry, High-field transport in wide-bandgap semiconductors. Phys. Rev. B **12**, 2361 (1975)
30. C. Canali, E. Gatti, S.F. Kozlov, P.F. Manfredi, C. Manfredotti, F. Nava, A. Quirini, Electrical properties and performances of neutral diamond nuclear radiation detectors. Nuclear Instrum. Methods **160**, 73 (1979)
31. C. Canali, E. Gatti, S.F. Kozlov, P.F. Manfredi, C. Manfredotti, F. Nava, A. Quirini, Electronic archive: new semiconductor materials, characteristics and properties. Available from http://www.ioffe.ru/SVA/NSM/Semicond/index.html. Last accessed on Sept 2019
32. S.M. Sze, R.M. Ryder, Microwave avalanche diodes. Proc. IEEE. Special Issue Microw. Semiconductor Dev. **59**, 1140–1154 (1971)
33. A. Acharyya, J. Chakraborty, K. Das, S. Datta, P. De, S. Banerjee, J.P. Banerjee, Large-signal characterization of DDR silicon IMPATTs operating up to 0.5 THz. Int. J. Microw. Wirel. Technol. **5**(5), 567–578 (2013)
34. H.K. Gummel, J.L. Blue, A small-signal theory of avalanche noise in IMPATT diodes. IEEE Trans. Electron Dev. **14**, 569–580 (1967)
35. S.K. Roy, M. Sridharan, R. Ghosh, B.B. Pal, Computer method for the dc field and carrier current profiles in the IMPATT device starting from the field extremum in the depletion layer. in *Proceedings of the 1st Conference on Numerical Analysis of Semiconductor Devices (NASECODE I)*, ed. by J.H. Miller (Dublin, Ireland, 1979), pp. 266–274
36. S.K. Roy, J.P. Banerjee, S.P. Pati, A computer analysis of the distribution of high frequency negative resistance in the depletion layer of IMPATT Diodes. in *Proceedings of 4th Conference on Numerical Analysis of Semiconductor Devices (NASECODE IV)* (Dublin, Ireland, 1985), pp. 494–500
37. J.P. Banerjee, J.F. Luy, F. Schaffler, Comparison of theoretical and experimental 60 GHz silicon IMPATT diode performance. Electron. Lett. **27**, 1049–1050 (1991)
38. A. Acharyya, M. Mukherjee, J.P. Banerjee, Effects of tunnelling current on mm-wave IMPATT Devices. Int. J. Electron. **102**(9), 1429–1456 (2015)
39. W.J. Evans, G.I. Haddad, A large-signal analysis of IMPATT diodes. IEEE Trans. Electron Dev. **15**(10), 708–717 (1968)
40. D.L. Scharfetter, H.K. Gummel, Large-signal analysis of a silicon read diode oscillator. IEEE Trans. Electron Dev. **6**(1), 64–77 (1969)
41. M.S. Gupta, R.J. Lomax, A current-excited large-signal analysis of IMPATT devices and its circuit implementations. IEEE Trans. Electron Dev. **20**, 395–399 (1973)
42. A. Acharyya, S. Banerjee, J.P. Banerjee, Effect of junction temperature on the large-signal properties of a 94 GHz silicon based double-drift region impact avalanche transit time device. J. Semiconduct. **34**(2), 024001–0240012 (2013)

43. A. Acharyya, A. Mallik, D. Banerjee, S. Ganguli, A. Das, S. Dasgupta, J.P. Banerjee, IMPATT devices based on group III–V compound semiconductors: prospects as potential terahertz radiators. HKIE Trans. **21**(3), 135–147 (2014)
44. A. Acharyya, S. Banerjee, J.P. Banerjee, Large-signal simulation of 94 GHz pulsed DDR silicon IMPATTs including the temperature transient effect. Radioengineering **21**(4), 1218–1225 (2012)
45. A. Acharyya, J. Goswami, S. Banerjee, J.P. Banerjee, Estimation of most favorable optical window position subject to achieve finest optical control of lateral DDR IMPATT diode designed to operate at W-band. Radioengineering **23**(2), 739–753 (2014)
46. A. Acharyya, S. Banerjee, J.P. Banerjee, Optical control of large-signal properties of millimeter-wave and sub-millimeter-wave DDR Si IMPATTs. J. Comput. Electr. **13**, 408–424 (2014)
47. A. Acharyya, A. Mallik, D. Banerjee, S. Ganguli, A. Das, S. Dasgupta, J.P. Banerjee, Large-signal characterizations of DDR IMPATT devices based on group III–V semiconductors at millimeter-wave and terahertz frequencies. J. Semiconductors **35**, 084003 (2014)
48. A. Acharyya, S. Banerjee, J.P. Banerjee, A proposed simulation technique to study the series resistance and related millimeter-wave properties of Ka-band Si IMPATTs from the electric field snap-shots. Int. J. Microw. Wirel. Technol. **5**(1), 91–100 (2013)
49. A. Acharyya, S. Banerjee, J.P. Banerjee, Influence of skin effect on the series resistance of millimeter-wave of IMPATT devices. J. Comput. Electron. **12**(3), 511–525 (2013)
50. M. Tschernitz, J. Freyer, 140 GHz GaAs double-read IMPATT diodes. Electron. Lett. **31**(7), 582–583 (1995)
51. M.G. Adlerstein, S.L.G. Chu, GaAs IMPATT diodes for 60 GHz. IEEE Electron Dev. Lett. **5**, 97–98 (1984)
52. H. Eisele, C.C. Chen, G.O. Munns, G.I. Haddad, The potential of InP IMPATT diodes as high-power millimetre-wave sources: first experimental results. IEEE MTT-S Int. Microw. Symp. Digest **2**, 529–532 (1996)
53. A. Acharyya, S. Chatterjee, J. Goswami, S. Banerjee, J.P. Banerjee, Quantum drift-diffusion model for IMPATT devices. J. Comput. Electron. **13**, 739–752 (2014)
54. A. Acharyya, J. Goswami, S. Banerjee, J.P. Banerjee, Quantum corrected drift-diffusion model for terahertz IMPATTs based on different semiconductors. J. Comput. Electron. **14**, 309–320 (2015)
55. A. Acharyya, K. Datta, R. Ghosh, M. Sarkar, R. Sanyal, S. Banerjee, J.P. Banerjee, Diamond based DDR IMPATTs: prospects and potentiality as millimeter-wave source at 94 GHz atmospheric window. Radioengineering **22**(2), 624–631 (2013)
56. A. Acharyya, S. Banerjee, J.P. Banerjee, Potentiality of semiconducting diamond as base material of millimeter-wave and terahertz IMPATT devices. J. Semiconductors **35**(3), 034005 (2013)

Terahertz Radiators Based on Silicon Carbide Avalanche Transit Time Sources—Part II: Avalanche Noise Characteristics

S. J. Mukhopadhyay, P. Mukherjee, A. Acharyya and M. Mitra

Abstract Small-signal noise simulations have been performed to explore the potency of avalanche transit time (ATT) oscillators based upon wide bandgap (WBG) semiconducting substances like 3C-SiC and type-IIb diamond (C) as millimeter-wave (mm-wave) and terahertz (THz) wave generators; noise characteristics of those sources have been compared with the DDR IMPATTs on the basis of traditional substance, i.e., Si. The simulation studies show that the WBG semiconductor-based IMPATT sources possess significantly poor noise performance than the conventional Si-based IMPATT sources. However, significantly better RF power delivery capability of WBG IMPATT sources makes them superior than Si IMPATTs for mm-wave and THz applications.

Keywords Avalanche noise · 3C-SiC · Diamond · IMPATT · Millimeter-wave · Si · Terahertz

1 Introduction

IMPATT oscillators are indigenously noisy sources for mm-wave and THz frequency band applications [1]. The main origin of noise in IMPATT sources is the unsystematic nature of the uncovering mechanism of electron–hole pairs (EHPs) due to impact ionization. This fact causes a significant amount of vacillations in static electric field as well as current originated from the DC biasing of the reverse-biased IMPATT diodes. This random fluctuation appears as a small-signal alternating component to the DC biasing voltage even when the time-varying oscillating voltage across the

S. J. Mukhopadhyay · M. Mitra
Department of ETC, IIEST, Shibpur, Howrah, West Bengal 711103, India

P. Mukherjee
Department of Electrical Engineering, Cooch Bihar Government Engineering College, Cooch Behar, West Bengal 736170, India

A. Acharyya (✉)
Department of Electronics and Communication Engineering, Cooch Bihar Government Engineering College, Cooch Behar, West Bengal 736170, India
e-mail: ari_besu@yahoo.co.in

© Springer Nature Singapore Pte Ltd. 2020

A. Biswas et al. (eds.), *Emerging Trends in Terahertz Solid-State Physics and Devices*,
https://doi.org/10.1007/978-981-15-3235-1_3

device is absent. Generally, the small-signal assumptions are well valid for noise analysis of IMPATT diodes [2].

In the earlier chapter, the potentiality of 3C-SiC-based IMPATT sources was explored by presenting the large-signal characteristics of those at mm-wave and THz frequencies. However, the descriptions as well as the exploration of high-frequency performance of ATT sources stay inadequate without studying the avalanche noise properties of those around those frequency regimes. Therefore, this chapter is dedicated to the detailed presentation of the results of a co-relative research on noise performance of mm-wave and THz Si, 3C-SiC, and diamond-based IMPATT sources. Again, this comparative study will be very much useful for the researchers in order to understand the potency of 3C-SiC IMPATT sources as a suitable solid-state source at the specified frequency bands.

2 A Brief History

At the initial stage, in the year of 1965, A. S. Tager developed a model to estimate the noise in IMPATT sources as a function of frequency under small-signal condition [1]. Later, Hines [3] developed the theory for small-signal avalanche noise in IMPATT oscillators. He considered the interaction of the device with external circuits in his proposed model. He obtained the noise current spectrum of an amplifier under small-signal condition and applied the same to find out the noise figure of read-type avalanche diode amplifier (see Fig. 1). In his analysis, he assumed equal ionization rates for both types of charge carriers. Hines showed that the avalanche noise increases at high signal level due to increasingly nonlinear behavior of avalanche current caused by large amount of fluctuation in the initial current which is subsequently multiplied by avalanche process. Gummel and Blue [4] proposed a generalized small-signal model for investigating the noise characteristics of ATT devices having any arbitrary doping profile. They considered realistic field-dependent carrier ionization rates in their model but assumed that the drift velocity of charge carriers are saturated and field-independent even at the edges of the space charge layer. However, the effect of field-dependent velocity at the space charge layer edges was considered in estimating the noise measure as a function of parasitic resistance. Figure 2 illustrates some important findings of Gummel and Blue [4].

Earlier the noise generation under large-signal condition was analyzed by Inkson [5]. He pointed out that the noise power increases under large-signal condition. However, the above-mentioned approximation is valid under extreme large-signal condition and thus the theory failed to provide reliable information regarding the enhancement in noise power with the increase of signal level. Haus et al. [6] reported that the optimum noise measure is obtained if the field derivative of ionization coefficient is constant. They showed that the device would exhibit minimum noise for a transit angle of 2π. Kuvas [7] in 1972 reported that the homogeneous noise spectrum of the device can be extracted by separating the large signal and noise terms. He suggested that a complete design optimization for the power–noise characteristics

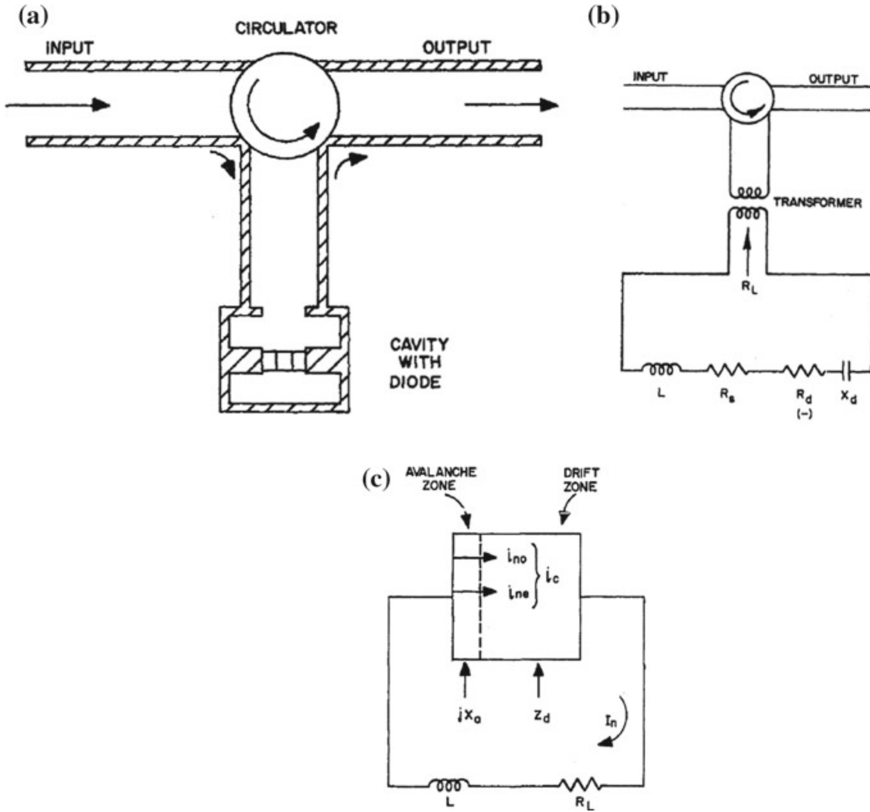

Fig. 1 **a** Schematic showing the reflection technique adopted by Hines [3] for realizing amplifier by using a negative-resistance diode, **b** corresponding equivalent circuit, and **c** circuit for calculating noise current

of IMPATT devices can be obtained if reliable ionization rate and drift velocity data are taken into consideration. Some important results of his study have been shown in Fig. 3. Etla and Haddad [8] in 1978 reported the existence of a clear trade-off between noise level and power output for MITATT mode operation.

In the year 1996, noise simulation of MITATT devices was reported [9]. Design of low-noise IMPATT diode having a noise measure of around 6.7 dB was achieved from the simulation studies [10]. Recently, the authors carried out studies on the influence of parasitic series resistance on the noise characteristics of DDR Si IMPATTs operating at W-band [11, 12]. Noise characteristics of 94 GHz DDR MITATT devices based on Si ~ $Si_{1-x}Ge_x$ heterostructure were investigated by Banerjee et al. [13] in 2012. They showed that the avalanche noise in IMPATTs can be significantly reduced by using anisotype Si ~ $Si_{1-x}Ge_x$ heterojunctions for which the preferred structure was also suggested see Fig. 4).

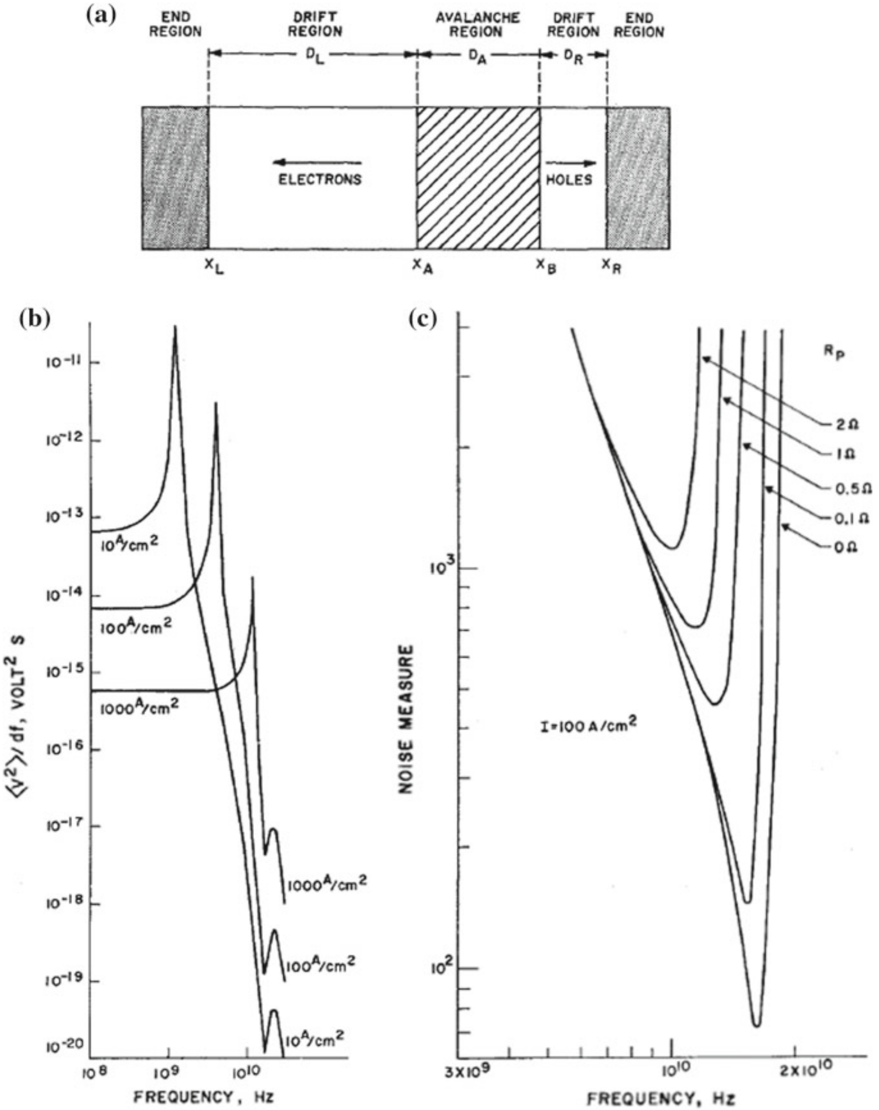

Fig. 2 **a** Schematic of the diode structure used for the analysis of Gummel and Blue [4], **b** variations of open-circuit noise spectral density with frequency for different bias current densities, and **c** variations of noise measure with frequency

3 Substance Parameters and Design Strategy

The brief descriptions of the field-dependent and field-independent material parameters of Si, 3C-SiC, and type-IIb diamond have already been included in the earlier

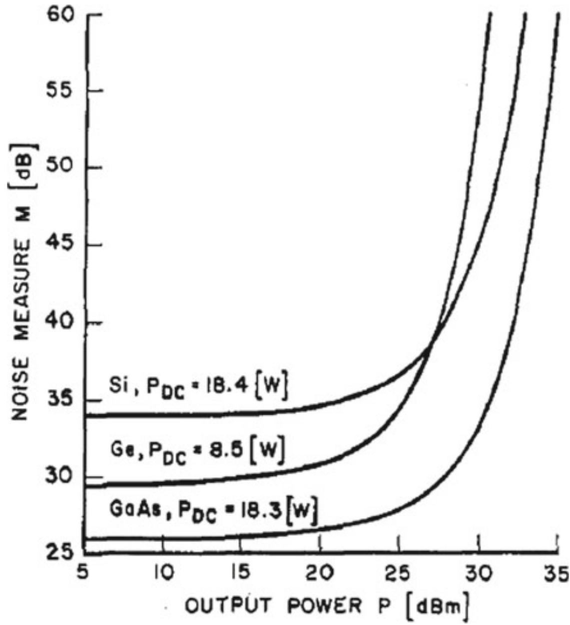

Fig. 3 Variations of noise measure (M) with output power (P) of 6 GHz GaAs, Si, and Ge diodes calculated by Kuvas [7]

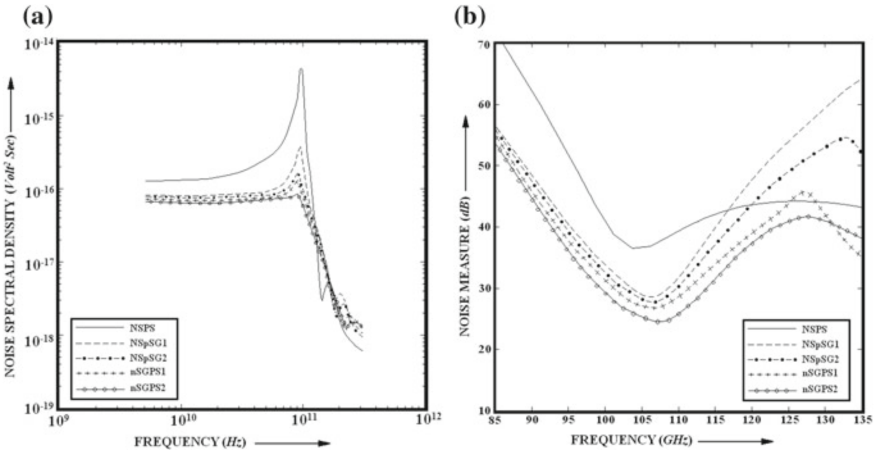

Fig. 4 **a** Noise spectral density and **b** noise measure versus frequency plots of Si ~ $Si_{1-x}Ge_x$ heterojunction DDR MITATT devices reported by Banerjee et al. [13]

Table 1 Design parameters

Base material	Design frequency, f_d (GHz)	n-layer thickness, W_n (nm)	p-layer thickness, W_p (nm)	n-layer doping concentration, N_D ($\times 10^{23}$ m^{-3})	p-layer doping concentration, N_A ($\times 10^{23}$ m^{-3})	n^+- and p^+-layer doping concentrations, N_{Sub} ($\times 10^{26}$ m^{-3})	Bias current density, J_0 ($\times 10^8$ A m^{-2})
Si	94	400.0	380.0	1.20	1.25	1.00	3.40
	140	280.0	245.0	1.80	2.10	1.00	5.80
	220	180.0	160.0	3.95	4.59	1.00	14.50
	300	132.0	112.0	6.00	7.30	1.00	24.50
	500	72.0	70.0	15.0	16.2	1.00	55.00
3C-SiC	94	410.0	410.0	2.50	2.50	1.00	6.00
	140	300.0	300.0	5.00	5.00	1.00	16.00
	220	200.0	200.0	8.00	8.00	1.00	30.00
	300	160.0	160.0	11.00	11.00	1.00	55.00
	500	103.0	103.0	16.50	16.50	1.00	104.00
	1000	57.0	57.0	23.50	22.50	1.00	135.00
Type-IIb diamond	94	780.0	780.0	0.460	0.530	1.00	4.00
	140	530.0	530.0	0.810	0.870	1.00	7.50
	220	320.0	320.0	1.350	1.490	1.00	13.00
	300	220.0	220.0	2.050	2.220	1.00	17.00
	500	120.0	120.0	3.750	4.100	1.00	25.00
	1000	52.0	52.0	9.500	10.00	1.00	39.00
	1500	30.0	30.0	36.00	37.00	1.00	48.00

chapter. The published literatures from which those parameters have been incorporated in the simulation study have also been mentioned in that chapter [14–20]. The earlier chapter also provides a brief note on the design of the mm-wave and THz DDR IMPATTs. However, for the sake of convenience of the readers, the design parameters are repeated once again in Table 1.

4 Small-Signal Noise Model

The avalanche noise simulation of an ATT device starts with the calculation of spatial distribution of noise field $e_n(x, x')$, where x is the space coordinate at which e_n is calculated and x' is the space coordinate at which an arbitrary noise supply $\gamma(x')$ is assumed to be present) within the space charge region of the device. Small-signal noise field is essentially a complex quantity having real and imaginary components, i.e., $e_{nr}(x, x')$ and $e_{ni}(x, x')$, respectively. Two second-order partial differential equations involving e_{nr} and e_{ni} can be derived under small-signal circumstance [9]; those have to be solved simultaneously subject to the boundary conditions imposed at the edges of the space charge layer, from which $e_{nr}(x, x')$ and $e_{ni}(x, x')$ can be obtained. This solution provides spatial distributions of $e_{nr}(x, x')$ and $e_{ni}(x, x')$ for a particular

position of $\gamma(x')$. Now, $\gamma(x')$ is shifted from one side of the space charge layer to another and the $e_n(x, x')$ is obtained for all positions of $\gamma(x')$. Noise voltage at x' can be obtained as

$$v_t\left(x^{'}\right) = \int\limits_{x=0}^{x=W} \left\{\left|e_{nr}\left(x, x^{'}\right)\right|^2 + \left|e_{ni}\left(x, x^{'}\right)\right|^2\right\}^2 \mathrm{d}x \tag{1}$$

Transfer impedance is given by

$$z_t\left(x^{'}\right) = \frac{v_t\left(x^{'}\right)}{i_n\left(x^{'}\right)}, \tag{2}$$

where $i_n(x')$ = value of average noise current within the space points x' and $(x' + dx')$ due to $\gamma(x')$. From this information, the mean-square noise voltage is obtained from [4]

$$\langle v_n^2 \rangle = 2q^2.\mathrm{d}f.A_j \int\limits_0^W \left|z_t\left(x^{'}\right)\right|^2 \gamma\left(x^{'}\right)\mathrm{d}x^{'}, \tag{3}$$

where A_j = junction area, $q = 1.6 \times 10^{-19}$ C = charge of an electron, and df = bandwidth under consideration. The parameter $\langle v_n^2 \rangle \big/ \mathrm{d}f$ is regarded as mean-square noise voltage per unit bandwidth or noise spectral density (NSD), and its unit is given by V^2 s.

By using the NSD from noise simulation and negative resistance (Z_R) and positive series resistance (R_S) from the large-signal simulation [21], one important noise performance defining parameter, i.e., noise measure (M_N) can be obtained by using the following expression [4, 6]

$$M_\mathrm{N} = \frac{\langle v_n^2 \rangle/\mathrm{d}f}{4k_\mathrm{B}T_j(-|Z_\mathrm{R}| - R_\mathrm{S})}, \tag{4}$$

where $k_\mathrm{B} = 1.38 \times 10^{-23}$ J K^{-1} = Boltzmann constant and T_j = junction temperature of the device in Kelvin (K).

The variations of NSD and M_N with frequency describe the complete noise performance of an IMPATT source. The effects of some externally applied excitations like optical illumination, steady magnetic field, etc., as well as internal phenomena such as decreased ionization rates due to inter-carrier collisions can be investigated by using the small-signal noise simulation presented here. The said effects are discussed below in brief.

4.1 Effect of Optical Illumination

The influence of photo-irradiation on the noise characteristics of Si IMPATT sources has been studied by Acharyya et al. [22]. Top-mount (TM) and flip chip (FC) configurations of IMPATT diodes were considered for that study (see Fig. 5). It was observed that the optical illumination causes significant degradation in the noise performance of the source; however, this degradation is observed to be less in FC arrangement than the TM (Fig. 5).

4.2 Influence of Magnetic Field

Influence of steady transverse magnetic field on the noise characteristics of Si IMPATT sources was studied by Banerjee et al. [23]. It was found that the noise performance deteriorated due to this effect (see Fig. 6).

4.3 Effect of Reduced Impact Ionization Rate

The influence of reduced ionization rates as a consequence of the energy loss of charge carriers due to of inter-carrier collisions on noise properties of DDR Si IMPATT sources has been studied by Bandhyopadhyay et al. [24]. It was reported that the noise performance of the source slightly deteriorated as a result of this effect (see Fig. 7).

5 Noise Characterizes of 3C-SiC IMPATT Sources

Noise performance of 3C-SiC-based IMPATT sources have been investigated by using the simulation method described earlier in this chapter. The most important performance-evaluating parameters associated with the avalanche noise, i.e., noise measure of the above-mentioned sources, are calculated and those are compared with the same parameters of Si and diamond IMPATT sources. The noise measure values of Si, 3C-SiC, and diamond IMPATT sources obtained from fifteen trial simulation runs have been plotted against frequency (Fig. 8). The noise measures of WBG semiconductor (i.e., 3C-SiC and diamond)-based sources are found to be significantly higher than those of usual Si-based IMPATT oscillators. Wider multiplication zones of WBG IMPATT sources (see Fig. 8 of the earlier chapter) are responsible for higher noise in those as compared to the Si IMPATTs. Moreover, 3C-SiC IMPATTs possess slightly broader avalanche zones than the diamond IMPATTs (see Fig. 8 of the earlier

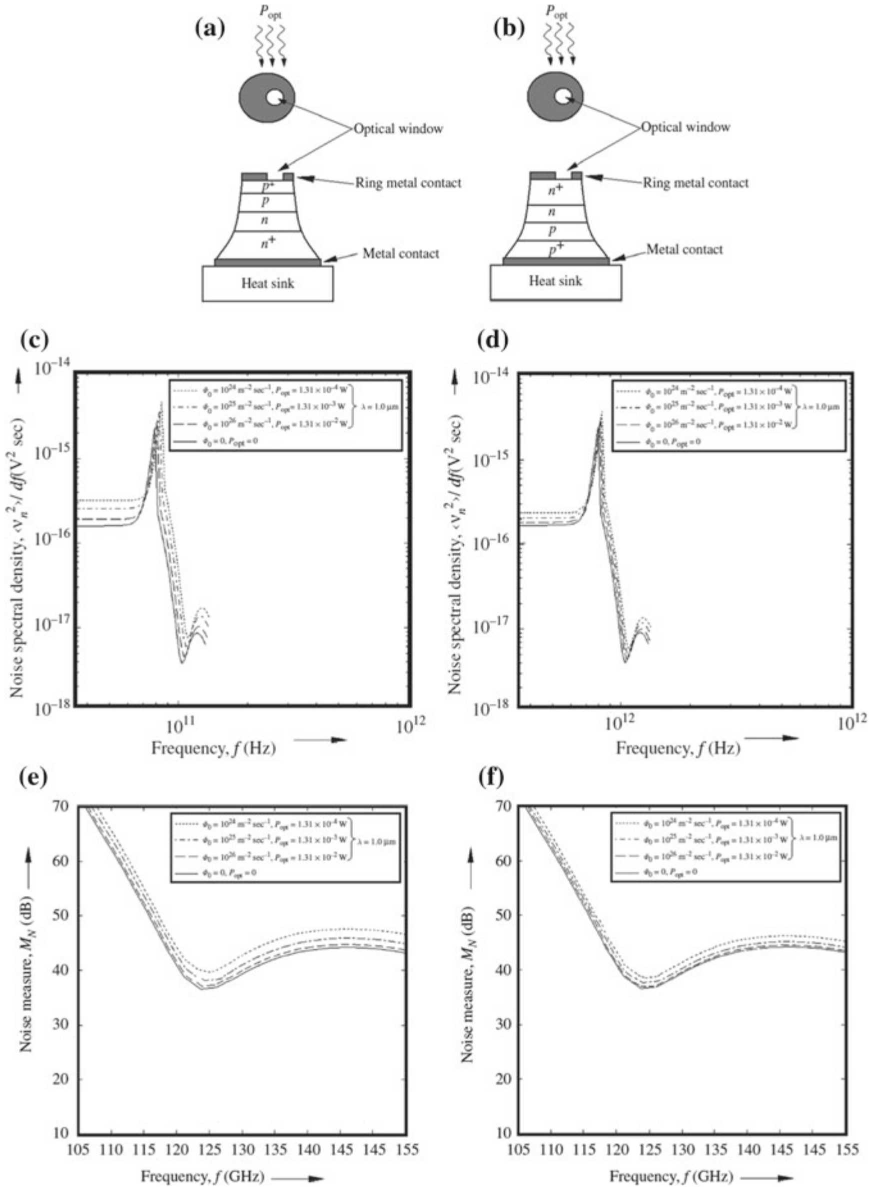

Fig. 5 Schematic of **a** top-mount (TM) and **b** flip chip (FC) arrangements, noise spectral density, and noise measure of **e** TM and **f** FC oscillators versus frequency plots under optical illumination of different incident photon flux densities having wavelength of 1000 nm [22]

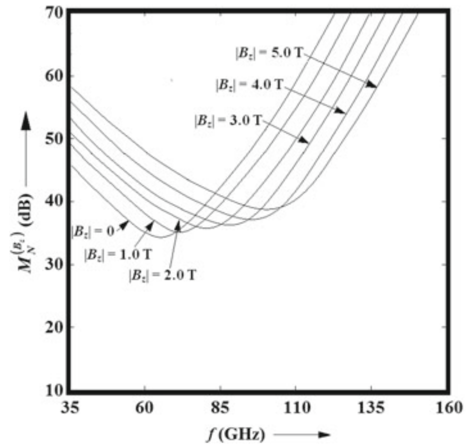

Fig. 6 Noise measure versus frequency graph for 94 GHz Si IMPATT source [23]

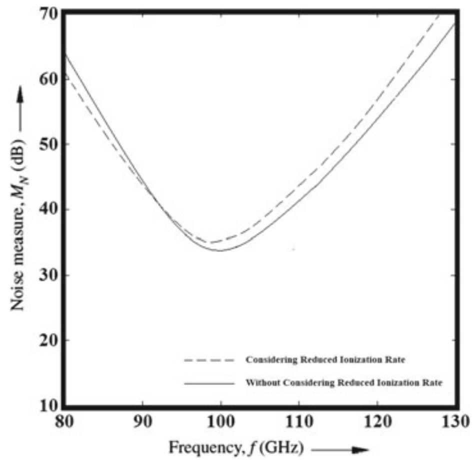

Fig. 7 Noise measure versus frequency graph for 94 GHz Si IMPATT source [24]

chapter); as a result of that noise, measures of 3C-SiC IMPATTs are slightly higher than those of diamond IMPATTs at all operating frequencies.

The experimentally measured noise measure of 94 GHz Si IMPATT source is around 35 dB [25], which is very close to the noise measure value obtained from the small-signal noise simulation. This close agreement of simulation obtained data with the experimental result validates the simulation methodology under concern. However, further validation of it is restricted as a result of the unavailability of the reported experimental data.

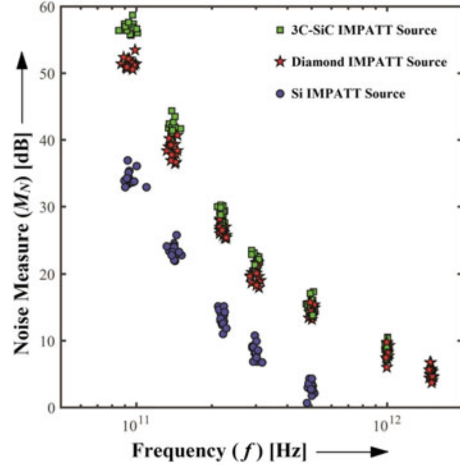

Fig. 8 Noise measure versus frequency graph associated with THz DDR IMPATT sources based on Si, 3C-SiC, and diamond

6 Conclusion

The small-signal avalanche noise simulation has been carried out and presented here in order to focus the potentialities of mm-wave and THz WBG semiconductors-based IMPATT sources like 3C-SiC and type-IIb diamond (C). Noise characteristics of those sources have been compared with the conventional semiconductor substance, i.e., Si-based IMPATTs. The simulation studies show that the WBG semiconductor-based IMPATT sources possess significantly poor noise performance than the conventional Si-based IMPATT sources. However, significantly better RF power delivery capability of WBG IMPATT sources makes them superior to Si IMPATTs for mm-wave and THz applications.

Acknowledgements The authors deeply feel and acknowledge the help and spontaneous support rendered by the authority of IIEST, Shibpur, West Bengal, by making a suitable arrangement to perform the research work smoothly.

References

1. A.S. Tager, Current fluctuations in semiconductor (dielectric) under the conditions of impact ionization and avalanche breakdown. Sov. Phys. Solid State **4**, 1919 (1965)
2. S.T. Fisher, Small-signal impedance of avalanche junctions with unequal electron and hole ionization rates and drift velocities. IEEE Trans. Electron Dev. **ED-14**, 313–322 (1967)
3. M.E. Hines, Noise theory of read type avalanche diode. IEEE Trans. Electron Dev. **ED-13**, 57 (1966)
4. H.K. Gummel, J.L. Blue, A small-signal theory of avalanche noise in IMPATT diodes. IEEE Trans Electron Dev. **14**, 569–580 (1967)
5. J.K. Inkson, Noise generation under large signal conditions in the read micro-wave avalanche diode. Int. J. Electron. **25**, 1 (1958)

6. H.A. Haus, H. Statz, R.A. Pucel, Optimum noise measure of IMPATT diode. IEEE Trans. MTT **MTT-19**, 801 (1971)
7. R.L. Kuvas, Noise in IMPATT diodes Intrinsic properties. IEEE Trans. Electron Dev. **ED-19**, 220 (1972)
8. M.E. Elta, G.I. Haddad, Mixed tunneling and avalanche mechanism in p-n junctions and their effects on microwave transit time devices. IEEE Trans. Electron Dev. **25**, 694–702 (1978)
9. G.N. Dash, J.K. Mishra, A.K. Panda, Noise in mixed tunneling avalanche transit time (MITATT) diodes. Solid State Electron. **39**(10), 1473–1479 (1996)
10. J.K. Mishra, A.K. Panda, G.N. Dash, An extremely low-noise heterojunction IMPATT. IEEE Trans. Electron Dev. **44**(ED-12), 2143–2148 (1997)
11. A. Acharyya, M. Mukherjee, J.P. Banerjee, Noise Performance of Millimeter-wave silicon based mixed tunneling avalanche transit time (MITATT) diode. Int. J. Electr. Electron. Eng. **4**(8), 577–584 (2010)
12. A. Acharyya, M. Mukherjee, J.P. Banerjee, Noise in millimeter-wave mixed tunneling avalanche transit time diodes. Arch. Appl. Sci. Res. **3**(1), 250–266 (2011)
13. S. Banerjee, A. Acharyya, J.P. Banerjee, Millimeter-wave and noise properties of Si ~ $Si_{1-x}Ge_x$ heterojunction double-drift region MITATT devices at 94 GHz. in *IEEE Conference CODEC* (Kolkata, India, 2012), pp. 1–4, 17–19 Dec 2012
14. W.N. Grant, Electron and hole ionization rates in epitaxial silicon. Solid State Electron. **16**, 1189–1203 (1973)
15. R. Mickevicius, J.H. Zhao, Monte Carlo study of electron transport in SiC. J. Appl. Phys. **83**, 3161–3167 (1998)
16. E.A. Konorova, Y.A. Kuznetsov, V.F. Sergienko, S.D. Tkachenko, A.K. Tsikunov, A.V. Spitsyn, Y.Z. Danyushevski, Impact ionization in semiconductor structures made of ion-implanted diamond. Sov. Phys. Semicond. **17**, 146 (1983)
17. C. Canali, G. Ottaviani, A.A. Quaranta, Drift velocity of electrons and holes and associated anisotropic effects in silicon. J. Phys. Chem. Solids **32**, 1707–1720 (1971)
18. D.K. Ferry, High-field transport in wide-bandgap semiconductors. Phys. Rev. B **12**, 2361 (1975)
19. C. Canali, E. Gatti, S.F. Kozlov, P.F. Manfredi, C. Manfredotti, F. Nava, A. Quirini, Electrical properties and performances of neutral diamond nuclear radiation detectors. Nuclear Instrum. Methods **160**, 73 (1979)
20. C. Canali, E. Gatti, S.F. Kozlov, P.F. Manfredi, C. Manfredotti, F. Nava, A. Quirini, *Electronic Archive: New Semiconductor Materials, Characteristics and Properties*. Available from http://www.ioffe.ru/SVA/NSM/Semicond/index.html. Last accessed on Sept 2019
21. A. Acharyya, S. Banerjee, J.P. Banerjee, Influence of skin effect on the series resistance of millimeter-wave of IMPATT devices. J. Comput. Electron. **12**(3), 511–525 (2013)
22. A. Acharyya, S. Banerjee, J.P. Banerjee, Effect of photo-irradiation on the noise properties of double-drift silicon MITATT device. Int. J. Electron. **101**(9), 1270–1286 (2014)
23. P. Banerjee, A. Acharyya, A. Biswas, A.K. Bhattacharjee, H. Inokawa, Noise performance of magnetic field tunable avalanche transit time source. Int. J. Electr. Commun. Eng. **12**(10), 718–728 (2018)
24. P.K. Bandyopadhyay, A. Biswas, A.K. Bhattacharjee, A. Acharyya, Influence of carrier-carrier interactions on the noise performance of millimeter-wave IMPATTs. IETE J. Res. **65**(4), 515–522 (2019)
25. H. Okamoto, M. Ikeda, A comparative study of noise properties of Si IMPATT diodes operating at 80 GHz. Proc. IEEE (Lett.) **64**, 367–368 (1976)

RF Performance of Ultra-wide Bandgap HEMTs

Rajan Singh, T. R. Lenka, D. Panda, R. T. Velpula, B. Jain, H. Q. T. Bui and H. P. T. Nguyen

Abstract In the current scenario of high-speed electronics technology, many application areas—broadband Internet access, fifth-generation (4G/5G) mobile systems, and cutting-edge military applications—are realizing very-fast to reality. To cater these ever-increasing demands, radio-frequency (RF) and microwave power amplifiers are in prime-attention, and will be constantly evaluated on price versus performance metrics. Ultra-wide bandgap (UWBG) high electron mobility transistors (HEMTs) are promising candidates for switching power applications owing to very-high breakdown strength of the material. And higher values of energy band gap (E_g) and electron mobility enabled low on-resistance (R_{ON}) guarantees superior power handling capability. UWBG HEMTs having two-dimensional electron gas (2DEG) channel with high carrier concentration and high electron mobility are fast gaining space in high frequency and power switching applications. Also, these UWBG materials having large optical phonon energy, E_{op} ~92 meV (GaN), ~45 meV (β-Ga_2O_3) make them most suitable semiconductor materials for the imminent terahertz (THz, 10^{12} Hz) frequency applications: THz imaging and spectroscopy. In this paper, we present latest technological developments of the gallium nitride (GaN)- and beta-phase of gallium oxide (β-Ga_2O_3)-based HEMTs, with careful and quantitative investigation of their suitability toward radio frequency (RF), high power device applications, and THz emerging applications.

R. Singh · T. R. Lenka (✉)
Department of Electronics and Communication Engineering, National Institute of Technology Silchar, Silchar, Assam 788010, India
e-mail: t.r.lenka@ieee.org

R. Singh
e-mail: rajan_singh@ieee.org

D. Panda
School of Electronics, VIT-AP University, Amaravati, Andhra Pradesh 522237, India

R. T. Velpula · B. Jain · H. Q. T. Bui · H. P. T. Nguyen
Department of Electrical and Computer Engineering, New Jersey Institute of Technology, Newark, NJ 07102, USA

© Springer Nature Singapore Pte Ltd. 2020

A. Biswas et al. (eds.), *Emerging Trends in Terahertz Solid-State Physics and Devices*,
https://doi.org/10.1007/978-981-15-3235-1_4

Keywords Ultra-wideband gap · Gallium nitride · Gallium oxide · RF performance · Terahertz · Imaging · Spectroscopy · Bandwidth · High electron mobility transistor · HEMT

1 Introduction

Outstanding material parameters of ultra-wideband gap (UWG) semiconductors have provided a solid platform for conclusive research and rapid development of RF power device applications. With advent of Internet-of-Everything (IoE), systematic connection of data, things, processes and people, recent time witnessed an upsurge in high-speed wireless communication market, which has further fuelled demand for next-generation power devices: high-efficiency power converters, power amplifiers, and many more. Furthermore, quest for sustainable renewable energy systems and adoption of electric-vehicles (EV) have pushed additional demand of the power-efficient electronic devices, employing Ga_2O_3-, GaN-, and SiC-based transistors and amplifiers in microwave frequency regime. Table 1 lists different figures of merit (FOMs): Johnson's figure of merits (JFO) [1]—a critical FOM for RF power devices, used to quantify high power RF devices based on material characteristics by calculating power-frequency limits (pf^2). Baliga figure of merit (BFOM) [2]—the resistive losses of the devices at lower frequencies, Baliga high-frequency figure of merit (BHFFOM) [3]—switching losses show at high frequencies (shown in Table 1).

For power electronic applications, a device should have small value of on-resistance (R_{on}) and high breakdown voltage (V_{Br}), which leads to a trade-off between the two key parameters [4], shown in Fig. 1a. Trans-conductance (g_m) and cut-off frequency are also important parameters of RF and high power device applications. In order to minimize the switching losses in the power devices, it is necessary to

Table 1 Material properties of various semiconductor materials relating power performance

Parameters	Materials			
	Si	4H-SiC	GaN	β-Ga_2O_3
Energy band gap, E_g (eV)	1.1	3.2–3.3	3.4	4.5–4.9
Intrinsic carrier concentration, n_i (cm^{-3})	10^{10}	10^{-9}	10^{-10}	10^{-24}
Electric breakdown field, E_{Br} (MV cm^{-1})	0.3	3.0	3.3	8.0
Relative dielectric constant, ε_r	11.8	10	9.0	10
Electron mobility, μ_n (cm^2 V^{-1} s^{-1})	1350	700	2000 (2DEG)[a]	200[d]
Saturation velocity, v_{sat} (10^7 cm s^{-1})	1.0	2.0	2.0–2.5[b]	1.1–1.5[e]
Thermal conductivity, k (W cm^{-1} K^{-1})	1.5	3.3–4.5	1.3	0.21[c]
$JFOM_{Si}$, ($v_{sat}E_{Br}/2\pi$)	1.0	20	27.5	40
$BFOM_{Si}$, (μ_n ε_r E_{Br}^3)	1.0	439	1503	2380
$BHFFOM_{Si}$, (μ_n E_{Br}^2)	1.0	51.8	179.2	105

Refs.—[a][60], [b][61], [c][58], [d][62], [e][63, 64]

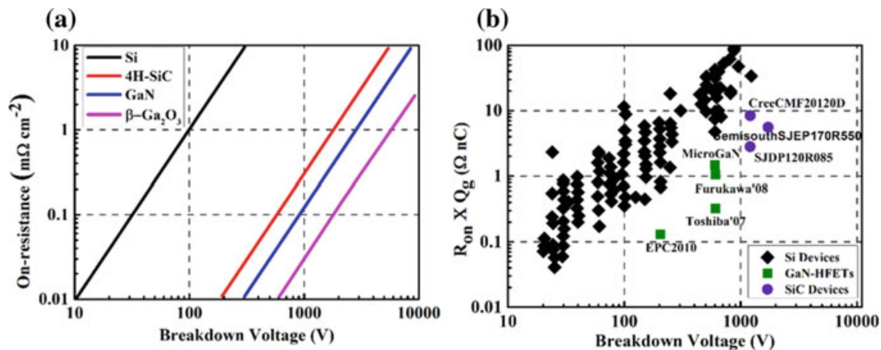

Fig. 1 **a** On-resistance versus breakdown voltage, **b** $R_{\mathrm{on}} \times Q_{\mathrm{g}}$ versus breakdown voltage

not only reduce the on-resistance but the input capacitance as well and particularly a low gate charge (Q_{g}). And another important FOM, the product term $Q_{\mathrm{g}} \times R_{\mathrm{on}}$ [5], for switching efficiency for different device families are shown in Fig. 1b. The UWBG HEMTs have the key features: large carrier concentration, quantum well confinement due to large conduction band offset at the heterojunction led very-high electron mobility, results in higher current density with low R_{ON}, make them highly suitable for switching and RF applications [6].

Lower switching losses of UWBG HEMTs facilitates higher switching frequencies which further allows reduced size of passive components: inductors and capacitors and finally guarantees significant reduction in volume and weight of these systems; new possibilities can be explored for system applications [7, 8]. It is established that an ideal power switching device should have small R_{ON} and high V_{Br}; High breakdown devices should have sufficiently large drift regions; but R_{ON} increases due to more and more resistive elements are added to the device, so device technologies showing high V_{Br} with comparably small drift regions would find an optimum solution [7].

THz frequency region is still less explored, and nowadays in strong demand in variety of applications: basic science—biochemical spectroscopy, astronomy, and materials science to practical science—environmental science, medicine, agriculture, and security [7]. Due to low photon energy (1–100 meV) in THz regime, it can be transmitted through non-metallic materials; though x-ray photons can also traverse through objects opaque to visible lights, their high energy ionizes the molecules of the objects which results in cancer for live tissues [7, 9], degradation of semiconductor devices [10]. Although adverse effects of intense THz radiation on DNA is reported, THz wave considered more safe than x-ray in many areas: security, detection of drugs trafficking and hazardous materials, agriculture, water-content monitoring, and medicine, imaging of cancer cells [7]. In spite of the emerging THz applications, THz systems are affected by two major problems: photon energy of the THz wave is much lower than band gap energy of semiconductors and low spatial resolution due to much longer wavelengths of the THz waves compared to those of visible light [7].

In the upper THz frequency band, THz imaging and spectroscopy systems need higher photon densities to overcome diffraction, absorption, and the large beam diameter issue. UWBG semiconductor devices with high output power and high-frequency operation provide promising features for implementing such devices [11].

Here, we discuss key technological development of GaN and β-Ga_2O_3 based HEMTs, quantitative valuation of corresponding parameters reported to date in terms of their performance for RF and DC high power applications, and their possible role in imaging and spectroscopy of THz systems.

2 GaN-Based HEMTs

AlGaN/GaN HEMTs having spontaneous and piezoelectric polarization induced 2DEG channel of carrier density ~10^{13} cm^{-2} with high electron mobility up to ~2000 cm^2 $V^{-1}s^{-1}$ (epi-layer) facilitates a low resistive channel, resulting in exceptionally low device on-resistance. The reasonable high saturation velocity ~2×10^7 cm s^{-1} enabled high current densities—high P_{OUT}, and efficient RF power operation. Higher value of E_g supported high critical electric field of GaN, which is ten times higher than Si. AlGaN/GaN HEMTs possesses large blocking voltage and high drain voltage resulting high P_{OUT} density with high output impedance. This facilitates easier matching between multistage amplifiers with lower reflective losses.

2.1 *GaN Power Amplifier*

Excellent progress in material growth techniques such as epitaxy (MBE) and chemical vapor deposition (MOCVD) enabled high electron mobility in GaN-based HEMTs. Moreover, high breakdown voltage-empowered GaN HEMTs find applications as power amplifiers (PAs) with sufficient power added efficiency (PAE), also show higher output power and significant power density over materials such as Si, GaAs, or InP. For better thermal conductivity, SiC substrate is preferred, which made this technology to be commercialized for various applications: pulsed radars, cable television (CATV) amplifier modules, and mobile base stations [8]. After the demonstration of first GaN-based HEMT by Asif Khan et al. [12] in year 1994, in a couple of years, Wu et al. [13] demonstrated first RF measurement on an AlGaN/GaN HEMT with $P_{OUT} = 1.1$ W/mm at 2 GHz with a PAE = 18.6%. Although due to 'dispersion' microwave output power of earlier GaN devices were severely affected, primarily because of trap related phenomena [1, 14, 15]. Subsequent research addressed the issue by the use Si_3N_4 passivation [16] of undoped AlGaN/GaN HEMTs, which pave the way for increased output power up to 32.2 W/mm [17–29], and 40 W/mm [24] at 4 GHz using field plate (FP).

In most of the RF power applications, high values of PAs and PAE are required; reduced power consumption of the high power devices have less cooling requirement, which facilitates reduced device size and density of the system [8]. More output power was achieved using longer FP (up to a certain length), although gate-connected FP causes additional gate-to-drain capacitance (C_{gd}) which deteriorates current gain and power-gain cut-off frequencies [6]. Recently, Romanczyk et al. [30] demonstrated N-polar GaN HEMTs which maintains the same output power density at different frequencies: 10, 30, and 94 GHz, with peak power density 8 W/mm (total output power = 600 mW, power density × gate width ~0.7 μm). Further, improved power performance was shown by POC HEMT [31] with peak PAE of 71.6% and power density 10.4 W/mm at 5 GHz. High-efficiency RF devices with high P_{OUT} are vital to fully exploit the superior qualities of GaN material [8]. For high-frequency RF applications, higher current gain cut-off frequency (f_T) and maximum power-gain oscillation frequency (f_{MAX}) are required for operation beyond Ka-band (26–40 GHz). Device scaling has successfully increased f_T and f_{MAX} of GaN HEMTs but at the cost of lower breakdown voltage [8]. AlGaN/GaN HEMT were grown by metal-organic vapor phase epitaxy (MOVPE) on sapphire substrates with different Al concentrations (20, 27, and 35%) showed f_T (24.9, 34.6, and 50 GHz) and f_{MAX} (54.9, 61.8, and 100.9 GHz) [32]. Additionally, high-frequency GaN HEMTs for RF MMIC application-based devices [29, 33–36] such as: enhancement-mode (E-mode) GaN HEMT with ultrashort gate length (160 nm) achieved f_T of 85 GHz and f_{MAX} of 150 GHz [33], 60-nm-gate-length HEMT with recessed AlGaN barrier layer exhibited f_{MAX} of 300 GHz [34], and using tall-stem T-gate N-polar GaN/InAlN HEMT achieved f_{MAX} of 400 GHz [35]. Figure 2 shows small signal RF performance of GaN-based HEMTs, Refs. [34, 35].

To improve the performance of GaN HEMTs for mm-wave applications, researchers have developed new process and device technologies—non-alloyed ohmic contact [37, 38] using ion-implantation to get smooth surface and so reduced gate-drain as well as gate-source spacing which results in further lowering the

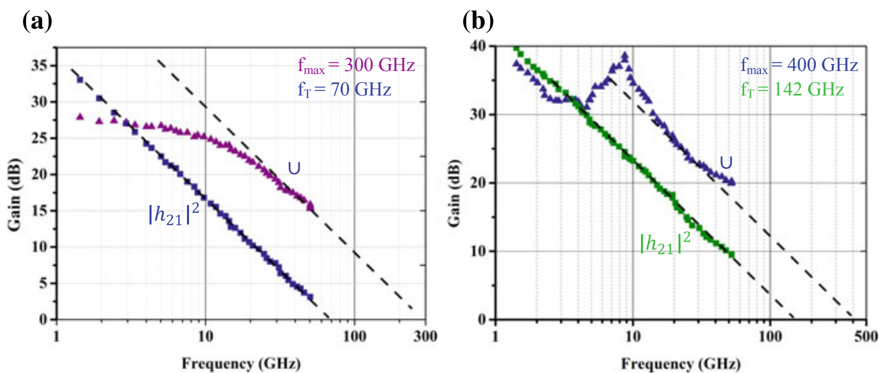

Fig. 2 Small signal RF performance of GaN HEMTs. **a** L_G = 60 nm, W = 50 μm, V_{DS} = 16 V. **b** L_G = 100 nm, W = 25 μm, V_{DS} = 8 V

access resistance, and capless annealing process [39]. AlGaN/GaN HEMT with non-alloyed ion implanted ohmic contacts [40] showed PAE of 72% and power density of 6.8 W/mm at 4 GHz. More recently, InAlN/GaN HMET fabricated with non-alloyed regrown n+-GaN ohmic contacts demonstrated f_{MAX} of 405 GHz for PA applications in G-band (140–220 GHz) [41].

A comparison of different semiconductor device technologies based on continuous-wave (CW) output power versus operating frequency is shown in Fig. 3a, which shows GaN power amplifiers output power decreases with increase in frequency by $1/f$ up to 30 GHz, $1/f^2$ between 30 and 100 GHz, and $1/f^3$ beyond 100 GHz due to maximum operational drain voltage and total gate periphery. Although using different FP arrangements, higher P_{OUT} was achieved. Most RF applications with high P_{OUT} and high PAE are critically important to reduce power consumption and heat dissipation in a significant manner, that led less requirements of cooling arrangements which helps in reducing size and weight of the overall system [8]. Figure 3b depicts power output efficiency versus frequency from 2 to 94 GHz for GaN HEMTs power amplifiers. It is noted that performance of power amplifiers in terms of efficiency also affected below-frequency range <10 GHz due to the lower cut-off frequency and limited gain [8].

As GaN materials have LO phonon of ~92 meV, power devices based on GaN materials have shown good performance up to 10 THz frequencies (THz upper band) at room temperature. Way back in '90s, pioneers Dyakonov and Shur [42] first proposed theoretical explanation of applications of FETs for THz spectroscopy by predicting plasma waves enabled variation in FET channel current. Subsequent years witnessed, FET as an efficient broadband THz detector and their possible application for THz imaging [43–46], Si-MOSFET efficient room temperature detectors of sub-THz radiation [47]. In a major technology breakthrough, Sun et al. [45] fabricated AlGaN/GaN HEMTs using optical lithography and detected terahertz radiation at room temperature via self-mixing, with a responsivity (3.6 kV/W). The device having gate length of 2 μm and floating antennas isolated electrically from

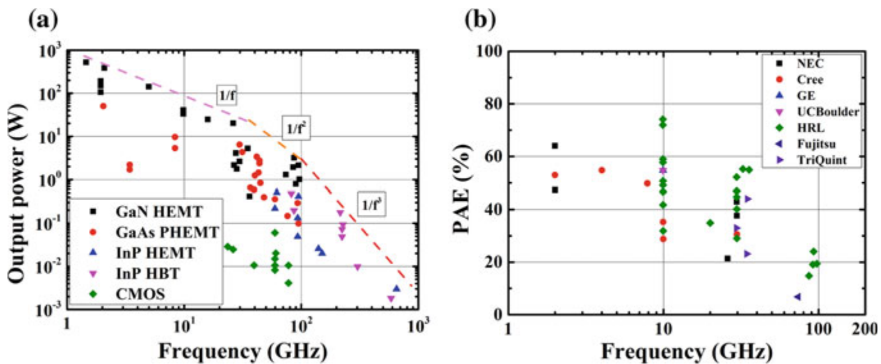

Fig. 3 Comparison of GaN power amplifiers. **a** CW output power as a function of frequency, **b** power added efficiency versus frequency

the conducting channel, and asymmetrical device geometry led localized self-mixing results into nanometer spatial sensitivity. Further quasistatic self-mixing model [46, 48] developed by taking account the localized THz fields and described the important features of THz response and non-uniform THz fields; hence, local self-mixing are investigated by selectively depleting the 2DEG near the edges of the channel. The device used AlGaN HEMT as THz detectors [48] by self-mixing, used $In_{0.17}Al_{0.83}N$(24 nm)/GaN heterostructure with detector details: gate length of 2 μm integrated with an asymmetric antenna, two patch antennas having gap of 3 μm next to the gate, and the ohmic contacts (source and drain) kept close to the patch antenna. An MSM-2DEG varactor [49] based on AlGaN/GaN HEMT was proposed for THz multiplication, and most recently—bow-tie TeraFET [50] is demonstrated with improved sensitivity by a factor of two in THz detection over other TeraFET based on AlGaN/GaN HEMT. The device is an improved FETs furnished with in-chip broadband bow-tie antenna (bow-tie TeraFET) for THz detection, and realized a AlGaN/GaN HEMTs with 100 nm GaN MMIIC process, with a separation of $d =$ 12 nm between gate and channel (width = 3 μm), gate length $L_g = 100$ nm and two 300 nm wide access regions (ungated). AlGaN/GaN epitaxial layers were grown on 470 μm thick semi-insulating SiC substrate for THz frequencies. The THz radiation was coupled through this transparent substrate. The THz detector used a broadband antenna (bow-tie-type) which was fabricated using gold material of thickness 650-nm. The 60 μm first wing antenna was designed with an wide angle of 60° to receive the optimum radiated power. The second wing of the antenna is observed as MIM capacitor and is realized as the capacitance two source and gate contacts separated with a dielectric layer of SiNx 200-nm-thick (not shown in figure). Schematic of cross-section of both versions of THz detector (TeraFET) is shown in Fig. 4.

Recent progress of device scaling technologies in GaN HEMTs paved the way for many desirable characteristics: high frequency, low resistance, high-blocking voltage, and low-noise, to name a few. These new features offer many practical advantages in RF MMICs: high-efficiency switched-mode PAs, PA MMICs operation in G-band and beyond, LNAs with low dc power dissipation, and robust low-loss

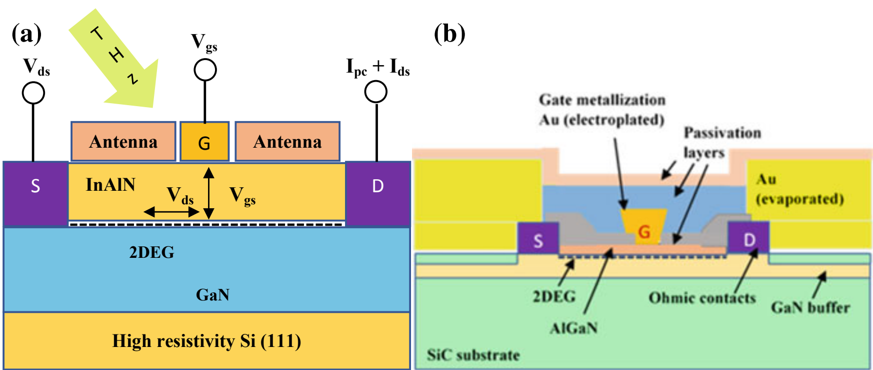

Fig. 4 Cross section of the device schematic **a** GaN HEMT detector, **b** AlGaN/GaN TeraFET

RF switches. Furthermore, high-speed E-/D-mode GaN HEMTs can be integrated to realize complex circuits ranging from mixed signal to digital logic [8].

3 RF Performance of β-Ga_2O_3 Devices

Current trend of research of Ga_2O_3 device technology is already in a fast lane and achieving key milestones [51–54] supported by adequate process development and vital material advancement. Excellent material characteristics of β-Ga_2O_3 enabled high value of JFOM (40, Table 1)—Johnson's FOM—a important parameter describing power-frequency product for RF operation, paved the way for β-Ga_2O_3 transistors to operate as high-efficiency RF power amplifiers, RF switches, and power switches capable of GHz switching speeds [8]. Also large bandgap (E_g ~4.9 eV) enabled high value of breakdown field (E_{Br} ~8 MV cm^{-1}) of β-Ga_2O_3, facilitated higher values of almost all FOMs: JFOM ($\propto E_{Br}$), BFOM ($\propto E_{Br}^3$), and BHFFOM ($\propto E_{Br}^2$), thus finds suitable for power switching and RF applications.

First RF performance of β-Ga_2O_3 MOSFETs [55], by combination of low contact resistance and shorter gate length through gate recess, showed large signal CW RF operation—power output density of 0.23 W/mm (normalized on device width) and power added efficiency (PAE) of 6.3% at frequency of 800 MHz. The device had a gate length of 0.7 μm, width 2 × 50 μm with gate-recess technology, showed a cut-off frequency (f_T) and maximum oscillating frequency (f_{MAX}) of 3.3 GHz and 12.9 GHz, respectively. The device fabrication sequence starts with a semi-insulating substrate followed by a moderately doped homo-epitaxially β-Ga_2O_3 channel. To improve ohmic contact formation, a thin highly-doped β-Ga_2O_3 cap layer is grown on channel layer. Large signal (or power) and small signal performances of the device are shown in Fig. 5.

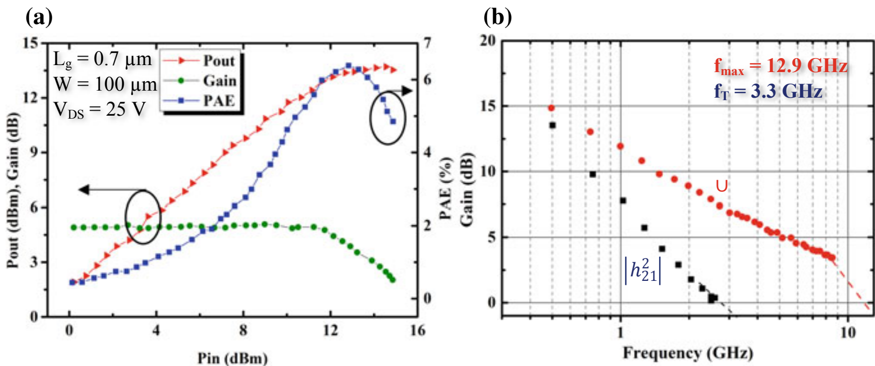

Fig. 5 RF performance of β-Ga_2O_3 MOSFET. **a** Large signal CW output power (13.7 dBm), gain (5.1 dB), and PAE_{MAX} (6.3%) versus input power (P_{in}) at 800 MHz, **b** small signal gain as a function of operating frequency

Further optimization is expected due to ongoing reporting of devices having lower values of on-resistance (R_{ON}), contact resistance (R_C), and sheet-resistance (R_{SH}); there are tangible benefits of significant improvements in power switching and RF performance of devices: reduced size of passive components and so small device size, and facilitate integration of both hybrid and monolithic RF and robust switch technology [56].

Comparison of large signal CW and pulsed RF performance of β-Ga_2O_3 field-plated MOSFETs demonstrated by Singh et al. [57], and highlighted benefit of pulsed signal circumventing device heating; poor heat dissipation of Ga_2O_3 devices restricts high-voltage operations as thermal conductivity of Ga_2O_3 material is very low (~0.2 W cm^{-1} K^{-1}) [58]. The device consists of 1.2 μm width β-Ga_2O_3 unintentional-doped (UID) epi-layer on an Fe-doped semi-insulating (SI) Ga_2O_3 (010) substrate, channel area of width 0.3 μm defined by selective doping by Si-ion implants (3 × 10^{17} cm^{-3}). Low contact resistance for improved RF operation facilitated by highly-doped (5 × 10^{19} cm^{-3}) source (*S*) and drain (*D*) contact regions, and capless implant annealing at an elevated temperature for 30 min; A 20 nm Al_2O_3 is deposited as gate-dielectric by using plasma atomic layer deposition at 250 °C followed by growing 0.4 μm thick SiO_2 dielectric using chemical vapor deposition; device schematic cross-section is shown in Fig. 6a.

The device had a gate length of 2 μm, width of 500 μm, and gate field plate of length 1 μm. Large signal pulsed RF measurements performed at $V_{DS} = 40$ V, $I_{DS} =$ 5 mA for 10 μs signal, and showed a maximum power density of 0.13 W/mm (P_{out} = 0.13 × 0.5 = 0.065 W) with a PAE of 12% at 1 GHz, also peak value of drain efficiency ~22%. These results are better than CW RF records: peak power density of 0.11 W/mm (P_{out} = 0.055 W)—an 18% decrement, PAE (9.1%)—a 33.3% loss and drain efficiency (19.5%)—a 12.8% decline; the deterioration in RF CW performance

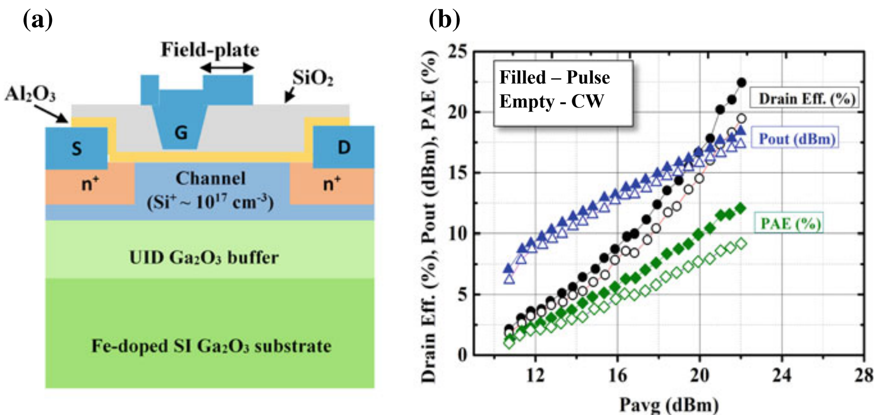

Fig. 6 Field-plate β-Ga_2O_3 MOSFET. **a** Schematic cross-section, **b** Pulsed and CW large signal measurements at 1 GHz ($V_{DS} = 40$ V with $I_{DS} = 5$ mA)

mainly due to self-heating: channel temperature during CW RF is 58 °C while 28 °C for pulsed RF. Large signal CW and pulsed RF performance of the device are shown in Fig. 6b.

4 Limits to RF and DC Performance (GaN and Ga_2O_3 HEMTs)

Prospective RF and DC power applications of HEMTs beg the question asking for suitability of GaN or Ga_2O_3 devices; the question is addressed by Kumar et al. [59], and stated that β-Ga_2O_3 HEMTs can deliver more RF output power over GaN HEMTs in low-frequency system (S-, L-, C-, and X-bands), but having a lower cut-off frequency (f_T),a drop of 50%, as power dissipation scaled by 600% due to higher values of thermal resistance (TR) and significant rise in channel temperature. Vis-à-vis dc power switching, despite of higher breakdown voltage, much lower electron mobility of β-Ga_2O_3 HEMTs limit its on-state performance: efficiency, loss, and current carrying capability. Comparison of RF performance done on the basis of three metrics: pf^2 limit (JFOM), cut-off frequency (f_T), and output power (P_{out}). Cut-off frequency (f_T) as a function of 2DEG density for both GaN and Ga_2O_3 HEMTs is redrawn in Fig. 7a. For β-Ga_2O_3, cut-off frequency can be increased (beyond 100 GHz) provided further minimization of contact and access region resistances (<1.5 Ω-mm) is achieved. The RF performance of the device depends critically on heat dissipation; thermal conductivity of active layer, and substrate material plays a key role. Channel temperature versus output power for both GaN and Ga_2O_3 HEMTs for different substrate materials is shown in Fig. 7b.

Increase in device RF output power obviously results in high channel temperature, for P_{out} of 10 W/mm, channel temperature of GaN HEMT stays below 160 °C (< 255 °C) on different substrate like SiC (GaN) having thickness of 350 μm. Channel

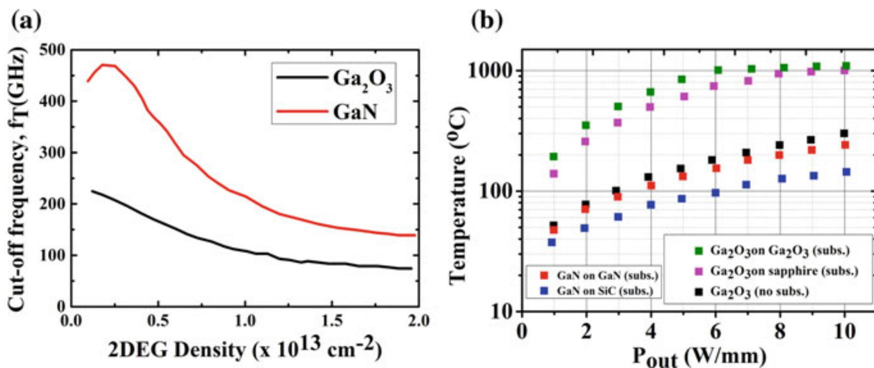

Fig. 7 **a** Ga_2O_3 and GaN HEMTs, plot of f_T versus 2DEG density (for gate length of 50 nm), **b** channel temperature versus output power using different substrates (channel thickness of 1 μm)

temperature of Ga_2O_3 HEMT on sapphire and Ga_2O_3 remains around 200 °C limited to P_{out} ~2 W/mm; however Ga_2O_3 with channel thickness of 1 μm and with no substrate, can deliver P_{out} ~7 W/mm. Furthermore, due to significant low electron mobility in Ga_2O_3 (~200 $cm^2\ V^{-1}s^{-1}$), Ga_2O_3 HEMTs pose a dismal picture in terms of efficiency and power dissipation on comparison of GaN HEMTs (electron mobility ~2000 $cm^2\ V^{-1}s^{-1}$) vis-à-vis power switching applications; large periphery of Ga_2O_3 devices required to match GaN switching performance.

5 Conclusion

Ultra-wide bandgap materials: GaN-, Ga_2O_3-based HEMTs show good performance metrics to achieve high output power density with large operating voltage and up to THz frequency range; these devices can well serve the requirement of rapidly expanding consumer applications: High-speed mobile Internet, hybrid and electric vehicle, efficient data centers, wireless charging, renewable energy systems, to name a few. GaN-based HEMTs have achieved significant progresses relating to RF applications in variety of areas: from material growth, device structure, processing technology, MMIC and intersubband (ISB) technologies, to THz spectroscopy, and imaging systems. GaN-based devices: HEMT successfully operated at ~600 GHz, for THz detection, PAs MMIC achieved P_{out} ~50 W/mm. Ga_2O_3 having unique material properties and large-size substrate availability (as compared to GaN), which improve its cost/performance metric over GaN, and finds exclusive applications—high power RF devices operating at low frequency—military-owned low-frequency high-voltage application, and AC-to-DC conversion utilities. Ga_2O_3 based HEMTs achieved CW output power of 13.7 dBm at 800 MHz with PAE of 6.3%, while small signal cut-off frequency of 3.3 GHz. Although very low electron mobility and poor thermal conductivity of β-Ga_2O_3 restrict high power operation due to significant increase in channel temperature led reduced electron mobility, although highly scaled devices having ballistic transport may address the issue. It is concluded that GaN- and β-Ga_2O_3 HEMTs can fully serve the entire RF power electronics application field based on commercial and technical aspects to choose the perfect one for the right application.

Acknowledgements This publication is an outcome of the R&D work undertaken by the project under the Visvesvaraya Ph.D. Scheme of Ministry of Electronics and Information Technology (MeitY), Govt. of India, being implemented by Digital India Corporation. Acknowledgement also goes to New Jersey Institute of Technology (NJIT), Newark, USA, for facilitating the visit of T. R. Lenka for collaborative research work.

References

1. E.O. Johnson, Physical limitation on frequency and power parameters of transistors. RCA Rev. 163–176 (1965)
2. B.J. Baliga, Semiconductors for high-voltage, vertical channel field-effect transistors. J. Appl. Phys. **53**(3), 1759–1764 (1982)
3. B.J. Baliga, Power semiconductor device figure of merit for high-frequency applications. IEEE Electron Device Lett. **10**(10), 455–457 (1989)
4. M. Higashiwaki, K. Sasaki, A. Kuramata, T. Masui, S. Yamakoshi, Gallium oxide (Ga2O3) metal-semiconductor field-effect transistors on single-crystal β-Ga2O3 (010) substrates. Appl. Phys. Lett. **100**(1), 013504 (2012)
5. R. Reiner, P. Waltereit, F. Benkhelifa, S. Muller, S. Müller, H. Walcher, S. Wagner, R. Quay, M. Schlechtweg, O. Ambacher, Fractal structures for low-resistance large area AlGaN/GaN power transistors, in *2012 24th International Symposium on Power Semiconductor Devices and ICs*, IEEE, 3 June 2012, pp. 341–344
6. U.K. Mishra, L. Shen, T.E. Kazior, Y.F. Wu, GaN-based RF power devices and amplifiers. Proc. IEEE **96**(2), 287–305 (2008)
7. J.H. Choi, High-speed devices and circuits with THz applications (CRC Press, 2014)
8. F. Medjdoub, Gallium nitride (GaN): physics, devices, and technology. (CRC Press, 2015)
9. J.L. Prince, J.M. Links, *Medical imaging signals and systems* (Pearson Prentice Hall, Upper Saddle River, 2006)
10. X. Wan, W.S. Zhou, S. Ren, D.G. Liu, J. Xu, H.L. Bo, E.X. Zhang, R.D. Schrimpf, D.M. Fleetwood, T.P. Ma, SEB hardened power MOSFETs with high-K dielectrics. IEEE Trans. Nucl. Sci. **62**(6), 2830–2836 (2015)
11. K. Ahi, Review of GaN-based devices for terahertz operation. Opt. Eng. **56**(9), 090901 (2017)
12. M. Asif Khan, J.N. Kuznia, D.T. Olson, W.J. Schaff, J.W. Burm, M.S. Shur, Microwave performance of a 0.25 μm gate AlGaN/GaN heterostructure field effect transistor. Appl. Phys. Lett. **65**(9), 1121–1123 (1994)
13. Y.F. Wu, B.P. Keller, S. Keller, D. Kapolnek, S.P. Denbaars, U.K. Mishra, Measured microwave power performance of AlGaN/GaN MODFET. IEEE Electron Device Lett. **17**(9), 455–457 (1996)
14. M.A. Khan, M.S. Shur, Q.C. Chen, J.N. Kuznia, Current/voltage characteristic collapse in AlGaN/GaN heterostructure insulated gate field effect transistors at high drain bias. Electron. Lett. **30**(25), 2175–2176 (1994)
15. S.C. Binari, K. Ikossi, J.A. Roussos, W. Kruppa, D. Park, H.B. Dietrich, D.D. Koleske, A.E. Wickenden, R.L. Henry, Trapping effects and microwave power performance in AlGaN/GaN HEMTs. IEEE Trans. Electron Devices **48**(3), 465–471 (2001)
16. B.M. Green, K.K. Chu, E.M. Chumbes, J.A. Smart, J.R. Shealy, L.F. Eastman, The effect of surface passivation on the microwave characteristics of undoped AlGaN/GaN HEMTs. IEEE Electron Device Lett. **21**(6), 268–270 (2000)
17. Y.F. Wu, D. Kapolnek, J. Ibbetson, N.Q. Zhang, P. Parikh, B.P. Keller, U.K. Mishra, High Al-content AlGaN/GaN HEMTs on SiC substrates with very high power performance, in *International Electron Devices Meeting 1999, Technical Digest (Cat. No. 99CH36318)*, IEEE, 5 Dec 1999, pp. 925–927
18. N.X. Nguyen, M. Micovic, W.S. Wong, P. Hashimoto, L.M. McCray, P. Janke, C. Nguyen, High performance microwave power GaN/AlGaN MODFETs grown by RF-assisted MBE. Electron. Lett. **36**(5), 468–469 (2000)
19. Y. Ando, Y. Okamoto, H. Miyamoto, T. Nakayama, T. Inoue, M. Kuzuhara, 10-W/mm AlGaN-GaN HFET with a field modulating plate. IEEE Electron Device Lett. **24**(5), 289–291 (2003)
20. J.R. Shealy, V. Kaper, V. Tilak, T. Prunty, J.A. Smart, B. Green, L.F. Eastman, An AlGaN/GaN high-electron-mobility transistor with an AlN sub-buffer layer. J. Phys. Condens. Matter **14**(13), 3499 (2002)

21. W.L. Pribble, J.W. Palmour, S.T. Sheppard, R.P. Smith, S.T. Allen, T.J. Smith, Z. Ring, J.J. Sumakeris, A.W. Saxler, J.W. Milligan, Applications of SiC MESFETs and GaN HEMTs in power amplifier design, in *2002 IEEE MTT-S International Microwave Symposium Digest (Cat. No. 02CH37278)*, IEEE, vol. 3, 2 June 2002, pp. 1819–1822
22. Y.F. Wu, A. Saxler, M. Moore, R.P. Smith, S. Sheppard, P.M. Chavarkar, T. Wisleder, U.K. Mishra, P. Parikh, 30-W/mm GaN HEMTs by field plate optimization. IEEE Electron Device Lett. **25**(3), 117–119 (2004)
23. Y. Okamoto, Y. Ando, K. Hataya, T. Nakayama, H. Miyamoto, T. Inoue, M. Senda, K. Hirata, M. Kosaki, N. Shibata, M. Kuzuhara, A 149 W recessed-gate AlGaN/GaN FP-FET, in *2004 IEEE MTT-S International Microwave Symposium Digest (IEEE Cat. No. 04CH37535)*, IEEE, vol. 3, 6 June 2004, pp. 1351–1354
24. Y.F. Wu, M. Moore, A. Saxler, T. Wisleder, P. Parikh, 40-W/mm double field-plated GaN HEMTs, in *2006 64th Device Research Conference*, IEEE, 26 June 2006, pp. 151–152
25. M.Y. Kao, C. Lee, R. Hajji, P. Saunier, H.Q. Tserng, AlGaN/GaN HEMTs with PAE of 53% at 35 GHz for HPA and multi-function MMIC applications, in *2007 IEEE/MTT-S International Microwave Symposium*, IEEE, 3 June 2007, pp. 627–629
26. Y. Murase, A. Wakejima, T. Inoue, K. Yamanoguchi, M. Tanomura, T. Nakayama, Y. Okamoto, K. Ota, Y. Ando, N. Kuroda, K. Matsunaga, CW 20-W AlGaN/GaN FET power amplifier for quasi-millimeter wave applications, in *2007 IEEE Compound Semiconductor Integrated Circuits Symposium*, IEEE, 14 Oct 2007, pp. 1–4
27. D.C. Dumka, T.M. Chou, F. Faili, D. Francis, F. Ejeckam, AlGaN/GaN HEMTs on diamond substrate with over 7 W/mm output power density at 10 GHz. Electron. Lett. **49**(20), 1298–1299 (2013)
28. P.C. Chao, K. Chu, J. Diaz, C. Creamer, S. Sweetland, R. Kallaher, C. McGray, G.D. Via, J. Blevins, GaN-on-diamond HEMTs with 11 W/mm output power at 10GHz. MRS Advances **1**(2), 147–155 (2016)
29. M. Micovic, D.F. Brown, D. Regan, J. Wong, Y. Tang, F. Herrault, D. Santos, S.D. Burnham, J. Tai, E. Prophet, I. Khalaf, High frequency GaN HEMTs for RF MMIC applications, in *2016 IEEE International Electron Devices Meeting (IEDM)*, IEEE, 3 Dec 2016, pp. 3–3
30. B. Romanczyk, S. Wienecke, M. Guidry, H. Li, E. Ahmadi, X. Zheng, S. Keller, U.K. Mishra, Demonstration of constant 8 W/mm power density at 10, 30, and 94 GHz in state-of-the-art millimeter-wave N-polar GaN MISHEMTs. IEEE Trans. Electron Devices **65**(1), 45–50 (2017)
31. Y. Lu, X. Ma, L. Yang, B. Hou, M. Mi, M. Zhang, J. Zheng, H. Zhang, Y. Hao, High RF performance AlGaN/GaN HEMT fabricated by recess-arrayed ohmic contact technology. IEEE Electron Device Lett. **39**(6), 811–814 (2018)
32. W. Lu, V. Kumar, E.L. Piner, I. Adesida, DC, RF, and microwave noise performance of AlGaN-GaN field effect transistors dependence of aluminum concentration. IEEE Trans. Electron Devices **50**(4), 1069–1074 (2003)
33. T. Palacios, C.S. Suh, A. Chakraborty, S. Keller, S.P. DenBaars, U.K. Mishra, High-performance E-mode AlGaN/GaN HEMTs. IEEE Electron Device Lett. **27**(6), 428–430 (2006)
34. J.W. Chung, W.E. Hoke, E.M. Chumbes, T. Palacios, AlGaN/GaN HEMT With 300-GHz $f_{\max}$. IEEE Electron Device Lett. **31**(3), 195–197 (2010)
35. D. Denninghoff, J. Lu, M. Laurent, E. Ahmadi, S. Keller, U.K. Mishra, N-polar GaN/InAlN MIS-HEMT with 400-GHz $f_{\max}$, in *70th Device Research Conference*, IEEE, 18 June 2012, pp. 151–152
36. A.G. Baca, B.A. Klein, J.R. Wendt, S.M. Lepkowski, C.D. Nordquist, A.M. Armstrong, A.A. Allerman, E.A. Douglas, R.J. Kaplar, RF performance of Al 0.85 Ga 0.15 N/Al 0.70 Ga 0.30 N high electron mobility transistors with 80-nm gates. IEEE Electron Device Lett. **40**(1), 17–20 (2018)
37. D. Qiao, Z.F. Guan, J. Carlton, S.S. Lau, G.J. Sullivan, Low resistance ohmic contacts on AlGaN/GaN structures using implantation and the “advancing” Al/Ti metallization. Appl. Phys. Lett. **74**(18), 2652–2654 (1999)
38. H. Yu, L. McCarthy, S. Rajan, S. Keller, S. Denbaars, J. Speck, U. Mishra, Ion implanted AlGaN-GaN HEMTs with nonalloyed ohmic contacts. IEEE Electron Device Lett. **26**(5), 283–285 (2005)

39. F. Recht, L. McCarthy, S. Rajan, A. Chakraborty, C. Poblenz, A. Corrion, J.S. Speck, U.K. Mishra, Nonalloyed ohmic contacts in AlGaN/GaN HEMTs by ion implantation with reduced activation annealing temperature
40. F. Recht, L. McCarthy, L. Shen, C. Poblenz, A. Corrion, J.S. Speck, U.K. Mishra, AlGaN/GaN HEMTs with large angle implanted nonalloyed ohmic contacts, in *2007 65th Annual Device Research Conference*, IEEE, 18 June 2007, pp. 37–38
41. X.C. Fu, Y. Lv, L.J. Zhang, T. Zhang, X.J. Li, X. Song, Z. Zhang, Y. Fang, Z. Feng, High-frequency InAlN/GaN HFET with $f_{\max}$ over 400 GHz. Electron. Lett. **54**(12), 783–785 (2018)
42. M. Dyakonov, M. Shur, Shallow water analogy for a ballistic field effect transistor: new mechanism of plasma wave generation by dc current. Phys. Rev. Lett. **71**(15), 2465 (1993)
43. W. Knap, M. Dyakonov, D. Coquillat, F. Teppe, N. Dyakonova, J. Łusakowski, K. Karpierz, M. Sakowicz, G. Valusis, D. Seliuta, I. Kasalynas, Field effect transistors for terahertz detection: Physics and first imaging applications. J. Infrared Millim. Terahertz Waves **30**(12), 1319–1337 (2009)
44. F. Friederich, W. Von Spiegel, M. Bauer, F. Meng, M.D. Thomson, S. Boppel, A. Lisauskas, B. Hils, V. Krozer, A. Keil, T. Loffler, THz active imaging systems with real-time capabilities. IEEE Trans. Terahertz Sci. Technol **1**(1), 183–200 (2011)
45. J.D. Sun, Y.F. Sun, D.M. Wu, Y. Cai, H. Qin, B.S. Zhang, High-responsivity, low-noise, room-temperature, self-mixing terahertz detector realized using floating antennas on a GaN-based field-effect transistor. Appl. Phys. Lett. **100**(1), 013506 (2012)
46. J.D. Sun, H. Qin, R.A. Lewis, Y.F. Sun, X.Y. Zhang, Y. Cai, D.M. Wu, B.S. Zhang, Probing and modelling the localized self-mixing in a GaN/AlGaN field-effect terahertz detector. Appl. Phys. Lett. **100**(17), 173513 (2012)
47. A. Lisauskas, M. Bauer, S. Boppel, M. Mundt, B. Khamaisi, E. Socher, R. Venckevičius, L. Minkevičius, I. Kašalynas, D. Seliuta, G. Valušis, Exploration of terahertz imaging with silicon MOSFETs. J. Infrared Millim. Terahertz Waves **35**(1), 63–80 (2014)
48. H. Hou, Z. Liu, J.H. Teng, T. Palacio, S.J. Chua, Modelling of GaN HEMTs as terahertz detectors based on self-mixing. Proc. Eng. **1**(141), 98–102 (2016)
49. Q. Li, N. An, Y. Tang, J. Jiang, L. Li, J. Zeng, W. Tan, Metal-semiconductor-metal (MSM) varactor based on AlGaN/GaN heterostructure with cutoff frequency of 914.5 GHz for terahertz frequency multiplication, in *2018 IEEE 3rd International Conference on Integrated Circuits and Microsystems (ICICM)*, IEEE, 24 Nov 2018, pp. 86–89
50. M. Bauer, A. Rämer, S.A. Chevtchenko, K. Osipov, D. Čibiraitė, S. Pralgauskaitė, K. Ikamas, A. Lisauskas, W. Heinrich, V. Krozer, H.G. Roskos, A high-sensitivity AlGaN/GaN HEMT terahertz detector with integrated broadband bow-tie antenna. IEEE Trans. Terahertz Sci. Technol. (2019)
51. M. Higashiwaki, G.H. Jessen, Guest editorial: the dawn of gallium oxide microelectronics. Appl. Phys. Lett. **112**(6), 060401. https://doi.org/10.1063/1.5017845
52. S.J. Pearton, F. Ren, M. Tadjer, J. Kim, Perspective: Ga_2O_3 for ultra-high power rectifiers and MOSFETS. J. Appl. Phys. **124**(22), 220901 (2018)
53. J. Yang, F. Ren, M. Tadjer, S.J. Pearton, A. Kuramata, Ga_2O_3 Schottky rectifiers with 1 ampere forward current, 650 V reverse breakdown and 26.5 MW cm^{-2} figure-of-merit. AIP Advances **8**(5), 055026 (2018)
54. H. Dong, H. Xue, Q. He, Y. Qin, G. Jian, S. Long, M. Liu, Progress of power field effect transistor based on ultra-wide bandgap Ga_2O_3 semiconductor material. J. Semiconductors **40**(1), 011802 (2019)
55. A.J. Green, K.D. Chabak, M. Baldini, N. Moser, R. Gilbert, R.C. Fitch, G. Wagner, Z. Galazka, J. Mccandless, A. Crespo, K. Leedy, β-Ga_2O_3 MOSFETs for radio frequency operation. IEEE Electron Device Lett. **38**(6), 790–793 (2017)
56. G. Jessen, K. Chabak, A. Green, N. Moser, J. McCandless, K. Leedy, A. Crespo, S. Tetlak, Gallium oxide technologies and applications, in *2017 IEEE Compound Semiconductor Integrated Circuit Symposium (CSICS)*, IEEE, 22 Oct 2017, pp. 1–4
57. M. Singh, M.A. Casbon, M.J. Uren, J.W. Pomeroy, S. Dalcanale, S. Karboyan, P.J. Tasker, M.H. Wong, K. Sasaki, A. Kuramata, S. Yamakoshi, Pulsed large signal RF performance of field-plated Ga_2O_3 MOSFETs. IEEE Electron Device Lett. **39**(10), 1572–1575 (2018)

58. M.D. Santia, N. Tandon, J.D. Albrecht, Lattice thermal conductivity in β-Ga_2O_3 from first principles. Appl. Phys. Lett. **107**(4), 041907 (2015)
59. S. Kumar, R. Soman, A.S. Pratiyush, R. Muralidharan, D.N. Nath, A performance comparison between β-Ga_2O_3 and GaN HEMTs. IEEE Trans. Electron Devices **66**(8), 3310–3317 (2019)
60. R. Gaska, J.W. Yang, A. Osinsky, Q. Chen, M.A. Khan, A.O. Orlov, G.L. Snider, M.S. Shur, Electron transport in AlGaN–GaN heterostructures grown on 6H–SiC substrates. Appl. Phys. Lett. **72**(6), 707–709 (1998)
61. L. Ardaravičius, A. Matulionis, J. Liberis, O. Kiprijanovic, M. Ramonas, L.F. Eastman, J.R Shealy, A. Vertiatchik, Electron drift velocity in AlGaN/GaN channel at high electric fields. Appl. Phys. Lett. **83**(19) (2003) 4038–4040; F. Medjdoub, Gallium nitride (GaN): Physics, devices, and technology. CRC Press (2015)
62. Y. Kang, K. Krishnaswamy, H. Peelaers, C.G. Van de Walle, Fundamental limits on the electron mobility of β-Ga2O3. J. Phys. Condens. Matter **29**(23), 234001 (2017)
63. K. Ghosh, U. Singisetti, Ab initio velocity-field curves in monoclinic β-Ga_2O_3. J. Appl. Phys. **122**(3), 035702 (2017)
64. Y. Zhang, Z. Xia, J. Mcglone, W. Sun, C. Joishi, A.R. Arehart, S.A. Ringel, S. Rajan, Evaluation of low-temperature saturation velocity in β-$(Al_xGa_{1-x})_2O_3/Ga_2O_3$ modulation-doped field-effect transistors. IEEE Trans. Electron Devices **66**(3), 1574–1578 (2019)

Potentiality of Impact Avalanche Transit Time Diode as Terahertz Source Based on Group IV and III–V Semiconducting Materials

Girish Chandra Ghivela, S. J. Mukhopadhyay, Joydeep Sengupta and M. Mitra

Abstract Through the numerical approach, we have determined the response time in avalanche and drift regions of the double drift region (DDR) impact ionization avalanche transit time (IMPATT) diode based on group IV materials like silicon (Si), germanium (Ge) and group III–V materials like wurtzite gallium nitride (WzGaN), gallium arsenide (GaAs) and indium phosphide (InP) at the window frequency of 0.094–30 THz. The study of response time reveals that it has impact on the limitation on high frequency power generated by the IMPATT as terahertz source. A comparison is being made for all the materials so that diode can be designed with suitable material as per the requirement for THz applications. Also DC-to-radio frequency (RF) conversion efficiency for InP, GaAs, Si, Ge and WzGaN is computed through the numerical technique. The efficiency obtained for all the materials are compared at the corresponding THz frequency.

Keywords Impact ionization · Avalanche · Drift · Response time · THz · Semiconductors

1 Introduction

Impact ionization avalanche transit time (IMPATT) diode is used to generate the high power at microwave, millimeter wave and sub-millimeter wave regions [1]. It has high power capability compared to other diodes [2, 3]. Its operation provides a phase shift through avalanche and drift delays [4–6]. Phase noise due to phase shift causes a negative resistance in IMPATT. Operations at these regions are highly disturbed due to phase noise [7]. The negative resistance is arising from these delays as reported in [4–6, 8–12]. These delays are indirectly affecting the phase noise through negative resistance, and the phase noise degrades the conversion efficiency. But, the phase noise and DC-to-RF conversion efficiency mainly depend on base

G. C. Ghivela (✉) · J. Sengupta
ECE Department, VNIT, Nagpur 440010, India
e-mail: girishvnit2012@gmail.com

S. J. Mukhopadhyay · M. Mitra
E&TC Department, IIEST, Shibpur, Howrah, India

© Springer Nature Singapore Pte Ltd. 2020

A. Biswas et al. (eds.), *Emerging Trends in Terahertz Solid-State Physics and Devices*,
https://doi.org/10.1007/978-981-15-3235-1_5

material [13]. Therefore, here, we have taken Si, Ge, GaAs, InP and WzGaN as base substrate material to study the conversion efficiency and the delay amount. Under actual operating condition, considerable amount of DC current flow through the diode and the space charges modifies the electric field distribution which in turn affects the current density profiles of electrons and holes by changing the magnitude of ionization rates. So, through simultaneous solution of the Poisson and current continuity equations (Eqs. 1 and 2) [14–18], using the computer simulation program, we can accurately investigate the conversion efficiency, delay amount, inductance-capacitance values in avalanche region and resonant frequencies of IMPATT diode. IMPATT has been modeled as shown in Fig. 1 [18–21] at 0.094–30 THz. In Fig. 1, field maximum (E_m) is at X_0, W comprises of drift layer width for electrons (d_n), drift layer width for holes (d_p) and avalanche layer width (X_A), and J_0 represents total current density.

The Poisson's equation and current continuity equation are, respectively, given by

$$\frac{\partial E(x)}{\partial x} = \frac{q}{\varepsilon}[N_\mathrm{D} - N_\mathrm{A} + p(x) - n(x)] \tag{1}$$

and

$$-\frac{\partial J_n}{\partial x} = \frac{\partial J_p}{\partial x} = \alpha_n J_n + \alpha_p J_p \tag{2}$$

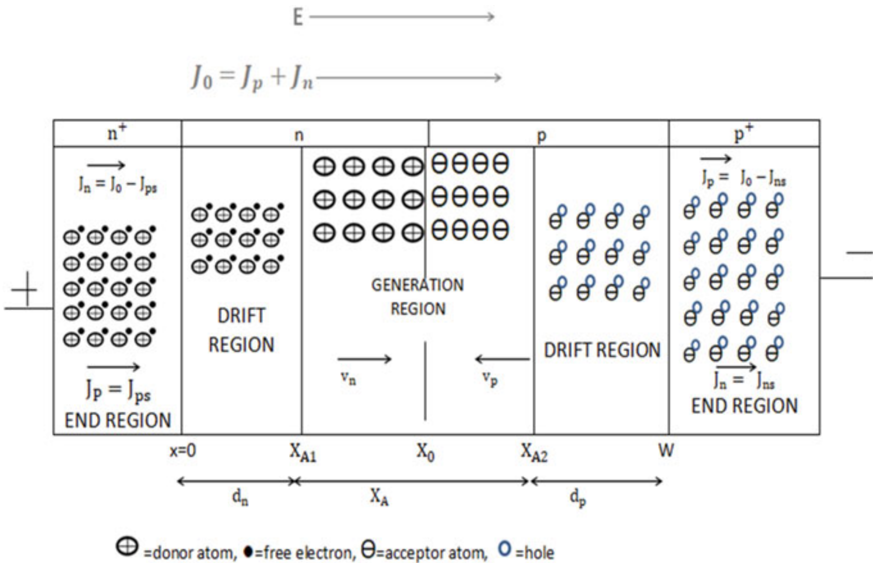

Fig. 1 Mathematical model of DDR IMPATT

where $E(x)$ and q are electric field profile and electronic charge, $\varepsilon = \varepsilon_0 \varepsilon_s$ is permittivity of semiconductor, N_D and N_A are donor and acceptor densities, n and p for electron and hole, and J and α are current density and ionization rate [14].

2 Numerical Method and Design Parameters

To find the conversion efficiency, the numerical method is initiated from X_0 with E_m. E_m and X_0 are initially chosen suitably for the fitted doping profile and current density. Then, Eqs. (1) and (2) are solved simultaneously by taking space steps of very small width (0.001 nm). Iteration over E_m and X_0 is carried out till boundary conditions are being satisfied at $x = 0$ and W. Thus, electric field and current distribution are obtained from the computations. The method described above gives the avalanche breakdown characteristics and the avalanche layer width X_A. Computer simulation using MATLAB is carried out, and the width of the epilayers is accordingly chosen using the transit time formula, $W_{n,p} = ((0.5 \times V_{ns,ps})/f)$ with π transit angle, where V_s and f are saturation velocity and frequency [17]. The breakdown voltage (V_B) and avalanche drop (V_A) are found using Eq. (3) [17, 22–28].

$$V_B = \int_0^W E(x)\mathrm{d}x \text{ and } V_A = \int_{XA_1}^{X_{A_2}} E(x)\mathrm{d}x \tag{3}$$

Then, the drift voltage drop is $V_D = V_B - V_A$. The DC-to-RF conversion efficiency is

$$\eta(\%) = \frac{2m V_D}{\pi V_B} \tag{4}$$

where m is the modulation index.

The avalanche response time is obtained by solving Eq. (5)

$$\tau_A \frac{\partial J}{\partial t} = -(J_p - J_n)|_0^{X_A} + 2J \int_0^{X_A} \alpha \mathrm{d}x \tag{5}$$

where $\tau_A = X_A/v_s$ is avalanche transit time with saturation velocity (v_s) and $J = J_n + J_p$ [7].

Equivalent circuit of IMPATT is shown in Fig. 2, where G, B and R_s are conductance, susceptance and series resistance of diode, respectively. Further internal circuitry in terms of inductance and capacitance effect of the IMPATT in avalanche and drift region is shown in Fig. 3. The inductive and capacitive natures in the avalanche region are having parallel effect, but the inductance in the drift region is in

series with drift region capacitance [12]. However, the effect of this series inductance is less as compared to drift capacitive impedance and can be neglected.

The avalanche inductance and capacitance are

$$L_A = \frac{\tau_A}{2J_0\alpha' A}$$

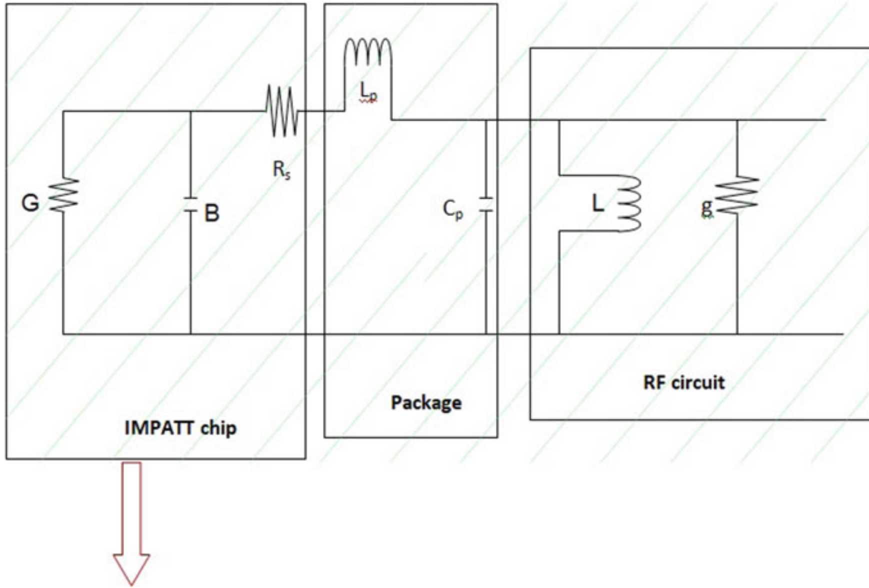

Fig. 2 Equivalent circuit of IMPATT diode with packaging

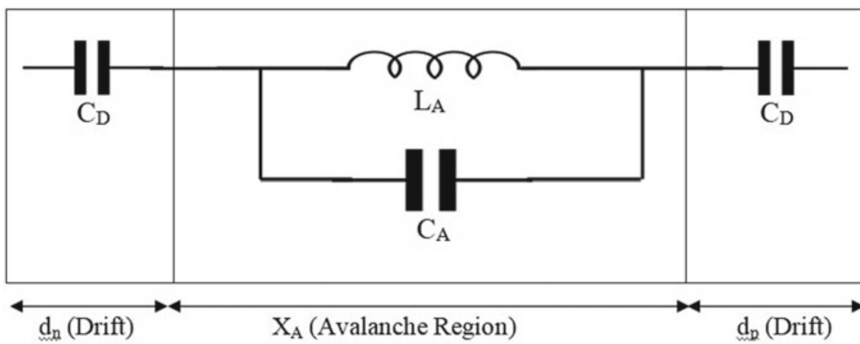

Fig. 3 Inductive and capacitive nature at avalanche and drift region of IMPATT

$$= \frac{\tau_{\mathrm{A}}}{2J_s\alpha' A}\left(1 - \int_0^W \langle\alpha\rangle \mathrm{d}x\right)$$

$$= \frac{\tau_{\mathrm{A}}}{2J_s\left(\frac{\partial\alpha}{\partial E}\right)A}\left(1 - \int_0^W \langle\alpha\rangle \mathrm{d}x\right) \tag{6}$$

$$C_{\mathrm{A}} = \frac{\varepsilon_s A}{X_{\mathrm{A}}} \tag{7}$$

and the resonant frequency of this L-C combination is given by

$$\omega_r = 2\pi f_r = \sqrt{\frac{2\alpha' v_s J_0}{\varepsilon_s}} \tag{8}$$

where J_0 is the DC current density, $\alpha' = (\partial\alpha/\partial E)$, A and α are diode area and ionization integrand, respectively [7]. Drift response time is given by

$$\tau_{\mathrm{D}} = \frac{(W - X_{\mathrm{A}})}{v_s} \tag{9}$$

and the drift capacitance is

$$C_{\mathrm{Drift}} = \frac{A\varepsilon_s}{(W - X_{\mathrm{A}})} \tag{10}$$

Recently reported design parameters have been used in our numerical study [17].

3 Results and Discussion

The frequency, where maximum efficiency is obtained, is termed here as peak frequency. IMPATT's efficiencies by using different materials are given in Table 1. The highest efficiency of 14.12% is obtained from InP at 20 THz, which is the maximum among all. InP has better efficiency at all corresponding frequencies. GaAs has the closest value to InP. Si and Ge have moderate level, whereas WzGaN has very low efficiency. Peak frequencies for GaAs, Si, Ge and WzGaN are 20 THz, 20 THz, 22 THz and 22 THz, respectively.

Table 1 Efficiency values over THz frequencies

Frequency (in THz)	DC-to-RF power conversion efficiency of DDR IMPATT based on				
	InP	GaAs	Si	Ge	WzGaN
0.094	6.51	6.18	4.79	5.92	3.25
01	6.70	6.25	4.88	6.05	3.35
02	6.75	6.81	5.69	6.24	4.01
04	8.68	7.06	6.43	6.36	4.12
06	10.24	7.58	7.31	7.40	4.39
08	10.86	8.03	7.95	7.73	4.65
10	11.21	8.26	8.22	8.25	4.75
12	11.53	8.64	8.49	8.51	4.95
14	12.02	9.44	8.70	8.84	5.12
16	13.15	10.35	9.28	10.02	5.25
18	13.95	12.22	9.73	10.49	5.45
20	14.12	11.46	10.28	10.62	5.75
22	13.31	10.98	9.62	11.02	5.97
24	12.94	10.86	9.49	10.44	6.38
26	12.77	10.26	9.19	10.02	6.05
28	12.36	9.64	8.88	9.31	5.54
30	11.71	9.08	8.54	8.78	5.42

3.1 Avalanche Response Time Determination

The avalanche response time (τ_A) is determined for n^+-n-p-p^+ DDR IMPATT based on Si, Ge, WzGaN, GaAs and InP at window frequencies of 0.094–30 THz. Dependency of avalanche response time in frequencies is shown in Fig. 4. τ_A value of InP is much higher than that of Si, Ge, GaAs and WzGaN. Si- and WzGaN-based IMPATTs are having lowest τ_A values and both are close to each other in the range of 0.5–0.9 ps at the corresponding frequencies. GaAs and Ge are having in the range of 1.3–1.8 ps. As Si and WzGaN are having the lowest values, the charge carriers are quickly generating more number of carriers and can produce high frequency power. Due to higher avalanche response time, InP cannot produce high frequency power. However, InP is having highest DC-to-RF conversion efficiencies as shown in Table 1.

3.2 Drift Response Time Calculation

A comparative drift response time with frequency variation is shown in Fig. 5. In the drift region, InP-based charge carriers are taking less time to reach the n-p junction

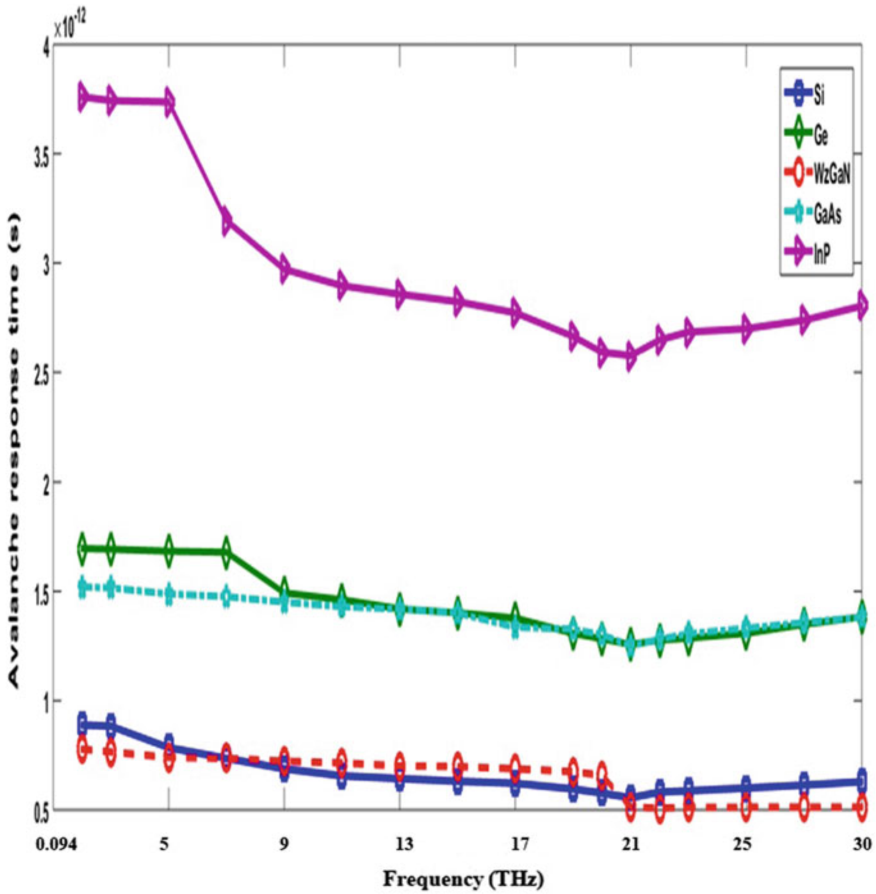

Fig. 4 Avalanche response time as a function of frequency

as compared to its Si, Ge, WzGaN and GaAs counterparts. From the obtained results, it can be understood that though WzGaN and Si have higher drift response time, still those values are close to that of others.

3.3 Drift Capacitance and Resonant Frequency

In the THz band frequencies, drift capacitance and resonant frequency in IMPATT are computed and listed in Tables 2 and 3. The drift capacitance is increasing with frequency for all the materials. Ge-based IMPATT has higher drift capacitance variation from 0.0685 to 0.1113 F, and its WzGaN counterpart is having lower variation from 0.0061 to 0.0142 F. InP is having lower resonant frequencies as compared to

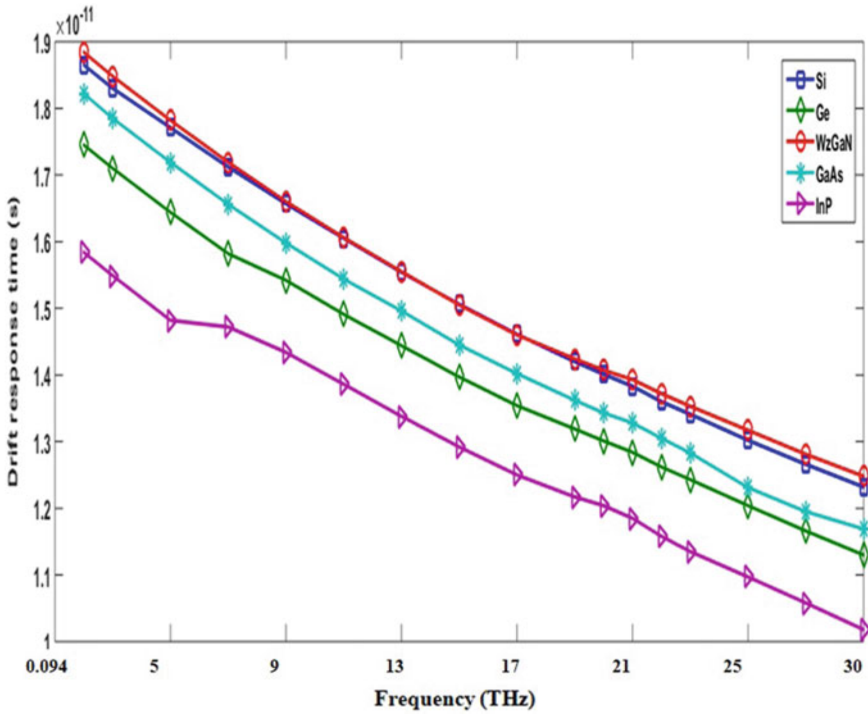

Fig. 5 Dependency of drift response time on frequency

others at the corresponding frequencies. From these variations of drift capacitance, we can get an idea about the time constant of the device.

4 Conclusion

Maximum conversion efficiencies are obtained from the InP-based IMPATT as compared to Si, Ge, GaAs and WzGaN at the THz band of 0.094–30 THz. Since no experimental results are available based on response time determination, inductance and capacitance profiles measurement and efficiency calculation over the entire frequency range of THz band for all the materials, no comparison could be made. However, these results can be helpful for the practical realization of IMPATT and to improve the IMPATT performance based on doping, avalanche and drift widths selection with proper semiconducting material.

Table 2 Computed drift capacitance

f (in THz)	Si	Ge	WzGaN	GaAs	InP
	C_{Drift} (F)	C_{Drift} (F)	C_{Drift} (F)	C_{Drift} (F)	C_{Drift} (F)
0.094	0.0405	0.0685	0.0061	0.0428	0.0666
01	0.0415	0.0701	0.0063	0.0438	0.0683
02	0.0432	0.0734	0.0069	0.0459	0.0719
04	0.0451	0.0766	0.0072	0.0481	0.0724
06	0.0469	0.0789	0.0082	0.0501	0.0746
08	0.0488	0.082	0.0085	0.0523	0.0775
10	0.0507	0.0849	0.0094	0.0544	0.0807
12	0.0526	0.0881	0.0098	0.0565	0.0297
14	0.0545	0.0912	0.0107	0.0586	0.087
16	0.0564	0.0939	0.0109	0.0606	0.0896
18	0.0573	0.0954	0.0115	0.0616	0.0908
20	0.0582	0.0968	0.0117	0.0624	0.0924
22	0.0593	0.0986	0.0121	0.0637	0.0948
24	0.0503	0.1003	0.0124	0.0649	0.0968
26	0.0624	0.1038	0.0129	0.0673	0.1006
28	0.0645	0.1075	0.0135	0.0698	0.1047
30	0.0666	0.1113	0.0142	0.0722	0.1092

Table 3 Computed resonant frequency

f (in THz)	Si	Ge	WzGaN	GaAs	InP
	ω_r ($\times 10^7$ rad/s)	ω_r ($\times 10^7$ rad/s)	ω_r ($\times 10^7$ rad/s)	ω_r ($\times 10^7$ rad/s)	ω_r ($\times 10^7$ rad/s)
0.094	9.51	7.352	9.52	4.556	0.851
01	9.36	7.227	8.03	4.474	0.82
02	8.588	7.07	7.662	4.18	0.776
04	8.071	6.775	7.452	4.007	0.592
06	7.418	6.177	7.01	3.774	0.46
08	7.037	6.009	7.75	3.579	0.397
10	6.816	5.611	7.37	3.447	0.353
12	6.613	5.413	7.12	3.291	0.313
14	6.434	5.2	6.928	3.070	0.267
16	6.184	4.776	6.675	2.856	0.202
18	6.033	4.617	6.356	2.732	0.164
20	5.882	4.455	5.129	2.544	0.149
22	6.04	4.5	5.054	2.612	0.165
24	6.019	4.5	5.012	2.666	0.169
26	5.895	4.516	4.96	2.697	0.155
28	5.872	4.614	4.851	2.739	0.151
30	5.859	4.674	4.803	2.78	0.718

References

1. T.A. Midford, R.L. Bernick, Millimeter wave CW IMPATT diodes and oscillators. IEEE Trans. Microw. Theory Tech. **27**(5), 483–492 (1979)
2. D. Ke-Lin, M.N.S. Swamy, *Wireless Communication Systems: From RF Subsystems to 4G Enabling Technologies* (Cambridge University Press, Cambridge, 2010), pp. 416–417
3. J.H. Chris, S.R. Balmer, Diamond as an electronic material. Mater. Today **11**, 22–28 (2008)
4. W.T. Read, A proposed high-frequency negative-resistance diode. Bell Syst. Tech. J. **37**(2), 401–446 (1958)
5. R.L. Johnston, B.C. De Loach Jr., B.G. Cohen, A silicon diode microwave oscillator. Bell Syst. Tech. J. **44**(2), 369–372 (1965)
6. C.A. Lee, R.L. Batdorf, W. Wiegmann, G. Kaminski, The read diode-an avalanching, transit-time, negative resistance oscillator. Appl. Phys. Lett. **6**(5), 89–91 (1965)
7. S.M. Sze, K.K. Ng, *Physics of Semiconductor Devices* (Wiley, New Jersey, 2007), pp. 466–488
8. W. Shockley, Negative resistance arising from transit time in semiconductor diode. Bell Syst. Tech. J. **33**(4), 799–826 (1954)
9. B.C. DeLoach Jr., The IMPATT story. IEEE Trans. Electron. Dev. **23**(7), 657–660 (1976)
10. T. Misawa, Negative resistance in p-n junction under avalanche breakdown conditions, part I. IEEE Trans. Electron. Dev. **13**(1), 137–143 (1966)
11. T. Misawa, Negative resistance in p-n junction under avalanche breakdown conditions, part II. IEEE Trans. Electron. Dev. **13**(1), 143–151 (1966)
12. M. Gilden, M.E. Hines, Electronic tuning effects in the read microwave avalanche diode. IEEE Trans. Electron. Dev. **13**(1), 169–175 (1966)

13. Electronic archive: New semiconductor materials, characteristics and properties. http://www.ioffe.ru/SVA/NSM/Semicond
14. D.N. Datta, S.P. Pati, J.P. Banerjee, B.B. Pal, S.K. Roy, Computer analysis of DC field and current density profiles of DAR impatt diode. IEEE Trans. Electron. Devices **29**(11), 1813–1816 (1982)
15. S.K. Roy, M. Sridharan, R. Ghosh, B.B. Pal, *Computer method for the DC field and carrier current profiles in the field extremum in the depletion layer* (NASECODEI Proc, Dublin (Ireland), 1982), pp. 266–274
16. G.C. Ghivela, J. Sengupta, Prospects of impact avalanche transit-time diode based on chemical-vapor-deposited diamond substrate. J. Electron. Mater. **48**(2), 1044–1053 (2019)
17. G.C. Ghivela, J. Sengupta, M. Mitra, Space charge effect of IMPATT diode using Si, Ge, GaAs, InP, WzGaN, 4H-SiC at Ka band. IETE J. Edu. **58**(2), 61–66 (2017)
18. G.C. Ghivela, J. Sengupta, Estimation of power density in IMPATT using different materials. Inter. J. Electron. https://doi.org/10.1080/00207217.2019.1672810
19. J. Sengupta, G.C. Ghivela, A. Gajbhiye, M. Mitra, Measurement of noise and efficiency of 4H-SiC Impatt diode at Ka band. Int. J. Electron. Lett. **4**(2), 134–140 (2016)
20. G.C. Ghivela, J. Sengupta, M. Mitra, Ka band noise comparison for Si, Ge, GaAs, InP, WzGaN, 4H-SiC based IMPATT diode. Int. J. Electron. Lett. **7**(1), 107–116 (2019)
21. G.C. Ghivela, J. Sengupta, Noise performance of avalanche transit–time devices in the presence of acoustic phonons. J. Comput. Electron. **18**(1), 222–230 (2019)
22. G.C. Ghivela, J. Sengupta, Modeling and computation of double drift region transit time diode performance based on graphene-SiC. Int. J. Numer. Model **32**(5), 01–11 (2019)
23. G.C. Ghivela, J. Sengupta, Effect of acoustic phonon scattering on impact ionization rate of electrons in monolayer graphene nanoribbons. Appl. Phys. A **124**(762), 01–08 (2018)
24. G.C. Ghivela, J. Sengupta, M. Mitra, Quantum corrected drift diffusion based noise model for impact avalanche and transit time diode. Superlattices Microstruct. **128**, 402–407 (2019)
25. P. Banerjee, A. Acharyya, A. Biswas, A.K. Bhattacharjee, Effect of magnetic field on the RF performance of millimeter-wave IMPATT source. J. Comput. Electron. **15**(1), 210–221 (2016)
26. P.K. Bandyopadhyay, S. Chakraborty, A. Biswas, A. Acharyya, A.K. Bhattacharjee, Large-signal characterization of millimeter-wave IMPATTs: effect of reduced impact ionization rate of charge carriers due to carrier-carrier interactions. J. Comput. Electron. **15**(2), 646–656 (2016)
27. P.K. Bandyopadhyay, A. Biswas, A.K. Bhattacharjee, A. Acharyya, Influence of carrier–carrier interactions on the noise performance of millimeter-wave IMPATTs. IETE J. Res. (2018). https://doi.org/10.1080/03772063.2018.1433078
28. A. Biswas, S. Sinha, A. Acharyya, A. Banerjee, S. Pal, H. Satoh, H. Inokawa, 1.0 THz GaN IMPATT source: Effect of parasitic series resistance. J. Infrared Millim. Terahertz Waves **39**(10), 954–974 (2018)

Analysis of InN-Based Surrounded Gate Tunnel Field-Effect Transistor for Terahertz Applications

Ritam Dutta and Nitai Paitya

Abstract The analysis of a proposed surrounded gate pocket intrinsic tunnel field-effect transistor (SG-PI-TFET) has been reported based on indium nitride (InN). The device structure has been simulated and analyzed using TCAD device simulator taking non-local band-to-band tunneling (BTBT) into consideration. We have accounted the fundamental limits of InN tunnel FET devices arising from the basic material properties by numerical simulation and analytical calculations. The tunneling current is evaluated and the effects are analyzed with a change in different device parameters to create the TFET design rule. The cut-off frequency (f_t) of the device is found to be 0.45 THz which makes it appropriate for high-frequency applications.

Keywords Tunnel field-effect transistor (TFET) · SG-PI-TFET · Band-to-band tunneling (BTBT) · InN · TCAD device simulator

1 Introduction

In the modern era, tunnel field-effect transistor (TFET) is contemplated as one of the most promising contenders for low-power application post-CMOS logic devices to overcome the short-channel effects (SCE) and reduced OFF current. TFETs operate on the basis of quantum mechanical phenomenon of band-to-band tunneling (BTBT) and possess excellent switching properties, and on the other side, TFETs suffer from a low drive current (I_{ON}). So, various techniques to improve I_{ON} in tunnel FET have been reported [1–6]. With the advent of recent TFET research work, new approaches emerged but the preferred channel material and geometry for the TFET are still unresolved. To enhance the performance efficiency of tunnel FET devices, device engineering has been carried out where III-N heterojunctions are forcing a number of new insights in junction design and doping for low-power applications. The possibility of indium nitride for high-speed electronic devices is thoroughly documented [7, 8].

R. Dutta · N. Paitya (✉)
Department of Electronics and Communication Engineering, Sikkim Manipal Institute of Technology, Sikkim Manipal University, Gangtok, Sikkim 737136, India
e-mail: nitai.p@smit.smu.edu.in

© Springer Nature Singapore Pte Ltd. 2020

A. Biswas et al. (eds.), *Emerging Trends in Terahertz Solid-State Physics and Devices*,
https://doi.org/10.1007/978-981-15-3235-1_6

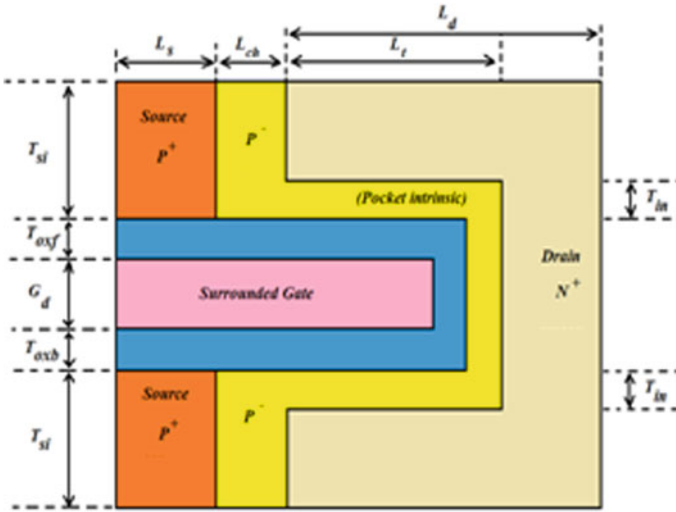

Fig. 1 Cross-sectional view of proposed SG-PI tunnel FET

This paper deliberates a proposed surrounded gate pocket intrinsic tunnel FET (SG-PI-TFET) based on InN, where the performance of indium nitride tunnel FET is assessed using two-dimensional numerical device simulations. Here, we have focused on analyzing the high-frequency performance.

2 Device Structure and Simulation

2.1 Different Device Models

The proposed SG-PI-TFET structure is depicted in Fig. 1 with tunneling length (L_t) extended to 45 nm, resulting in the intrinsic channel length scaled down to 10 nm.

The extended overlapping region between the drain and surrounded gate results in high chance of carrier transport. Since the channel has been reduced, a considerable amount of high drain current is obtained. The proposed TFET structure includes thin pocket regions as per design and underlies the gate dielectric to cause band-to-band tunneling.

2.2 Device and Electrical Parameter Analysis

Necessary parameter for device structure and for DC analysis is considered for the device development, mentioned in Table 1.

Table 1 Typical parameters

Parameters	SG-PI-TFET
Channel length (L_{ch})	10 nm
Tunneling length (L_t)	45 nm
Source length (L_S)	20 nm
Drain length (L_d)	70 nm
Effective oxide thickness—front gate (T_{oxf})	2 nm
Effective oxide thickness—back gate (T_{oxf})	2 nm
InN film thickness (T_{si})	10 nm
Source doping	1×10^{20} per cm^3
Drain doping	1×10^{17} per cm^3
Intrinsic channel doping	1×10^{15} per cm^3
Pocket intrinsic thickness (T_{in})	5 nm
Gate depth (G_d)	4 nm
Metal work function (Φ)	4.3 eV
Gate-source voltage (V_{GS})	1 V
Supply voltage (V_{DS})	1 V

2.3 Proposed Methodology and Simulation Framework

The device makes a transition from OFF-state to ON-state, since the device electrostatics is not much influenced by mobile charges [9]; therefore, the 2-D Poisson's equation is used to determine the surface potential. Therefore, we can write:

$$\frac{\partial^2 \psi(x, y)}{\partial x^2} + \frac{\partial^2 \psi(x, y)}{\partial y^2} = \frac{q N_R}{\varepsilon_i} \quad \text{for } 0 \le x \le L, 0 \le y \le T_{si} \tag{1}$$

where $\psi(x, y)$ is electrostatic bias, q is charge, ε_i is permittivity of InN, and N_R is doping concentration of the region considered. Total channel length is L where $L = L_{ch} + L_t$ and t_{si} is the channel thickness.

The surface potential is approximated by segregating the channel region laterally into effective regions. Young's approximation is used to obtain $\psi(x, y)$ by assuming the necessary boundary conditions [10].

For the electric field modeling, lateral field (E_x) and vertical field (E_y) are attained by following formula:

$$E_x = -\frac{\partial \psi(x, y)}{\partial x} \text{ and } E_y = -\frac{\partial \psi(x, y)}{\partial y} \tag{2}$$

After simplifying the above expressions, the total electric field can be obtained as:

$$E = \sqrt{E_x^2 + E_y^2} \tag{3}$$

Now, the drain or tunneling current can be obtained by using Kane's model [11, 12].

$$I_{\text{tun}} = q \iint G_{\text{BTBT}} \mathrm{d}x \mathrm{d}y \tag{4}$$

where the carrier generation rate is

$$G_{\text{BTBT}} = A_{\text{K}} \frac{|E|^D}{\sqrt{E_{\text{g}}}} \exp\left(-\frac{B_{\text{K}} E_{\text{g}}^{3/2}}{|E|}\right) \tag{5}$$

Here, A_{K} and B_{K} are the effective mass-dependent device parameters [13]. D is the constant for DBG and IDBG materials [14], whereas E_{g} is energy gap of InN channel and E is the local electric field [4].

The proposed SG-PI-TFET is designed with device simulator. Since reduction of defect-assisted transport processes faces serious challenges in tunnel FET design, therefore, the Shockley–Read–Hall (SRH) model is used to assimilate recombination effects. This simulates leakage current due to thermal generation. Non-local band-to-band tunneling (BTBT) model is used in this work.

3 Results and Discussion

3.1 DC Characteristics

To overcome the limitations of boosting I_{ON} and for making fast switching TFET, the I_{ON} characteristics plays an important role. In addition to this, low I_{OFF} is also desirable for low leakage current. In Fig. 2, we can see that oxide thickness variation affects I_{ON} significantly. Oxide thickness is varied from 2 to 8 nm keeping doping of 1×10^{17} cm^{-3} in drain region.

From Fig. 2, it is evident that a steep slope is obtained that leads to boost in drain current I_{DS} for minimum oxide thickness. The metal work function for SG-PI-TFET is chosen as 4.3 eV.

Figure 3 shows the $I_{\text{DS}} - V_{\text{GS}}$ characteristics of InN-based SG-PI-TFET in which the drain current increases with increasing gate-source bias.

Figure 4 shows a surface potential variation for gate bias along the channel. The TCAD simulated results are validated with analytical model.

Figure 5 represents an electric field behaved laterally along the x-axis with the channel to study SCE.

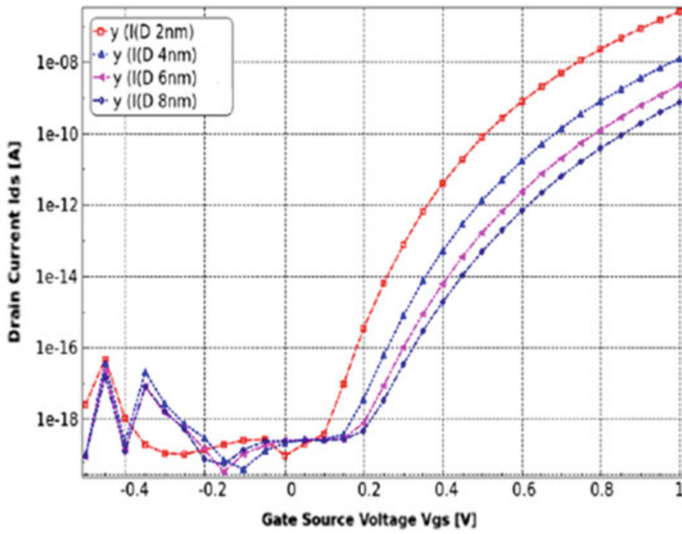

Fig. 2 Transfer characteristics for both I_{ON} and I_{OFF} for SG-PI-TFET under oxide thickness variation

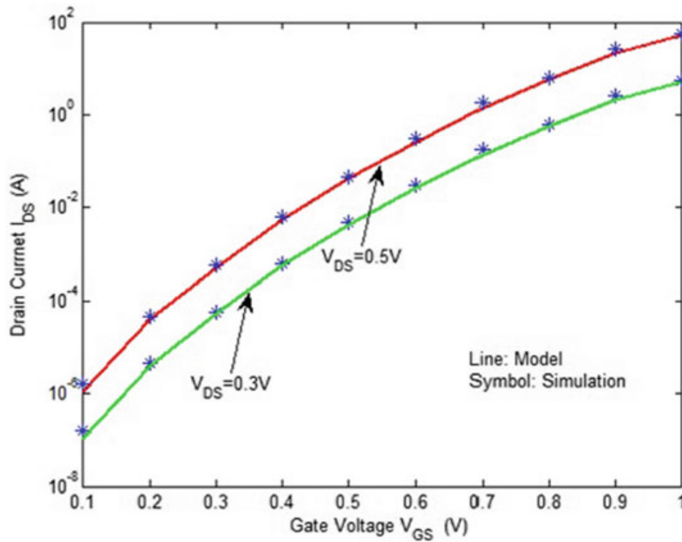

Fig. 3 Transfer characteristics for SG-PI-TFET under channel length $L_t = 45$ nm with $V_{DS} = 0.3$ and 0.5 V

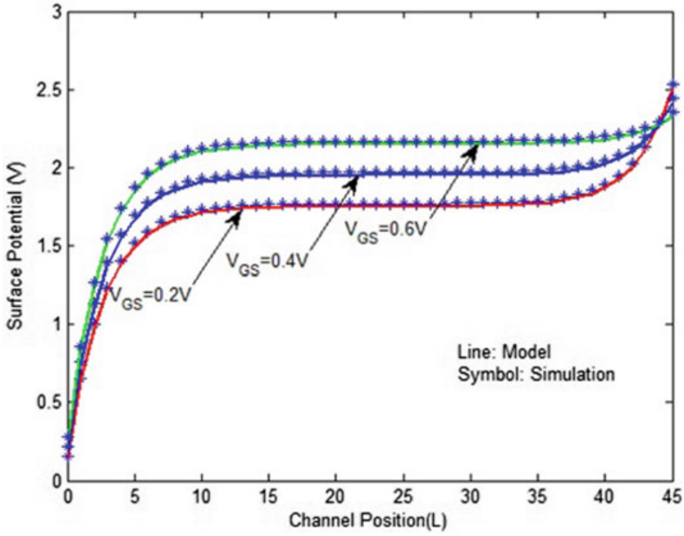

Fig. 4 Surface potential variation for SG-PI-TFET under channel length $L_t = 45$ nm with different gate biases, keeping $V_{DS} = 0.5$ V

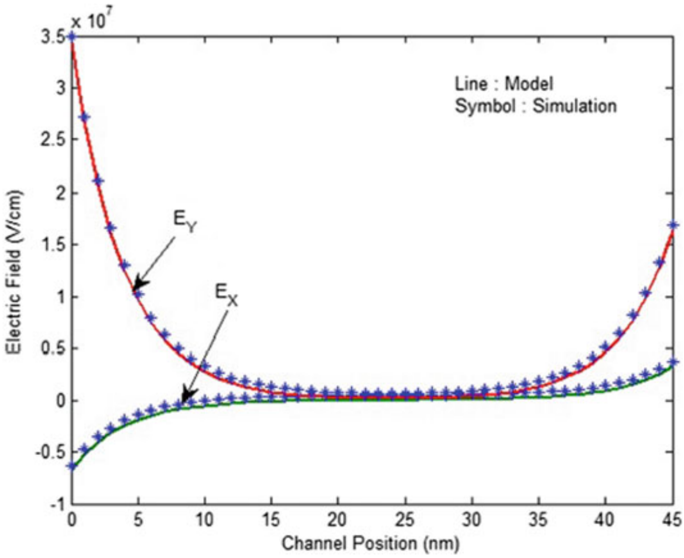

Fig. 5 Electric field profile for SG-PI-TFET under channel length $L_t = 45$ nm, keeping $V_{DS} = 0.5$ V

Figure 5 proves that the vertical e-field reaches its peak in source region. High electric field for SG-PI-TFET indicates higher tunneling rate traversed from source to channel.

3.2 *Small-Signal Analysis*

After establishing the dc biasing, we simulate the small-signal performance of the proposed device under different V_{ds}. The cut-off frequency [15] is:

$$f_t = \frac{g_m}{2\pi(C_{gs} + C_{gd})},$$

where g_m is the transconductance of the device; C_{gs} and C_{gd} are capacitance values between gate-source and gate-drain regions, respectively.

In order to analyze the small-signal characteristics, a 1 MHz source is applied to the gate varied from 0 to 1 V, C_{gs} and C_{gd} are extracted. C_{gs} and C_{gd} along with g_m are utilized to evaluate (f_t). It is clear [16] that lower gate capacitance, that lower gate capacitance ($C_{gg} = C_{gs} + C_{gd}$) and higher transconductance (g_m) of tunnel FET help to attain better THz performance.

From Fig. 6a, b, it can be observed that major increase in g_m occurs due to consecutive effect of an increase in tunneling possibility and a reduction of electrons because of high barrier height at drain-channel region at higher V_{ds}.

The combined effort of reducing C_{gg} and raising g_m uplifts the cut-off frequency f_t. Our proposed SG-PI TFET provides a maximum cut-off frequency $f_t = 0.45$ THz at $V_{ds} = 1$ V.

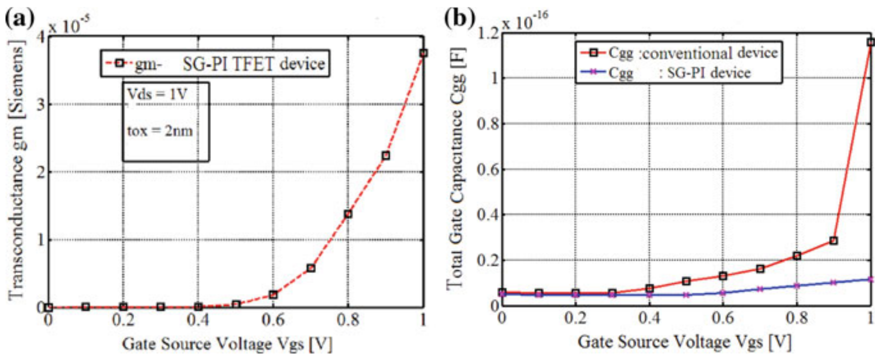

Fig. 6 **a** Transconductance plot for SG-PI-TFET, **b t**otal gate-capacitance plot

4 Conclusion

In summary, a TFET design is proposed which has the potential of high-power THz applications. We have conducted a thorough analysis on the high-frequency performance of SG-PI-TFET based on InN with suitable simulation results for the first time with systematical studies and analyses of the device performance for future development of other InN devices.

References

1. T. Nirschl, S. Henzler, J. Fischer et al., Scaling properties of the tunneling field effect transistor (TFET): device and circuit. Solid State Electron. **50**(1), 44–51 (2006)
2. Q. Zhang, W. Zhao, A. Seabaugh, Low-subthreshold-swing tunnel transistors. IEEE Electron Device Lett. **27**(4), 297–300 (2006)
3. W.Y. Choi, B.G. Park, J.D. Lee, Tunneling field effect transistor (TFET) with subthreshold swing (SS) less than 60 mV/dec. IEEE Electron Device Lett. **28**(8), 743–745 (2007)
4. A.S. Verhulst, D. Leonelli, R. Rooyackers, G. Groeseneke, Drain voltage dependent analytical model of tunnel field-effect transistors. J. Appl. Phys. **110**(2), 024510 (2011)
5. S. Brocard, M. Pala, D. Esseni, Design options for heterojunction tunnel FETs with high on current and steep sub-VT slope, in *Proceedings of IEEE International Electron Devices Meeting (IEDM)*, (San Francisco, CA, USA, 2012), pp. 1, 4, 5
6. W. Lee, W.Y. Choi, Influence of inversion layer on tunneling field-effect transistors. IEEE Electron Device Lett. **32**(9), 1191–1193 (2011)
7. K.T. Tsen, C. Poweleit, D.K. Ferry, H. Lu, W.J. Schaff, Observation of large electron drift velocities in InN by ultrafast Raman spectroscopy. Appl. Phys. Lett. **86**(22), 222103 (2005)
8. S.K. O'Leary, B.E. Foutz, M.S. Shur, L.F. Eastman, Potential performance of indium-nitride-based devices. Appl. Phys. Lett. **88**(15), 152113 (2006)
9. C. Shen, S.-L. Ong, C.-H. Heng, G. Samudra, Y.-C. Yeo, A variational approach to the two-dimensional nonlinear poisson's equation for the modeling of tunneling transistors. IEEE Electron Device Lett. **29**, 1252–1255 (2008)
10. P. Wisniewski, B. Majkusiak, Modeling the tunnel field-effect transistor based on different tunneling path approaches. IEEE Trans. Electron Devices **65**(6), 2626–2631 (2018)
11. E.O. Kane, Theory of tunneling. J. Appl. Phys. **32**(1), 83–91 (1961)
12. M.G. Bardon, H.P. Neves, R. Puers, C. Van Hoof, Pseudo two-dimensional model for double-gate tunnel FETs considering the junctions depletion regions. IEEE Trans. Electron Devices **57**(4), 827–834 (2010)
13. E.O. Kane, Zener tunneling in semiconductors. J. Appl. Phys. Chem. Solids **12**(2), 181–188 (1960)
14. Y. Khatami, K. Banerjee, Steep subthreshold slope n and p-type tunnel-FET devices for low-power and energy efficient digital circuits. IEEE Trans. Electron Devices **56**(11), 2752–2761 (2009)
15. S. Cho, J.S. Lee, K.R. Kim, B.G. Park, J.S. Harris, I.M. Kang, Analyses on small—signal parameters and radio-frequency modeling of gate-all-around tunneling field effect transistors. IEEE Trans. Electron Devices **58**(12), 4164–4171 (2011)
16. J. Madan, R. Chaujar, Numerical simulation of N+ source pocket PIN-GAA-tunnel FET: impact of interface trap charges and temperature. IEEE Trans. Electron Devices **64**(4), 1482–1488 (2017)

On the Quantum Capacitance of Quantum Wire Field-Effect Transistors of Compound Semiconductors

A. H. Seikh, N. Alharthi, P. K. Bose and K. P. Ghatak

Abstract This chapter explores the quantum capacitance (C_g) in quantum wire field-effect transistors (QWFETs) manufactured from completely different technologically vital nonstandard materials by using all types of anisotropies of band structures in addition to splitting of bands due to large fields of the crystals inside the framework of Kane's matrix methodology that successively generates new 1D dimensional electron energy versus wave vector relation. We derive the C_g under very low temperature so that the Fermi function tends to unity for QWFETs of Cd_3As_2, $CdGeAs_2$, InSb, $Hg_{1-x}Cd_xTe$, InAs, GaAs, $In_{1-x}Ga_xAs_yP_{1-y}$ IV–VI, stressed materials,Te, GaP,$PtSb_2$, Bi_2Te_3, Ge, GaSb and II–V compounds using the appropriate band models. The C_g becomes the functions of the thickness of the quantum-confined transistors. The C_g varies with varying film thickness in various quantized steps and saw-tooth manners with different numerical values.

Keywords Quantum capacitance · Quantum wire field effect transistors · Compound semiconductors · Film thickness

The C_g for the QWFETs of all the materials as considered here increases with increasing 1D electron statistics in step-like fashion and decreases in an oscillatory way with the increasing gate voltage. All the results for all models gets simplified to the

A. H. Seikh
Centre of Excellence for Research in Engineering Materials, Deanship of Scientific Research, King Saud University, Riyadh 11421, Saudi Arabia

N. Alharthi
Department of Mechanical Engineering, College of Engineering, King Saud University, Riyadh 11421, Saudi Arabia

P. K. Bose
Department of Mechanical Engineering, Swami Vivekananda Institute of Science and Technology, Dakshin Gobindapur Sonarpur, Kolkata, West Bengal 700145, India

K. P. Ghatak (✉)
Department of Basic Science Institute of Engineering and Management, D-1, Management House, Salt Lake, Sector-V, Kolkata, West Bengal 700091, India
e-mail: kamakhyaghatakcu@gmail.com

© Springer Nature Singapore Pte Ltd. 2020

A. Biswas et al. (eds.), *Emerging Trends in Terahertz Solid-State Physics and Devices*,
https://doi.org/10.1007/978-981-15-3235-1_7

result of C_g in QWFET having wide energy band gap materials subjected to various constraints which exhibit the mathematical compatibility of our simplified theory.

1 Introduction

A carrier in semiconducting samples moves on the closed 3D wave vector (k) space wherever the overall electron energy (E) is constant. The system spatiality will manufacture 1D electron motion once; these carriers are forced to move in one direction, whereas the other two wave vector components assume quantized values. Hence, the one-dimensional energy wave vector dispersion relations become straight lines whose length decreases with the increase of the size quantum numbers leading to quantization. The physical properties of such 1D system have been investigated in the recent literature extensively [1–40]. Although many researchers had reported their investigations in various forms, it seems that the study of other new aspects of such 1D structure is becoming more and more necessary. One such important quantum quantity that in recent years generates substantial interest is that the quantum capacitance (C_g) of quantum wire field-effect transistors (QWFET) which is biased by a gate voltage creating a large surface field of force[41–44]. The 1D carrier statistics in such 1D layer will rather simply be varied by varying V_g that, in turn, brings an amendment of the electric field of force, the C_g depends on the gate voltage. This variation has been investigated for QWFETs of wide band gap materials shows few necessary periodical characteristics of such devices. In this chapter, we shall study the C_g in QWFET of all the materials as stated in the abstract.

2 Theoretical Background

In QWFET, the C_g can be expressed by the following equation

$$C_g = e\bar{D}n_s \tag{1}$$

where e is the electron charge, $\bar{D} = \frac{\partial}{\partial V_g}$, V_g is the gate voltage and n_s is the 1D electron statistics.

2.1 The C_g in QWFET of Tetragonal Materials

The derivation of C_g depends on n_s and the same can be derived by using Heisenberg's scientific theory at low temperatures with the unit value of Fermi–Dirac function without using the difficult DOS technique as used by us in [41] as

$$n_{\mathrm{s}} = \frac{2g_v}{\pi} S\big[B_{11}\big(E'_{\mathrm{F}}, n_x, n_y\big)\big] \tag{2}$$

where, $S = \sum_{n_x=1}^{n_{z}\max} \sum_{n_y=1}^{n_y\max}$, $E'_{\mathrm{F}} = [e\bar{V}_{\mathrm{g}} - E_{\mathrm{fb}} - \frac{e^2 n_0}{C_{\mathrm{ins}}}]$, E_{fb} is Fermi energy of the bulk material, $C_{\mathrm{ins}} = \frac{2\pi\varepsilon_{\mathrm{ins}}}{\ln\left(\frac{2t_{\mathrm{ins}}+t_{\mathrm{wire}}}{t_{\mathrm{wire}}}\right)}$, $\varepsilon_{\mathrm{ins}}$ is the permittivity of the insulator layer, t_{ins} is the thickness of the insulator layer and t_{wire} is the diameter of the wire. And the other notations are given in [41].

Using (1) and (2) the C_{g} can be expressed as

$$C_{\mathrm{g}} = \left[\frac{2g_v e^2}{\pi} S(\theta_1)\right]\left[1 + \frac{2g_v e^2}{\pi C_{\mathrm{ins}}} S(\theta_1)\right]^{-1} \tag{3}$$

where, $\theta_1 = \frac{\partial}{\partial E'_{\mathrm{F}}}\big(B_{11}\big(E'_{\mathrm{F}}, n_x, n_y\big)\big)$.

2.2 *The C_g in QWFET of Kane-Type Compounds*

(i) **The Three-band model of Kane**

Under certain constraints, Eqs. (2) and (3) get simplified as

$$n_{\mathrm{s}} = \frac{2g_v}{\pi} S\big[B_{13}\big(E'_{\mathrm{F}}, n_x, n_y\big)\big] \tag{4}$$

$$C_{\mathrm{g}} = \left[\frac{2g_v e^2}{\pi} S(\theta_2)\right]\left[1 + \frac{2g_v e^2}{\pi C_{\mathrm{ins}}} S(\theta_2)\right]^{-1} \tag{5}$$

where, $\theta_2 = \frac{\partial}{\partial E'_{\mathrm{F}}}\big(B_{13}(E'_{\mathrm{F}}, n_x, n_y)\big)$ and $B_{13}(E'_{\mathrm{F}}, n_x, n_y)$ are defined in [41].

(ii) **The Two-band model of Kane**

Under certain constraints, Eqs. (4) and (5) assume the forms

$$n_{\mathrm{s}} = \frac{2g_v}{\pi} S\big[B_{15}\big(E'_{\mathrm{F}}, n_x, n_y\big)\big] \tag{6a}$$

$$C_{\mathrm{g}} = \left[\frac{2g_v e^2}{\pi} S(\theta_3)\right]\left[1 + \frac{2g_v e^2}{\pi C_{\mathrm{ins}}} S(\theta_3)\right]^{-1} \tag{6b}$$

where, $\theta_3 = \frac{\partial}{\partial E'_{\mathrm{F}}}\big(B_{15}\big(E'_{\mathrm{F}}, n_x, n_y\big)\big)$ and $B_{15}\big(E'_{\mathrm{F}}, n_x, n_y\big)$ are defined in [41].

(iii) **The isotropic parabolic energy bands**

Under the condition of very large band gap, Eqs. (6a) and (6b) assume the forms

$$n_{\mathrm{s}} = \frac{2g_v}{\pi} S\big[\bar{B}_{15}\big(E'_{\mathrm{F}}, n_x, n_y\big)\big] \tag{7a}$$

$$C_{\mathrm{g}} = \left[\frac{2g_v e^2}{\pi} S(\bar{\theta}_3)\right]\left[1 + \frac{2g_v e^2}{\pi C_{\mathrm{ins}}} S(\bar{\theta}_3)\right]^{-1} \tag{7b}$$

where, $\bar{B}_{15}\big(E'_{\mathrm{F}}, n_x, n_y\big) = \left[\frac{2\bar{m}_{\mathrm{c}}}{\hbar^2}\big(E'_{\mathrm{F}}\big) - \left(\left(\frac{n_x\pi}{d_x}\right)^2 + \left(\frac{n_y\pi}{d_y}\right)^2\right)\right]^{1/2}$ and $\bar{\theta}_3 = \frac{\partial}{\partial E'_{\mathrm{F}}}\big(\bar{B}_{15}\big(E'_{\mathrm{F}}, n_x, n_y\big)\big)$.

(iv) **The model of Stillman et al.**

The 1D electron statistics under the condition of unity Fermi function at low temperatures can be written following [41] as

$$n_{\mathrm{s}} = \frac{2g_v}{\pi} S\big[B_{17}\big(E'_{\mathrm{F}}, n_x, n_y\big)\big] \tag{8}$$

Using (1) and (8) the C_{g} can be expressed as

$$C_{\mathrm{g}} = \left[\frac{2g_v e^2}{\pi} S(\theta_4)\right]\left[1 + \frac{2g_v e^2}{\pi C_{\mathrm{ins}}} S(\theta_4)\right]^{-1} \tag{9}$$

where, $\theta_4 = \frac{\partial}{\partial E'_{\mathrm{F}}}\big(B_{17}\big(E'_{\mathrm{F}}, n_x, n_y\big)\big)$.

(v) **The model of Newson and Kurobe**

The 1D electron statistics under the condition of unity Fermi function at low temperatures can be written following [41] as

$$n_{\mathrm{s}} = \frac{2g_v}{\pi} S\big[B_{19}\big(E'_{\mathrm{F}}, n_x, n_y\big)\big] \tag{10}$$

Using (1) and (10) the C_{g} can be expressed as

$$C_{\mathrm{g}} = \left[\frac{2g_v e^2}{\pi} S(\theta_5)\right]\left[1 + \frac{2g_v e^2}{\pi C_{\mathrm{ins}}} S(\theta_5)\right]^{-1} \tag{11}$$

where, $\theta_5 = \frac{\partial}{\partial E'_{\mathrm{F}}}\big(B_{19}\big(E'_{\mathrm{F}}, n_x, n_y\big)\big)$.

(vi) **The model of Palik et al.**

The 1D electron statistics under the condition of unity Fermi function at low temperatures can be written following [41] as

$$n_{\mathrm{s}} = \frac{2g_v}{\pi} S\left[B_{21}\left(E'_{\mathrm{F}}, n_x, n_y\right)\right] \tag{12}$$

Using (1) and (12) the C_{g} can be expressed as

$$C_{\mathrm{g}} = \left[\frac{2g_v e^2}{\pi} S(\theta_6)\right]\left[1 + \frac{2g_v e^2}{\pi C_{\mathrm{ins}}} S(\theta_6)\right]^{-1} \tag{13}$$

where, $\theta_6 = \frac{\partial}{\partial E'_{\mathrm{F}}}\left(B_{21}\left(E'_{\mathrm{F}}, n_x, n_y\right)\right)$.

2.3 The $\mathrm{C_g}$ *in QWFET of II–VI Materials*

The 1D electron statistics under the condition of unity Fermi function at low temperatures can be written following [41] as

$$n_{\mathrm{s}} = \frac{g_v}{\pi\sqrt{B_0}} S\left[t_7\left(E'_{\mathrm{F}}, n_x, n_y\right)\right] \tag{14}$$

Using (1) and (14) the C_{g} can be expressed as

$$C_{\mathrm{g}} = \left[\frac{g_v e^2}{\pi\sqrt{B_0}} S(\theta_7)\right]\left[1 + \frac{g_v e^2}{C_{\mathrm{ins}}\pi\sqrt{B_0}} S(\theta_7)\right]^{-1} \tag{15}$$

where, $\theta_7 = \frac{\partial}{\partial E'_{\mathrm{F}}}\left(t_7\left(E'_{\mathrm{F}}, n_x, n_y\right)\right)$.

2.4 The $\bar{C}_G$ *in QWFET of IV–VI Materials*

The 1D electron statistics under the condition of unity Fermi function at low temperatures can be written following [41] as

$$n_{\mathrm{s}} = \frac{2g_v}{\pi} S\left[B_{32}\left(E'_{\mathrm{F}}, n_x, n_y\right)\right] \tag{16}$$

Using (1) and (16) the C_{g} can be expressed as

$$C_{\mathrm{g}} = \left[\frac{2g_v e^2}{\pi} S(\theta_8)\right]\left[1 + \frac{2g_v e^2}{\pi C_{\mathrm{ins}}} S(\theta_8)\right]^{-1} \tag{17}$$

where, $\theta_8 = \frac{\partial}{\partial E'_{\mathrm{F}}}\left(B_{32}\left(E'_{\mathrm{F}}, n_x, n_y\right)\right)$.

2.5 The C_g in QWFET of Stressed Materials

The 1D electron statistics under the condition of unity Fermi function at low temperatures can be written following [41] as

$$n_{\mathrm{s}} = \frac{2g_v}{\pi} S\left[B_{34}\left(E'_{\mathrm{F}}, n_x, n_y\right)\right] \tag{18}$$

Using (1) and (18) the C_{g} can be expressed as

$$C_{\mathrm{g}} = \left[\frac{2g_v e^2}{\pi} S(\theta_9)\right]\left[1 + \frac{2g_v e^2}{\pi C_{\mathrm{ins}}} S(\theta_9)\right]^{-1} \tag{19}$$

where, $\theta_9 = \frac{\partial}{\partial E'_{\mathrm{F}}}\left(B_{34}\left(E'_{\mathrm{F}}, n_x, n_y\right)\right)$.

2.6 The C_g in QWFET of GaP Material

The 1D electron statistics under the condition of unity Fermi function at low temperatures can be written following [41] as

$$n_{\mathrm{s}} = \frac{2g_v}{\pi} S\left[B_{38}\left(E'_{\mathrm{F}}, n_x, n_y\right)\right] \tag{20}$$

Using (1) and (20) the C_{g} can be expressed as

$$C_{\mathrm{g}} = \left[\frac{2g_v e^2}{\pi} S(\theta_{10})\right]\left[1 + \frac{2g_v e^2}{\pi C_{\mathrm{ins}}} S(\theta_{10})\right]^{-1} \tag{21}$$

where, $\theta_{10} = \frac{\partial}{\partial E'_{\mathrm{F}}}\left(B_{38}\left(E'_{\mathrm{F}}, n_x, n_y\right)\right)$.

2.7 The C_g in QWFET of $PtSb_2$ Material

The 1D electron statistics under the condition of unity Fermi function at low temperatures can be written following [41] as

$$n_{\mathrm{s}} = \frac{2g_v}{\pi} S\big[B_{40}\big(E'_{\mathrm{F}}, n_x, n_y\big)\big] \tag{22}$$

Using (1) and (22) the C_{g} can be expressed as

$$C_{\mathrm{g}} = \left[\frac{2g_v e^2}{\pi} S(\theta_{11})\right]\left[1 + \frac{2g_v e^2}{\pi C_{\mathrm{ins}}} S(\theta_{11})\right]^{-1} \tag{23}$$

where, $\theta_{11} = \frac{\partial}{\partial E'_{\mathrm{F}}}\big(B_{40}\big(E'_{\mathrm{F}}, n_x, n_y\big)\big)$.

2.8 The C_g in QWFET of Bi_2Te_3 Material

The 1D electron statistics under the condition of unity Fermi function at low temperatures can be written following [41] as

$$n_{\mathrm{s}} = \frac{2g_v}{\pi} S\big[B_{42}\big(E'_{\mathrm{F}}, n_x, n_y\big)\big] \tag{24}$$

Using (1) and (24) the C_{g} can be expressed as

$$C_{\mathrm{g}} = \left[\frac{2g_v e^2}{\pi} S(\theta_{12})\right]\left[1 + \frac{2g_v e^2}{\pi C_{\mathrm{ins}}} S(\theta_{12})\right]^{-1} \tag{25}$$

where, $\theta_{12} = \frac{\partial}{\partial E'_{\mathrm{F}}}\big(B_{42}\big(E'_{\mathrm{F}}, n_x, n_y\big)\big)$.

2.9 The C_g in QWFET of Ge

α. **Model of Cardona et al.**

The 1D electron statistics under the condition of unity Fermi function at low temperatures can be written following [41] as

$$n_s = \frac{2g_v}{\pi} S\left[B_{44}(E'_F, n_x, n_y)\right] \tag{26}$$

Using (1) and (26) the C_g can be expressed as

$$C_g = \left[\frac{2g_v e^2}{\pi} S(\theta_{13})\right]\left[1 + \frac{2g_v e^2}{\pi C_{ins}} S(\theta_{13})\right]^{-1} \tag{27}$$

where, $\theta_{13} = \frac{\partial}{\partial E'_F}\left(B_{44}\left(E'_F, n_x, n_y\right)\right)$.

β. **Model of Wang and Ressler**

The 1D electron statistics under the condition of unity Fermi function at low temperatures can be written following [41] as

$$n_s = \frac{2g_v}{\pi} S\left[B_{46}\left(E'_F, n_x, n_y\right)\right] \tag{28}$$

Using (1) and (28) the C_g can be expressed as

$$C_g = \left[\frac{2g_v e^2}{\pi} S(\theta_{14})\right]\left[1 + \frac{2g_v e^2}{\pi C_{ins}} S(\theta_{14})\right]^{-1} \tag{29}$$

where, $\theta_{14} = \frac{\partial}{\partial E'_F}\left(B_{46}\left(E'_F, n_x, n_y\right)\right)$.

2.10 The C_g in QWFET of GaSb

The 1D electron statistics under the condition of unity Fermi function at low temperatures can be written following [41] as

$$n_s = \frac{2g_v}{\pi} S\left[B_{48}\left(E'_F, n_x, n_y\right)\right] \tag{30}$$

Using (1) and (30) the C_g can be expressed as

$$C_g = \left[\frac{2g_v e^2}{\pi} S(\theta_{15})\right]\left[1 + \frac{2g_v e^2}{\pi C_{ins}} S(\theta_{15})\right]^{-1} \tag{31}$$

where, $\theta_{15} = \frac{\partial}{\partial E'_F}\left(B_{48}\left(E'_F, n_x, n_y\right)\right)$.

2.11 The C_g in QWFET of II–V Materials

The 1D electron statistics under the condition of unity Fermi function at low temperatures can be written following [41] as

$$n_s = \frac{2g_v}{\pi} S\left[B_{49}\left(E'_F, n_x, n_y\right)\right] \tag{32}$$

Using (1) and (32) the C_g can be expressed as

$$C_g = \left[\frac{2g_v e^2}{\pi} S(\theta_{16})\right]\left[1 + \frac{2g_v e^2}{\pi C_{ins}} S(\theta_{16})\right]^{-1}$$

where, $\theta_{16} = \frac{\partial}{\partial E'_F}\left(B_{49}\left(E'_F, n_x, n_y\right)\right)$.

3 Results and Discussion

The normalized C_g in QWFETs made of $CdGeAs_2$ with film thickness as the independent variable has been premeditated in Fig. 1 by taking the different values of the energy band parameters as given in [41] using (a) Eq. 3 (orange), (b) Eq. 3 with $\delta = 0$ (brown), (c) Eq. 5 (green), (d) Eq. 6b (red), and (e) Eq. 7b (blue). From Fig. 1, it appears that the normalized C_g enhances in quantized saw-tooth manner with increasing film thickness. The normalized C_g in QWFETs made of InAs with film thickness as the independent variable has been premeditated in Fig. 2 by taking the different values of the energy band parameters as given in [41] using (a) Eq. 5

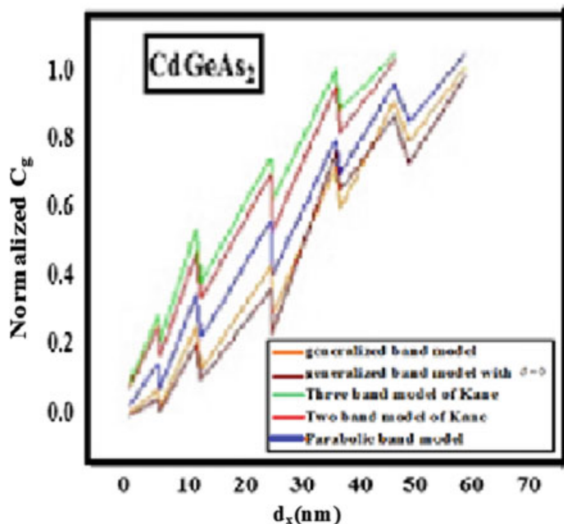

Fig. 1 The normalized C_g in QWFETs made of $CdGeAs_2$ with film thickness as the independent variable has been premeditated using (a) Eq. 3 (orange), (b) Eq. 3 with $\delta = 0$ (brown), (c) Eq. 5 (green), (d) Eq. 6b (red), and (e) Eq. 7b (blue)

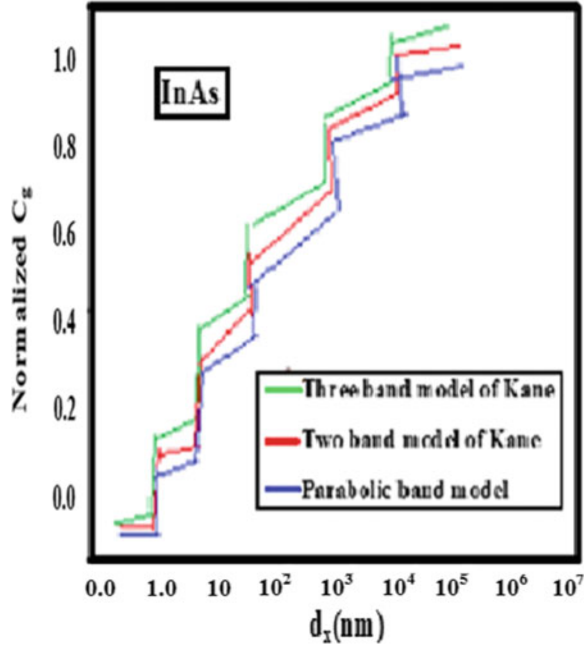

Fig. 2 The normalized C_g in QWFETs made of InAs with film thickness as the independent variable has been premeditated using (a) Eq. 5 (green) (d) Eq. 6b, (red) and (e) Eq. 7b (blue)

(green), (d) Eq. 6b (red), and (e) Eq. 7b (blue). From Fig. 2, it appears that the normalized C_g enhances in quantized distorted saw-tooth manner with increasing film thickness. The normalized C_g in QWFETs made of InSb with film thickness as the independent variable has been premeditated in Fig. 3 by taking the different values of the energy band parameters as given in [41] using (a) Eq. 5 (green), (d) Eq. 6b (red), and (e) Eq. 7b (blue). From Fig. 3, it appears that the normalized C_g in this

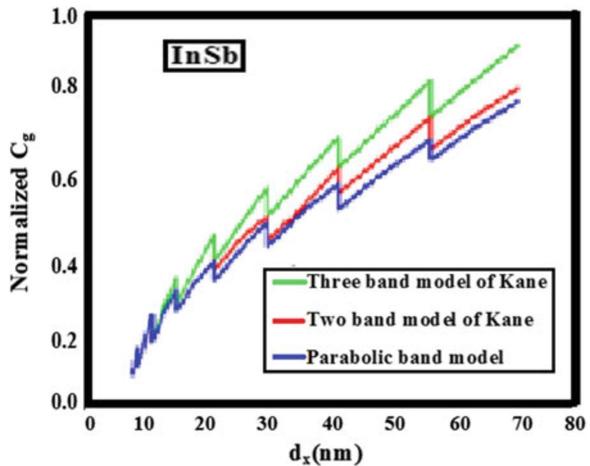

Fig. 3 The normalized C_g in QWFETs made of InSb with film thickness as the independent variable has been premeditated using (a) Eq. 5 (green), (d) Eq. 6b (red), and (e) Eq. 7b (blue)

case enhances in quantized saw-tooth manner with increasing film thickness. The normalized C_g in QWFETs made of $Hg_{1-x}Cd_xTe$ with film thickness as the independent variable has been premeditated in Fig. 4 by taking the different values of the energy band parameters as given in [41] using (a) Eq. 5 (green), (d) Eq. 6b (red), and (e) Eq. 7b (blue). From Fig. 4, it appears that the normalized C_g in this case enhances in quantized saw-tooth manner with increasing film thickness. The normalized C_g in QWFETs made of $Ga_{1-x}Al_xAs$ with film thickness as the independent variable has been premeditated in Fig. 5 by taking the different values of the energy band parameters as given in [41] using (a) Eq. 5 (green), (d) Eq. 6b (red), and (e) Eq. 7b (blue). From Fig. 5, it appears that the normalized C_g in this case enhances in quantized saw-tooth manner with increasing film thickness.

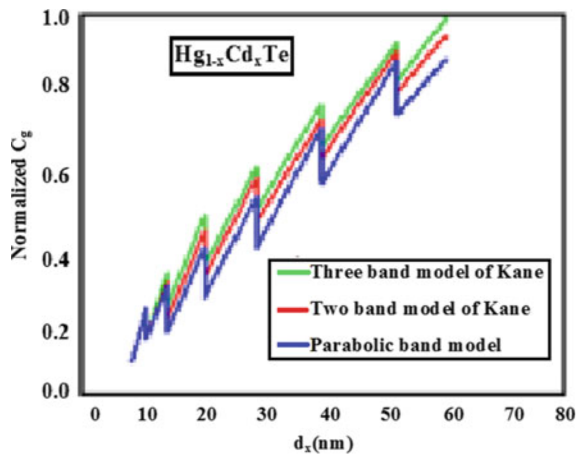

Fig. 4 The normalized C_g in QWFETs made of $Hg_{1-x}Cd_xTe$ with film thickness as the independent variable has been premeditated using (a) Eq. 5 (green), (d) Eq. 6b (red), and (e) Eq. 7b (blue)

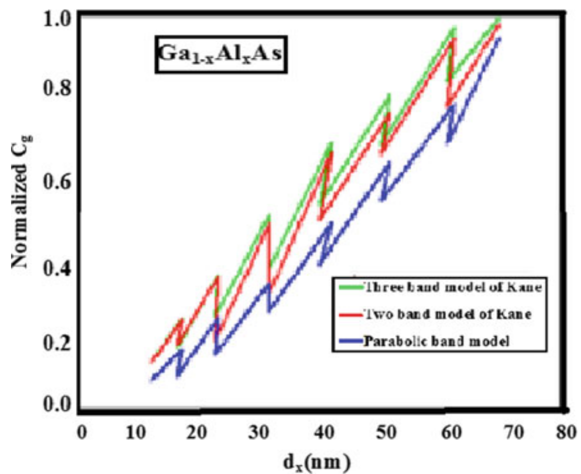

Fig. 5 The normalized C_g in QWFETs made of $Ga_{1-x}Al_xAs$ with film thickness as the independent variable has been premeditated using (a) Eq. 5 (green), (d) Eq. 6b (red), and (e) Eq. 7b (blue)

The normalized C_g in QWFETs made of $In_{1-x}Ga_xAs_yP_{1-y}$ with film thickness as the independent variable has been premeditated in Fig. 6 by taking the different values of the energy band parameters as given in [41] using (a) Eq. 5 (green), (d) Eq. 6b (red), and (e) Eq. 7b (blue). From Fig. 6, it appears that the normalized C_g enhances in quantized saw-tooth manner with increasing film thickness. The normalized C_g in QWFETs made of Cd_3As_2 with 1D electron statistics as the independent variable has been premeditated in Fig. 7 by taking the different values of the energy band

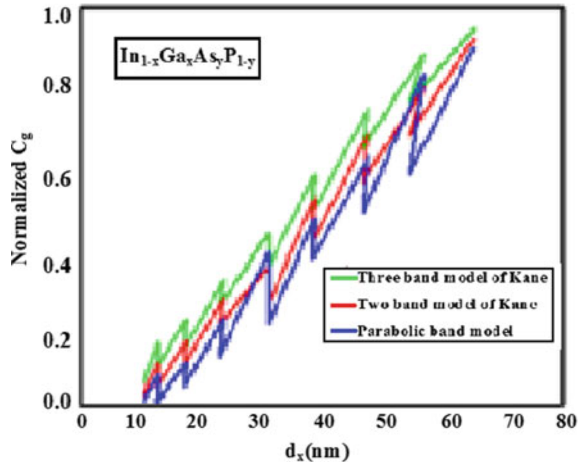

Fig. 6 The normalized C_g in QWFETs made of $In_{1-x}Ga_xAs_yP_{1-y}$ with film thickness as the independent variable has been premeditated using (a) Eq. 5 (green), (d) Eq. 6b (red), and (e) Eq. 7b (blue)

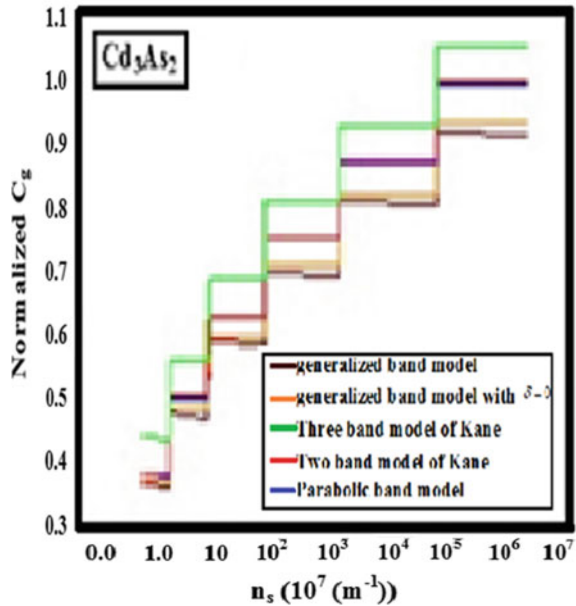

Fig. 7 The normalized C_g in QWFETs made of Cd_3As_2 with 1D electron statistics as the independent variable has been premeditated using (a) Eq. 3 (brown) (b) Eq. 3 with $\delta = 0$ (orange), (c) Eq. 5 (red), (d) Eq. 6b (green), and (e) Eq. 7b (blue)

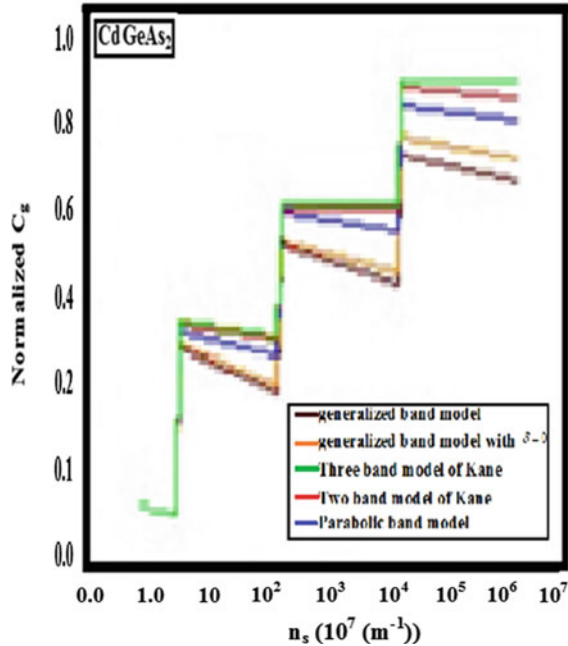

Fig. 8 The normalized C_g in QWFETs made of $CdGeAs_2$ with 1D electron statistics as the independent variable has been premeditated using (a) Eq. 3 (brown), (b) Eq. 3 with $\delta = 0$ (orange), (c) Eq. 5 (green), (d) Eq. 6b (red), and (e) Eq. 7b (blue)

parameters as given in [41] using (a) Eq. 3 (brown), (b) Eq. 3 with $\delta = 0$ (orange), (c) Eq. 5 (red), (d) Eq. 6b (green), and (e) Eq. 7b (blue). From Fig. 7, it appears that the normalized C_g enhances in quantized step-like manner with increasing 1D electron statistics. The normalized C_g in QWFETs made of $CdGeAs_2$ with 1D electron statistics as the independent variable has been premeditated in Fig. 8 by taking the different values of the energy band parameters as given in [41] using (a) Eq. 3 (brown), (b) Eq. 3 with $\delta = 0$ (orange), (c) Eq. 5 (green), (d) Eq. 6b (red), and (e) Eq. 7b (blue). From Fig. 8, it appears that the normalized C_g in this case enhances in quantized step-like manner with increasing 1D electron statistics. The normalized C_g in QWFETs made of InAs with 1D electron statistics as the independent variable has been premeditated in Fig. 9 by taking the different values of the energy band parameters as given in [41] using (a) Eq. 5 (green), (d) Eq. 6b (red), and (e) Eq. 7b (blue). From Fig. 9, it appears that the normalized C_g enhances in quantized step-like manner with increasing 1D electron statistics. The normalized C_g in QWFETs made of InSb with 1D electron statistics as the independent variable has been premeditated in Fig. 10 by taking the different values of the energy band parameters as given in [41] using (a) Eq. 5 (green) (d) Eq. 6b (red), and (e) Eq. 7b (blue). From Fig. 10, it appears that the normalized C_g enhances in quantized step-like manner with increasing 1D electron statistics.

The normalized C_g in QWFETs made of $Hg_{1-x}Cd_xTe$ with 1D electron statistics as the independent variable has been premeditated in Fig. 11 by taking the different values of the energy band parameters as given in [41] using (a) Eq. 5 (green), (d)

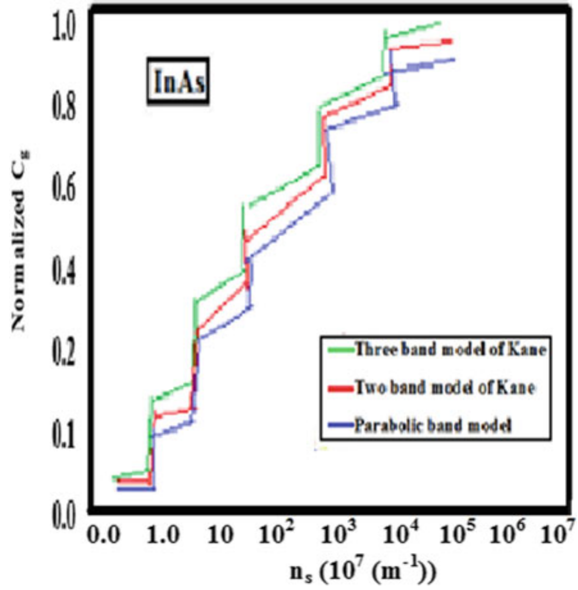

Fig. 9 The normalized C_g in QWFETs made of InAs with 1D electron statistics as the independent variable has been premeditated using (a) Eq. 5 (green), (d) Eq. 6b (red), and (e) Eq. 7b (blue)

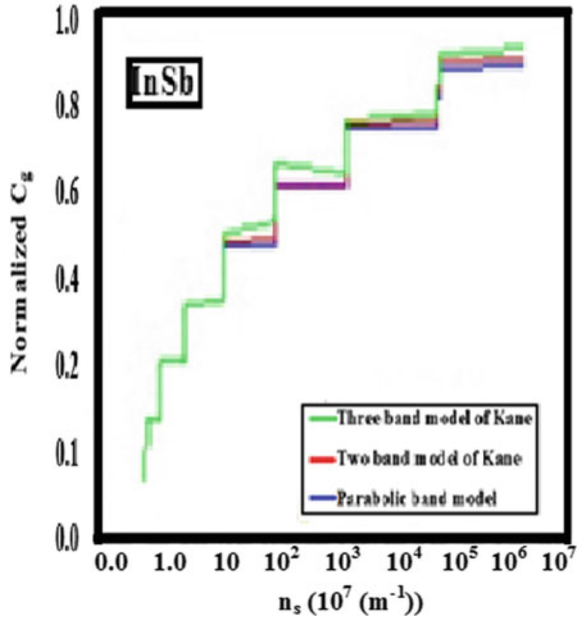

Fig. 10 The normalized C_g in QWFETs made of InSb with 1D electron statistics as the independent variable has been premeditated using (a) Eq. 5 (green), (d) Eq. 6b (red), and (e) Eq. 7b (blue)

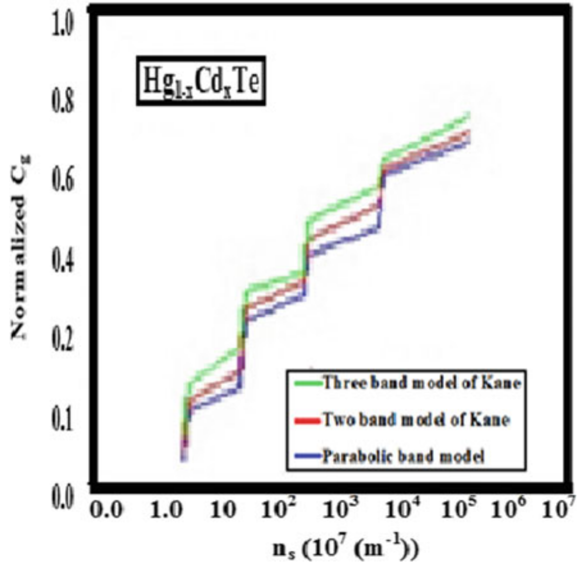

Fig. 11 The normalized C_g in QWFETs made of $Hg_{1-x}Cd_xTe$ with 1D electron statistics as the independent variable has been premeditated using (a) Eq. 5 (green), (d) Eq. 6b (red), and (e) Eq. 7b (blue)

Eq. 6b (red), and (e) Eq. 7b (blue). From Fig. 11, it appears that the normalized C_g enhances in quantized step-like manner with increasing 1D electron statistics. The normalized C_g in QWFETs made of $Ga_{1-x}Al_xAs$ with 1D electron statistics as the independent variable has been premeditated in Fig. 12 by taking the different

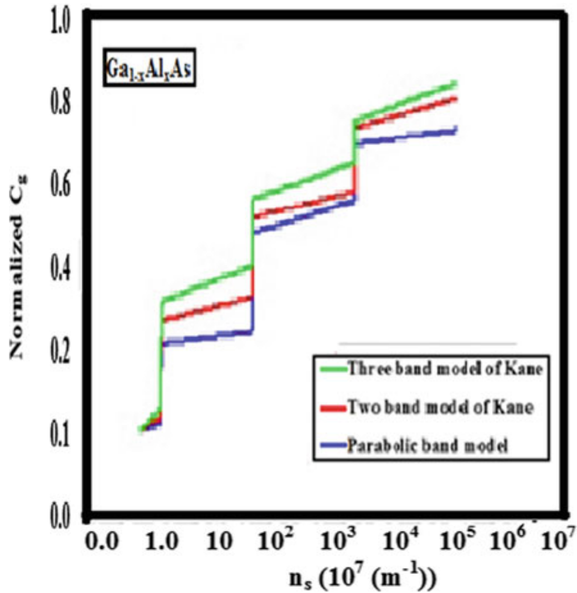

Fig. 12 The normalized C_g in QWFETs made of $Ga_{1-x}Al_xAs$ with 1D electron statistics as the independent variable has been premeditated using (a) Eq. 5 (green), (d) Eq. 6b (red), and (e) Eq. 7b (blue)

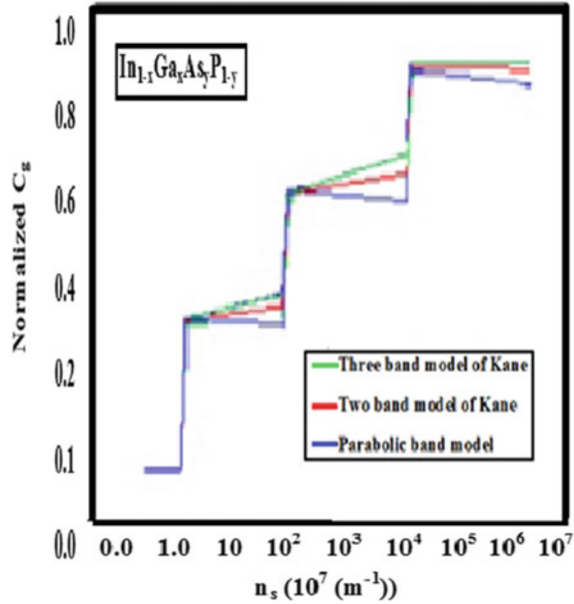

Fig. 13 The normalized C_g in QWFETs made of $In_{1-x}Ga_xAs_yp_{1-y}$in with 1D electron statistics as the independent variable has been premeditated using (a) Eq. 5 (green), (d) Eq. 6b (red), and (e) Eq. 7b (blue)

values of the energy band parameters as given in [41] using (a) Eq. 5 (green), (d) Eq. 6b (red), and (e) Eq. 7b (blue). From Fig. 12, it appears that the normalized C_g enhances in quantized step-like manner with increasing 1D electron statistics. The normalized C_g in QWFETs made of $In_{1-x}Ga_xAs_yp_{1-y}$in with 1D electron statistics as the independent variable has been premeditated in Fig. 13 by taking the different values of the energy band parameters as given in [41] using (a) Eq. 5 (green), (d) Eq. 6b (red), and (e) Eq. 7b (blue). From Fig. 13, it appears that the normalized C_g enhances in quantized step-like manner with increasing 1D electron statistics. The normalized C_g in QWFETs made of Cd_3As_2 with V_g as the independent variable has been premeditated in Fig. 14 by taking the different values of the energy band parameters as given in [41] using (a) Eq. 3 (Violet), (b) Eq. 3 with $\delta = 0$ (orange), (c) Eq. 5 (green), (d) Eq. 6b (red), and (e) Eq. 7b (blue). From Fig. 14, it appears that the normalized C_g decreases with increasing gate voltage in quantized oscillatory fashion for all cases as consider in this case. The rate of oscillatory decrease changes from one type of band model to another type.

The normalized C_g in QWFETs made of $CdGeAs_2$ with V_g as the independent variable has been premeditated in Fig. 15 by taking the different values of the energy band parameters as given in [41] using (a) Eq. 3 (brown), (b) Eq. 3 with $\delta = 0$ (orange), (c) Eq. 5 (green), (d) Eq. 6b (red), and (e) Eq. 7b (blue). From Fig. 15, it appears that the normalized C_g decreases with increasing gate voltage in quantized oscillatory fashion for all cases as consider in this case. The rate of oscillatory decrease changes from one type of band model to another type. The normalized C_g in QWFETs made of InAs with V_g as the independent variable has been premeditated in Fig. 16 by taking the different values of the energy band parameters as given in [41]

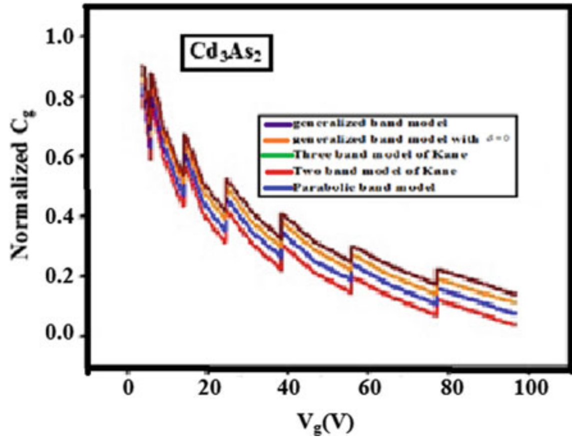

Fig. 14 The normalized C_g in QWFETs made of Cd_3As_2 with V_g as the independent variable has been premeditated using (a) Eq. 3 (violet), (b) Eq. 3 with $\delta = 0$ (orange), (c) Eq. 5 (green), (d) Eq. 6b (red), and (e) Eq. 7b (blue)

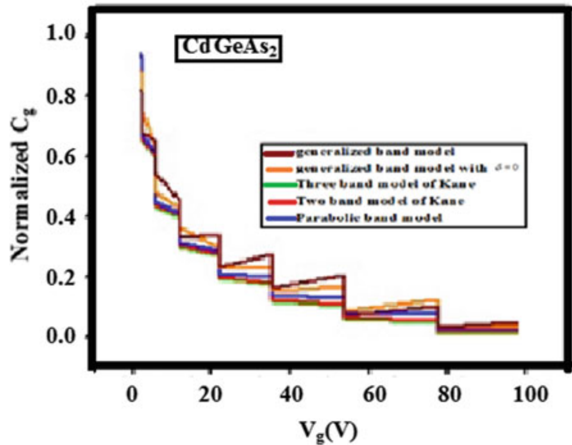

Fig. 15 The normalized C_g in QWFETs made of $CdGeAs_2$ with V_g as the independent variable has been premeditated using (a) Eq. 3 (brown), (b) Eq. 3 with $\delta = 0$ (orange), (c) Eq. 5 (green), (d) Eq. 6b (red), and (e) Eq. 7b (blue)

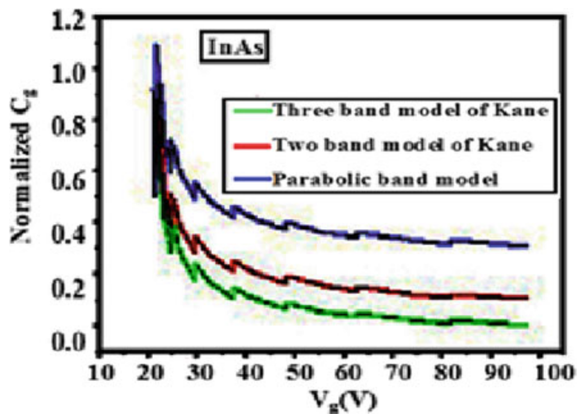

Fig. 16 The normalized C_g in QWFETs made of InAs with V_g as the independent variable has been premeditated using (a) Eq. 5 (green), (d) Eq. 6b (red), and (e) Eq. 7b (blue)

using (a) Eq. 5 (green), (d) Eq. 6b (red), and (e) Eq. 7b (blue). From Fig. 16, it appears that the normalized C_g decreases with increasing gate voltage in quantized oscillatory fashion for all cases as consider in this case. The rate of oscillatory decrease changes from one type of band model to another type. The normalized C_g in QWFETs made of InSb with V_g as the independent variable has been premeditated in Fig. 17 by taking the different values of the energy band parameters as given in [41] using (a) Eq. 5 (green), (d) Eq. 6b (red), and (e) Eq. 7b (blue).

From Fig. 17, it appears that the normalized C_g decreases with increasing gate voltage in quantized oscillatory fashion for all cases as consider in this case. The rate of oscillatory decrease changes from one type of band model to another type. The normalized C_g in QWFETs made of $Hg_{1-x}Cd_xTe$ with V_g as the independent variable has been premeditated in Fig. 18 by taking the different values of the energy band

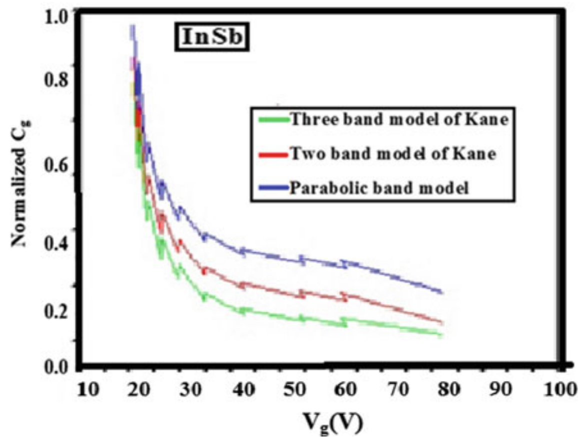

Fig. 17 The normalized C_g in QWFETs made of InSb with V_g as the independent variable has been premeditated using (a) Eq. 5 (green), (d) Eq. 6b (red), and (e) Eq. 7b (blue)

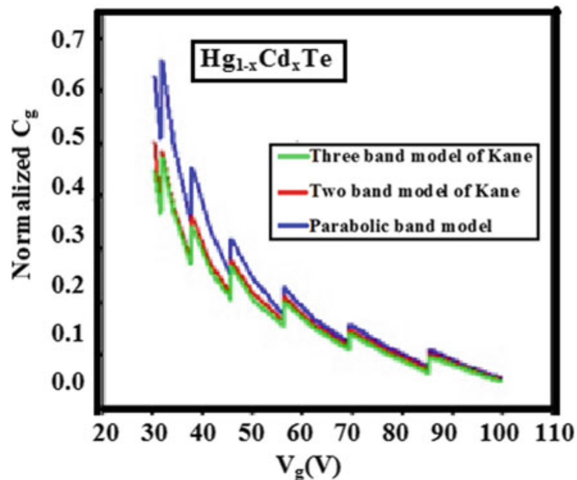

Fig. 18 The normalized C_g in QWFETs made of $Hg_{1-x}Cd_xTe$ with V_g as the independent variable has been premeditated using (a) Eq. 5 (green), (d) Eq. 6b (red), and (e) Eq. 7b (blue)

parameters as given in [41] using (a) Eq. 5 (green), (d) Eq. 6b (red), and (e) Eq. 7b (blue). From Fig. 18, it appears that the normalized C_g decreases with increasing gate voltage in quantized oscillatory fashion for all cases as consider in this case. The rate of oscillatory decrease changes from one type of band model to another type. The normalized C_g in QWFETs made of $Ga_{1-x}Al_xAs$ with V_g as the independent variable has been premeditated in Fig. 19 by taking the different values of the energy band parameters as given in [41] using (a) Eq. 5 (green), (d) Eq. 6b (red), and (e) Eq. 7b (blue).

From Fig. 19, it appears that the normalized C_g decreases with increasing gate voltage in quantized oscillatory fashion for all cases as consider in this case. The rate of oscillatory decrease changes from one type of band model to another type. The normalized C_g in QWFETs made of $In_{1-x}Ga_xAs_yP_{1-y}$ with V_g as the independent variable has been premeditated in Fig. 20 by taking the different values of the energy band parameters as given in [41] using (a) Eq. 5 (green), (d) Eq. 6b (red), and

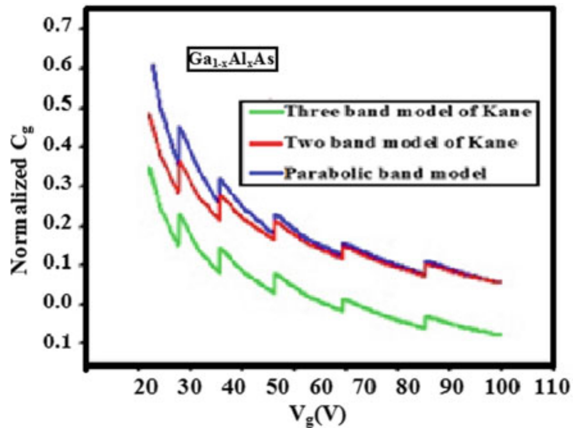

Fig. 19 The normalized C_g in QWFETs made of $Ga_{1-x}Al_xAs$ with V_g as the independent variable has been premeditated using (a) Eq. 5 (green), (d) Eq. 6b (red), and (e) Eq. 7b (blue)

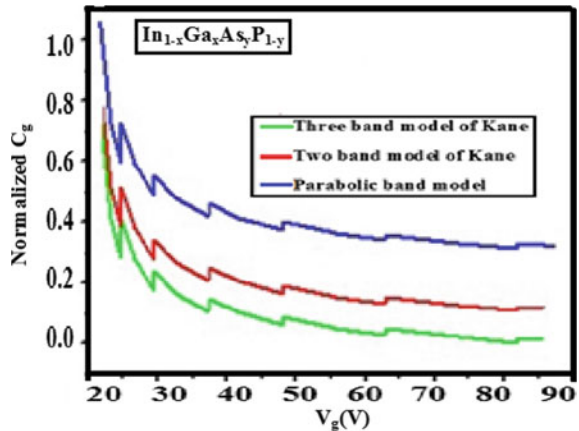

Fig. 20 The normalized C_g in QWFETs made of $In_{1-x}Ga_xAs_yP_{1-y}$ with V_g as the independent variable has been premeditated using (a) Eq. 5 (green), (d) Eq. 6b (red), and (e) Eq. 7b (blue)

(e) Eq. 7b (blue). From Fig. 20, it appears that the normalized C_g decreases with increasing gate voltage in quantized oscillatory fashion for all cases as consider in this case. The rate of oscillatory decrease changes from one type of band model to another type.

We conclude that the impact of investigation in this context is rather large, since the C_g in QWFET is a very important quantity for the purpose of technical application and experimental studies of physical properties of quantum-confined QWFET. It should be noted that for rigorous treatment the multicarrier effects and therefore the contribution of the non-idealities should be considered; our simplified approach shows the fundamental qualitative behavior of the C_g in QWFETs of small energy gap materials, since these compounds obey the model of Kane, wherever as our study is predicted by extending $\vec{k}.\vec{p}$ theory.

References

1. K.P. Ghatak, M. Mondal, J. Appl. Phys. **70**, 299 (1991)
2. K.P. Ghatak, S.N. Biswas, J. Vac. Sci. Technol. **7B**, 104 (1989)
3. B. Mitra, K.P. Ghatak, J. Solid-State Electron. **32**, 177 (1989)
4. K.P. Ghatak, M. Mondal, J. Appl. Phys. **62**, 922 (1987)
5. M. Mondal, K.P. Ghatak, J. Magn. Magn. Mater. **62**, 115 (1986)
6. M. Mondal, K.P. Ghatak, J. Phys. Scr. **31**, 613 (1985)
7. K.P. Ghatak, M. Mondal, J. Zeitschrift für Physik B Condens Matter. **64**, 223 (1986)
8. K.P. Ghatak, S.N. Biswas, J. Solid-State Electron. **37**, 1437 (1994)
9. K.P. Ghatak, N. Chattopadhyay, M. Mondal, J. Appl. Phys. A **48**, 365 (1989)
10. K.P. Ghatak, M. Mondal, Z. fur Physik B **64**, 223 (1986)
11. K.P. Ghatak, S.N. Biswas, Sol. State Electron. **37**, 1437 (1994)
12. D.R. Choudhury, A.K. Chowdhury, K.P. Ghatak, A.N. Chakravarti, Phys. Stat. Sol. (b) **98**, K141 (1980)
13. A.N. Chakravarti, A.K. Chowdhury, K.P. Ghatak, Phys. Stat. Sol. (a) **63**, K97 (1981)
14. M. Mondal, K.P. Ghatak, Acta Phys. Polon. A **67**, 983 (1985); M. Mondal, K.P. Ghatak, Phys. Stat. Sol. (b) **128**, K21 (1985)
15. M. Mondal, K.P. Ghatak, Phys. Stat. Sol. (a) **93**, 377 (1986)
16. K.P. Ghatak, M. Mondal, Phys. Stat. Sol. (b) **135**, 819 (1986)
17. M. Mondal, K.P. Ghatak, Phys. Stat. Sol. (b) **139**, 185 (1987)
18. K.P. Ghatak, N. Chattopadhyay, S.N. Biswas, OE/Fibers' **87**, 203 (1987)
19. K.P. Ghatak, N. Chatterjee, M. Mondal, Phys. Stat. Sol. (b) **139**, K25 (1987)
20. K.P. Ghatak, M. Mondal, Phys. Stat. Sol. (b) **148**, 645 (1988); K.P. Ghatak, A. Ghosal, Phys. Stat. Sol. (b) **151**, K135 (1989); K P. Ghatak, N. Chattopadhyay, M. Mondal, Phys. A **48**, 365 (1989)
21. P.K. Das, K.P. Ghatak, J. Nanosci. Nanotechnol. **19**, 2909 (2019); K.P. Ghatak, S. Chakrabarti, B. Chatterjee, Mater. Focus **7**, 361 (2018); K.P. Ghatak, S. Chakrabarti, B. Chatterjee, P.K. Das, P. Dutta, A. Halder, Mater. Focus **7**, 390 (2018); B. Chatterjee, N. Debbarma, M. Mitra, T. Datta, K.P. Ghatak, J. Nanosci. Nanotechnol. **17**, 3352 (2017)
22. K.P. Ghatak, D. De, Mater. Focus **6**, 114 (2017); P.K. Das, P. Dutta, A. Halder, J. Pal, N. Debbarma, S. Debbarma, K.P. Ghatak, Mater. Focus **6**, 167 (2017); P.K. Das, P. Dutta, A. Halder, R. Bhattacharjee, K.P. Ghatak, Mater. Focus **6**, 133 (2017); R. Bhattacharjee, K.P. Ghatak, J. Nanosci. Nanotechnol. **17,** 640 (2017)

23. M. Mitra, T.N. Sen, T. Datta, R. Bhattacharjee, L.S. Singh, K.P. Ghatak, J. Nanosci. Nanotechnol. **17**, 256 (2017); T.N. Sen, K.P. Ghatak, Quantum Matter **5,** 732 (2016); T.N. Sen, K.P. Ghatak, Quantum Matter **5**, 721 (2016); K.P. Ghatak, K. Sarkar, S. Chakrabarti, M. Kumar, M. Debbarma, T.N. Sen, M. Chakraborty, Rev. Theor. Sci. **4,** 199 (2016)
24. R. Bhattacharya, K. Sarkar, M. Kumar, B. Chatterjee, K.P. Ghatak, Quantum Matter **5**, 557 (2016); K.P. Ghatak, K. Sarkar, N. Debbarma, L. Suraj Singh, Quantum Matter **5**, 427 (2016); K.P. Ghatak, D. De, J. Nanoeng. Nanomanuf. **6**, 1 (2016); S.K. Biswas, M. Mitra, K.P. Ghatak, J. Nanoeng. Nanomanuf. **6**, 63 (2016)
25. N. Paitya, K.P. Ghatak, Quantum Matter **5**, 191 (2016); B. Chatterjee, S. Chakrabarti, S.K. Sen, M. Mitra, K.P. Ghatak, Quantum Matter **5**, 85 (2016); K.P. Ghatak, in *Magneto Thermoelectric Power in Heavily Doped Quantized Structures* (Series on the Foundations of Natural Science and Technology, World Scientific Publishing Company, 2016), vol. 7, pp. 758; K.P. Ghatak, in *Dispersion Relations in Heavily-Doped Nanostructures* (Springer International Publishing, 2016), p. 615
26. B. Chatterjee, K. Sarkar, K.P. Ghatak, in *Advances in Optical Science and Engineering* (Springer India, 2015), p. 621; K.P. Ghatak, in *Einstein's Photoemission* (Springer International Publishing, 2015), p. 295
27. S.M. Adhikari, K.P. Ghatak, J. Adv. Phys. **2**, 130 (2013); S. Bhattacharya, D. De, S. Ghosh, K.P. Ghatak, J. Comput. Theor. Nanosci. **10**, 664 (2013); N. Paitya, S. Bhattacharya, D. De, S. Ghosh, K.P. Ghatak, J. Nanoeng. Nanomanuf. **2**, 211 (2012)
28. S. Pahari, S. Bhattacharya, K.P. Ghatak, J. Comput. Theor. Nanosci. **6**, 2088 (2009); L.J. Singh, S. Choudhury, S. Singha Roy, K.P. Ghatak, Electr. Eng. **87**, 19 (2005); P.K. Chakraborty, G.C. Datta, K.P. Ghatak, Phys. Scr. **68**, 368 (2003)
29. K.P. Ghatak, J. Mukhopadhyay, J.P. Banerjee, SPIE Proc. Ser. **4746**, 1292 (2002); K.P. Ghatak, J. Mukhopadhyay, J.P. Banerjee, SPIE Proc. Ser. **4746**, 1296 (2002); K.P. Ghatak, J. Mukhopadhyay, J.P. Banerjee, Proceedings-SPIE Int. Soc. Opt. Eng. **2**, 1296 (2002); K.P. Ghatak, J. Mukhopadhyay, J.P. Banerjee, SPIE Proc. Ser. **4746**, 347 (2002)
30. K.P. Ghatak, P.K. Bose, J.P. Banerjee, SPIE Proc. Ser. **4746**, 351 (2002); K.P. Ghatak, SPIE Proc. Ser. **4746**, 292 (2002); K.P. Ghatak, J. Wave Mater. Interact. **14**, 157 (1999); K.P. Ghatak, P.K. Bose, J. Wave Mater. Interact. **12**, 53 (1997); K.P. Ghatak, B. Nag, J. Wave Mater. Interact. **12**, 85 (1997); B. Mitra, D.K. Basu, B. Nag, K.P. Ghatak, Nonlinear Optics-Read. **17**, 171 (1997); K.P. Ghatak, P.K. Bose, J. Wave Mater. Interact. **12**, 60 (1997); P.K. Bose, KP Ghatak, J. Wave Mater. Interact. **12**, 67 (1997)
31. K.P. Ghatak, P.K. Bose, G. Majumder, MRS Proc. **494**, 157 (1997); K.P. Ghatak, D.K. Basu, D. Basu, B. Nag, Il Nuovo Cimento D **18**, 947 (1996); K.P. Ghatak, S. Dutta, A. Ali, S. Banerjee, B. Nag, J. Wave Mater. Interact. **11**, 127 (1996); P.K. Chakrabarty, B. Nag, S. Dutta, K.P. Ghatak, J. Wave Mater. Interact. **11**, 55 (1996)
32. B. Nag, P.K. Chakrabarty, K.P. Ghatak, J. Wave Mater. Interact. **11**, 211 (1996); K.P. Ghatak, P.K. Chakrabarty, B. Nag, J. Wave Mater. Interact. **11**, 159 (1996); K.P. Ghatak, S.N. Banik, FIZIKA A-ZAGREB **5**, 31 (1996)
33. K.P. Ghatak, J.P. Banerjee, P.K. Chakrabarty, B. Nag, J. Wave Mater. Interact. **11**, 166 (1996); P.K. Chakraborty, B. Nag, S. Dutta, K.P. Ghatak, J. Wave Mater. Interact. **11**, 111 (1996)
34. K.P Ghatak, S. Bera, A. Ali, B. Nag, FIZIKA A-ZAGREB **5**, 111 (1996); K.P. Ghatak, J.P. Banerjee, B. Goswami, B. Nag, Nonlinear Optics-Read. **16**, 241 (1996); K.P. Ghatak, M. Mitra, B. Goswami, B. Nag, Nonlinear Optics-Read. **16**, 167 (1996); K.P. Ghatak, D. Bhattacharya, D. Basu, B. Nag, Phys. Status Sol. (b) **191**, 141 (1995)
35. K.P. Ghatak, B. Nag, M. Mitra, J.P. Bannerjee, J. Wave Mater. Interact. **10**, 11 (1995); K.P. Ghatak, D.K. Basu, B. Nag, J. Wave Mater. Interact. **10**, 29 (1995); K.P. Ghatak, S. Dutta, D. Basu, B. Nag, J. Wave Mater. Interact. **10**, 1 (1995)
36. K.P Ghatak, B. Nag, G. Mazumder, MRS Proc. **379**, 85 (1995); K.P. Ghatak, B. Nag, G. Mazumder, MRS Proc. **379**, 109 (1995); K.P. Ghatak, S. N Banik, FIZIKA A **3**, 155 (1994); S.N. Banik, K.P. Ghatak, S.N. Biswas, FIZIKA A **3**, 77 (1994); K.P. Ghatak, Fizika A **2**, 133 (1993); K.P. Ghatak, S.N. Biswas, MRS Proc. **313**, 375 (1993); K.P. Ghatak, S.N. Biswas, MRS Proc. **308**, 445 (1993)

37. K.P. Ghatak, D. Bhattacharyya, J. Wave Mater. Interact. **8**, 233 (1993); K.P. Ghatak, S.N. Biswas, Acta Phys. Slovaca **43**, 425 (1993); K.P. Ghatak, S.N. Biswas, Nanostruct. Mater. **2**, 91 (1993)
38. K.P. Ghatak, M. Mondal, Fizika A **1**, 113 (1992); K.P. Ghatak, B. De, MRS Proc. **262**, 911 (1992); K.P. Ghatak, B. De, MRS Proc. **242**, 373 (1992); K.P. Ghatak, B. De, MRS Online Proc. Libr. Archive **228**, (1992); K.P. Ghatak, Fizika A **1**, 197 (2006)
39. K.P. Ghatak, S. Bhattacharyya, S.N. Biswas, Acta Phys. Hung. **70**, 83 (1991); K.P. Ghatak, Acta Phys. Hung. **69**, 121 (1991); K.P. Ghatak, B. De, MRS Proc. **234**, 59 (1991); K.P. Ghatak, B. De, MRS Proc. **234**, 55 (1991); K.P. Ghatak, Acta Phys. Hung. **68**, 253 (1990); K.P. Ghatak, Acta Phys. Hung. **67**, 407 (1990); K.P. Ghatak, MRS Proc. **216**, 469 (1990); K.P. Ghatak, MRS Proc. **216**, 465 (1990)
40. K.P. Ghatak, B. De, M. Mondal, S.N. Biswas, MRS Proc. **184**, 261 (1990); K.P. Ghatak, B. De, M. Mondal, S.N. Biswas, MRS Proc. **198**, 333 (1990); B. Mitra, K.P. Ghatak, Solid-State Electron. **32**, 810 (1989); K.P. Ghatak, M. Mondal, J. Appl. Phys. **62**, 922 (1987); S.N. Biswas, K.P. Ghatak, Megagauss Technol. Pulsed Power Appl. **8**, 219 (1987); M. Mondal, K.P. Ghatak, Czechoslovak J. Phys. **36**, 1396 (1986); A. Arti, K.P. Ghatak, K.K. Ghosh, S. Ghosh, A. Dhar, Physica Status Solidi B-Basic Res. **103**, K55(1981)
41. S. Bhattacharya, K.P. Ghatak, *Fowler-Nordheim Field Emission, Springer Series in Solid-State Sciences*, vol. 170 (Springer-Verlag, Germany, 2012), pp. 1–338

Heterostructure Devices for THz Signal Recognition

Amit Bhattacharyya, Manash Chanda and Debashis De

Abstract Terahertz region, practically related near the frequency range commencing 100 GHz–10 THz (30 μm toward 3 mm), has drawn great attention during preceding few decades owing to its hopeful relevance into biological, health and manufacturing fields, wideband and welfare memorandum, radio astronomy, space-borne radar technology, etc. Terahertz spacing suggests to a huge contest yet exists, proposed for Terahertz mechanisms as this is inside the borderline of electrons and light-based machinery. The negative differential resistance supported devices, for instance Gunn diode, impact avalanche transit time (IMPATT) diode, resonant tunneling diode and space-plasma wave based nanometer field effect transistors (FETs) are extensively explored for Terahertz frequency range. Commencing elevated region, devices supported by photon akin to quantum cascade laser (QCL) expand the emission spectra starting mid- and far-infrared to Terahertz spectral variety. Every attempt is to follow the effectual radiation and recognition of THz signals. Radiation power along with recognition sensitivity of Terahertz systems is enormously poor contrasted through the millimeter (MM) band and optoelectronic appliances. In modern days, 2D-plasmon in a GaN hetero-structure-based high electron mobility transistor has concerned a lot of interest owing to the characteristics of aiding emission/recognition of electromagnetic radiation within the Terahertz span. An assessment of the figure-of-merits (FoMs) among GaN and GaAs compounds illustrates that an advanced

A. Bhattacharyya
Department of Electronics and Communication Engineering, Haldia Institute of Technology, Haldia 721657, India
e-mail: amit_elec06@yahoo.com

M. Chanda (✉)
Department of Electronics and Communication Engineering, Meghnad Saha Institute of Technology, Kolkata 700150, India
e-mail: manash.bst@gmail.com

D. De
Department of Computer Science and Engineering, Maulana Abul Kalam Azad University of Technology, Kolkata 700064, India
e-mail: dr.debashis.de@gmail.com

© Springer Nature Singapore Pte Ltd. 2020

A. Biswas et al. (eds.), *Emerging Trends in Terahertz Solid-State Physics and Devices*,
https://doi.org/10.1007/978-981-15-3235-1_8

essential field can provide superior output power density; a superior electron saturation velocity may provide very high-speed conversion time; hence, advanced frequency with a high thermal conductivity may undergo since advanced functioning temperature used for GaN-supported devices.

Keywords Terahertz · Hetero-structure field-effect transistors · QCLs · HEMT · Gunn diodes · Tera field-effect transistor

1 Introduction

In the present proposal, design of GaN-supported HEMT structures which comprise electrons and light-based mechanisms is examined with highlighting over the hypothetical and experimental expansions of QCLs, plasma wave field-effect transistors and NDR-based devices. The outcomes exhibit that GaN is a hopeful compound for Terahertz semiconductor devices including a brilliant presentation in functioning temperature, frequency and achieved power. During the study of recent THz electronics, progress of compressed, controllable and coherent sources and detectors functioning at Terahertz frequency range is entirely newest concerns. Two-dimensional plasmon in semiconductor structures similar to HEMT with III–V compound semiconductor hetero-structures has drawn a lot of awareness owing to the character of endorsing discharge/recognition of EM-radiation during Terahertz variety [1–6]. Plasma oscillation belongs to a quantum of spatio-sequential combined fluctuation of electron or hole densities whose typical frequency bands are quantized. The prospect of the Terahertz recognition is because of nonlinear characteristics of the 2-D plasmon that directs to the renovation of AC current persuaded with the arriving Terahertz radiation. Accordingly, a photoresponse emerges during the appearance of a DC potential among source and drain which is comparative near the radiation intensity (photo-voltaic consequence). Conversely, carbon configurations supported on monolayer of carbon atoms structuring intense honeycomb 2-D crystals specifically separate graphene layers (GLs) [7] arrange capable for various nano-electronic and optoelectronic appliances. Plasma waves in 2D electron or hole arrangement in graphene layers organized through an extremely conducted gate are considered hypothetically [8, 9]. This is disclosed to the gated graphene hetero-structures which may spectacularly develop the presentation of potential controllable THz detection systems.

2 Imaging with Sensing Technique of Terahertz Utilizing III–V HEMTs

2.1 Device Manufacturing

HEMT manufactured with gallium arsenide-supported hetero-structure material is commonly used for recognition/discharge of THz radiation [3, 4]. In order to achieve an enhanced responsivity and recognition sensitivity to Terahertz radiation, most of the researchers initiate InAlAs/InGaAs HEMT on an InP substrate arrangement [10]. Here 80-nm length of gate region of a HEMT manufactured affords a unity-gain cutoff frequency (f_τ) of 298 GHz with a transconductance (g_m) of 700 mS/mm [11]. High electron mobility transistor is focused toward 0.3-THz, 2-mW radiation to distinguish the recognition belongings. Gold-made ribbon wires for pad-covering interconnect may perform like antenna.

2.2 Demonstrations for Imaging and Sensing of Terahertz

Primarily, the sensitivity due to recognition of high electron mobility transistor was estimated [10]. The computation framework is exposed in Fig. 1. Being HEMT susceptibility computation, either model is eliminated. Design of usual photoresponse to 292-GHz and 2-mW radiation is illustrated in Fig. 2. Intrinsic susceptibility devoid of every antenna has been approximated to be nearly 30 V/W. Here, photocurrent ΔI_d indicates the rectification element of the Terahertz radiation inside the drain current I_d. It has been noticed that ΔI_d enhances comparatively by the rise in drain

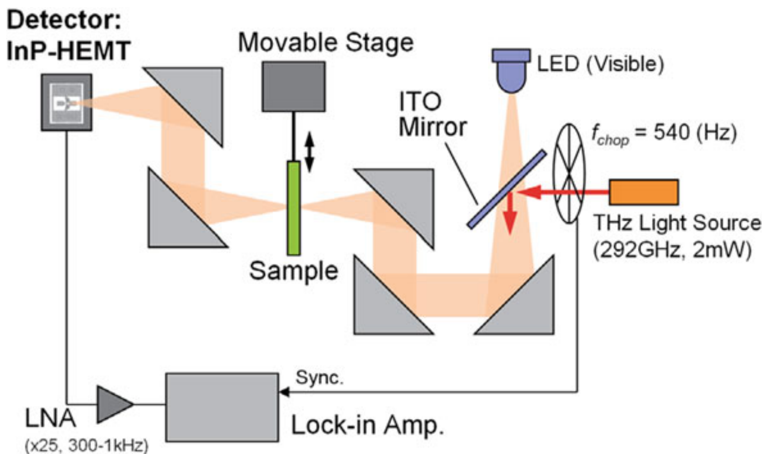

Fig. 1 THz imaging organization instrumentation [5]

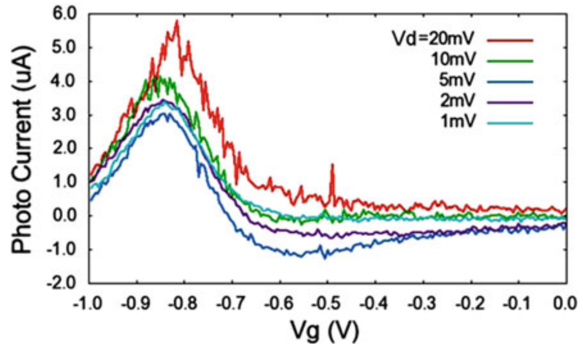

Fig. 2 Photoresponse for high electron mobility transistor toward the 0.3 THz, 2 mW radiation [5]

voltage V_d capable of -20 mV. Conversely, about higher than 20 mV powerful noise will be viewed. Hence, allowing for the better S/N state V_d is preferred to 2 mV used for imaging purpose. Hence, the gate potential V_g is set about -0.87 V, while ΔI_d happens to be highest.

3 Terahertz Appliances

Terahertz imaging of pharmaceutical (Fig. 3), genetic (Fig. 4), industrial and business-related entities stays most significant demands of Terahertz skill (Fig. 5).

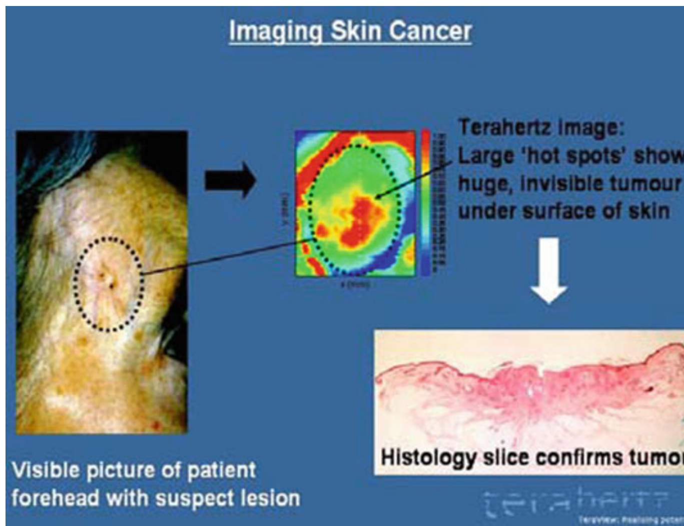

Fig. 3 Image of skin cancer [12]. Consideration in TeraView, Limited

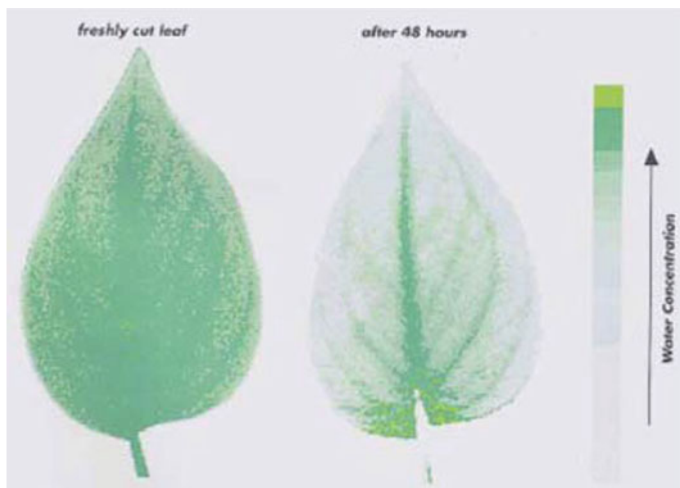

Fig. 4 Terahertz icons of a clean leaf along with the similar leaf subsequent to 48 h [12]. Consideration of TeraView, Limited

Fig. 5 Demonstration of sub-Terahertz skill for secret object recognition [12]

4 Production and Recognition of Terahertz Radiation

Sources of electronic Terahertz activate by the short margin of the Terahertz variety (commencing 300 GHz to ~1 THz). Around 300 GHz, GaAs and Si impact avalanche transit time (IMPATT) diodes convey powers beyond 1 W. The yield of Gunn diode may be employed to operate frequency multiplication unit for attaining sensible powers by Terahertz frequency range. Inside the research laboratory, a THz categorization arrangement utilizes 200 GHz along with 600 GHz radiation schemes supported by 100 GHz Gunn diode through frequency doubling unit (used for 200 GHz scheme) or doubling and tripling (for the 600 GHz scheme), see Fig. 6. An utmost productive power is regarding 3 mW for the 200 GHz scheme and 0.3 mW for the 600 GHz scheme, correspondingly. Besides, major frequency components (200 GHz as well as 600 GHz), the arrangement produces advanced harmonics by 800 GHz, 1 THz, and 1.2 THz as well. The comparative power of an advanced harmonics relies on Gunn diode along with on doubling and tripling modifications. This might accomplish a little percentage of the power discharged by central frequency components.

Virginia diode is contributing THz sources supported by Schottky diode frequency multipliers (Fig. 7). InGaAs/InP high electron mobility transistors and heterojunction bipolar transistor achieved unity-gain cutoff frequency with utmost frequency of process beyond 600 GHz [13–15]. Backward wave oscillator may envelop sub-THz along with a short hop of THz variety, observe, such as [16], while backward wave oscillator is employed toward production of nearly 45 mW of 120 GHz radiation.

Close to advanced frequency, sources of Terahertz photonic take leading performance. QCLs [17–23] expressed procedure by temperature above 164 K near 3 THz inside the pulse-shaped approach along with 117 K in the constant wave approach [19] with maximum powers resembling 50 mW [16]. Functional frequency below 1.9 THz has been detailed [21]. Next to a lot of smaller wavelengths (5–12 μm),

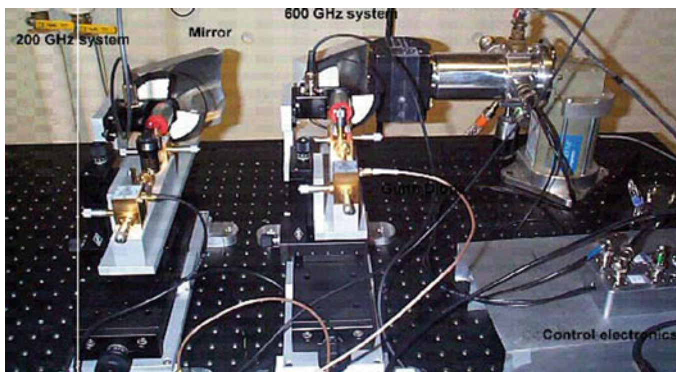

Fig. 6 THz generation system by means of a Gunn diode with frequency multiplier [10]

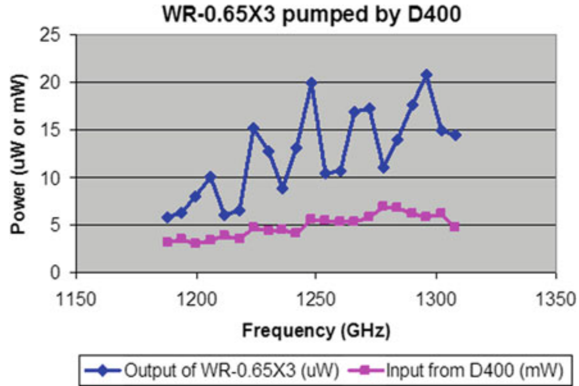

Fig. 7 Schottky diode multiplier unit. Consideration of Virginia diodes, Inc. Imitated with authorization [10]

quantum cascade lasers are currently accessible for business-related issue and utilize thermoelectric cooling [23].

5 GaN-Supported QCL

In case of traditional semiconductor lasers, a photon has been discharged because of the consequence of re-organization of a CB electron along with a VB hole. The energy gap among the CB and the VB, i.e., $E_{g,}$ divisioned with Planck constant; h actually provides the frequency of discharged photon. The photonic energy within the Terahertz variety is fewer over E_g of the substrate materials, and hence, for emitting Terahertz photons, E_g by means of lesser amount of energy is required. Inter-subbands are initiated via appreciating quantum wells. During nurturing numerous replicated stages of quantum wells, generally by molecular beam epitaxy, Terahertz quantum cascade laser has been executed. Never extensive following the primary execution in 1994 through a scientists group includes Alfred Y. Cho, recognized like the pioneer of molecular beam epitaxy, quantum cascade laser happened to utmost extensively employed proposals meant for production of Terahertz radiation [24]. The earliest Terahertz quantum cascade laser had accounted in 2002. This scheme was appreciated by GaAs/AlGaAs hetero-structures. This might discharge advanced produced powers above 2 mW by 4.4 THz. However, this might merely function on temperatures equal to 50 K in pulse-shaped approach [18]. This stated quantum cascade laser possibly will inactive in continuous wave approach. Nearly 2005, GaAs/AlGaAs supported quantum cascade laser has been advanced to drive by 164 and 117 K in pulse-shaped approach with continuous wave approach, correspondingly [19]. Yet, process of GaAs-supported quantum cascade lasers is restricted via longitudinal-optical phonon of 36 meV. Longitudinal-optical phonon used for GaN is placed by 92 meV [25]. In accordance with the examination via the Paiella and Moustakas's research group at University of Boston, exposed in Fig. 8, the inversion of population (PI) as well as the gain multiplier of GaN/AlGaN Quantum Wells belief

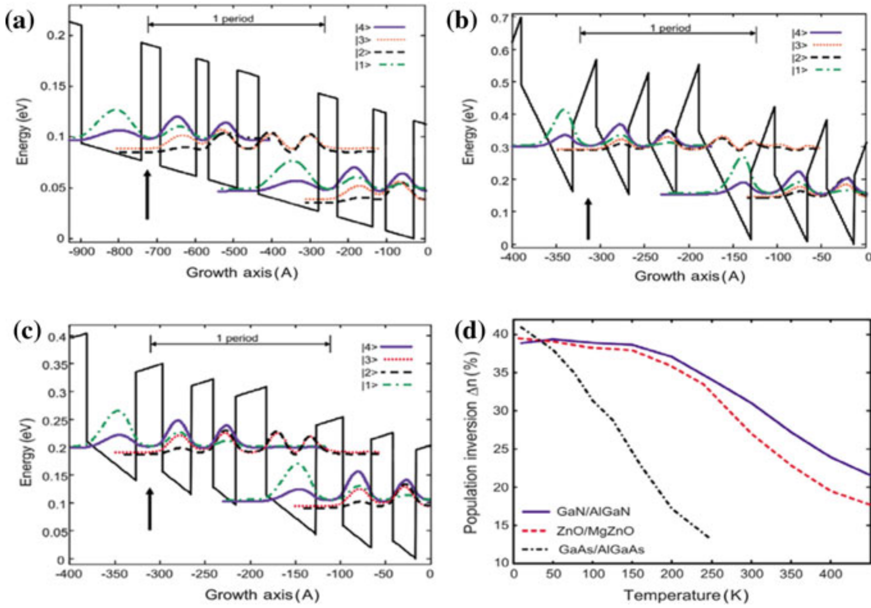

Fig. 8 CB outlines with square-shaped envelope functions of **a** the $GaAs/Al_{0.15}Ga_{0.85}As$, **b** the $GaN/Al_{0.15}Ga_{0.85}N$ and **c** the $ZnO/Mg_{0.15}Zn_{0.85}O$ quantum cascade gain medium regarded inside this context. **d** Computed partial PI of the Terahertz Quantum Cascade configurations of **a** (dash/dotted line), **b** (solid line) and **c** (dashed line), likely a temperature-based function. Reproduced as of [26], by authorization of the American Institute of Physics

on the temperature nearly three times less over that of GaAs/AlGaAs for Terahertz discharge. Hence, the gain constant for nitride device is sufficient for laser exploit [26–28].

Consequently, GaN-supported devices may activate into the higher Terahertz frequency range of 5–10 THz at $T = 300$ K which is unreachable with GaAs supported devices [29]. During 2003, introduce works detailed Terahertz discharge commencing InGaN/GaN various quantum wells [30, 31]. Within newest proposal during 2015, Terahertz-Quantum Cascade Lasers has been manufactured by RF-molcular beam epitaxy with a metal-organic chemical vapor deposition over MOCVD-developed AlGaN/AlN models cultivated over c-plane sapphire body. The quantity of dynamic sections with wave functions, donated to laser effect, had been restricted toward two quantum wells with three subband stages, correspondingly. Accordingly, laser effect by approximately 5.5 and 7.0 THz is appreciated; those were maximum informed secretions for Terahertz-Quantum Cascade Lasers advanced [29, 32, 33]. Within the latter research work, the discriminating insertion toward the higher lasing stage with a broad energetic variety of functioning current density is appreciated so as to realize a superior functioning temperature for Terahertz-Quantum Cascade Laser. Concerning this intend, indirect insertion method while exposed in Fig. 9a is regarded like active choice of functioning current density may not restricted via subband configuration of

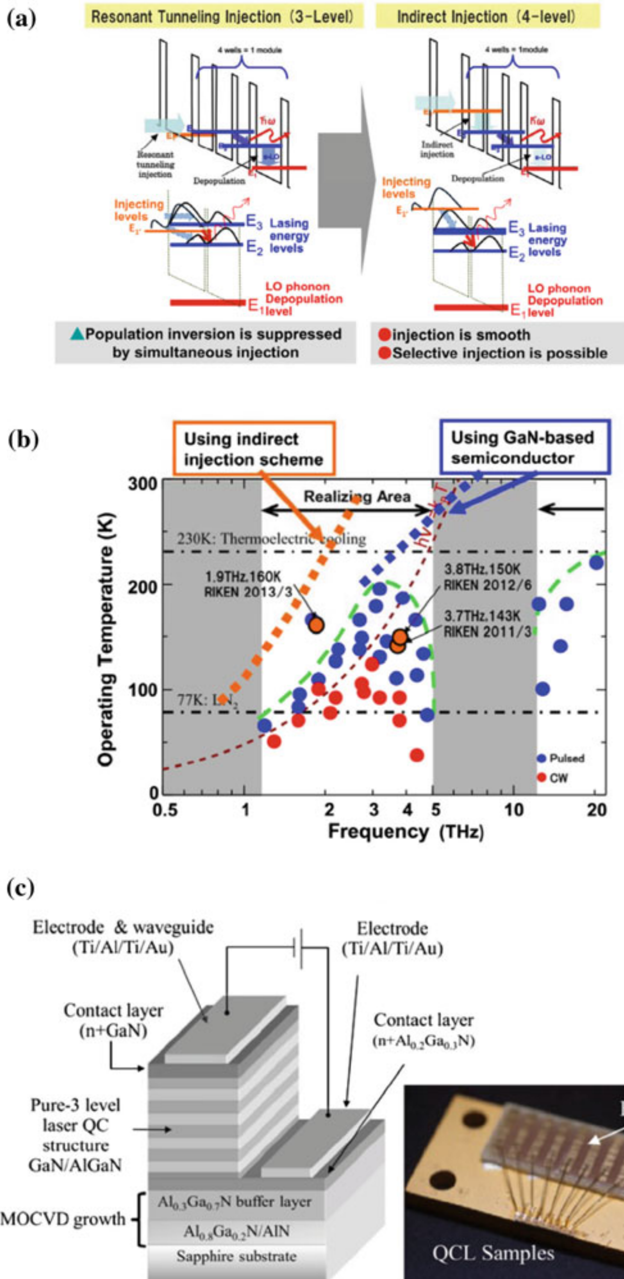

Fig. 9 **a** Outlook of quantum cascade arrangements meant for resonant tunneling insertion system (three stages) with indirect insertion system (four stages). **b** Advantage of GaN-supported quantum cascade lasers inside Terahertz range. **c** Outlook of the generally GaN-supported–Terahertz-quantum cascade laser model configuration with the model snap following has ascended to the heat sink. Reproduced from [29, 32], by authorization of International Society for Optics and Photonics

thin E_{32}. Since Fig. 9b illustrates, the mentioned uppermost functional temperature meant for GaAs/AlGaAs is 160 K meant for a 1.9-THz-Quantum Cascade Laser along with 150 K for a 3.8-THz-Quantum Cascade Laser, while GaN-supported Quantum Cascade Lasers may attempt at $T = 300$ K [34–36]. A diagrammatic for the generally GaN-supported Terahertz-Quantum Cascade Laser device is exposed in Fig. 9c. AlGaN/GaN quantum wells are moreover suggested meant for assimilation of Terahertz radiation [37]. Diminution in Al mole division affects the width of quantum well to rise, and hence, inter-subband conversions in these quantum wells are adaptable to be among 1.0–10 μm [38]. In favor of assimilation in the Terahertz frequency variety, plasma-assisted molecular beam Eepitaxy by adjustable assimilation commencing 53 toward 160 μm, regarding doping stage and mathematical deviations, has been described [39]. During 2016, a research group of Boston University highlighted peak value of photo-currents near 10 THz for Terahertz-inter-subband photodetectors that are expanded supported on GaN/AlGaN quantum wells developed over a freestanding semi-polar GaN body [40]. Spectrum of photocurrent with CB array of semi-polar GaN/AlGaN quantum well infrared photodetector extended via the group of researchers, as exposed in Fig. 10.

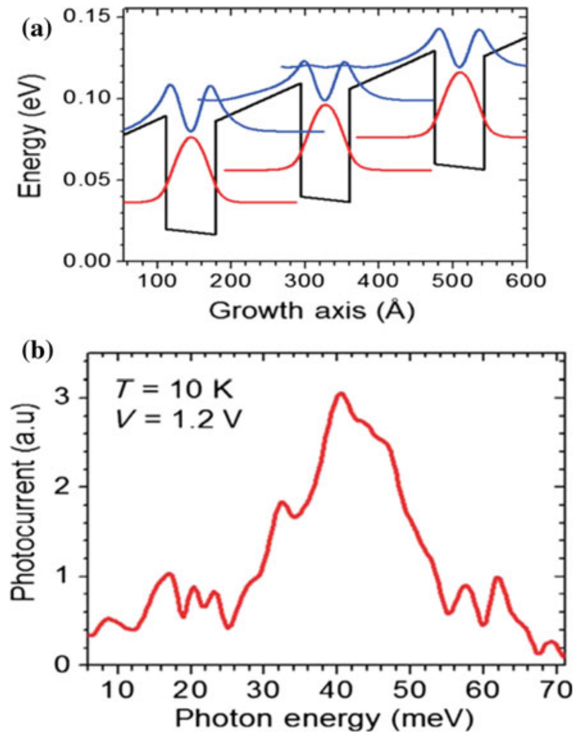

Fig. 10 **a** CB array of the semi-polar GaN/AlGaN quantum well infrared photodetector elaborated into this context, beneath an exterior functional potential of nearly 20 mV/period. The square-shaped envelope functions of the bound-state subbands of every well are moreover exposed, positioned to their individual energy stages. **b** Band of photocurrent computed at 10 K in a functional potential of 1.2 V. Reproduced from [40], by authorization of American Institute of Physics

6 GaN-Supported HEMTs Like THz Detection Systems Depend Over Self-mixing

Sun et al. [41] manufactured a GaN/AlGaN high electron mobility transistor utilizing optical lithography during 2011. These GaN/AlGaN HEMTs are able to perform at $T = 300$ K with identify Terahertz radiation by self-mixer unit having a responsivity of 3.6 kV/W. Through delightful concentrated Terahertz domains keen on description, they moreover enlarged a quasi-static self-mixer representation to illustrate the detecting features for instance amplitude and of photocurrent polarity [42]. During 2016, a research group from MIT with organization for science, technology and research in Singapore recommended an innovative representation for GaN-supported high electron mobility transistors. This representation may describe polarity as well as photocurrent amplitude. Moreover, this configuration assisted to propose GaN-supported high electron mobility transistors through asymmetric padding. With this representation, the recognition susceptibility is improved by a degree of amplitude [43]. The cross-sectional outlook of the suggested GaN-supported high electron mobility transistor detecting unit, antenna configurations with conventional symmetric gate, with the intended asymmetric gate are illustrated in Fig. 11.

7 Conclusion

In this chapter, the effect of the uses of GaN meant for fulfilling the engineering requirement meant for compressed, inexpensive, elevated resolution and elevated-power Terahertz image and spectroscopic arrangements has been deliberated. It has been assumed that GaN-supported appliances may be used like the structural units of an outlook Terahertz schemes that can offer Terahertz emission into the higher Terahertz frequency zone as well as with superior intensity of photon. Consequently, Terahertz spectroscopic and image arrangements by advanced dissemination depths and declarations can be appreciated. In this chapter, inclusive reviews over various GaN-supported appliances for creation and recognition of Terahertz radiation have been offered. This appraisal comprises an assessment over plasma hetero-FETs, negative differential resistances, impact ionization avalanche transit time, quantum cascade lasers, high electron mobility transistor, Gunn diodes and tera-FETs. This has been illustrated that because of the Terahertz spectroscopic unit were extensively accessible except awaiting ten years before, methods for categorization of substances in Terahertz frequency variety yet required to be advanced. Regarding this, an assessment of classification methods of GaN into Terahertz frequency variety has been supplied in this context too. Mainly, Terahertz time-domain spectroscopy, laser-persuaded Terahertz production spectroscopic unit with Terahertz-electromodulation spectroscopic entity for categorization of GaN are examined.

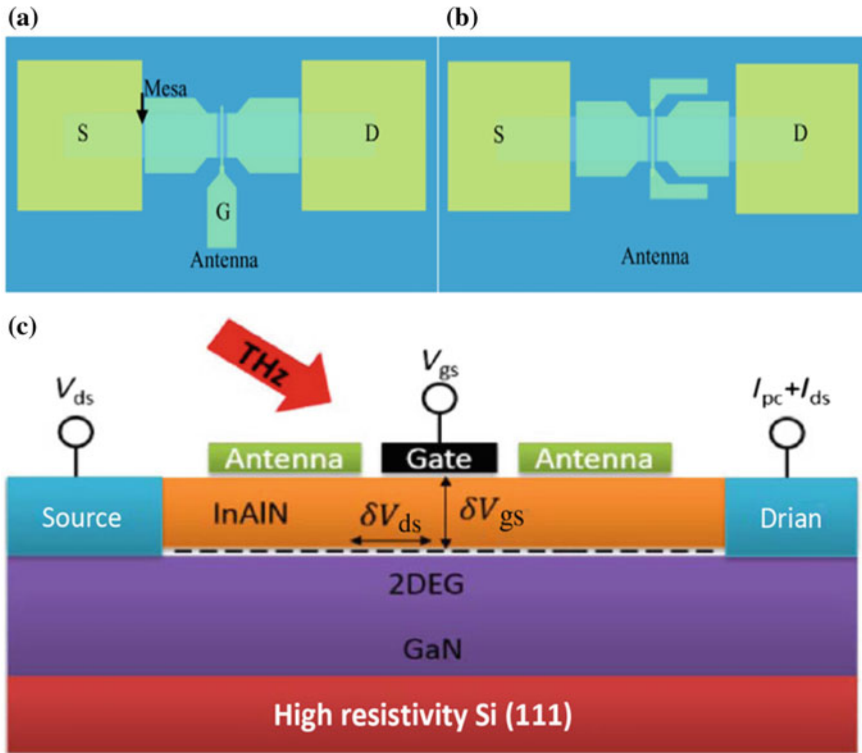

Fig. 11 Representation of the antenna configurations through **a** conventional symmetrical gate with **b** recommended asymmetrical gate. **c** Cross-sectional outlook of the projected GaN high electron mobility transistor detection unit. Reproduced from [43], by authorization of Elsevier Ltd. publication

References

1. M. Dyakonov, M. Shur, Shallow water analogy for a ballistic field effect transistor: new mechanism of plasma wave generation by dc current. Phys. Rev. Lett. **71**, 2465–2468 (1993)
2. M. Dyakonov, M. Shur, Detection, mixing, and frequency multiplication of terahertz radiation by two-dimensional electronic fluid. IEEE Trans. Electron Devices **43**, 380–387 (1996)
3. W. Knap, M. Dyakonov, D. Coquillat, F. Teppe, N. Dyakonova, J. Lusakowski, K. Karpierz, M. Sakowicz, G. Valusis, D. Seliuta, I. Kasalynas, A. El Fatimy, Y.M. Meziani, T. Otsuji, Field effect transistors for terahertz detection: physics and first imaging applications. J. Infrared Milli. Terahz Waves **30**, 1319–1337 (2009)
4. W. Knap, S. Nadar, H. Videlier, S. Boubanga-Tombet, D. Coquillat, N. Dyakonova, F. Teppe, K. Karpierz, J. Łusakowski, M. Sakowicz, I. Kasalynas, D. Seliuta, G. Valusis, T. Otsuji, Y. Meziani, A. El Fatimy, S. Vandenbrouk, K. Madjour, D. Théron, C. Gaquière, Field effect transistors for terahertz detection and emission. J. Infrared Milli. Terahz **32**, 618–628 (2011)
5. T. Otsuji, Y.M. Meziani, T. Nishimura, T. Suemitsu, W. Knap, E. Sano, T. Asano, V.V. Popov, "Emission of terahertz radiation from dualgrating- gates plasmon-resonant emitters fabricated with InGaP/InGaAs/GaAs material systems. J. Phys.: Condens. Matters **20**, 384206 (2008)

6. Y. Tsuda, T. Komori, A. El Fatimy, T. Suemitsu, T. Otsuji, Application of plasmonic microchip emitters to broadband terahertz spectroscopic measurement. J. Opt. Soc. Am. B **26**, A52–A57 (2009)
7. A.K. Geim, K.S. Novoselov, The rise of graphene. Nature Mat. **6**, 183–191 (2007)
8. V. Ryzhii, A. Satou, T. Otsuji, Plasma waves in two-dimensional electron-hole system in gated graphene heterostructures. J. Appl. Phys. **101**, 024509 (2007)
9. V.V. Popov, TYu. Bagaeva, T. Otsuji, V. Ryzhii, Oblique terahertz plasmons in graphene nanoribbon arrays. Phys. Rev. B **81**, 073404 (2010)
10. T. Watanabe, K. Akagawa, Y. Tanimoto, D. Coquillat, W. M. Knap, T. Otsuji, Terahertz imaging with InP high-electron-mobility transistors, in *SPIE Defense, Security & Sensing, Proc. SPIE*, vol 8023, p. 802325 (2011)
11. K. Akagawa, S. Fukuda, T. Suemitsu, T. Otsuji, H. Yokohama, G. Araki, Impact of T-gate electrode on gate capacitance in $In_{0.7}Ga_{0.3}As$ HEMTs. Phys. Status Solidi C **8**, 300–302 (2011)
12. From http://www.teraview.com/ab_imageLibrary.asp
13. M. Smith, S.J. Liu, M.Y. Kao, P. Ho, S.C. Wang, K.H.G. Duh, S.T. Fu, P.C. Chao, W-band high efficiency InP-based power HEMT with 600 GHz fmax. IEEE Microwave Guided Wave Lett. **5**, 230–232 (1995)
14. M.J.W. Rodwell (ed.), *High Speed Integrated Circuit Technology: Towards 100 GHZ Logic* (World Scientific, Singapore, 2001)
15. W. Hafez, M. Feng, Experimental demonstration of pseudomorphic heterojunction bipolar transistors with cutoff frequencies above 600 GHz. Appl. Phys. Lett. **86**, 152101 (2005)
16. W. Knap, F. Teppe, Y. Meziani, N. Dyakonova, J. Lusakowski, F. Bouef, T. Skotnicki, D. Maude, S. Rumyantsev, M.S. Shur, Plasma wave detection of millimeter wave radiation by silicon field effect transistors. Appl. Phys. Lett. **85**(4), 675–677 (2004)
17. G. Dehlinger, L. Diehl, U. Gennser, H. Sigg, J. Faist, K. Ensslin, D. Grützmacher, E. Müller,. Dehlinger, L. Diehl, U. Gennser, H. Sigg, J. Faist, K. Ensslin, D. Grützmacher, E. Müller, *Science*, pp. 2277–2280 (2000)
18. R. Kohler, A. Tredicucci, F. Beltram, H.E. Beere, E.H. Linfield, A.G. Davies, D.A. Ritchie, R.C. Iotti, F. Rossi, Terahertz semiconductor-heterostructure laser. Nature **417**, 156–159 (2002)
19. B.S. Williams, S. Kumar, Q. Hu, J.L. Reno, Operation of terahertz quantum-cascade lasers at 164 K in pulsed mode and at 117 K in continuous-wave mode. Opt. Express **13**, 3331–3339 (2005)
20. G. Scalari, N. Hoyler, M. Giovannini, J. Faist, Terahertz bound-tocontinuum quantum-cascade lasers based on optical phonon scattering extraction. Appl. Phys. Lett. **86**, 181101 (2005)
21. G. Scalari, S. Blaser, J. Faist, H. Beere, E. Linfield, D. Ritchie, G. Davies, Phys. Rev. Lett. **93**, 237403 (2004)
22. http://www.lasercomponents.de/wwwuk/products/quantum/main.htm
23. G. Dehlinger, L. Diehl, U. Gennser, H. Sigg, J. Faist, K. Ensslin, D. Grützmacher, E. Müller, Science **290**, 2277 (2000)
24. J. Faist et al., Quantum cascade laser. Science **264**, 553–556 (1994)
25. B. Mirzaei, A. Rostami, H. Baghban, Terahertz dual-wavelength quantum cascade laser based on GaN active region. Opt. Laser Technol. **44**, 378–383 (2012)
26. E. Bellotti et al., Monte Carlo simulation of terahertz quantum cascade laser structures based on wide-bandgap semiconductors. J. Appl. Phys. **105**, 113103 (2009)
27. E. Bellotti et al., Monte Carlo study of GaN versus GaAs terahertz quantum cascade structures. Appl. Phys. Lett. **92**, 101112 (2008)
28. F. Sudradjat et al., Sequential tunneling transport characteristics of GaN/AlGaN coupled-quantum-well structures. J. Appl. Phys. **108**, 103704 (2010)
29. W. Terashima, H. Hirayama, GaN-based terahertz quantum cascade lasers. Proc. SPIE **9483**, 948304 (2015)
30. D. Turchinovich et al., Ultrafast polarization dynamics in biased quantum wells under strong femtosecond optical excitation. Phys. Rev. B **68**, 241307 (2003)
31. D. Turchinovich, B.S. Monozon, P.U. Jepsen, Role of dynamical screening in excitation kinetics of biased quantum wells: nonlinear absorption and ultrabroadband terahertz emission. J. Appl. Phys. **99**, 013510 (2006)

32. H. Hirayama et al., Recent progress and future prospects of THz quantum-cascade lasers. Proc. SPIE **9382**, 938217 (2015)
33. W. Terashima, H. Hirayama, Terahertz frequency emission with novel quantum cascade laser designs, in *Proc. SPIE*, pp. 11–13 (2015)
34. S. Miho, T.-T. Lin, H. Hirayama, 1.9 THz selective injection design quantum cascade laser operating at extreme higher temperature above the kBT line. Phys. Status Solidi C **10**, 1448–1451 (2013)
35. T.-T. Lin, H. Hirayama, Improvement of operation temperature in GaAs/AlGaAs THz-QCLs by utilizing high Al composition barrier. Phys. Status Solidi C **10**, 1430–1433 (2013)
36. T.-T. Lin, L. Ying, H. Hirayama, Threshold current density reduction by utilizing high-al-composition barriers in 3.7 THz $GaAs/Al_xGa_{1-x}As$ quantum cascade lasers. Appl. Phys. Express **5**, 012101 (2012)
37. C. Edmunds et al., Terahertz intersubband absorption in non-polar mplane AlGaN/GaN quantum wells. Appl. Phys. Lett. **105**, 021109 (2014)
38. M. Beeler, E. Trichas, E. Monroy, III-nitride semiconductors for intersubband optoelectronics: a review. Semicond. Sci. Technol. **28**, 074022 (2013)
39. M. Beeler et al., Pseudo-square AlGaN/GaN quantum wells for terahertz absorption. Appl. Phys. Lett. **105**, 131106 (2014)
40. H. Durmaz et al., Terahertz intersubband photodetectors based on semi-polar GaN/AlGaN heterostructures. Appl. Phys. Lett. **108**, 201102 (2016)
41. J.D. Sun et al., High-responsivity, low-noise, room-temperature, self-mixing terahertz detector realized using floating antennas on a GaN-based field-effect transistor. Appl. Phys. Lett. **100**, 013506 (2012)
42. R.A. Lewis et al., Probing and modelling the localized self-mixing in a GaN/AlGaN field-effect terahertz detector. Appl. Phys. Lett. **100**, 173513 (2012)
43. H. Hou et al., Modelling of GaN HEMTs as terahertz detectors based on self-mixing. Proc. Eng. **141**, 98–102 (2016)

Data Transmission with Terahertz Communication Systems

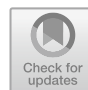

Mohammed El Ghzaoui and Sudipta Das

Abstract The need for high bandwidth in wireless systems has been increased because there is always unoccupied bandwidth for the current communication system. Therefore, the extension of communication systems to higher frequencies is required to offer high-capacity wireless applications. In order to achieve high capacity, the carrier frequencies requisite should be increased more than 100 GHz. Nowadays, academics are currently working on wireless communication systems at terahertz (THz) frequency which is attractive for wireless communications since they lead to high capacity. However, the THz channel is a harsh environment for signal transmission. So, the implementation of THz communication system requires the study of modulation schemes. Among various kinds of communication techniques, QPSK and BPSK are suitable due to their simplicity. In this work, quadrature phase shift keying (QPSK) and binary phase shift keying (BPSK) are assumed with incoherent and coherent receiver, respectively. When it comes to opting for the appropriate modulation techniques for THz communication system, there is always a compromise to be made between bandwidth efficiency and power efficiency. For that reason, the performance modulation schemes were analyzed in terms of data rate and power efficiency. Besides, multiple-input multiple-output (MIMO) can provide high capacity by using multiple transmit or receive antennas. This chapter evaluates the performance of QPSK/BPSK modulations for single-input single-output (SISO) and MIMO technics under different values of the roll-off factor considered for root raised cosine (RCC) filter; then we analyze the performance of MRC receiver in MIMO wireless channels with Alamouti encoding at THz frequencies.

Keywords THz communication system · Wireless channel · MIMO · Alamouti encoding · QAM · ASK · PSK · ISI · BER · SNR · MRC

M. El Ghzaoui
ENS-UMI, Moulay Ismail University of Meknes, Toulal, ENS, BP.3104, Meknes, Morocco

S. Das (✉)
Department of Electronics & Communication Engineering, IMPS College of Engineering & Technology, Chandipur, WB, India
e-mail: sudipta.das1985@gmail.com

© Springer Nature Singapore Pte Ltd. 2020
A. Biswas et al. (eds.), *Emerging Trends in Terahertz Solid-State Physics and Devices*,
https://doi.org/10.1007/978-981-15-3235-1_9

Abbreviations

ACLR	Adjacent Channel Leakage Ratio
ASK	Amplitude-Shift Keying
AWGN	Additive White Gaussian Noise
ADC	Analog to Digital Converter
BER	Bit Error Rate
BLE/BTLE	Bluetooth Low Energy
BPSK	Binary Phase Shift Keying
CDMA	Code division multiple access
GMSK	Gaussian minimum-shift-keying
GSM	Global System for Mobile Communications
HPA	High Power efficiency
MIMO	Multiple-Input Multiple-Output
MISO	Multiple-Input Single-Output
MSK	Minimum-Shift-Keying
MMIC	Monolithic Microwave Integrated Circuit
MRC	Maximum Ratio Combining
OFDM	Orthogonal Frequency Division Multiplexing
OOK	On Off Keying
OOB	Out Of Band
PSK	Phase Shift Keying
PAPR	Peak-to-Average Power Ratio
PSD	Power Spectral Density
QAM	Quadrature Amplitude Modulation
QPSK	Quadrature phase shift keying
RRC	Root Raised Cosine
SNR	Signal-to-Noise Ratio
THz	Terahertz
UMTS	Universal Mobile Telecommunications System
WPAN	Wireless Personal Area Network
WLAN	Wireless Local Area Network
WCDMA	Wideband Code Division Multiple Access

1 Introduction

WPAN and WLAN systems take an important place in our daily lives. However, current technologies such as Bluetooth or Wi-Fi which supports data rates up to 100 Mbps have to face their limits today. The next generation operating in the 60 GHz frequency band provides high capacity and spectrum efficiency.

Nowadays, academics are working on wireless communication systems at millimeter wave to provide a high data rate. THz waves are one of the promising systems for wireless communications technology because they provide huge bandwidth, which is crucial for increasing capacity. Nevertheless, the implementation of a THz communication system is controlled by various challenges. In this chapter, we work on some of the issues such as the challenges confronted in the transmitter and receiver sides.

Atmospheric Attenuation at THz Frequencies in wireless communication systems is larger than that at microwave frequency band [1]; this problem affects not only the coverture band, but it decreases the signal power of the communication system, which influences data rate. For that reason, we propose multiple-input multiple-output (MIMO) system to increase data rate too. MIMO system is one of the most promising technologies for providing the high capacity of wireless communication systems [2–4]. The growing admiration of the MIMO technique calls for a better understanding to improve the spectrum efficiency of the THz communications system. The basic premise of the MIMO system over single-input single-output (SISO) is that the theoretically capacity of the MIMO system is higher than for the SISO system which allows MIMO system to provide a significant gain [5, 6]. The demand for MIMO technology calls for a better understanding to improve the spectrum efficiency of THz communication system. Furthermore, MIMO systems affect positively both link reliability and power efficiency. To bring these advantages in practice, we need to be careful in the exploitation of large spatial dimensions.

To achieve ultra-high-speed THz communication system, authors have mainly focused on items such as modulation schemes and indoor/outdoor narrowband radio propagation models. There is still a lack of modulation techniques suitable for positioning applications; also, there is a need to study of propagation effects and THz hardware components. THz communication systems have a higher bandwidth compared to microwave technology. For that reason, we are mainly focusing on receiver techniques and MIMO technology to provide a data rate of 100 Gb/s over the THz communication system. In this work, QPSK and BPSK demodulation with incoherent and coherent receivers, respectively, are assumed. The performance of QPSK/BPSK modulation was analyzed for the MRC diversity techniques at the receiver for the deferent value of the roll-off-factor (α) considered for the RRC filter.

This chapter starts by introducing the concept and relevance of the THz communications system, then by discussing diverse modulation techniques, especially OOK, QPSK, QAM, MSK, GMSK and the feasibility of the techniques in THz communication system. After that, we represent ALAMOUTI scheme with 2×2 diversity order. We present also the simulation results of MRC receiver in MIMO wireless channels with Alamouti encoding at THz frequencies.

2 Choice of the Carrier Frequency

The THz requires accurate modeling of the channel before implementing the THz communication system. Implementing a system at a high carrier frequency allows one to achieve a higher bandwidth which consequently provides a high data rate wireless communications system at the expense of a reduced range. Within ten years, the promised capacity for the wireless system will allow customers to be able to access individual wavelengths at up to 100 Gbit/s. On the other side, academics have recently been searching using high-frequency radio waves more than 100 GHz to allow high data rate wireless communication system. The THz communications system would adopt a high data rate of about 100 Gbit/s using modulation techniques such as QAM thanks to their ultra-broad bandwidth [7–10].

For frequencies more than 100 GHz, elementary functional components like a mixer, frequency multiplier [11], electronic oscillator such as voltage-controlled oscillator [12] and electronic circuit like phase-locked loop, [13] and conventional radio transmitters and receivers circuits [14, 15] for wireless system, such as remote sensing (such as radar) and data communications, have been verified. The 120-GHz band has been developed to be used for wireless system. Thanks to the progress of the semiconductor electronics industry especially with respect to data rate, stability, distance, and cost [14]. Japan has officially modified the radio regulations, including new spectrum allocations (116 to 134 to 120 GHz band) to the wireless system for the data share. Japanese allocation was the first one of radio system using frequency more than 100 GHz. The data rate of the wireless channels has been progressed to 20 Gbit/s using QPSK as transmission technique [15]. Working at 240 GHz, carrier frequency corresponds to an on-chip wavelength of about 360 μm. Additionally, for long-range wireless communication link using transmitter lenses, the atmospheric attenuation in wireless systems in this band is low. Operating at 250 GHz corresponds to low cut off frequency with a maximum oscillation frequency fmax of 200 GHz in 65 nm bulk CMOS technology. In [16], an ASK receiver MMIC is integrated with an on-chip dipole antenna and RF module to operate at 300 GHz for THz communication for data transmission upto 24 Gbps over 0.3 m. For the next-generation wireless networks with high data rates, in particular, the band between 275 and 3000 GHz has not been allocated for particular usages until now. On the receiver side, a high voltage diode in the form of Schottky barrier is used for demodulation due to its high cutoff frequency.

3 Channel Modeling

The capacity of 100 Gbit/s would be probable in the next-generation wireless system. Many efforts have been taken to standardize the spectral efficiency; one of them has been introduced in [17] by Kürner et al. To model the channel, they take into

account: propagation channel models, interference with other applications such as radio astronomy and enabling technologies.

An effective implementation of THz technology needs the understanding of broadcast channel characteristics. However, because the THz communication systems have several attenuations and high diffraction losses, establishing radio links in the presence of shadowing conditions need beamforming to benefit from the scattering and reflection processes. To get hold of practical channel models for wireless channels in upcoming indoor THz technology, it is essential to understand the behavior of the wireless channel. Therefore, to design any channel model for the THz communication system, careful considerations should be given to the multi-path effects. In addition, it is needed to be acquainted with the knowledge of broadcast channels such as attenuation caused by building according to its material properties. The THz channel has been characterized experimentally at distances of less than 1 m, and it is compared with some model used frequencies, 290 and 310 GHz [18]. In [19], measurements have been done to determine the effect of materials properties of classic house materials on channel behavior. In order to determine the reflection coefficients, Fresnel's equations are used and demonstrated that the material reflectivity must be calculated to model the wireless channel for the upcoming generation THz technology together with NLOS scenarios. For example, in [20], a true interference scenario is analyzed. Recently, measurement of channel properties has been done for THz technology and compared with the simulation results obtained based on ray-tracing methods at 300 GHz [21].

4 Modulation Schemes

Single carrier modulations have been extensively used in cellular systems such as GSM, CDMA2000, and UMTS WCDMA. Thanks to their time domain symbol sequencing; they typically provide low PAPR. Improving the power efficiency of HPA and battery life can be extended. This makes a single carrier waveform particularly suited for use cases such as WiMAX and UMTS where battery power and coverage extension are the main optimization goals.

On the other hand, single carrier waveforms suffer link degradation under frequency selective channels and typically require the use of equalizer to obtain high spectral efficiency under the multi-path effect.

4.1 OOK Modulation

OOK modulation is a very popular modulation used in wireless system. This technique is used largely. Thanks to its simplicity, the needed limited bandwidth, and low implementation costs. OOK modulation has the advantage of allowing the modulator to be lazy when transmitting "zero." Therefore, it has low power consumption.

The drawback of OOK modulation technique arises in the presence of an undesired signal. OOK is spectrally efficient modulation, but more sensitive to noise because of the other types of modulation such as QAM, PSK, and FSK.

The energy consumed by one-bit interval is as follows:

$$E = \frac{A^2 T_\mathrm{b}}{2} \tag{1}$$

where A is the signal amplitude, and T_b is the bit duration. The average energy can be presented by:

$$e = \frac{A^2 T_\mathrm{b}}{4N_0} \tag{2}$$

So, the bit errors probability Pe of OOK modulation is given by:

$$\mathrm{Pe} = \left(\frac{1}{2}\right)\mathrm{erfc}\left[\left(\frac{e}{2}\right)^{\frac{1}{2}}\right] \tag{3}$$

where erfc is the complementary error function.

4.2 QPSK Modulation

Quadrature phase shift keying (QPSK) uses *our* possible phase shifts to encode two bits per symbol. QPSK is also a Double-sideband suppressed-carrier transmission (DSBCS) modulation technique in which two bits per symbol in a fixed duration can be sent (without the use of another carrier frequency). To transmit QPSK signal, we need half of the amount of radio frequency spectrum that required for BPSK signals, which in turn make area for additional consumers on the link. QPSK is an important modulation scheme which allows transitions of two bits per symbol for a fixed duration.

At the transmitter and after converting the analog signal to a digital one, the input encoded bits of i_{SS} th spatial stream is cracked into the symbols of N_{CBPS} bits, $\left(c_0^{(s)}, c_1^{(s)}, \ldots, c_{N_{\mathrm{CBPS}}-1}^{(s)}\right)$, where s denotes the symbol number. Each four bits $\left(c_{2k}^{(s)}, c_{2k+1}^{(s)}, c_{2k+2}^{(s)}, c_{2k+3}^{(s)}\right)$, $k = 0, 1, \ldots, N_{\mathrm{SD}}/2-1$, are transformed into the pair of complex points $\left(d\left(i_{\mathrm{SS}}, s, k\right), d\left(i_{\mathrm{SS}}, s, P(k)\right)\right)$. The modulation is performed in two steps:

- First, two QPSK points are modulated as $x_{2k}^{(q)} = \frac{1}{\sqrt{2}}\left(\left(2 \times c_{4k}^{(s)} - 1\right) + j\left(2 \times c_{4k+2}^{(s)} - 1\right)\right)$, $x_{2k+1}^{(s)} = \frac{1}{\sqrt{2}}\left(\left(2 \times c_{4k+1}^{(s)} - 1\right) + j\left(2 \times c_{4k+3}^{(s)} - 1\right)\right)$

- Second, two QPSK points $\left(x_{2k}^{(s)}, x_{2k+1}^{(s)}\right)$ are converted to two 16 QAM points $\left(d\left(i_{\mathrm{SS}}, s, k\right), d\left(i_{\mathrm{SS}}, s, P(k)\right)\right)$ by multiplication on mapping matrix Q as follows:

$$\begin{bmatrix} d\left(i_{\mathrm{SS}}, s, k\right) \\ d\left(i_{\mathrm{SS}}, s, P(k)\right) \end{bmatrix} = \underbrace{\frac{1}{\sqrt{5}}\begin{bmatrix} 1 & 2 \\ -2 & 1 \end{bmatrix}}_{=Q} \cdot \begin{bmatrix} x_{2k}^{(s)} \\ x_{2k+1}^{(s)} \end{bmatrix} \tag{4}$$

where index $P(k)$ is defined in the range $N_{\mathrm{SD}}/2$ to $N_{\mathrm{SD}}/2 - 1$. The qth modulated data block of i_{SS}th spatial stream is mapped to N_{SD} data subcarriers of qth OFDM symbol of i_{SS}th spatial stream.

Specifically, when QPSK modulation is chosen, it gives a constant amplitude waveform with 0 dB PAPR [22]. In practice, however, single carrier modulation is typically followed by a time-dispersive transmit pulse shaping filter that is more localized in frequency domain, to reduce out of band (OOB) leakage and meet adjacent channel leakage ratio (ACLR) requirements.

Figure 1 shows the PSD of QPSK modulation with and without transmit pulse shaping. To maximize the SNR, a matched filter must be introduced at the receiver part. To delete ISI, the pulse shaping filter is typically selected as a half-Nyquist filter; i.e., the impulse response of the filters has the Nyquist property. Explicitly, in Figure, plots the PSD for a RRC filter with a roll-off factor of $\alpha = 0.22$.

Notice that with transmit pulse shaping, the transmitted waveform is no longer constant envelope and has > 0 dB PAPR.

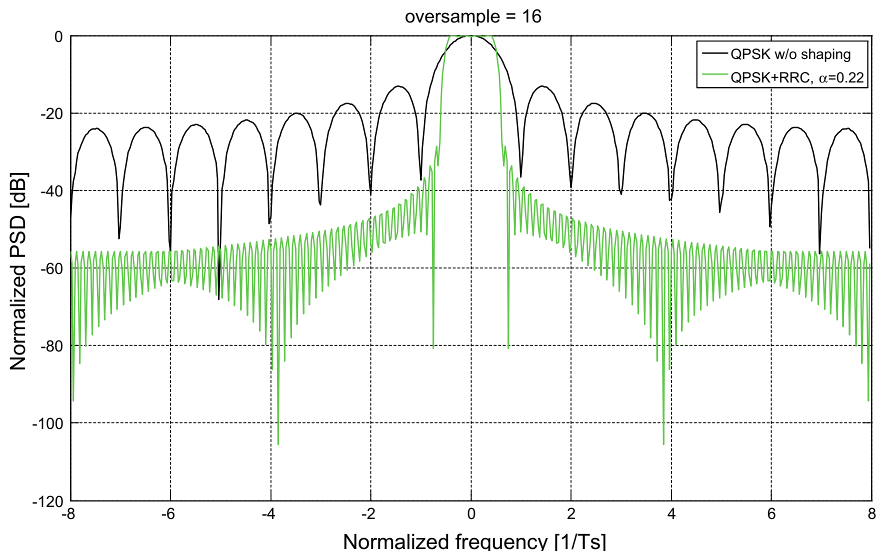

Fig. 1 PSD of QPSK

QAM Modulation

As mentioned before, higher orders of QAM can be used to achieve higher spectral efficiency with a single carrier waveform. QAM is extensively used in modern telecommunications to transmit data over wireless link. It is commonly used to transmit information because this modulation provides benefits over other modulation technique like PSK, while numerous forms of data transmission technique operate alongside each other.

QAM signal is a technique in which two sinusoidal carriers 90° are moderated and are summered to the result of both amplitude and phase variations.

QAM modulations are an extension of the MPSK modulations: Carrier sees its amplitude and/or phase "jump" with each change of symbol. This type of modulation is used in the DVB-T standard of digital TV (TNT): 64 QAM for TNT in France and 16 QAM for German TNT. For example, in 16-QAM, each symbol (4 bits) has a duration TS; phase and amplitude jumps can be observed between two successive symbols.

5 Spectral Efficiency of Single Carrier System

Developments in the field of modulation formats and signal processing for high-speed spectrally efficient wireless link, MW components like electronic oscillators such as voltage-controlled oscillator and electronic circuits like phase-locked loop, are taking a deep consequence on the increase of bite rate of point-to-point connections.

Current transmission techniques of high data rates such as 128-QAM are used extensively for stem/structure networks and modulation like 16-QAM and 32-QAM are progressively used for access connections. New devices can handle transmission techniques up to 1024-QAM or 4096-QAM systems which are commonly used in high-speed data transmission. Figure 2 shows the spectral efficiency versus bit-to-noise ratio at BER of 10^{-4}.

The suppleness in using higher modulation orders such as 1024-QAM and 4098-QAM to attain higher data rate in certain channel bandwidth might permit workers to crack capacity difficulties within the circumstances of spectrum scarcity in a specific frequency band.

The concrete growth in vehicle information with the transmission schemes follows an increasing tendency modulation order.

6 GMSK and MSK Modulation

The simplest solution to decrease complexity and increase the power of the transmitter also to high transmit efficiency is to employ a constant envelope waveform. The

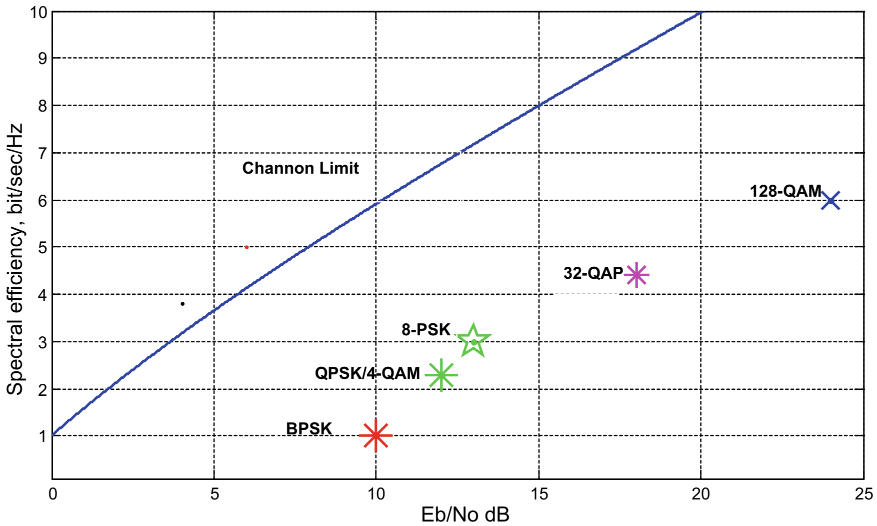

Fig. 2 Spectral efficiency versus bit-to-noise ratio

constant envelope modulation tolerates almost high power amplifier (HPA) to operate close to the saturation levels without clipping or a need for pre-compensation or post-compensation to account for clipping, thus maximizing power efficiency. The drawback to this mechanism is the high implementation cost particularly at the receiver side and also has been the inefficiency from a capacity standpoint relative to quadrature amplitude modulation that means constant envelope waveform has less data rate than non-constant envelope waveform such as QAM modulation. Nevertheless, for applications where the high data rate is not required, a constant envelope waveform is more appropriate since it achieves the highest PA efficiency.

MSK and GMSK are most popular constant envelope modulation and one of the most spectrally efficient waveforms available [23, 24]. These techniques belong to the class of continuous phase frequency-shift-keying (CPFSK) signals. Due to its constant envelope, MSK was adopted by the IEEE 802.15.4 standard, which offers the physical layer platform for ZigBee; in addition, it was adopted for the GSM cell phone standard. GMSK is also adopted by BTLE, Bluetooth, and GSM.

MSK modulation can be consistently considered as Offset-QPSK with sinusoidal pulse shaping, which offers efficient modulation and demodulation. Notice that a differential encoder is inserted before the modulator to avoid error propagation at the demodulator. This also helps to make modulation easier, as the differential encoder and differential decoder cancel each other.

GMSK is a modified version of MSK modulation scheme, where the signal is passed through a Gaussian filter before it is applied to an MSK modulator. The Gaussian filter is used to achieve high spectral efficiency of the MSK signal, with the penalty of intersymbol interference.

7 THz 16 QAM/QPSK Transmission

High data rate over wireless channels at THz frequencies is a challenging task because of the high bit error rate in these channels. THz communication with high efficiency has been demonstrated with advanced modulation schemes such as QPSK and 16-QAM which are crucial to optimize spectral efficiency over wireless networks [24]. To increase capacity, optimization of the channel bandwidth is required. One of the promising candidates is to use modulation format with a high modulation index; that is, the modulation format would be enhanced from QPSK to 16-QAM, 64-QAM, and so on. However, the required resolution of a digital-to-analog converter set at the transmitter side and an analog-to-digital converter, which is located at the receiver, would become higher. Thus, increasing the degree of the multi-levels is difficult because of its electrical device issue. In addition, on the receiver side, it is necessary to use high resolution analog-to-digital converter (ADC), which generally translates into high power consumption per conversion. Therefore, the ADC resolution bits must be kept as low as possible to decrease the cost and power consumption. Consequently, increasing the bits resolution of an ADC will lead to high precision DSP elements, which are unwanted for wireless transceivers.

Another possible solution is a space-division-multiplexing technique, so-called a multi-input-multi-output (MIMO) technique. The spectral efficiency in the space is augmented easily as the number of the antenna at the transmitter and receiver side increases, and thus, the total capacity of the MIMO link will increase. Moreover, the diversity effect under multi-antenna configuration can enhance an effective SNR.

7.1 Power Spectral Density

As it was mentioned before, GMSK is a variant of MSK. We can also note that with the introduction of Gaussian filtering, the GMSK signal can no longer be viewed as Offset-QPSK.

Usually, the receiver of GMSK is a linear estimation of the MSK, and this technique might be treated as a sum of pulse PAM signals. Based on this approximation, we can use the Viterbi detector to receive the signal. Notice that lower complexity demodulator for GMSK is typically used for low power devices, such as BTLE. In Figs. 3 and 4, we compare the PSD for MSK and GMSK with the PSD for QPSK with oversampling factor of 16, respectively.

Figures 3 and 4 show that the spectral efficiency of GMSK modulation is significantly better than the spectral efficiency of QPSK and MSK modulations. One can be seen from this figure that the width of the spectrum of GMSK is mainly narrow for the low level of the signal (-60 dBm). Consequently, the GMSK modulation does not disturb adjacent radio channels.

In addition, the spectrum of the MSK modulation occupies the same main lobe spectrum as the QPSK modulation.

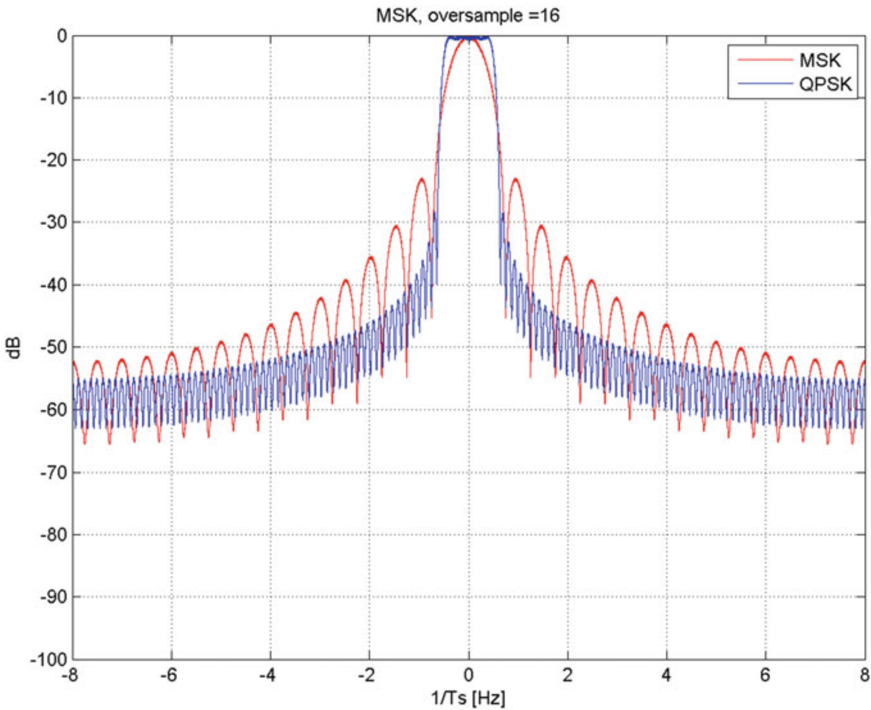

Fig. 3 PSD of MSK and QPSK transmitters for bit rate of 15 Mbps

7.2 Alamouti Scheme for MIMO System

The Alamouti technique is a transmit diversity shames which can be used with MIMO wireless system of two transmitter and four receiver to offer a diversity gain of 2 × 2. As p is the time slots which is used to transmit j symbols, the bite rate R given by $R = j/p$. For example, the rate of 2 × 2 MIMO configuration is one. The Alamouti scheme works independently of the number of receive ports.

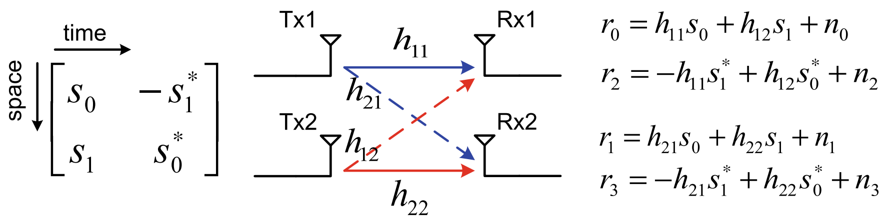

The Alamouti code 0 is the most known ST coding scheme with full diversity and code rate one. The received signal can be written as follows:

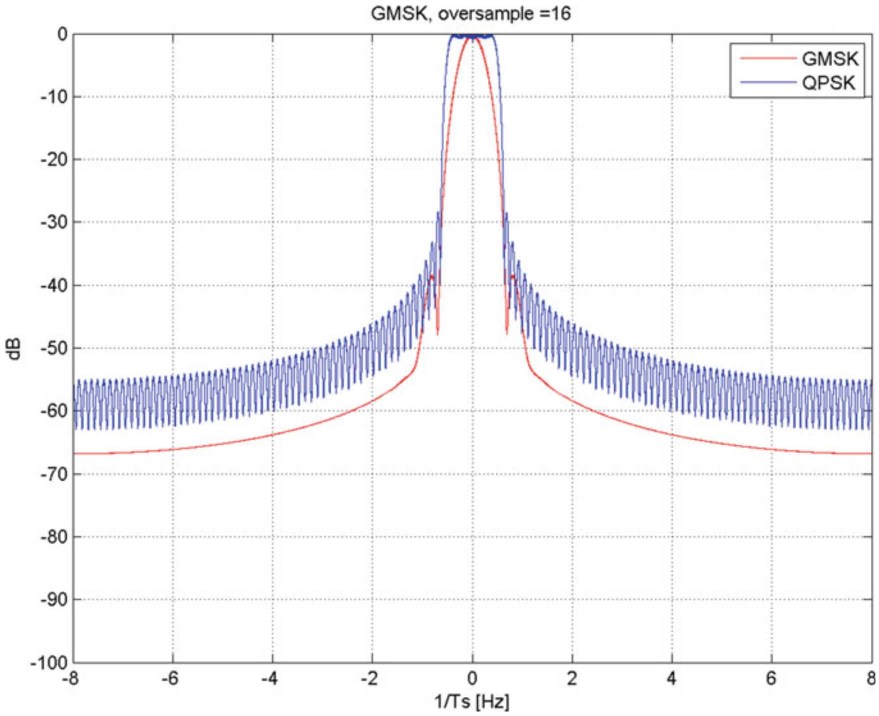

Fig. 4 PSD of GMSK and QPSK transmitters for bit rate of 15 Mbps

$$\begin{bmatrix} r_0 \\ r_1 \\ r_2^* \\ r_3^* \end{bmatrix} = \underbrace{\begin{bmatrix} h_{11} & h_{12} \\ h_{21} & h_{22} \\ h_{12}^* & -h_{11}^* \\ h_{22}^* & -h_{21}^* \end{bmatrix}}_{\mathbf{H}} \begin{bmatrix} s_0 \\ s_1 \end{bmatrix} + \begin{bmatrix} n_0 \\ n_1 \\ n_2 \\ n_3 \end{bmatrix} \tag{5}$$

The advantage of the Alamouti coding scheme is that it creates an orthogonal MIMO channel structure; i.e., $H^{\mathrm{H}}H$ is diagonal matrix, which enables low-complexity maximum-likelihood (ML) symbol detection using the simple zero forcing (ZF) decoding:

$$\hat{\mathbf{s}} = \left(\mathbf{H}^{\mathrm{H}}\mathbf{H}\right)^{-1}\mathbf{H}^{\mathrm{H}}\mathbf{r} \tag{6}$$

The difficulty of this technique is that all four channel links, i.e., h_{11}, h_{12}, h_{21}, and h_{22} should be estimated to decode the received signal. As a result, it needs twice pilots as much as that is needed for SISO system.

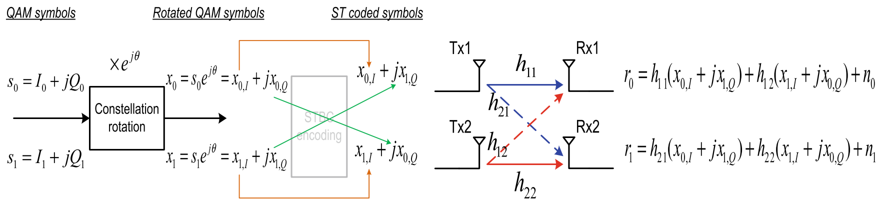

The second way to enhance the performance of spatial multiplexing techniques in THz channel is to adopt the idea of the rotated QAM constellations technique. The data for each antenna is first rotated to associate the in-phase (I) and quadrature (Q) components with an angle θ. After rotation, the data symbols can be expressed as follows:

$$x_0 = s_0 e^{j\theta} = \underbrace{(I_0 \cos\theta - Q_0 \sin\theta)}_{x_{0,I}} + j\underbrace{(I_0 \sin\theta + Q_0 \cos\theta)}_{x_{0,Q}}, \tag{7}$$

$$x_1 = s_1 e^{j\theta} = \underbrace{(I_1 \cos\theta - Q_1 \sin\theta)}_{x_{1,I}} + j\underbrace{(I_1 \sin\theta + Q_1 \cos\theta)}_{x_{1,Q}}. \tag{8}$$

7.3 Maximum Ratio Combining

Different sources of diversity are available to regular the channel variations due to multi-path fading in wireless environment. The typical method consists of using MRC of the signals received at several antennas.

Indeed, MRC diversity uses an algorithm to calculate the weights that maximize the SNR at the output of the RMC receiver. Consequently, RMC receiver is optimal in terms of SNR. While SNR is improving by a factor of ln(N) for the selection diversity, it is improving by a factor of N for the selection diversity. That means the performance of MRC receivers is better than for selection diversity. As well, the BER decreases with a factor of N.

$$P_e = 1/\text{SNR} \tag{9}$$

At a high value of SNR in a diversity system, it is expected that the BER varied linearly with the SNR [25].

Antenna diversity, known as spatial diversity, can be achieved by using multiple antennas at the transmitter or receiver side [26]. Transmitter diversity might be obtained by using space time coding (STC) schemes.

Figure 5 illustrates the configuration for two separate receive antennas. The two antennas are weighted to get the best out of the received SNR. In such a technique the antennas must be co-phased at an equal gain before being summed in order to get the best out of diversity gain. Then, the received signals are passed in a demodulator.

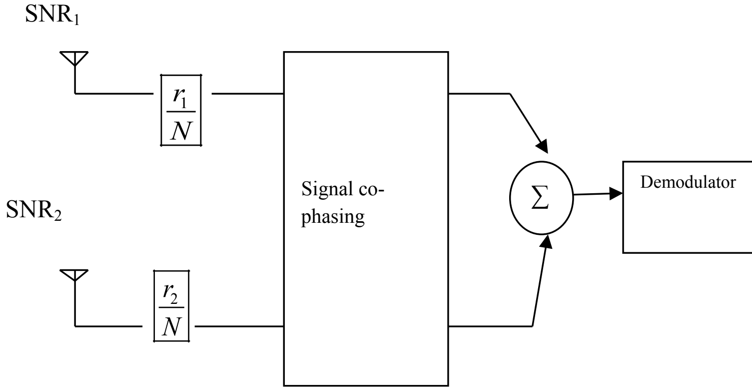

Fig. 5 2-branch MRC receiver

In MRC receiver, the signal amplitude at the transmitter at a given time t_i, is $A_{S,\,M}(t_0)$ it can be expressed as

$$V_{S,M}(t_0) = r_1(t_0)\left(\frac{r_1(t_i)}{N}\right) + r_2(t_0)\left(\frac{r_2(t_i)}{N}\right) = \frac{r_1(t_i)^2 + r_2(t_i)^2}{N} \tag{10}$$

$$V_{N,M}(t_0) = n_1\left(\frac{r_1(t_i)}{N}\right) + n_2\left(\frac{r_2(t_i)}{N}\right) = \frac{n_1 r_1(t_i) + n_2 r_2(t_i)}{N} \tag{11}$$

The instantaneous voltage to noise power ratios must be multiplied at t_i by their received signal enveloper.

$$P_{N,\,M}(t_0) = \frac{r_1(t_i)^2}{N^2} E\left[n_1^2\right] + \frac{r_2(t_i)^2}{N^2} E\left[n_2^2\right] = \frac{r_1(t_i)^2 + r_2(t_i)^2}{N}$$

So,

$$\mathrm{SNR}_{P_M}(t_0) = \frac{r_1(t_i)^2 + r_2(t_i)^2}{N} = \frac{1}{N}\left(r_1(t_i)^2 + r_2(t_i)^2\right) \tag{12}$$

$$\text{MGC Output(dB)} = \text{SNR1} + \text{SNR2} \tag{13}$$

7.4 Alamouti Code in MIMO System with RMC Receiver

To show the basic concept of the Alamouti code in THZ communication system with RMC receiver, we have considered two transmitting and two receiving antenna block coding systems. Let h_{lj} be the impulse response from transmitter j to receiver l. We

take up that the signal at the receiver side is $Z(t)$, and at the first receive antenna ($l = 1$), we have

$$Z_1 = h_{11}\begin{pmatrix} s_1 \\ -s_2^* \end{pmatrix} + h_{12}\begin{pmatrix} s_2 \\ s_1^* \end{pmatrix} + \begin{pmatrix} \aleph_{11} \\ \aleph_{12} \end{pmatrix} \tag{14}$$

We obtain

$$Z_1 = \begin{pmatrix} h_{11}s_1 + h_{12}s_2 \\ h_{12}s_1^* - h_{11}s_2^* \end{pmatrix} + \begin{pmatrix} \mathcal{R}_{11} \\ \mathcal{R}_{12} \end{pmatrix} = Gh_1 + \mathcal{R}_1; G = \begin{pmatrix} s_1 & s_2 \\ -s_2^* & s_1^* \end{pmatrix} \tag{15}$$

where $h_1 = (h_{11}h_{12})^t$.

Likewise, for the second antenna, we can write

$$Z_2 = h_{21}\begin{pmatrix} s_1 \\ -s_2^* \end{pmatrix} + h_{22}\begin{pmatrix} s_2 \\ s_1^* \end{pmatrix} + \begin{pmatrix} \aleph_{21} \\ \aleph_{22} \end{pmatrix} \tag{16}$$

We obtain

$$Z_1 = \begin{pmatrix} h_{21}s_1 + h_{22}s_2 \\ h_{22}s_1^* - h_{21}s_2^* \end{pmatrix} + \begin{pmatrix} \mathcal{R}_{21} \\ \mathcal{R}_{22} \end{pmatrix} = Gh_2 + \mathcal{R}_2; G = \begin{pmatrix} s_1 & s_2 \\ -s_2^* & s_1^* \end{pmatrix} \tag{17}$$

where $h_2 = (h_{21}h_{22})^t$.

Z_l might be mapped into $r_l = \mathcal{M}_l s + N_l$ by altering the second vector Z_{l2} of $Z_l = (Z_{l1}Z_{l2})^t$ with its complex conjugate vector. So, considering $s = (s_1 s_2)^t$, we can write

$$r_l = \mathcal{M}_l s + N_l = \begin{pmatrix} Z_{l1} \\ Z_{l2}^* \end{pmatrix}, l = 1, 2 \tag{18}$$

Thus,

$$r_l = \begin{pmatrix} h_{11} & h_{12} \\ h_{12}^* & -h_{11}^* \end{pmatrix}\begin{pmatrix} s_1 \\ s_2 \end{pmatrix} + \begin{pmatrix} \aleph_{11} \\ \aleph_{12} \end{pmatrix} \tag{19}$$

Or

$$r_1 = \mathcal{M}_1 s + N_1, \mathcal{M}_1 = \begin{pmatrix} h_{11} & h_{12} \\ h_{12}^* & -h_{11}^* \end{pmatrix}, \mathcal{M}_1^*\mathcal{M}_1 = \|h_1\|^2 \tag{20}$$

Similarly,

$$r_2 = \mathcal{M}_2 s + N_2, \mathcal{M}_2 = \begin{pmatrix} h_{21} & h_{22} \\ h_{22}^* & -h_{21}^* \end{pmatrix}, \mathcal{M}_2^*\mathcal{M}_2 = \|h_2\|^2 I_2 \tag{21}$$

Consequently, at the lth antenna, we can write the decision variable b_l as

$$b_l = \mathcal{M}_l^*(\mathcal{M}_l s + N_l) = \|h_l\|^2 s + \mathcal{M}_l^* N_l \tag{22}$$

That means:

$$b_1 = \|h_1\|^2 s + \mathcal{M}_1^* N_1 \tag{23}$$

$$b_2 = \|h_2\|^2 s + \mathcal{M}_2^* N_2 \tag{24}$$

The MRC decision variable can be written as the sum of b_1 and b_2 over the normalized impulse response. For $h_2 = (h_{21}\ h_{22}\ h_{21}\ h_{22})^t$, we have

$$b = \frac{1}{\|h\|}(b_1 + b_2) = \frac{\|h_1\|^2 + \|h_2\|^2}{\|h\|} s + \frac{1}{\|h\|}\left(\mathcal{M}_1^* N_1 + \mathcal{M}_2^* N_2\right) \tag{25}$$

Since, $\|h_1\|^2 + \|h_2\|^2 = |h_{21}|^2 + |h_{11}|^2 + |h_{12}|^2 + |h_{22}|^2$, we get the resulting MRC weighting vector:

$$b = \|h\| s + N \tag{26}$$

and the noise is $N = \frac{\mathcal{M}_1^* N_1 + \mathcal{M}_2^* N_2}{\|h\|}$, the covariance of noise N is given by

$$E\left(NN^*\right) = \mathcal{M}_1^* E\left(N_1 N_1^*\right)\mathcal{M}_1 + \mathcal{M}_2^* E\left(N_2 N_2^*\right)\mathcal{M}_2 \tag{27}$$

Since $E\left(N_l N_l^*\right) = 2\sigma^2 I_2, l = 1, 2,$ we obtain:

$$E\left(NN^*\right) = 2\sigma^2 \frac{\|h_1\|^2 + \|h_2\|^2}{\|h\|^2} I_2 = 2\sigma^2 I_2 \tag{28}$$

7.5 Discussion of the Results and Their Context

Via computer simulation, the BER performance of the QPSK/BPSK over a wireless channel with AWGN and atmospheric absorption is presented. The capacity of the wireless channel is calculated built on the Shannon theorem. The impulse response $h(t)$ is simulated using the channel model describing in [7]. The performance criteria to compare QPSK and BPSK wireless demodulator are governed by the BER of the receiver versus SNR of the incoming signal. The block diagram of single input single output QPSK/BPSK transceiver system is shown in Fig. 6.

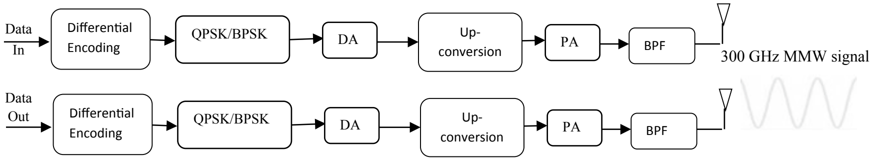

Fig. 6 Block diagram of SISO-QPSK/BPSK transceiver system

Figures 7 and 8 show simulation results for QPSK/BPSK system with a roll off = 0.1, 0.2 and 0.25. The bit error rate is plotted versus the SNR.

We notice from Figs. 7 and 8 that, for a fixed roll off, the performance of BPSK is better than the QPSK system in terms of BER. However, QPSK modulation provides the maximum data transmission rate of the system. The second, from these figures, it can be seen that with roll off decrease the system requires augmenting the SNR to achieve a certain BER. So, roll off should not take too small value when SNR is limited. The block diagram of multiple input multiple output QPSK/BPSK transceiver system is shown in Fig. 9.

In the second part of this section, via computer simulation, we analyze the performance of the proposed system under the proposed channel model conditions. Intersymbol interference (ISI) is an important factor constraining BER performance of MIMO-QPSK/BPSK high-speed THz systems. MRC receivers can be used to eliminate ISI.

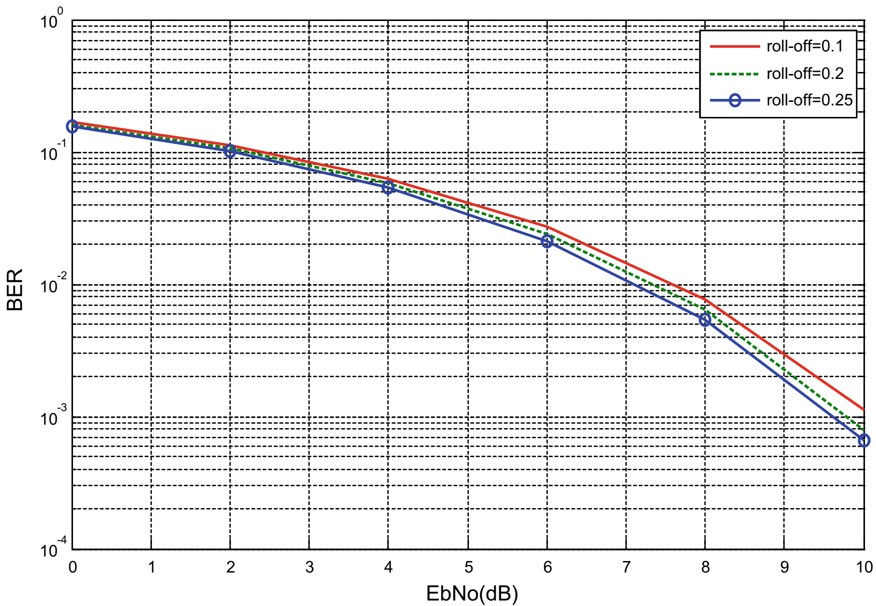

Fig. 7 BER versus SNR of BPSK modulation under proposed channel model

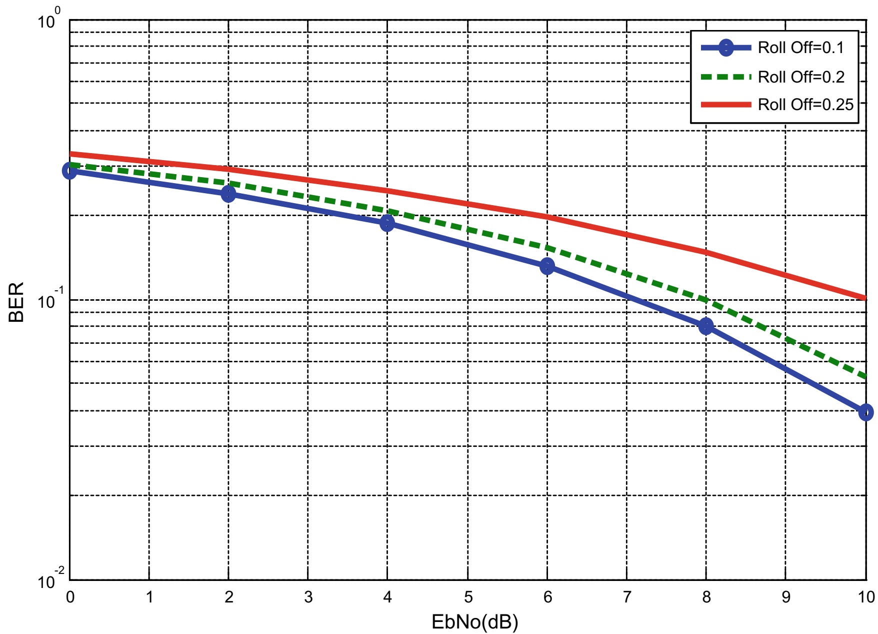

Fig. 8 BER of QPSK modulation under proposed channel model

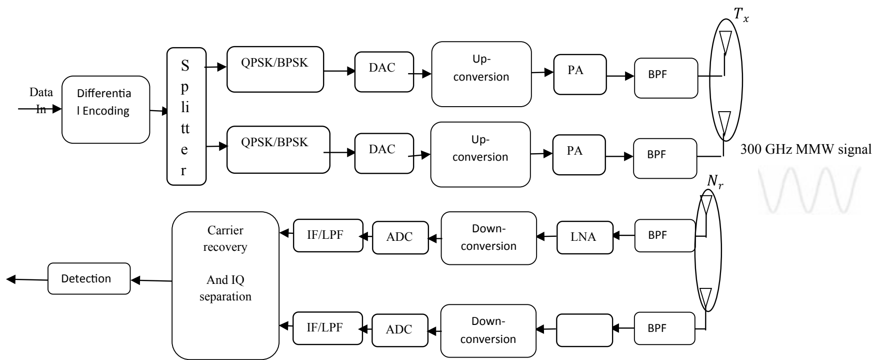

Fig. 9 Block diagram of MIMO-QPSK/BPSK transceiver system

Pseudorandom bit sequence generator having a block length of 229-1 is passed on the 300-GHz symbol modeled by QPSK/BPSK schemes. The central frequency of the received IF signal was 55.5 GHz and the bandwidth is about 60 GHz. At phase demodulator, the digital signal which modulates the amplitude of carrier, as well as the phase of the carrier, was multiplied with a complex sinusoidal signal to separate the I and Q components. To reduce the signal processing complexity, our studies are mainly founded on a BPSK/QPSK system with receiving techniques like frequency

domain equalization (FDE) and channel estimation technics [27]. The FDE might be used to I and Q components in a similar way like in wire-line digital coherent receiving schemes.

The 300 GHz carrier frequency can be generated using intermediate frequencies of 16.460 GHz flowed by an amplifier and two tripler. The received IF signal with lower IF frequency permits to generate a high output power as it is quite slight related to the cutoff frequency of the device. Nevertheless, when the received IF signal has low IF frequency, it is recommended to use high frequency multiplication ratio which results in a higher conversion loss due to the difficulty in preserving circuit balance over the whole bandwidth.

In Fig. 10, the performance of BPSK-MIMO is compared with QPSK-MIMO over the proposed channel model. Over the region, $0\ \text{dB} \leq \text{SNR} \leq 3\ \text{dB}$, the QPSK-MIMO technique performs well than the BPSK-MIMO technique. However, at high SNR, the BPSK-MIMO system is shown to outperform QPSK-MIMO system. Notice that QPSK modulation provides more data transmission rate of the system than BPSK.

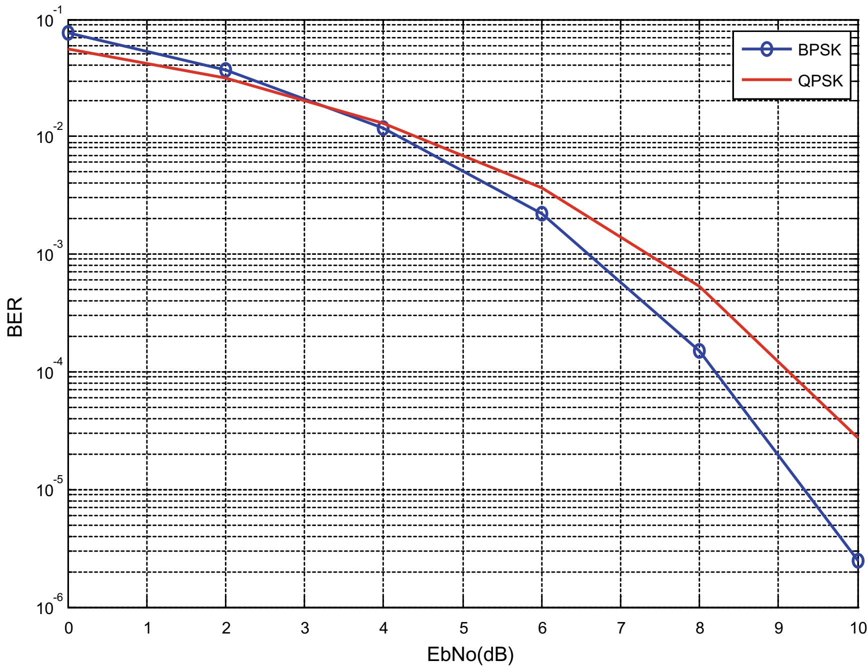

Fig. 10 BER of 2 * 2 MIMO-BPSK/QPSK system with a roll off of 0.2

8 Conclusion

In this chapter, a design of the THz system is presented. The choice of central frequency is based on previous work in this area. Several techniques used for the transmitter/receiver implementation relating to the THz technology node were discussed. Conventional modulation schemes such as OOK, QPSK, and BPSK were analyzed to be applied for THz communication, and they show their viability for millimeter-wave wireless communications system.

To achieve ultra-high-speed THz communications, we are mainly focusing on coherence detection and MIMO processing. In this work, QPSK modulation with incoherent receiver is supposed with AWGN. Also, BPSK modulation with coherent receiver is analyzed. To evaluate the performance of QPSK/BPSK modulation for SISO and MIMO system under deferent values of roll-off factor, simulation results of MRC receiver in MIMO wireless channels with Alamouti encoding at THz frequencies were presented.

References

1. Attenuation by Atmospheric Gases, ITU-R Recommendation, pp. 676–678 (2009)
2. S. Weber, X. Yang, J.G. Andrews, G. Veciana, Transmission capacity of wireless ad hoc networks with outage constraints. IEEE Trans. Inf. Theory **51**(12), 4091–4102 (2005)
3. S. Weber, J.G. Andrews, N. Jindal, An overview of the transmission capacity of wireless networks. IEEE Trans. Commun. **58**(12), 3593–3604 (2010)
4. A. Hunter, J.G. Andrews, S. Weber, The transmission capacity of ad hoc networks with spatial diversity. IEEE Trans. Wireless Commun. **7**(12), 5058–5071 (2008)
5. E. Teletar, Capacity of multi-antenna Gaussian channels. Euro. Trans. Telecommun. **10**(6), 585–595 (1999)
6. E. Biglieri et al., *MIMO Wireless Communications* (Cambridge University Press, Cambridge, 2007)
7. J. Federici, L. Moeller, Review of terahertz and subterahertz wireless communications. J. Appl. Phys. **107**, 111101–111101-22 (2010)
8. T. Kleine-Ostmann, T. Nagatsuma, A review on terahertz communications research. J. Infrared Milli. Terhz. Waves **32**, 143–171 (2011)
9. H.-J. Song, T. Nagatsuma, Present and future of terahertz communications. IEEE Trans. Terahertz Sci. Technol. **1**, 256–263 (2011)
10. T. Nagatsuma, S. Horiguchi, Y. Minamikata, Y. Yoshimizu, S. Hisatake, S. Kuwano, N. Yoshimoto, J. Terada, H. Takahashi, Terahertz communications based on photonics technologies. Opt. Express **21**, 23736–23747 (2013)
11. M. Urteaga, M. Seo, J. Hacker, Z. Griffith, A. Young, R. Pierson, P. Rowell, A. Skalare, M.J.W. Rodwell, InP HBTs for THz frequency integrated circuits, in *Proceedings of the 2011 IEEE Indium Phosphide and Related Materials* (Berlin, Germany, May 2011)
12. M. Seo, M. Urteaga, J. Hacker, A. Young, Z. Griffith, V. Jain, R. Pierson, P. Rowell, A. Skalare, A. Peralta, R. Lin, D. Pukala, M. Rodwell, InP HBT IC technology for terahertz frequencies: fundamental oscillators up to 0.57 THz. IEEE J. Solid-State Circuits **46**(10), 2203–2214 (2011)
13. M. Seo, M. Urteaga, M. Rodwell, M.-J. Choe, A 300 GHz PLL in an InP HBT technology, in *2011 International Microwave Symposium Digest (MTT)* (Baltimore, MD, June)

14. A. Tessmann, H. Massler, U. Lewark, S. Wagner, I. Kallfass, A. Leuther, Fully integrated 300 GHz receiver S-MMICs in 50 nm metamorphic HEMT technology, in *2011 IEEE Compound Semiconductor Integrated Circuit Symposium (CSICS)* (Oct. 16–19, 2011), pp. 1–4
15. Z. Griffith, M. Urteaga, R. Pierson, P. Rowell, M. Rodwell, B. Brar, A 204.8 GHz static divide-by-eight frequency divider in 250 nm InP HBT, in *2010 IEEE Compound Semiconductor IC Symposium Digest* (Monterey, CA, Oct. 2010)
16. H.-J. Song, J.-Y. Kim, K. Ajito, M. Yaita, N. Kukutsu, Fully integrated ASK receiver MMIC for terahertz communications at 300 GHz. IEEE Trans. Terahertz Sci. Technol. **3**(4), 445–452 (2013)
17. T. Kürner, S. Priebe, Towards THz communications-status in research, standardization and regulation. J. Infrared, Millimeter, Terahertz Waves **35**(1), 53–62 (2014)
18. M. Jacob, S. Priebe, T. Kurner, C. Jastrow, T. Kleine-Ostmann, T. Schrader, An overview of ongoing activities in the field of channel modeling, spectrum allocation and standardization for mm-Wave and THz indoor communications, in *Proceedings of the IEEE GLOBECOM Workshops* (2009)
19. R. Piesiewicz, T. Kleine-Ostmann, N. Krumbholz, D. Mittleman, M. Koch, T. Kurner, Terahertz characterisation of building materials. Electron. Lett. **41**, 1002–1004 (2005)
20. C. Jansen, R. Piesiewicz, D. Mittleman, T. Kurner, M. Koch, The impact of reflections from stratified building materials on the wave propagation in future indoor terahertz communication systems. IEEE Trans. Antennas Propag. **56**(5), 1413–1419 (2008)
21. S. Priebe, M. Jacob, C. Jastrow, T. Kleine-Ostmann, T. Schrader, X. Ku, T. Rner, A comparison of indoor channel measurements and ray tracing simulations at 300 GHz, *35th International Conference on Infrared, Millimeter, and Terahertz Waves* (Rome, 2010), pp. 1–2
22. J. Belkadid, A. Benbassou, M. El Ghzaoui, PAPR reduction in CE-OFDM system for numerical transmission via PLC channel. Int. J. Commun. Antenna Propagation **3**(5), 267–272 (2013)
23. K. Murota, K. Hirade, GMSK modulation for digital mobile radio telephony. IEEE Trans. Comm. **COM-29**)(7) (1981)
24. D.A. Guimaraes, Contributions to the understanding of the MSK Modulation. REVISTA Telecommu. **11**(01) (2008)
25. J. Mestoui, M. El Ghzaoui, M. Fattah et al., Performance analysis of CE-OFDM-CPM Modulation using MIMO system over wireless channel. J. Ambient Intell. Human. Comput. (2019). https://doi.org/10.1007/s12652-019-01628-0
26. E.K. Al-Hussaini, A.A.M. Al-Bassiouni, Performance of MRC diversity systems for the detection of signals with Nakagami fading. IEEE Trans. Commun. **COM-33**(12), 1315–1319 (1985)
27. M. Jamal, G. El Mohammed, H. Abdelmounim, F. Jaouad, BER performance improvement in CE-OFDM-CPM system using equalization techniques over frequency-selective channel. Proc. Comput. Sci. **151**, 1016–1021 (2019). https://doi.org/10.1016/j.procs.2019.04.143

Advances in Terahertz Imaging

Arijit Saha

Abstract Since the discovery of photography in the mid-1820s, imaging technology has moved far beyond the visible wavelength range. On one hand x-ray radiography is such an imaging technique which uses subatomic wavelengths, whereas on the other hand radars employ waves with wavelengths of several metres. However, it is seen that in last several years the field of terahertz imaging technology has become an area of interest, due to its various advantages. Actually discovery of new technologies in generation and detection of terahertz radiation have revolutionized this field. Promising applications for terahertz imaging, spectroscopy and sensing have generated much of this interest. By terahertz, generally the electromagnetic spectrum within frequency range of 0.1-10 THz is meant, which corresponds to 3000-30 μm. Terahertz waves are non-ionizing and non-invasive and hence have no risk for living organisms. Also they can provide images which are comparable to x-ray images. Though some of the techniques of THz imaging have been borrowed from well-established techniques like x-ray computed tomography, synthetic aperture radar etc., but several techniques have been exclusively developed for terahertz imaging. Compared to microwaves the THz radiation has much smaller wavelengths and thus provides higher image resolution. However, due to long wavelengths of THz radiation compared to visible wavelengths, far-field imaging using THz radiations has low resolution compared to optical systems. It is found that THz imaging has tremendous potential in applications like security screening, inspection of foods, inspection of semiconductors, pharmaceutical inspection, 2D and 3D imaging, including medical diagnosis to name a few.

Keywords THz-TDS · Reflection spectroscopy · Transmission spectroscopy · THz pulsed imaging

A. Saha (✉)
Department of Electronics and Communication Engineering, B. P. Poddar Institute of Management and Technology, Kolkata, India
e-mail: arijit_sh@yahoo.com

© Springer Nature Singapore Pte Ltd. 2020

A. Biswas et al. (eds.), *Emerging Trends in Terahertz Solid-State Physics and Devices*,
https://doi.org/10.1007/978-981-15-3235-1_10

1 Introduction

In today's world, the technology of imaging has developed a lot since the invention of photographic techniques in the mid-1820s. With the passage of time, lots of research works have been done in this area, and as a result, many novel imaging technologies have emerged. In modern days, imaging technology has moved far beyond visible wavelength range. On one hand in X-ray imaging, subatomic wavelengths are used, whereas on the other hand in radars, wavelengths of several metres are employed. In fact, for various applications, different parts of the available electromagnetic spectrum are now utilized. However, in this chapter, the focus is only on a small part of this huge spectrum—the terahertz range.

By terahertz generally, the range of frequency within 0.1–10 THz is considered. In terms of wavelengths, it is from 3000 to 30 µm (Fig. 1). This shows that the THz spectrum exists between microwave and infrared range. Hence, it can be said that this THz range lies on the borderline of the electronic and photonic world. However, it is found that both electronic and optical methods are inefficient in this range of spectrum.

Out of several applications of THz frequency, the advances in imaging technology using THz frequency are the point of focus of this chapter. It is seen that since mid-1990s, the terahertz imaging technology had made astonishing progress. This is due to the fact that some unique techniques for investigating matter are offered by terahertz radiation [1].

In fact, terahertz imaging has some distinct advantages. As terahertz range falls in a different spectral region, these images are capable of providing complementary information compared to those obtained with other sources like X-ray, ultraviolet rays, visible light, infrared rays or microwave images. Owing to shorter wavelengths, THz images have superior resolution compared to images captured using longer wavelengths or lower frequencies. Moreover, due to the non-ionizing property of THz

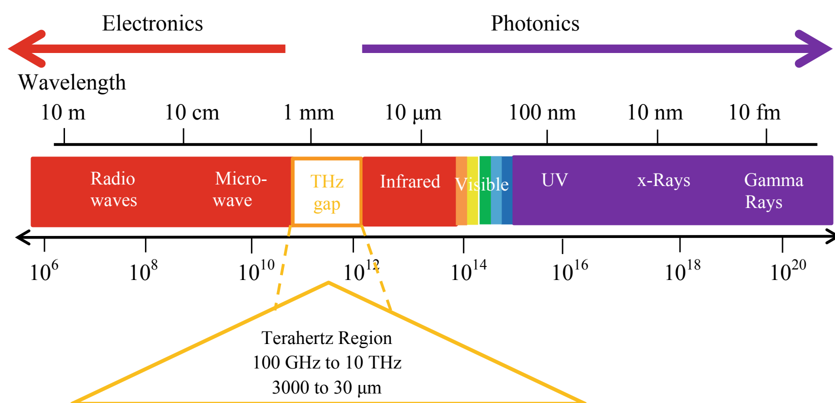

Fig. 1 Electromagnetic spectrum showing the terahertz gap

radiation other than heating, no health risks are known. Also, this type of radiation has higher sensitivity to water content and dust than mm-waves, but can still pass through different materials which are generally opaque with respect to visible light waves. Terahertz waves can pass through dielectric materials, like fabric, leather, wood, plastic, paper, etc. Also, metals reflect terahertz waves highly. Owing to these facts, THz imaging is being used in biomedical [2–4] imaging, agricultural [5, 6] applications, security and defence, technical diagnostic systems and industrial quality assurance systems.

In recent times, Terahertz technology has been selected as a major emerging technology out of ten emerging technologies which are expected to change the world by MIT Technology Review. It is predicted that the terahertz technology market will grow to $570 million in 2021 [7].

2 Terahertz Imaging Components

THz imaging systems typically require a source, different components and a detector. The source generates the THz radiation, whereas detectors detect the radiation. Components mainly include lenses, mirrors and polarizers, which manipulate the radiation. Terahertz mirrors are usually made of metal, and lenses are typically made of plastics.

However, detectors are perhaps the biggest problem in THz technology. At present, mostly photonic detectors are being used for research but again they require cooling. Among electronic solutions, Schottky diode-based heterodyne detectors have reached 3 THz and beyond [8]. Another significant problem is to generate THz signals with useful power levels. Quantum cascade lasers can generate several mW of power in the 5 THz range, but they require cooling to liquid nitrogen temperatures or below. Six major types of terahertz sources are listed by Lewis [9], which can be broadly classified as thermal [10, 11], solid-state electronic [12, 13], vacuum electronic [14–16], mechanical excitation [17, 18], lasers [19, 20] and sources pumped by lasers [21, 22]. The choice of the terahertz source depends on the type of imaging technique utilized. But it is to be remembered that sources generating low power actually needs more demanding detection devices like cryogenic cooled sensors. Now, it is seen that output power for most of the devices falls in the mid-terahertz range. However, of late different THz wave generation techniques are already available commercially, viz. THz IMPATT diodes, backward-wave oscillators, optically pumped terahertz lasers, quantum cascade lasers, etc.

However, a major limitation of terahertz imaging is the time taken to form a THz image. Image formation is normally done by acquisition of data serially for each pixel. This process is usually slow as it requires mechanical scanning of either the object [23] or of the terahertz illuminating beam [24]. As an alternative, if an array of parallel detectors can be used, the image acquisition speed can be enhanced. Usually, for frequencies below 100 GHz, conventional antenna structures with integrated electronic amplifiers at each pixel are used for array detectors [25, 26]. However, in spite of recent progress, it is still a big challenge to fabricate such integrated multi-pixel devices in the terahertz range.

Table 1 Detection schemes of terahertz non-destructive analysis [27]

Mode	Imaging parameter	2D/3D	Main methods
Passive	Power	2D	THz camera
Active transmission	Power	2D	QCL with THz camera Mapping by QCL with detector
		3D	CT by QCL with detector
	Spectroscopy	2D	Mapping by TDS Mapping by FTIR Mapping by tuneable THz light source
		3D	CT by TDS
	Phase	2D	Mapping TDS
		3D	CT by TDS
Active reflection	Power	2D	QCL with THz camera Mapping by QCL with detector
	Spectroscopy Differential time	2D 1D (depth)	Mapping by TDS Mapping by FTIR Mapping by tuneable terahertz light source TOF
		3D	Mapping TOF

Generally, THz methods may be divided into two types—active and passive. Active solutions can be either pulsed or continuous wave (CW). A comparison of various detection schemes used in non-destructive analysis technology is given in Table 1 [27].

Terahertz radiation detection systems can be broadly classified into two types: narrowband or coherent detection systems, and broadband or incoherent detection systems. In the former type of detection systems, free-space electro-optic samplings and photoconductive samplings methods are commonly used [28]. In the later type, mainly direct detectors using thermal absorption are used. The most common ones are pyroelectric infrared detectors and bolometers [29]. Since high-power radiation sources are difficult to develop and also thermal background radiation causes noise, methods to detect THz radiation needs to be highly sensitive.

3 Imaging Methods for Terahertz Waves

Several classical imaging techniques for terahertz waves, which have been developed over the past twenty years, are discussed in this section. Here, the relevant principles of image reconstruction of the following THz imaging techniques (i) terahertz time-domain spectroscopy system imaging; (ii) terahertz reflection, transmission and conductivity imaging; (iii) terahertz pulsed imaging; (iv) terahertz computed tomography; and (v) terahertz near-field imaging are discussed.

3.1 THz Time-Domain Spectroscopy System Imaging

Terahertz radiation was initially measured with the terahertz time-domain spectroscopy system. Using nonlinear optical methods or with the help of photoconductive antenna, broadband terahertz pulses are generated and detected. Using this method, it is possible to measure the amplitude as well as the phase of the THz electric field in the time domain.

As an example to obtain an image with THz-TDS, Guerboukha et al. used a transmission mode THz-TDS. They imaged a triangle constructed of high-density polyethylene (HDPE), a metallic washer and a star constructed of paper [30]. The three samples were placed on top of a sheet of paper which is surrounded by a metallic aperture made of aluminium foil. A two-dimensional image of any object can be obtained by raster-scanning the sample and by recording each point of the individual traces by a pre-collimated THz beam [30]. This results in a three-dimensional data cube, where the third dimension is time.

To obtain a hyperspectral image, the Fourier transform can be performed with respect to time. In order to convert the obtained raw data of frequency or time into some physically significant values, normalization is required [31–33]. Generally, contrast of the image is enhanced by normalization.

Figure 2 (time domain) and Fig. 3 (frequency domain) present different cases of normalizations [30]. Figure 2a shows typically acquired THz pulses across the sample. These pulses can be delayed, attenuated or broadened during interaction with the sample. The electric field amplitude at time $t_0 = 27.6$ ps is illustrated in Fig. 2b. By this technique of visualization of the electric field, the dynamics of irradiation is revealed at the picosecond scale. Again the normalized maximum peak in time domain is shown in Fig. 2c. Here, the terahertz pulse which is measured in air is used as the reference. The resultant image exhibits the reflection, scattering or absorption losses in the material. In order to generate the image which is shown in Fig. 2d, the time delay suffered by the main peak is mapped with respect to the reference measurement. Thus, the optical path change across the sample, given as $\Delta(x, y) = n(x, y)d(x, y)$, can be mapped.

Fourier transform for the third dimension of the data cube gives the amplitude and the phase of the spectrum. This is illustrated in Fig. 3a, b, respectively. A general indication of the losses can be obtained from the amplitude. The amplitude generally increases with the frequency. On the other hand, the sample refractive index and its thickness are related to the phase. It is observed that spatial resolution is proportional with the terahertz frequency. The amplitude and the phase at 0.475 THz are illustrated in Fig. 3c, d, respectively.

The maximum losses in the material occur during the propagation through the metallic washer, which is shown in the amplitude image. Again, the scattering losses are observable at the borders of the HDPE triangle. Inside the HDPE triangle and the star paper, phase image has better contrast compared to the amplitude image.

However, classical set-ups of THz-TDS for real-time operation of terahertz time-domain spectroscopy imaging systems suffer from two major problems. As already

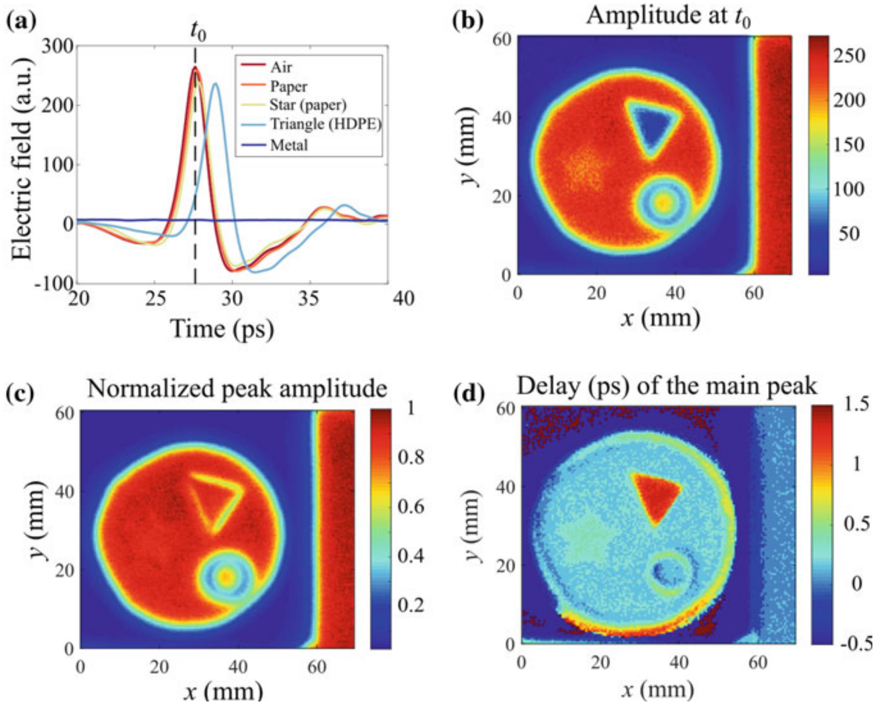

Fig. 2 **a** Typically acquired THz traces at different positions throughout the sample. **b** The electric field amplitude at $t_0 = 27.6$ ps: $E_{xy}(t_0)$. **c** Normalized amplitude of the main peak: $\max\left(\left|E_{xy}(t)\right|\right)/\max(|E_{\text{ref}}(t)|)$. **d** Delay between the main peak and a reference peak: $t\left\{\max\left[\left|E_{xy}(t)\right|\right]\right\} - t\{\max[|E_{\text{ref}}(t)|]\}$. Adapted with permission from [30] © The Optical Society

discussed in the previous section, the slow rate of THZ image formation is the first problem. This happens due to the use of single-pixel THz detectors which are easily available commercially. Hence, to produce an image, a serial point-by-point mechanical scanning of the sample is required. Alternatively, 2D THz-TDS photoconductive antenna arrays or 2D electro-optic sampling (EOS) can be used. The second problem is that, to obtain the temporal/spectral dimension, an optical delay line is required. Usually, a pair of mirrors mounted on a micropositioning stage forms the optical delay line. But it is difficult to move the delay line mechanically in real-time operation.

3.2 *Terahertz Reflection, Transmission and Conductivity Imaging*

It is seen that for a terahertz waveform, both the amplitude and the phase can be extracted in the THz-TDS measurements. The refractive index which is complex in

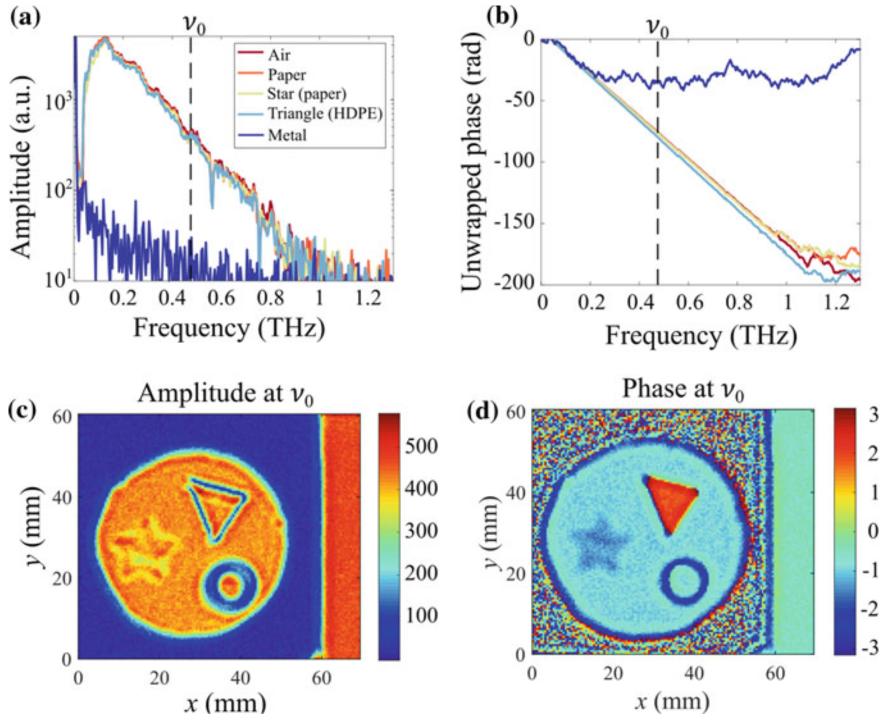

Fig. 3 **a** Amplitude, **b** unwrapped phase of the spectrum, **c** amplitude and **d** phase images at $_0 =$ 0.475 THz. Adapted with permission from [30] © The Optical Society

nature can then be obtained with appropriate numerical treatment by using the Fresnel coefficients which are expressed by the relevant refractive indices of the material. An interface is assumed between media 1 and media 2, where each media has its own refractive index given as $\tilde{n}_{1,2} = n_{1,2} - ik_{1,2}$. Now, consider that a parallel terahertz beam is passing into media 2 from media 1. So, the corresponding reflection and transmission coefficients can be expressed as

$$\text{Reflection coefficient } r_{12} = \frac{\tilde{n}_1 - \tilde{n}_2}{\tilde{n}_1 + \tilde{n}_2}$$
$$\text{Transmission coefficient } t_{12} = \frac{2\tilde{n}_1}{\tilde{n}_1 + \tilde{n}_2} \tag{1}$$

The material complex refractive indices can then be extracted by experimentally fitting the measured reflection and transmission coefficients with the corresponding analytical expressions shown in Eq. (1). In this way, the refractive index distribution across the material sample can be imaged directly. A collimated THz beam can be used, though in classical imaging normally raster scanning is done for every point

with a terahertz beam which is focused at the plane of a sample. In the following subsections, THz reflection, transmission and conductivity imaging are discussed.

3.2.1 Reflection Spectroscopy

Here, an explanation is given about how the complex sample refractive index can be extracted by interpreting the complex reflection data. A collimated THz beam is assumed. However, the same algorithm can also be used with minor modifications for THz beams which are focused and used for imaging every point. A sample with thickness l (media 3) and characterized by complex refractive index $\tilde{n}_3$ is considered [34], which is located behind media 1 and 2, characterized by complex refractive indices $\tilde{n}_1$ and $\tilde{n}_2$, respectively. It is assumed that probing terahertz wave is incident normally.

The equations for normalized reflection function (depending on polarization of the collimated THz beam as well as incidence angle) can be derived using Eq. (1). A schematic of reflection spectroscopy experimental set-up is illustrated in Fig. 4a. A window having thickness l (media 2) is placed in air (media 1), and the sample for which the study (media 3) is to be done is placed behind the window. Both THz emitter and receiver are assumed to be on the same side and a THz beam is incident normally on the sample. This set-up has been used to characterize liquids in plastic bottles [35–39]. For sufficiently thick window, the traces reflected from air–window interface, $E_{\mathrm{aw}}(\omega)$, and that reflected from window–sample interface, $E_{\mathrm{ws}}(\omega)$, can be separated in time domain. In this case for the window neglecting the Fabry–Perot effect, the normalized function for reflection can be written as

$$S_r(\omega) = \frac{E_{\mathrm{ws}}(\omega)}{E_{\mathrm{aw}}(\omega)} = \frac{t_{12}r_{23}t_{21}}{r_{12}} \exp\left(-\frac{i\tilde{n}_2\omega l}{c}\right) = \frac{4\tilde{n}_1\tilde{n}_2}{\tilde{n}_1^2\tilde{n}_2^2} \exp\left(-\frac{i\tilde{n}_2\omega l}{c}\right)\frac{\tilde{n}_2 - \tilde{n}_3}{\tilde{n}_2 + \tilde{n}_3} \quad (2)$$

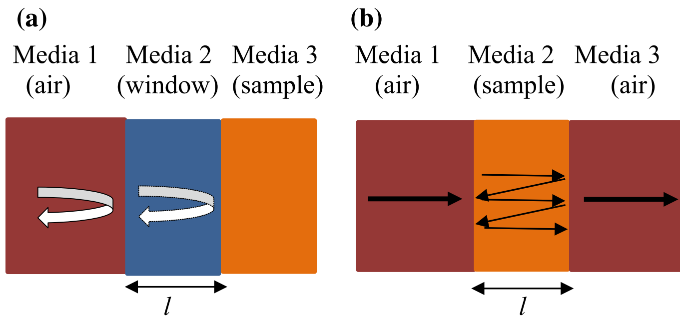

Fig. 4 Schematic experimental set-ups for measurements of **a** reflection and **b** transmission coefficients

If refractive index of media 1 is 1 (i.e. media 1 is air) and the refractive index of media 2, which is a window is $\tilde{n}_2 = \tilde{n}_w$, then Eq. (2) can be written as

$$S_r(\omega) = \frac{E_{\text{ws}}(\omega)}{E_{\text{aw}}(\omega)} = \frac{1 - \tilde{n}_w^2}{4\tilde{n}_w} \exp\left(-\frac{i\tilde{n}_w \omega l}{c}\right) \frac{\tilde{n}_w - \tilde{n}_3}{\tilde{n}_w + \tilde{n}_3} \tag{3}$$

Form Eq. (3), the unknown sample refractive index can be analytically obtained as

$$\tilde{n}_3(\omega) = \left[\frac{1 - S_r(\omega)}{1 + S_r(\omega)}\right] \tilde{n}_w(\omega) \tag{4}$$

For highly absorbing sample, reflection spectroscopy gives good results as in this case transmission of the radiation through the sample is not relied upon, but the accuracy of phase and amplitude of the reflected signal is used. Hence, the maximum coefficient of absorption depends on the SNR, which is the ratio of average signal to its standard deviation [40]. In fact, reflection geometry is used in many biomedical applications of THz waves as in the THz spectral range water shows strong absorption property [41, 42].

3.2.2 Transmission Spectroscopy

In this section, the interpretation of complex transmission data is performed to get the complex sample refractive index. In this case, the sample having thickness l (media 2) and complex refractive index $\tilde{n}_2$ is placed in between media 1 and 3, which are characterized by complex refractive indices $\tilde{n}_1$ and $\tilde{n}_3$, respectively. Similar to the previous case, it is assumed that probing THz wave is incident normally. For a collimated terahertz beam in order to get the normalized transmission function $S_t(\omega)$, it is required to perform two measurements—one is the transmission of THz beam through an empty system (without sample) $E_{\text{ref}}(\omega)$ and the other is the transmission of THz beam through the sample $E_s(\omega)$. Now, the normalized transmission function can be expressed as

$$\begin{aligned} S_t(\omega) = \frac{E_s(\omega)}{E_{\text{ref}}(\omega)} &= \frac{t_{12} t_{23} \exp\left(\frac{i\tilde{n}_2 \omega l}{c}\right)}{t_{13} \exp\left(\frac{i\tilde{n}_1 \omega l}{c}\right)} F(l, \omega) \\ &= \frac{2\tilde{n}_2(\tilde{n}_1 + \tilde{n}_3)}{(\tilde{n}_1 + \tilde{n}_2)(\tilde{n}_2 + \tilde{n}_3)} \exp\left[i(\tilde{n}_2 - \tilde{n}_1)\frac{\omega l}{c}\right] F(l, \omega) \end{aligned} \tag{5}$$

where

$$F(l, \omega) = \sum_{k=0}^{\infty} \left[r_{23} r_{21} \exp\left(\frac{i2\tilde{n}_2 \omega l}{c}\right)\right]^k = \frac{1}{1 - \left(\frac{\tilde{n}_2 - \tilde{n}_1}{\tilde{n}_2 + \tilde{n}_1}\right)\left(\frac{\tilde{n}_2 - \tilde{n}_3}{\tilde{n}_2 + \tilde{n}_3}\right) \exp\left(i2\tilde{n}_2 \frac{\omega l}{c}\right)} \tag{6}$$

is known as Fabry–Perot reflections which happens due to multiple reflections within the sample. For optically thick sample, this term may be neglected, but while characterizing thin films, this term becomes important [43]. Now, if there is sufficient separation in time among the multiple reflections, and only the wave transmitted directly is sampled during the time-domain measurement, then the sample is considered to be optically thick [34]. Again, the sample can also be considered as optically thick when the sample material loss is high enough (i.e. the exponential term in Eq. 3 $\gg 1$). In that case, the amplitude of the multiple reflected waves is very small and may be neglected.

Equation (5) may be solved in different methods [34, 44–46]. Neglecting the Fabry–Perot term neglected ($F(l, \omega) = 1$) and if the sample having refractive index $\tilde{n}_2 = \tilde{n} = (n - ik)$, is in air with refractive index $\tilde{n}_3 = \tilde{n}_1 = \tilde{n}_{\text{air}} = 1$, then Eq. (5) becomes

$$S_t(\omega) = \frac{4\tilde{n}}{(1+\tilde{n})^2} \exp\left[-k\frac{\omega l}{c}\right] \exp\left[i(n-1)\frac{\omega l}{c}\right] \tag{7}$$

Rearranging it gives

$$n(\omega) = \frac{c}{\omega l}\left\{\arg\left[\frac{(\tilde{n}+1)^2}{4\tilde{n}} S_t(\omega)\right]\right\} + 1, \tag{8}$$

$$k(\omega) = -\frac{c}{\omega l} \ln\left[\left|\frac{(\tilde{n}+1)^2}{4\tilde{n}} S_t(\omega)\right|\right] \tag{9}$$

Here, the phase of the complex number z is given by arg (z). The values for $n(\omega)$ and $k(\omega)$ in Eqs. (8) and (9) can be solved by using a fixed-point algorithm [45, 47]. For this method, initial values of $k_0(\omega)$ and $n_0(\omega)$ can be assumed which will calculate new values of $k(\omega)$ and $n(\omega)$. Using iteration, we can find a fixed point for which $k(\omega)$ and $n(\omega)$ converge. Initially, it may be assumed that $4\tilde{n}/(\tilde{n}+1)^2 = 1$ 48]. Then,

$$n_0(\omega) = \frac{c}{\omega l}\{\arg[S(\omega)]\} + 1, \tag{10}$$

$$k(\omega) = -\frac{c}{\omega l} \ln[|S(\omega)|] \tag{11}$$

For small material losses, i.e. $k \ll n$, this approximation gives a very good result.

However, for optically thick samples, complex refractive index can also be measured by using cut-back method. This technique is advantageous as without resorting to iterative algorithms, we can obtain the complex refractive index analytically. In this technique, for two sample lengths, l_1 and l_2, measurements for transmission are done. If it is assumed that there is no contribution of Fabry–Perot terms (i.e. $F(l_1, \omega) = F(l_2, \omega) = 1$, then no Fresnel coefficients will be included in the relative transmission function. Hence, transmission function can be written as

$$S_t(\omega) = \frac{E_2(\omega)}{E_1(\omega)} = \frac{t_{12}t_{23}\exp\left(\frac{i\tilde{n}\omega l_2}{c}\right)}{t_{12}t_{23}\exp\left(\frac{i\tilde{n}\omega l_1}{c}\right)} = \exp\left[i\frac{\tilde{n}\omega}{c}(l_2 - l_1)\right]$$
$$= \exp\left[-\frac{k\omega}{c}(l_2 - l_1)\right]\exp\left[i\frac{n\omega}{c}(l_2 - l_1)\right] \quad (12)$$

Now, analytically computing the complex refractive index $\tilde{n} = n + ik$ we have

$$n(\omega) = \frac{c}{\omega(l_2 - l_1)}\arg[S_t(\omega)], \quad (13)$$

$$k(\omega) = -\frac{c}{\omega(l_2 - l_1)}\ln[|S_t(\omega)|] \quad (14)$$

However, the maximum dynamic range of the THz-TDS system is the limiting factor for transmission spectroscopy.

3.2.3 Conductivity Imaging

To electrically characterize a material, it is often required to find out the complex permittivity for the material. Here, the technique of extraction of electrical properties of a material from the complex refractive index is discussed. Through THz-TDS, the complex permittivity can be measured easily by the contactless experimental set-up. We can obtain the complex permittivity $\tilde{\varepsilon}(\omega)$ as [49, 50]:

$$\tilde{\varepsilon}(\omega) = \varepsilon_1(\omega) + i\varepsilon_2(\omega) = 1 + i\frac{\tilde{\sigma}}{\varepsilon_0\omega},$$
$$\varepsilon_1(\omega) = n(\omega)^2 - k(\omega)^2,$$
$$\varepsilon_2(\omega) = 2n(\omega)k(\omega) \quad (15)$$

Complex conductivity $\tilde{\sigma}(\omega)$ relates the complex permittivity as $\tilde{\varepsilon}(\omega) = 1 + i\tilde{\sigma}(\omega)/\varepsilon_0\omega$, where ε_0 is the permittivity of vacuum. Hence,

$$\tilde{\sigma}(\omega) = \sigma_1(\omega) + i\sigma_2(\omega),$$
$$\sigma_1(\omega) = \varepsilon_0\varepsilon_2(\omega)\omega,$$
$$\sigma_2(\omega) = -[\varepsilon_1(\omega) - 1]\varepsilon_0\omega \quad (16)$$

Also, by using THz pulses, the dynamics of the charge carrier can be understood at the picosecond time scale. Time-resolved terahertz spectroscopy (TRTS) is also named as optical-pump–THz-probe spectroscopy. Here, the charge carrier in the sample is photo-excited by an optical pump. An optical delay line is used with the THz pulse to probe the transient conductivity of the material. To study conductive materials, this method is often used.

Similar to the THz-TDS imaging system, challenges are faced for real-time THz spectroscopy and conductivity imaging. To acquire images faster, a 2D array detector is required, and also by using a fast optical delay line, it is required to obtain the spectrum rapidly. Again, for operation in real-time problems may occur as to find out the complex refractive index, iterative algorithms are needed. But sometimes solutions can be obtained analytically.

3.3 THz Pulsed Imaging

In this technique, the times required by the THz pulses to arrive at the detector are measured. This is also named as time-of-flight imaging (TOF). In fact, the time delay among the reflected pulses helps to understand the sample internal structure. Here, the measurement is performed using reflection geometry.

Initially, THz pulse imaging was demonstrated by capturing image of the internal structure of a 3.5 in. floppy disk [51]. In this technique, the time delay of the pulse Δt is directly related to the optical path travelled by the pulse. It is considered that the refractive index n does not change over the entire THz frequency range under consideration. In such a case, the distance d between the sample surface and the sample internal surface can be calculated by measuring the time delay between the pulses reflected from the sample surface and the sample internal surface, respectively. The distance can be calculated from the following expression:

$$d = \frac{c\Delta t}{2n} \tag{17}$$

THz pulse imaging technique has practical applications in various fields like in art conservation, pharmaceutical industry, etc. to name a few. As a non-destructive method in the field of art conservation, THz pulsed imaging has been used to study the layers of paint in ancient masterpieces [52–56]. By using THz imaging technique, the hidden information from different paintings can be investigated. By X-ray imaging technique also the same investigation is possible, but as X-ray has ionizing property, it may destroy layers of paint and also radiometric dating may be compromised by this. Additionally, it is to be noted that THz pulsed imaging technique provides supplementary information like the paint thickness, whereas X-ray basically investigates the paint losses. Another very important application of TPI has been demonstrated in the pharmaceutical industry [57–60]. Since most of the dry tablets are semi-transparent to THz radiation, it is possible to take images of the tablets up to high penetration depths. This proves to be very beneficial in the quality control of the tablets.

However, for real-time imaging, several things are to be taken care of. In this technique, optical delay line is a very important component as the TPI method detects the reflected echoes generated in the temporal data of the THz-TDS system. Mechanical

movement of the sample can be avoided by using 2D arrays for faster image acquisition. Again, it is to be kept in mind that for a sample having multiple layers, multiple reflections occur with THz imaging technique. Hence, some manual intervention is also required to identify the temporal intervals which occur due to the distinct reflected echoes. However, in order to get rid of human intervention, mechanisms involving artificial intelligence can be developed.

3.4 THz Computed Tomography

Of late 3D imaging technology is becoming a field of active research. For THz imaging, it opens up a new possibility, as many materials happen to be quite transparent to THz waves. Owing to this, the internal structure of a material can be revealed by 3D THz imaging technique like THz computed tomography (THz-CT). The technique is similar to the X-ray CT which is often used in the biomedical applications.

A set-up for THz-CT is considered. It is assumed that the THz beam incident onto a sample is parallel in mature and is suffering from local optical losses which may be considered to be distributed following $f(x, y)$. An auxiliary function is defined as $g(x, y) = -f(x, y)$. Here, (x, y) are the coordinates in the local coordinate system which is associated with the sample. A rotational stage rotated by an instantaneous angle θ is considered on which a sample is placed. Then, with the sample rotation, the detector moves by distance d along a fixed line. In this procedure, a sinogram $P(\theta, t)$ is constructed. Here, the sinogram physically shows some measure of the cumulative optical loss which occurs as because of transmission through the sample along a certain straight line $L(\theta, t)$ defined by the detector position and the stage rotation angle [61]:

$$P(\theta, t) = \int_{L(\theta,t)} g(x, y)\mathrm{d}l \tag{18}$$

The operation shown in Eq. (18) is called Radon transform. It is the line integral over $L(\theta, t)$. The detector is rotated and moved laterally, and the sinogram is measured. By computing the inverse Radon transform, the original object is reconstructed.

There is a basic difference between X-ray CT and THZ-CT. In X-ray CT, we see that the size of wavelength (~nm) is quite smaller compared to the size of the object (~mm). Hence, self-diffraction of the illuminating beam can be ignored and can be considered as strictly parallel. But the focusing optics diameter size in THz-CT is of the order of ~10 cm, while the wavelength of THz light can be maximally several mm. Hence, in THz range, for better reconstructions, Gaussian beam approximation is to be used in the propagation model instead of parallel beam approximation [62]. Recur et al. showed that a non-diffractive Bessel THz beam improved the quality of the reconstruction [63]. It is to be noted that in X-ray CT, measurement is done only for

losses occurring due to absorption, but in THz-CT, for non-uniform samples having a large refractive index, losses occurring due to reflection and refraction become important.

However, it is challenging to perform real-time THZ-CT as it is required to measure the sample angular rotation also. But to reconstruct the internal structure of an object, the time-domain/spectral information is not required for THz-CT. Alternatively, techniques can be used where only the transmitted amplitude/intensity THz radiation is required.

3.5 THz Near-Field Imaging

Far-field imaging system can show resolution for only features of an object which are comparable to or larger than the wavelength of the THz beam used. To have resolution for subwavelength features of the object, near-field region imaging system has to be incorporated. Thus, detection of the evanescent fields at small distances from the object is required. This imaging technique is called THz near-field imaging [64–67]. Different techniques have been used for subwavelength THz imaging.

A pair of apertures (pinholes) is used in the confocal THz near-field imaging technique. This acts as a spatial filter to restrict terahertz radiation passing out of the cone of light. This increases the resolution for both lateral and depth features [68–71]. The pinhole diameter can be reduced to improve the lateral resolution. But, the diameter can be reduced only up to a certain threshold limit, below which no signal is collected at all.

On the other hand, more throughput light intensity can be obtained in solid-lens immersion approach. In this technique, a lens is used which is designed specially to generate a smaller spot size compared to the diffraction limit in the evanescent field region following the lens. Chernomyrdin et al. [72] used a combination of a truncated sphere and an aspheric lens, and at 0.5 THz, they achieved a resolution of $\lambda/3.1$, which is obviously better than the resolution ($\lambda/1.2$) of a simple aspheric lens. However, in this case, the properties of the material of the immersion lens fundamentally limit the spatial resolution.

The sample is placed in contact with a subwavelength detector in the direct-contact method. Here, the detector is a femtosecond optical beam which investigates the change of polarization in a nonlinear crystal. In this case, it is possible to measure the THz electric field directly in the near-field region since the crystal is in direct touch with the sample. This technique can be used for real-time near-field THz imaging. Recently, technology of SiGe heterojunction bipolar transistor has been used by Grzyb et al. [73] for direct-contact near-field imaging. Most of the techniques for real-time near-field imaging depend on the scanning of subwavelength apertures mechanically, which makes it difficult for the acquisition of multiple images.

4 Terahertz Imaging Cameras

For a lot of scientific as well as engineering applications, one of the primary requirements is cost-effective imaging. But unfortunately for a long time, THz frequency range lacked an inexpensive and efficient imaging device. However, recently intensive research is going on to develop THz cameras. But before these types of cameras become universally acceptable, they have to satisfy some requirements. Firstly, the total power consumption by a THz camera should not be high and also the size and weight should not be large so that they may be integrated into industrial imaging systems. Secondly, the process of fabrication of the terahertz cameras has to be in line with modern fabrication techniques. Thirdly, while high sensitivity of the THz cameras is still retained, techniques need to be introduced so that systems can operate at room temperatures and thus the expensive and cumbersome cryogenic cooling systems can be avoided. Last but not the least, a THz camera has to be highly sensitive so it is possible to record high frame rate THz videos. However, in most available THz cameras, only intensity can be detected, whereas ideally complex electric fields have to be detected. However, one of the major disadvantages is the scarcity of cheap, high-power THz sources

Generally, the responsivity and the noise-equivalent power (NEP) are two essential figures of merit of any detector. Noise-equivalent power or NEP is the measure of the minimum power that can be detected, and is defined as the input power that gives SNR $= 1$, with a 1 Hz bandwidth output. A lower NEP indicates a more sensitive detector. On the other hand, responsivity is the direct detector response (either in amperes or volts) to the incident power of the THz radiation (in watts). It is expressed in A/W or V/W. The total incident power is to be measured to measure the responsivity. If it is assumed that all incident THz radiation is captured by the imaging array in a THz camera, then per pixel responsivity can be calculated by dividing the summation of the voltages of all the pixels by the total incident power. Generally, a higher responsivity indicates a better performing detector. In recent literatures, two main types of THz cameras are reported. They are THz FET-based cameras and THz thermal cameras.

4.1 Terahertz FET-Based Cameras

Rectification in the field-effect transistor (FET) is a major technological trend in terahertz cameras. Response at frequencies much higher than the cut-off frequency of the transistor is enabled by plasma wave excitations. Theoretical demonstration shows that for THz detection plasma waves could be used in the FET channel [74]. A schematic representation of the proposed FET for detection of THz radiation is illustrated in Fig. 5. From the figure, it is seen that between the source and the gate a DC voltage U_0 is applied. However, an alternating voltage U_a is caused by the incident THz radiation. A constant drain-to-source voltage is generated due to the

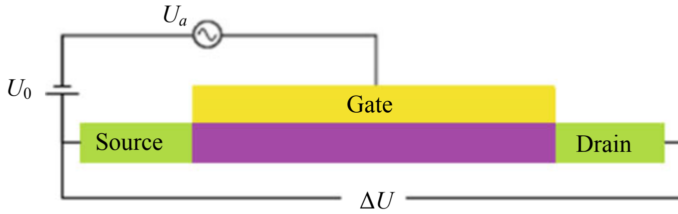

Fig. 5 Schematic representation of THz detection by the field-effect transistor

nonlinear properties of the plasma waves and the asymmetric boundary conditions, and is given as $\Delta U \propto U_a^2$.

Predictions were done about the resonant (frequency-specific) and non-resonant (broadband) detection mechanisms with reference to the electron momentum relaxation time τ. The resonant case occurs when $\omega\tau > 1$, i.e. the channel conductivity is large for incident THz radiation of frequency ω. If the length l of the channel is sufficiently small, the plasma waves travel to the drain side of the channel and then reflect back. Thus, a standing wave is created. Then between the drain and the source, a wavelength-specific DC voltage is developed [74]:

$$\Delta U^R = \frac{e\tau^2}{l^2 m}\left[\frac{U_a^2}{4(\omega - m\omega_0)^2\tau^2 + 1}\right] \tag{19}$$

where $m = 1, 3, 5, 7, \ldots$.

When $\omega\tau < 1$, i.e. in the non-resonant case, the plasma waves fail to reach fully to the opposite side of the channel of the transistor as they are overdamped. Here, a DC photoresponse between the source and the drain exists which is given as [75]:

$$\Delta U^{\text{NR}} = \frac{U_a^2}{4U_0}\left[1 - \exp(-2x/l_c)\right] \tag{20}$$

Here, the source distance is given by x and the characteristic decay length is indicated by l_c. Silicon FETs exhibit broadband detection of this type. NEP of silicon FETs comparable to conventional THz detectors operating at room temperature was shown by Tauk et al. [76]. An efficient 3 × 5 pixel array of FET detectors was designed by Lisauskas et al. using 250 nm CMOS process technology [77]. In their system, every pixel had a patch antenna designed to operate at 0.65 THz. A minimum NEP value of 300 $\text{pW}/\sqrt{\text{Hz}}$ was achieved by attaching the system to a FET detector and a voltage amplifier. The inner side of an envelope was imaged by them.

4.2 Terahertz Thermal Cameras

Terahertz thermal cameras detect the generated heat due to incident THz radiation. Generally, three types of THz radiation thermal detectors are available: (1) pyroelectric sensors; (2) Golay cells; and (3) bolometers. The detectors are generally used with a modulated source for reducing the ambient noise. However, at the same time, the possible overall maximum frame rate at room temperature is also reduced. On the contrary, the spectral range of operation of thermal detectors is broad, and this is an advantage.

Pyroelectric crystals are those crystals for which electrical polarizability changes when heated. The changes can be detected by pyroelectric sensors. Actually, a temporary voltage is generated when the heat is transferred to the crystal by an absorbing layer. Some common examples of pyroelectric crystals are lithium tantalite ($LiTaO_3$), barium titanate ($BaTiO_3$), triglycine sulphate (TGS) and deuterated triglycine sulphate (DTGS). Among these, the highest sensitivities at THz frequencies are exhibited by TGS and DTGS [78], for which at a modulation frequency of ~10 Hz, typical NEP and responsivity are $1\,\mathrm{nW}/\sqrt{\mathrm{Hz}}$ and ~1 kV/W, respectively. Fortunately pyroelectric detectors are available as array cameras commercially [79]. The pyroelectric detector sensitivity can be improved by increasing absorption of THz radiation in the coating layer of the crystal and by reducing the thickness of the crystal. For commercial pyroelectric cameras, minimum detectable power is typically in the range between 50 and 100 nW [30].

The Golay cell is used mainly for infrared spectroscopy. It is a type of opto-acoustic detector. A gas-filled enclosure with a material for absorbing infrared radiation and a flexible diaphragm or membrane is integral part of Golay cell. The generated heat is transferred to the expanding gas cell in Golay cells. Then, optical method of moving mirrors is used to measure the increased pressure [80]. However, as Golay cells depend on the movement of the membrane mechanically, they are generally slow detectors. As the operating principle of Golay cells are quite simple, they are used widely for measuring power of THz radiation. But to integrate Golay cells into dense arrays of detectors is difficult, and this makes them suitable in single-pixel detection scheme. Typical Golay cells NEP range between 0.1 and $10\,\mathrm{nW}/\sqrt{\mathrm{Hz}}$ [30].

Thermal bolometers are used as individual pixels in another type of THz cameras. Bolometer imaging arrays have generated much interest in real-time terahertz imaging as they are highly sensitive and their fabrication technology is also established. In this technique, bolometer pixel measures the changes in resistance which is dependent on temperature [30]. The primary constituents of a bolometer as described by Richards [81] have been shown in Fig. 6a.

The THz beam radiation power P_{THz} falls on an absorber having heat capacity C_{A}. This is again connected to a heat sink at temperature T_{s} via a thermal link of conductance G_{L}. The temperature of the absorber T_{A} rises at a rate $\mathrm{d}T_{\mathrm{A}}/\mathrm{d}t = P_{\mathrm{THz}}/C_{\mathrm{A}}$ to the limiting value $T_{\mathrm{A}} = T_{\mathrm{s}} + \frac{P_{\mathrm{THz}}}{G_{\mathrm{L}}}$, with the thermal time constant $\tau = C_{\mathrm{A}}/G_{\mathrm{L}}$. Figure 6b shows that on turning off the illumination, the temperature

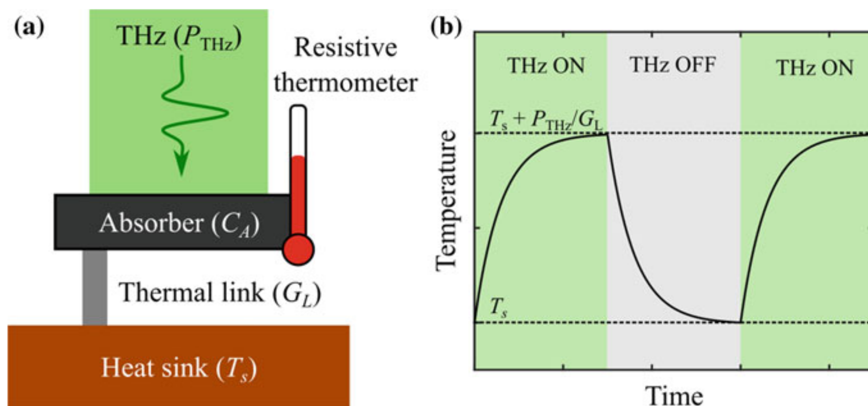

Fig. 6 **a** Primary components of the bolometer. **b** Rise and fall of the temperature in the absorber as a function of time. Adapted with permission from [30] © The Optical Society

T_A relaxes back with the same time constant to T_s. A resistive thermometer which is connected to the absorber measures the change in temperature as shown in Fig. 6a.

Advantage of microbolometers is that their operation principle is not wavelength-specific. So, microbolometers which were initially used for real-time THz imaging were actually commercial microbolometers designed for infrared radiation [82–85]. Actually, microbolometers happen to be arrays of bolometers which are mounted onto readout integrated circuits for focal-plane camera operation. Of late, microbolometers which can operate in the THz range were specifically designed. In fact, they achieved NEP in the range of $10^{-16}\,\mathrm{W}/\sqrt{\mathrm{Hz}}$ [86], when background thermal noise was removed by cooling at cryogenic temperatures. However, microbolometers can show high sensitivities even at room temperatures with proper design modifications. This opens the possibility of using them for various industrial imaging applications. Several research works are being carried on in this regard on increasing sensitivity and faster response time of the detectors. In the sub-THz region, generally the microbolometers are underperforming, and hence to increase the sensitivity, resonant cavity structure [87] was used. To develop a very fast-operating real-time spectrometer, microbolometer was used in conjunction with a diffraction grating [88]. In order to increase the terahertz radiation, absorption metamaterials are also investigated [89–93].

5 Applications

Wide ranges of applications are opening up with advances of terahertz sources and detection techniques. In this section, few THz applications from different research areas are discussed. Some very interesting imaging applications in THz region is found in the areas of medical applications like 2D and 3D imaging, which includes

medical diagnosis of the structure of tooth, skin cancer and tumours, security imaging, inspection of semiconductor, food, pharmaceutical and very-high bandwidth communications. Also, materials research and computing applications are gaining attention.

5.1 Biomedical Applications

Already properties of terahertz radiation have been discussed that they have very low photon energy, sensitivity to water and characteristic spectral signatures for many substances. This makes THz imaging suitable for many biomedical applications. It is already mentioned that owing to the non-ionizing character of terahertz radiation, this is less harmful to living tissues than X-ray. This unique feature makes THz imaging an interesting candidate for medical applications including cancer diagnosis [2]. Imaging the structure of teeth and the identification of dental caries is another area where terahertz imaging can be used as an alternative to other diagnostic technologies [94]. Wound assessment is also another interesting application, where the terahertz reflection pulse imaging technique can image skin through wound dressings [95]. Also, TPI has the potential to image both ductal carcinoma and invasive breast carcinomas, and this has been discussed by Pickwell and Wallace [4]. Using seven oral tissues, oral cancer has been detected by terahertz imaging [96]. Different dental tissues can also be distinguished by TPI and hence 3-D information can be gathered [97, 98].

5.2 Security Applications

Active military research is underway to develop THz imaging for different security applications. Specific security-related applications such as detecting illicit drugs [99–101], weapons and explosive devices [102–105], including the important task of land mine detection, are some potential applications of THz imaging. Though metallic packages are opaque to THz waves, still dangerous concealed metallic weapons like guns [106] or knives can be identified by their shapes using pattern recognition algorithm. This is why at present it is not possible to completely substitute X-ray scanners by THz spectrometers. But supplementary information about the sample is provided by THz spectrometers. THz imaging can detect even liquid explosives [37].

5.3 Food Industry

Food industry all over the world is suffering from potential hazards of contaminations. THz systems can detect both non-metallic and metallic contaminations [107]. Even the presence of different non-metallic and metallic inclusions within low water content foodstuff like chocolate bars can also be detected using THz imaging [108]. In the fresh food industry with packaging protection, the study of moisture quantification can also be an interesting application. Cardboard and plastic are transparent in the THz waveband. Utilizing this property, foreign object inside packaging is detected. Detection of potentially harmful contaminants such as pieces of wood, plastic, stone, glass or metal in food is one of the most important problems for the food industry. Terahertz technology can detect the presence of metallic as well as non-metallic materials in food items.

5.4 Art Conservation

To preserve cultural heritage artworks efficiently, it is required to have knowledge of materials science. Challenges are faced by THz technology in developing non-destructive analytical methods and to integrate it with new diagnostic techniques. However, THz investigations of mural paintings are performed [109]. Using THz-TDS technique, it is detected by Abraham et al. that a graphite drawing was present [110] under paint and plaster layers. Images of THz reflection from hidden paint layers [111] have been compared. Recently, THz imaging is used for the study of mummies also [112].

5.5 Pharmaceutical Industry

Recently, it is seen that the THz imaging has applications in the pharmaceutical industry [57, 59]. A lot of chemicals show characteristic spectral fingerprints in the terahertz waveband. This property may be used to identify and detect unwanted contamination at the time of production of drugs in the pharmaceutical industry [113]. THz is also suitable for quality control of tablet coatings [114].

5.6 Polymer and Paper Industries

Current trends in the areas of quality control and technical diagnostic applications demand non-destructive THz imaging. Its core uses are seen in the polymer and paper industries. THz systems can be utilized in polymer and paper industries to control

online production [115]. At the time of paper production, both moisture content and thickness need to be monitored. Technique to differentiate two different samples of paper by THz with similar accuracy to other sensors has been shown [116]. In the polymer industry, online supervision of polymeric processes, conductive properties, the fibre orientation, etc. has been demonstrated by terahertz systems. Most of the polymeric materials appear to be transparent for terahertz radiation. By measuring the decreasing THz transmission, wood polymer composites can be examined by THz spectroscopy to monitor the increase in water content within the material.

6 Conclusion

Though THz technology has gained boost with invent of various sources and detectors, however, many aspects have to be considered to implement THz technology on a commercial basis. At room temperatures, blackbody radiation is present at THz frequencies and hence detection of terahertz signals becomes difficult. SNR for terahertz images can be improved by mechanically scanning the sample each pixel-wise by using a coherent source. But, this is possible only for static objects. As it has already been discussed, that to overcome such an issue, imaging array is to be used. Again atmospheric transmission is a big concern for THz imaging, as the attenuation suffered by THz radiation in the atmosphere is much more severe compared to other spectral regions [117]. Appropriate optics selection for imaging systems is another major problem in THz domain. One of the major limitations of terahertz systems is the difficulty to construct advanced lenses. Similar to any other imaging systems, the diffraction phenomenon also limits THz solutions.

References

1. M. Mittleman Daniel, Twenty years of terahertz imaging. Opt. Express **26**(8), 9417–9431 (2018)
2. C. Yu, S. Fan, Y. Sun, E. Pickwell-Macpherson, The potential of terahertz imaging for cancer diagnosis: a review of investigations to date. Quant. Imaging Med. Surg. **2**(1), 33–45 (2012)
3. Z.D. Taylor, J. Garritano, S. Sung, N. Bajwa, D.B. Bennett, B. Nowroozi, P. Tewari, J.W. Sayre, J.P. Hubschman, S.X. Deng, E.R. Brown, W.S. Grundfest THz and mm-wave sensing of corneal tissue water content: in vivo sensing and imaging results. IEEE Trans. THz Sci. IEEE Trans. Terahertz Sci. Technol. **5**(2), 184–196 (2015)
4. E. Pickwell, V.P. Wallace, Biomedical applications of terahertz technology. J. Phys. D Appl. Phys. **39**(17), R301–R310 (2006)
5. S. Hadjiloucas, L.S. Karatzas, J.W. Bowen, Measurements of leaf water content using terahertz radiation. IEEE Trans. Microw. Theory Tech. **47**(2), 142–149 (1999)
6. M. Koch, S. Hunsche, P. Schumacher, M.C. Nuss, J. Feldmann, J. Fromm, THz-imaging: a new method for density mapping of wood. Wood Sci. Technol. **32**(6), 421–427 (1998)
7. J.H. Teng, A. Maier Stefan, D.D. Willis Karl, *9 Disruptive Technologies Changing The World*. Report 2015 (PreScouter Inc., 2015), p. 73

8. "Terahertz (THz) Technology: An Introduction and Research Update", High Frequency Electronics Copyright © 2008 Summit Technical Media, LLC (February 2008)
9. R.A. Lewis, A review of terahertz sources. J. Phys. D Appl. Phys. **47**, 374001 (2014)
10. C. Thacker, A. Cooray, J. Smidt, F. De Bernardis, K. M-Wynne, A. Amblard, R. Auld, M. Baes, D.L. Clements, A. Dariush, G. De Zotti, L. Dunne, S. Eales, R. Hopwood, C. Hoyos, E. Ibar, M. Jarvis, S. Maddox, M.J. Michalowski, E. Pascale, D. Scott, S. Serjeant, M.W.L. Smith, E. Valiante, P. van der Werf, H-Atlas: the cosmic abundance of dust from the far-infrared background power spectrum. The Astrophysical J. **768**, 58 (2013)
11. V.M. Zolotarev, R.K. Mamedov, A.N. Bekhterev, B.Z. Volchek, Spectral emissivity of a globar lamp in the 2–50 μm region. J. Opt. Technol. **74**(6), 378–384 (2007)
12. S. Pérez, T. González, D. Pardo, J. Mateos, Terahertz Gunn-like oscillations in GaAs/InAlAs planar diodes. Appl. Phys. Lett. **103**, 094516 (2008)
13. A. Maestrini, J.S. Ward, J.J. Gill, C. Lee, B. Thomas, R.H. Lin, G. Chattopadhyay, I. Mehdi, A frequency-multiplied source with more than 1 mW of power across the 900-GHz band. IEEE Trans. Microw. Theory Tech. **58**(7), 1925–1932 (2010)
14. W. He, C.R. Donaldson, L. Zhang, K. Ronald, P. McElhinney, A.W. Cross, High power wideband gyrotron backward wave oscillator operating towards the terahertz region. Phys. Rev. Lett. **110**, 165101 (2013)
15. V.L. Bratman, Y.K. Kalynov, V.N. Manuilov, Large-orbit gyrotron operation in the terahertz frequency range. Phys. Rev. Lett. **102**, 245101 (2009)
16. J.M. Byrd, W.P. Leemans, A. Loftsdottir, B. Marcelis, Michael C. Martin, W.R. McKinney, F. Sannibale, T. Scarvie, C. Steier, Observation of broadband self-amplified spontaneous coherent terahertz synchrotron radiation in a storage ring. Phys. Rev. Lett. **89**, 224801 (2002)
17. J. Horvat, R.A. Lewis, Peeling adhesive tape emits electromagnetic radiation at terahertz frequencies. Opt. Lett. **34**, 2195–2197 (2009). https://doi.org/10.1364/OL.34.002195
18. D.L. Cortie, R.A. Lewis, Terahertz surfoluminescence. Surf. Sci. **606**, 1573–1576 (2012)
19. Y. Chassagneux, R. Colombelli, W. Maineult, S. Barbieri, H.E. Beere, D.A. Ritchie, S.P. Khanna, E.H. Linfield, A.G. Davies, Electrically pumped photonic-crystal terahertz lasers controlled by boundary conditions. Nature **457**, 174–178 (2009)
20. B.S. Williams, Terahertz quantum-cascade lasers. Nat. Photonics **1**, 517–525 (2007)
21. X.L. Wu, S.J. Xiong, Z. Liu, J. Chen, J.C. Shen, T.H. Li, P.H. Wu, Paul K. Chu, Green light stimulates terahertz emission from mesocrystal microspheres. Nat. Nanotechnol. **6**, 103–106 (2011)
22. G. Jotzu, M. Cooper, P. Parkinson, M.B. Johnston, Virtual terahertz spectrometer (2009). https://www.thz.physics.ox.ac.uk
23. B.B. Hu, M.C. Nuss, Imaging with terahertz waves. Opt. Lett. **20**(16), 1716–1719 (1995)
24. K. Serita, S. Mizuno, H. Murakami, I. Kawayama, Y. Takahashi, M. Yoshimura, Y. Mori, J. Darmo, M. Tonouchi, Scanning laser terahertz near-field imaging system. Opt. Express **20**(12), 12959–12965 (2012)
25. J.J. Lynch, P.A. Macdonald, H.P. Moyer, R.G. Nagele, Passive millimeter wave imaging sensors for commercial markets. Appl. Opt. **49**(19), E7–E12 (2010)
26. V.G. Kolinko, S.H. Lin, A. Shek, W. Manning, C. Martin, M. Hall, O. Kirsten, J. Moore, D.A. Wikner, A passive millimeter-wave imaging system for concealed weapons and explosives detection. Proc. SPIE **5781**, (Optics and Photonics in Global Homeland Security, 2005), pp. 85–92. (19 May 2005)
27. H. Song, T. Nagatsuma, *Handbook of Terahertz Technologies: Devices and Applications*. 1st edn. (Jenny Stanford Publishing, 2015), p. 565
28. W.L. Chan, J. Deibel, D.M. Mittleman, Imaging with terahertz radiation. Rep. Prog. Phys. **70**, 1325 (2007)
29. Lee C. H. *Microwave Photonics*. 2nd edn. (CRC Press, 2013), p. 441
30. H. Guerboukha, K. Nallappan, M. Skorobogatiy, Toward real-time terahertz imaging. Adv. Opt. Photonics **10**(4), 843–938 (2018)
31. A.J. Fitzgerald, Classification of terahertz-pulsed imaging data from excised breast tissue. J. Biomed. Opt. **17**, 016005 (2012)

32. T. Löffler, K. Siebert, S. Czasch, T. Bauer, H.G. Roskos, Visualization and classification in biomedical terahertz pulsed imaging. Phys. Med. Biol. **47**, 3847–3852 (2002)
33. J.P. Guillet, B. Recur, L. Frederique, B. Bousquet, L. Canioni, I. Manek-Hönninger, P. Desbarats, P. Mounaix, Review of terahertz tomography techniques. J. Infrared Millim. Terahertz Waves **35**, 382–411 (2014)
34. L. Duvillaret, F. Garet, J.L. Coutaz, A reliable method for extraction of material parameters in terahertz time-domain spectroscopy. IEEE J. Sel. Top. Quantum Electron. **2**, 739–746 (1996)
35. L. Thrane, R.H. Jacobsen, P.U. Jepsen, S.R. Keiding, THz reflection spectroscopy of liquid water. Chem. Phys. Lett. **240**, 330–333 (1995)
36. P.U. Jepsen, B.M. Fischer, Dynamic range in terahertz time-domain transmission and reflection spectroscopy. Opt. Lett. **30**, 29–31 (2005)
37. P.U. Jepsen, U. Møller, H. Merbold, Investigation of aqueous alcohol and sugar solutions with reflection terahertz time-domain spectroscopy. Opt. Express **15**, 14717–14737 (2007)
38. P.U. Jepsen, J.K. Jensen, U. Møller, Characterization of aqueous alcohol solutions in bottles with THz reflection spectroscopy. Opt. Express **16**, 9318–9331 (2008)
39. U. Møller, D.G. Cooke, K. Tanaka, P.U. Jepsen, Terahertz reflection spectroscopy of Debye relaxation in polar liquids. J. Opt. Soc. Am. B **26**, A113–A125 (2009)
40. M. Naftaly, R. Dudley, Methodologies for determining the dynamic ranges and signal-to-noise ratios of terahertz time-domain spectrometers. Opt. Lett. **34**, 1213–1215 (2009)
41. R.M. Woodward, B.E. Cole, V.P. Wallace, R.J. Pye, D.D. Arnone, E.H. Linfield, M. Pepper, Terahertz pulse imaging in reflection geometry of human skin cancer and skin tissue. Phys. Med. Biol. **47**, 3853–3863 (2002)
42. S. Fan, Y. He, B.S. Ung, E. Pickwell-MacPherson, The growth of biomedical terahertz research. J. Phys. D **47**, 374009 (2014)
43. J.F. O'Hara, W. Withayachumnankul, I. Al-Naib, A review on thin-film sensing with terahertz waves. J. Infrared Millim. Terahertz Waves **33**, 245–291 (2012)
44. P.H. Bolivar, M. Brucherseifer, J.G. Rivas, R. Gonzalo, I. Ederra, A. Reynolds, M. Holker, P. de Maagt, Measurement of the dielectric constant and loss tangent of high dielectric constant materials at terahertz frequencies. IEEE Trans. Microw. Theory Tech. **51**, 1062–1066 (2003)
45. M. Naftaly, R.E. Miles, Terahertz time-domain spectroscopy for material characterization. Proc. IEEE **95**, 1658–1665 (2007)
46. I. Pupeza, R. Wilk, M. Koch, Highly accurate optical material parameter determination with THz time-domain spectroscopy. Opt. Express **15**, 4335–4350 (2007)
47. M. Hangyo, T. Nagashima, S. Nashima, Spectroscopy by pulsed terahertz radiation. Meas. Sci. Technol. **13**, 1727–1738 (2002)
48. W. Withayachumnankul, B. Ferguson, T. Rainsford, S.P. Mickan, D. Abbott, Simple material parameter estimation via terahertz time-domain spectroscopy. Electron. Lett. **41**, 800–801 (2005)
49. J. Lloyd-Hughes, T.I. Jeon, A review of the terahertz conductivity of bulk and nano-materials. J. Infrared Millim. Terahertz Waves **33**, 871–925 (2012)
50. F.A. Hegmann, O. Ostroverkhova, D.G. Cooke, Probing organic semiconductors with terahertz pulses, in *Photophysics of Molecular Materials* (Wiley, 2006), pp. 367–428
51. D.M. Mittleman, S. Hunsche, L. Boivin, M.C. Nuss, T-ray tomography. Opt. Lett. **22**, 904–906 (1997)
52. A.J.L. Adam, P.C.M. Planken, S. Meloni, J. Dik, Terahertz imaging of hidden paint layers on canvas, in *34th International Conference Infrared, Millimeter, Terahertz Waves (IRMMW-THz)*, vol. 17, pp. 904–906 (2009)
53. A. Cosentino, Terahertz and cultural heritage science: examination of art and archaeology. Technologies **4**, 1–13 (2016)
54. C. Seco-Martorell, V. López-Domínguez, G. Arauz-Garofalo, A. Redo-Sanchez, J. Palacios, J. Tejada, Goya's artwork imaging with terahertz waves. Opt. Express **21**, 17800–17805 (2013)
55. E. Abraham, K. Fukunaga, Terahertz imaging applied to the examination of artistic objects. Stud. Conserv. **60**, 343–352 (2015)

56. K. Fukunaga, M. Picollo, Terahertz spectroscopy applied to the analysis of artists' materials. Appl. Phys. A **100**, 591–597 (2010)
57. Y.-C. Shen, Terahertz pulsed spectroscopy and imaging for pharmaceutical applications: a review. Int. J. Pharm. **417**, 48–60 (2011)
58. J. Sibik, J.A. Zeitler, Direct measurement of molecular mobility and crystallisation of amorphous pharmaceuticals using terahertz spectroscopy. Adv. Drug Deliv. Rev. **100**, 147–157 (2016)
59. J.A. Zeitler, P.F. Taday, D.A. Newnham, M. Pepper, K.C. Gordon, T. Rades, Terahertz pulsed spectroscopy and imaging in the pharmaceutical setting—a review. J. Pharm. Pharmacol. **59**, 209–223 (2007)
60. M. Haaser, K.C. Gordon, C.J. Strachan, T. Rades, Terahertz pulsed imaging as an advanced characterisation tool for film coatings—a review. Int. J. Pharm. **457**, 510–520 (2013)
61. A. Brahm, M. Kunz, S. Riehemann, G. Notni, A. Tünnermann, Volumetric spectral analysis of materials using terahertz-tomography techniques. Appl. Phys. B **100**, 151–158 (2010)
62. B. Recur, J.P. Guillet, I. Manek-Hönninger, J.C. Delagnes, W. Benharbone, P. Desbarats, J.P. Domenger, L. Canioni, P. Mounaix, Propagation beam consideration for 3D THz computed tomography. Opt. Express **20**, 5817–5829 (2012)
63. B. Recur, H. Balacey, J. Bou Sleiman, J.B. Perraud, J.-P. Guillet, A. Kingston, P. Mounaix, Ordered subsets convex algorithm for 3D terahertz transmission tomography. Opt. Express **22**, 23299–23309 (2014)
64. W. Withayachumnankul, G.M. Png, X. Yin, S. Atakaramians, I. Jones, H. Lin, B.S.Y. Ung, J. Balakrishnan, B.W.H. Ng, B. Ferguson, S.P. Mickan, B.M. Fischer, D. Abbott, T-ray sensing and imaging. Proc. IEEE **95**, 1528–1558 (2007)
65. T. Yuan, J.Z. Xu, X.C. Zhang, Development of terahertz wave microscopes. Infrared Phys. Technol. **45**, 417–425 (2004)
66. A.J.L. Adam, Review of near-field terahertz measurement methods and their applications: how to achieve sub-wavelength resolution at THz frequencies. J. Infrared Millim. Terahertz Waves **32**, 976–1019 (2011)
67. F. Blanchard, A. Doi, T. Tanaka, K. Tanaka, Real-time, subwavelength terahertz imaging. Annu. Rev. Mater. Res. **43**, 237–259 (2013)
68. U.S. de Cumis, J.-H. Xu, L. Masini, R. Degl'Innocenti, P. Pingue, F. Beltram, A. Tredicucci, M.S. Vitiello, P.A. Benedetti, H.E. Beere, D.A. Ritchie, Terahertz confocal microscopy with a quantum cascade laser source. Opt. Express **20**, 21924–21931 (2012)
69. N.N. Zinov'ev, A.V. Andrianov, Confocal terahertz imaging. Appl. Phys. Lett. **95**, 011114 (2009)
70. M. Flammini, C. Bonsi, C. Ciano, V. Giliberti, E. Pontecorvo, P. Italia, E. DelRe, M. Ortolani, Confocal terahertz imaging of ancient manuscripts. J. Infrared Millim. Terahertz Waves **38**, 435–442 (2017)
71. M.A. Salhi, I. Pupeza, M. Koch, Confocal THz laser microscope. J. Infrared Millim. Terahertz Waves **31**, 358–366 (2010)
72. N.V. Chernomyrdin, A.O. Schadko, S.P. Lebedev, V.L. Tolstoguzov, V.N. Kurlov, I.V. Reshetov, I.E. Spektor, M. Skorobogatiy, S.O. Yurchenko, K.I. Zaytsev, Solid immersion terahertz imaging with sub-wavelength resolution. Appl. Phys. Lett. **110**, 221109 (2017)
73. J. Grzyb, B. Heinemann, U.R. Pfeiffer, Solid-state terahertz superresolution imaging device in 130-nm SiGe BiCMOS technology. IEEE Trans. Microw. Theory Tech. **65**, 4357–4372 (2017)
74. M.I. Dyakonov, M.S. Shur, Plasma wave electronics: novel terahertz devices using two dimensional electron fluid. IEEE Trans. Electron Devices **43**, 1640–1645 (1996)
75. W. Knap, M.I. Dyakonov, Field effect transistors for terahertz applications, in *Handbook of Terahertz Technology for Imaging, Sensing and Communications* (Elsevier, 2013), pp. 121–155
76. R. Tauk, F. Teppe, S. Boubanga, D. Coquillat, W. Knap, Y.M. Meziani, C. Gallon, F. Boeuf, T. Skotnicki, C. Fenouillet-Beranger, D.K. Maude, S. Rumyantsev, M.S. Shur, Plasma wave detection of terahertz radiation by silicon field effects transistors: responsivity and noise equivalent power. Appl. Phys. Lett. **89**, 253511 (2006)

77. A. Lisauskas, U. Pfeiffer, E. Öjefors, P.H. Bolvar, D. Glaab, H.G. Roskos, Rational design of high-responsivity detectors of terahertz radiation based on distributed self-mixing in silicon field-effect transistors. J. Appl. Phys. **105**, 114511 (2009)
78. Y.-S. Lee, Continuous-wave terahertz sources and detectors, in *Principles of Terahertz Science and Technology* (Springer, 2009), pp. 117–157
79. J. Yang, S. Ruan, M. Zhang, Real-time, continuous-wave terahertz imaging by a pyroelectric camera. Chin. Opt. Lett. **6**, 29–31 (2008)
80. M.J.E. Golay, The theoretical and practical sensitivity of the pneumatic infra-red detector. Rev. Sci. Instrum. **20**, 816–820 (1949)
81. P.L. Richards, Bolometers for infrared and millimeter waves. J. Appl. Phys. **76**, 1–24 (1994)
82. A.W.M. Lee, B.S. Wil, S. Kumar, Q. Hu, J.L. Reno, Real-time imaging using a 4.3-THz quantum cascade laser and a 320×240 microbolometer focal-plane array. IEEE Photon. Technol. Lett. **18**, 1415–1417 (2006)
83. M.A. Dem'yanenko, D.G. Esaev, B.A. Knyazev, G.N. Kulipanov, N.A. Vinokurov, Imaging with a 90 frames/s microbolometer focal plane array and high-power terahertz free electron laser. Appl. Phys. Lett. **92**, 131116 (2008)
84. A.W. Lee, Q. Hu, Real-time, continuous-wave terahertz imaging by use of a microbolometer focal-plane array. Opt. Lett. **30**, 2563–2565 (2005)
85. B.N. Behnken, G. Karunasiri, D.R. Chamberlin, P.R. Robrish, J. Faist, Real-time imaging using a 28 THz quantum cascade laser and uncooled infrared microbolometer camera. Opt. Lett. **33**, 440–442 (2008)
86. F. Sizov, A. Rogalski, THz detectors. Prog. Quantum Electron. **34**, 278–347 (2010)
87. N. Oda, S. Kurashina, M. Miyoshi, K. Doi, T. Ishi, T. Sudou, T. Morimoto, H. Goto, T. Sasaki, Microbolometer terahertz focal plane array and camera with improved sensitivity in the sub-terahertz region. J. Infrared Millim. Terahertz Waves **36**, 947–960 (2015)
88. N. Kanda, K. Konishi, N. Nemoto, K. Midorikawa, M. Kuwata-Gonokami, Real-time broadband terahertz spectroscopic imaging by using a highsensitivity terahertz camera. Sci. Rep. **7**, 42540 (2017)
89. K. Fan, J.Y. Suen, X. Liu, W.J. Padilla, All-dielectric metasurface absorbers for uncooled terahertz imaging. Optica **4**, 601–604 (2017)
90. B. Kearney, F. Alves, D. Grbovic, G. Karunasiri, Al/SiOx/Al single and multiband metamaterial absorbers for terahertz sensor applications. Opt. Eng. **52**, 013801 (2013)
91. W. Withayachumnankul, C.M. Shah, C. Fumeaux, B.S.Y. Ung, W.J. Padilla, M. Bhaskaran, D. Abbott, S. Sriram, Plasmonic resonance toward terahertz perfect absorbers. ACS Photon. **1**, 625–630 (2014)
92. F. Alves, B. Kearney, D. Grbovic, N.V. Lavrik, G. Karunasiri, Strong terahertz absorption using SiO_2/Al based metamaterial structures. Appl. Phys. Lett. **100**, 111104 (2012)
93. I.E. Carranza, J.P. Grant, J. Gough, D. Cumming, Terahertz metamaterials absorbers implemented in CMOS technology for imaging applications: scaling to large format focal plane arrays. IEEE J. Sel. Top. Quantum Electron. **23**, 4700508 (2017)
94. E. Leiss-Holzinger, K. Wiesauer, H. Stephani, B. Heise, D. Stifter, B. Kriechbaumer, S.J. Spachinger, C. Gusenbauer, G. Withalm, Imaging of the inner structure of cave bear teeth by novel non-destructive techniques, Palaeontol. Electron. **18** (2015)
95. E.M. Pogson, Thesis, Terahertz Applications in Medicine, the Environment and Optics, University of Wollongong, Australia, 2012
96. Y.C. Sim, J.Y. Park, K.M. Ahn, C. Park, J.H. Son, Terahertz imaging of excised oral cancer at frozen temperature. Biomed. Opt. Express **4**, 1413–1421 (2013)
97. D.A. Crawley, C. Longbottom, B.E. Cole, C.M. Ciesla, D. Arnone et al., Terahertz pulse imaging: a pilot study of potential applications in dentistry. Caries Res. **37**, 352–359 (2003)
98. D. Crawley, C. Longbottom, V.P. Wallace, B. Cole, D. Arnone et al., Three-dimensional terahertz pulse imaging of dental tissue. J. Biomed. Opt. **8**, 303–307 (2003)
99. K. Kawase, Terahertz imaging for drug detection and large-scale integrated circuit inspection. Opt. Photonics News **15**(10), 34–39 (2004)

100. J.F. Federici et al., THz imaging and sensing for security applications—explosives, weapons and drugs. Semicond. Sci. Technol. **20**(7), S266–S280 (2005)
101. M. Lu et al., Detection and identification of illicit drugs using terahertz imaging. J. Appl. Phys. **100**(10) (2006)
102. C. Baker et al., Detection of concealed explosives at a distance using terahertz technology. Proc. IEEE **95**(8), 1559–1565 (2007)
103. H. Zhong, A. Redo-Sanchez, X.C. Zhang, Identification and classification of chemicals using terahertz reflective spectroscopic focal-plane imaging system. Opt. Express **14**(20), 9130–9141 (2006)
104. M.C. Kemp, Explosives detection by terahertz spectroscopy—a bridge too far? IEEE Trans. Terahertz Sci. Technol. **1**(1), 282–292 (2011)
105. D.G. Allis, T.M. Korter, Theoretical analysis of the terahertz spectrum of the high explosive PETN. ChemPhysChem **7**(11), 2398–2408 (2006)
106. R. Appleby, R.N. Anderton, Millimeter-wave and submillimeter-wave imaging for security and surveillance. Proc. IEEE **95**(8), 1683–1690 (2007)
107. H. Seong-Tae et al., Development of a compact sub-terahertz gyrotron and its application to t-ray real-time imaging for food inspection, in *2012 37th International Conference on Infrared, Millimeter, and Terahertz Waves (IRMMW-THz)* 2012
108. C. Jördens, M. Koch, Detection of foreign bodies in chocolate with pulsed terahertz spectroscopy. Opt. Eng. **47**(3), 037003 (2008)
109. J.B. Jackson et al., Terahertz imaging for non-destructive evaluation of mural paintings. Opt. Commun. **281**(4), 527–532 (2008)
110. E. Abraham et al., Broadband terahertz imaging of documents written with lead pencils. Opt. Commun. **282**(15), 3104–3107 (2009)
111. A.J.L. Adam et al., TeraHertz imaging of hidden paintlayers on canvas. Opt. Express **17**(5), 3407–3416 (2009)
112. L. Oehrstroem et al., Technical note: terahertz imaging of ancient mummies and bone. Am. J. Phys. Anthropol. **142**(3), 497–500 (2010)
113. M. Walther, B.M. Fischer, A. Ortner, A. Bitzer, A. Thoman, H. Helm, Chemical sensing and imaging with pulsed terahertz radiation. Anal. Bioanal. Chem. **397** (2010)
114. Y.C. Shen, P.F. Taday, Development and application of terahertz pulsed imaging for non-destructive inspection of pharmaceutical tablet. IEEE J. Sel. Top. Quantum Electron. **14**(2), 407–415 (2008)
115. E.K. Rahani et al., Mechanical damage detection in polymer tiles by THz radiation. IEEE Sens. J. **11**(8), 1720–1725 (2011)
116. P. Mousavi et al., Simultaneous composition and thickness measurement of paper using terahertz timedomain spectroscopy. Appl. Opt. **48**(33), 6541–6546 (2009)
117. D.T. Nguyen, Ph.D. Thesis: Design, Modelling, and Characterization of Innovative THz Detectors. Université de Grenoble, 2012

Terahertz Emission Mechanisms in III–V Semiconductors: The Influence of Isoelectronic Dopants

Rajeev N. Kini and C. P. Vaisakh

Abstract The generation of terahertz (THz) radiation by ultrafast optical excitation of III–V semiconductors has been studied extensively in the last three decades. One of the widely used THz sources/detectors is photoconductive antennas (PCAs) based on low-temperature grown GaAs (LT-GaAs). These PCAs have acted as reliable table-top sources of THz radiation required for different applications ranging from spectroscopy to imaging. THz radiation is generated from these semiconductors by transient photocurrents or by the nonlinear optical phenomenon. In the case of low-bandgap semiconductors, like InAs or GaSb, THz emission is mainly due to transient photocurrents. The transient photocurrent arises due to the built-in surface field or due to the difference in the mobility of electrons and holes generated by the intense laser pulse. III–V semiconductors doped with isoelectronic elements like bismuth have shown interesting properties like giant bandgap bowing, (e.g., 80–90 meV/% of Bi in GaAsBi), increase in hole concentration, and giant spin-orbit bowing. In this chapter, we discuss the effect of Bi incorporation on the THz emission and the mechanisms responsible for THz phenomena in two typical III–V semiconductors, viz. GaAs and GaSb. Even though the THz emission mechanism in these two alloys is different, an enhancement in the THz emission efficiency in both the alloys with increased Bi concentration has been reported. We discuss potential applications of these III–V: Bi alloys.

1 Introduction

Semiconductors hold a special place in terahertz science and technology. They are among the crucial components of terahertz technology ever since the beginning of investigations in this spectral realm. Ultrafast optical excitation of semiconductors

R. N. Kini (✉) · C. P. Vaisakh
Indian Institute of Science Education and Research Thiruvananthapuram (IISER-TVM), Maruthamala PO, Vithura, Thiruvananthapuram, Kerala, India
e-mail: rajeevkini@iisertvm.ac.in

C. P. Vaisakh
e-mail: vaisakhjayadevan@iisertvm.ac.in

© Springer Nature Singapore Pte Ltd. 2020

A. Biswas et al. (eds.), *Emerging Trends in Terahertz Solid-State Physics and Devices*,
https://doi.org/10.1007/978-981-15-3235-1_11

is one of the most popular techniques used to produce terahertz (THz) radiation in table-top spectroscopic systems of the day. A large number of II–VI and III–V semiconductors emit THz radiation upon femtosecond optical excitation due to various physical mechanisms. Studying the THz emission from these materials not only reveals the emission mechanisms but also guides the search for efficient broadband sources of THz radiation. In this chapter, we discuss the influence of isoelectronic alloying of III–V semiconductors in the THz emission phenomenon.

2 THz Emission from Semiconductors

Femtosecond lasers deliver extraordinary optical energy, setting forth interesting processes in materials. Terahertz emission from semiconductors relies on the transient phenomenon (fs-ps) powered by ultrafast optical pulses. It either takes a nonlinear optical route or a transient current route. The nonlinear optical route relies on a process called optical rectification (OR). OR leads to rapid variation in the electric polarization in the semiconductor crystal, and the time-varying polarization acts as the source of THz radiation [1].

$$P_i^{\{2\}}\left(\omega = \omega_p - \omega_q\right) \approx \varepsilon_o \sum_{jk} \sum_{pq} \chi_{ijk}^{\{2\}}\left(\omega = \omega_p - \omega_q; \omega_p, \omega_q\right) E_j\left(\omega_p\right) E_k\left(\omega_q\right) \quad (1)$$

Here, $P_i^{\{2\}}$ is the second-order polarization in the material, $\chi_{ijk}^{\{2\}}$ is the susceptibility tensor and $E(\omega)$ is the electric field of the excitation wavelength. The III–V semiconductor systems like GaAs, InP, GaP, InAs, and II–VI systems like ZnTe, CdTe display broadband THz emission via OR. Like most other nonlinear processes, OR is subject to phase-matching condition and depends on the orientation of crystal axis with respect to the optical polarization of the excitation light. The THz emission could happen through a second-order nonlinear phenomenon in the bulk of the semiconductor and is called the bulk OR. Besides, terahertz radiation could also emerge by a third-order nonlinear process taking place at the semiconductor surface. This phenomenon is called the surface field-induced OR. The femtosecond excitation of the semiconductor generates electron-hole pairs near the surface. The photocarriers undergo drift and diffusion near the surface, constituting transient currents. The strength and nature of transient currents depend on the material system and the photon energy. These transient currents with characteristic subpicosecond lifetimes act as a source of THz radiation.

Semiconductor surfaces host unique energy states called surface states [2, 3]. The surface states play a vital role in the electrical behavior of semiconductors. Several experiments have demonstrated localization of surface states to a narrow band near the mid-bandgap. Hence, it is safe to assume that the surface Fermi level is close to the mid-bandgap. However, in the bulk interior, the Fermi level could be away from the mid-bandgap, and parameters like doping density and donor/acceptor

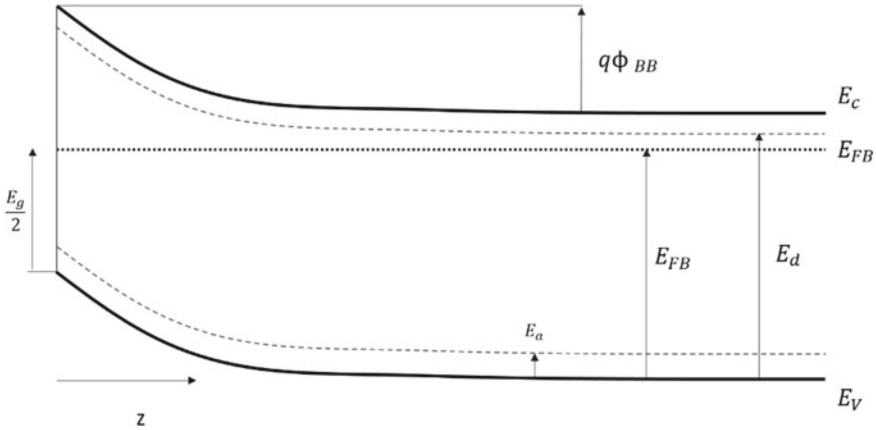

Fig. 1 Band bending at the surface of an *n*-doped semiconductor, which has a bandgap of E_g and whose Fermi level is E_{FB} away from the valance band edge E_V. E_a and E_d represent the position of acceptor and donor levels, respectively, above E_V. The quantity $q\phi_{BB}$ represent the maximum extent of band bending (at the surface) measured from the conduction band edge E_c in bulk

levels determine its position. Due to this, there is a mismatch between the Fermi levels at the bulk and the surface. This mismatch leads to band bending, charge separation, and establishment of the electric field near the surface (depletion region). This phenomenon is called the Fermi-level pinning [2] (Fig. 1).

Ultrafast excitation of the semiconductor surface introduces new carriers in the depletion region, and these carriers accelerate due to the surface electric field. These transient drift photocurrents lead to radiation in the THz frequency range. Wide-bandgap semiconductors like GaAs and InP have higher Fermi-level mismatch and stronger surface fields. Hence, drift currents constitute the prominent emission mechanism. Drift currents form the basis of popular THz source called the photoconductive antenna (PCA). PCAs are made using wideband semiconductors with biased electrodes on the surface where the external electric field drives the drift photocurrent. PCAs, compared to bare surface emitters, offer better flexibility in terms of dipole strength, dipole orientation, spectral tunability, etc.

However, low-bandgap materials do not form strong surface fields. InAs, which is a low-bandgap material, shows the highest amplitude THz emission among III–V semiconductors at 800 nm excitation, and the emission is due to carrier diffusion. In a low-bandgap material that has a short absorption length at 800 nm, when excited with an ultrafast near-infrared (NIR) pulse, a dense pool of hot carriers is created close to the surface. The gradient in carrier density between the bulk and surface drives the diffusion of carriers into the bulk. The hole has a higher effective mass and lower mobility compared to electrons. Hence, the inhomogeneous carrier distribution created by ultrafast optical excitation evolves with a net movement of electrons toward

the bulk. This is called the photo–Dember effect. The transient diffusion current thus generated results in THz emission. Carriers attain high excess kinetic energy and carrier temperature in lower-bandgap materials, making diffusion stronger in them [4].

Drift and diffusion photocurrents coexist in semiconductor systems. However, their relative and absolute strengths depend on many factors, including the bandgap, the position of satellite valleys, mobility, doping density, pump photon energy, etc. Guessing the THz emission mechanisms in a semiconductor system is not easy, as one needs to consider a large number of factors that are at play. For instance, when excited with ultrafast pulses with photon energy ~1.5 eV (λ ~ 800 nm), GaAs with a bandgap, E_g of ~1.42 eV, is a surface field-assisted drift current emitter [5]. On the other hand, studies have shown GaAs transforming into a diffusion emitter when excited at 3.1 eV due to high carrier excess energy [4]. Following this reasoning, one might be tempted to conclude that pumping a system with higher photon energy would force stronger diffusion leading to the photo–Dember effect. However, in the case of InAs (E_g ~ 0.35 eV), pumping with photon energies above ~1.6 eV decreases photo–Dember emission. When excited high up to the conduction band, electrons encounter an increased probability of scattering to the low-mobility satellite valleys [6]. Similar reasoning explains the higher photo–Dember THz emission from InAs compared to the InSb at 1.5 eV excitation, even though InSb has a lower bandgap [7].

Similarly, one would also expect heavy doping as a way to create a higher surface field and leading to higher drift currents. Even though high doping density enhances the field strength, the depletion region becomes very narrow, and hence a large fraction of photocarriers are generated outside the depletion region where there is no field to accelerate the charges. Moreover, the increased screening [8, 9] and high carrier–carrier scattering [10] sharply reduced the THz emission efficiency at high doping levels.

The excitation density of the pump beam is a vital factor in determining the emission mechanism. Let us look at THz emission from InAs. At low intensities, the THz emission happens via the photo–Dember effect [11]. However, at higher fluence, the surface field-assisted OR takes over as the dominant mechanism [12]. Moreover, the drift and diffusion currents tend to saturate at higher fluences (photocarrier–carrier density). The nonlinear phenomenon, on the other hand, might get stronger and show saturation only at much higher excitation densities.

In short, the THz emission from semiconductors is a complex phenomenon that cannot be easily generalized. Multiple emission mechanisms can coexist and compete in a single material system. One has to study the physical system and THz emission carefully to elucidate the underlying emission mechanisms. Such investigations are vital in the pursuit of the identification and design of efficient broadband sources of THz radiation, which have the potential for spectroscopic and technological applications.

3 Isoelectronic Doping

Alloying is a common technique used to tailor the optoelectronic properties of a semiconductor so that it fits the desired application. The process involves the introduction of new isoelectronic elements into the host material. Various isoelectronic species that have characteristics like atomic radii, ionicity, and electronegativity, similar to the host, are preferred. However, exceptions to this also exist. Isoelectronic alloying in III–V semiconductors is one of the heavily investigated areas of semiconductor sciences in the past decades [13, 14]. Such processes often drastically alter the structural, optoelectronic, and transport properties of the parent material. The interest in these alloys is two-fold: scientific curiosities on the nature of perturbations that come along with alloying as well as rich and diverse applications these alloys potentially hold.

The introduction of isoelectronic species perturbs the host semiconductor bandstructure. As mentioned earlier, alloying is a tool to *tune* several material parameters. One could easily see that tertiary alloys encompass a richer diversity of physical systems compared to binary systems. The introduction of new isoelectronic species and its compositional variation generates material systems with a broad spectrum of properties. The following are a few properties influenced and tuned by isoelectronic compositional variation.

- Structural parameters like lattice parameters and crystallinity.
- Optoelectronic parameters like bandgap, spin–orbit splitting energy, and the temperature sensitivity of bandgap.
- Transport properties like doping, electron–hole mobility.

Bandgap and lattice engineering of isoelectronic III–V alloys pushes its applicability to the fabrication of hybrid solar cells, LEDs, and lasers [13–15].

The strong influence of isoelectronic alloying on the structural, optoelectronic, and transport properties would inevitably modify the terahertz emission properties also.

4 III–V Bismide Alloys

Bismuth is the heaviest stable member in group V. Bismuth sets itself apart from the rest of the members with its highest atomic radius and lowest electronegativity. It acts as an isoelectronic substituent in III–V semiconductor systems. Bismuth incorporation into many of these III–V systems brings distinct modifications to the host semiconductors. Many of these characteristics have potential applications in the fabrication of optoelectronic devices ranging from detectors to solar cells and lasers. Some of the critical modifications introduced by Bi incorporation in III–V systems are discussed below.

5 Structural Properties

Lattice constant: Bismuth is the largest member of group V with an atomic radius of 230 pm. The anionic substitution of Bi necessarily leads to lattice expansion in general due to the high lattice mismatch. X-ray diffraction studies have revealed a definite shift in the characteristic peaks [16–18]. The studies have shown a monotonic increase in lattice constant with increasing Bi content in the case of GaAs. The lattice parameter data obtained from the XRD technique is often used to assess the Bi content in the alloy with the help of Vegard's law.

Crystallinity: The researchers always struggle with creating highly crystalline bismide alloys with large bismuth content. The anion mismatch is one of the important reasons, and the lattice expansion makes it difficult to achieve a lattice matching with the substrate [19].

6 Optoelectronic Properties

Bandgap: At dilute concentrations, Ga containing III–V: Bi alloys display a linear decrease in the bandgap [20]. In the case of $GaSb_{1-y}Bi_y$, the reduction happens at a rate of 30–40 meV/% of Bi [21, 22]. As the disparity between the anions increases, as in the case of the $GaAs_{1-x}Bi_x$ system, the bandgap drop is more pronounced and happens at a rate of ~80–90 meV/% of Bi [18, 23–26]. Many theoretical approaches have predicted bandgap bowing effects in III–V systems. Quantum dielectric theory [27], tight-binding method [28], DFT [22], virtual crystal approximation (VCA) [27], band anticrossing model (BAC) [29], etc., are the main theoretical approaches used to model the bandgap reduction with Bi incorporation in III–V semiconductors. Out of these, the BAC model fits well with the GaAsBi system, and a combination of BAC and VCA models provides a satisfactory explanation for the observed bandgap reduction in GaSbBi (Fig. 2).

Large spin–orbit splitting energy: The large spin–orbit splitting in III–V semiconductors doped with bismuth is also due to valance band anticrossing. The interaction of electron spin–orbital angular momentum with heavy Bi atom leads to the shift of the spin–orbit band of the new system to lower energy. This phenomenon, along with the movement of the valance band to higher energy, results in large spin–orbit splitting [24, 26, 33]. Such effects are useful for applications in spintronics.

7 Transport Properties

Unintentional doping: Bi-related states appear close to the valence band maxima of the host semiconductor, which in turn mainly affects the hole transport in the bismide alloys. One of the most crucial characteristics in all the gallium-containing

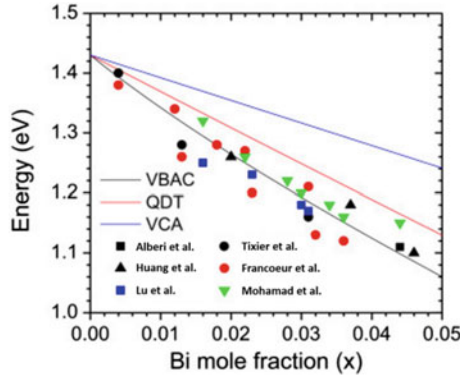

Fig. 2 Bandgap (E_g) reduction in GaAsBi observed from various studies reported in references [18, 23, 26, 30–32]. The figure also shows the comparison of experimental results to the theoretical calculations based on valance band anticrossing (VBAC), quantum dielectric theory (QDT), and virtual crystal approximation (VCA) [27]

III–V bismides is the introduction of the unintentional *p*-type character. The *p*-nature arises due to the formation of acceptor-like states induced by Bi, whose concentration increases at higher Bi content. One of the possible explanations for the acceptor states comes from the ability of Bi to have a valency of 3 as in Bi_2Te_3 or Bi_2Se_3 [34]. The valency of 3 comes as a consequence of large energy separation between $6s^2$ and $6p^3$ atomic orbitals in a heavy atom like Bi. A small fraction of Bi remains like this in the bismide alloys. In such a scenario, Bi can act as a double acceptor when residing in group V sub-lattice. Hence, a higher Bi concentration could lead to a higher hole density. An alternate route to explain the increased *p*-nature is the fact that Bi shifts the valence band edge to higher energies, closer to Fermi-level stabilization energy. The reduced activation energy favors the formation of acceptor-like defect states. This effect is observed in many bismide alloys, including GaAsBi [35–37] and GaSbBi [38, 39] (Fig. 3).

Hole mobility: The hole mobility shows remarkable degradation with Bi incorporation [35, 36, 40, 41]. The decrease in hole mobility is due to increased scattering rate by isolated as well as clustered Bi atoms. These sites could act as potential well for holes. Along with the drop in hole mobility, there is an increase in carrier effective mass with increasing Bi content in the alloy. This effect happens due to the strong hybridization of Bi-related levels with the host's VB. In short, the perturbation of Bi on CB is much weaker than that on VB, and consequently, the mobility of the electron is less affected compared to holes.

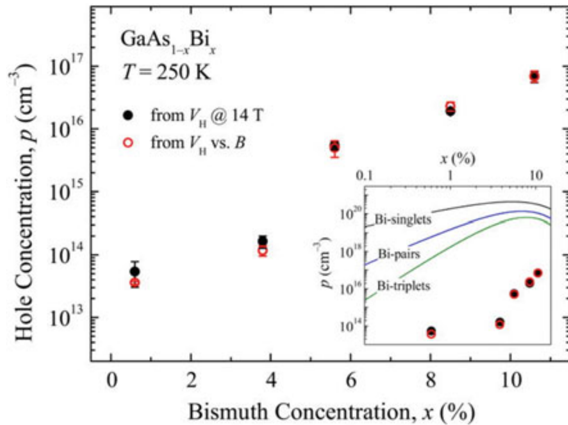

Fig. 3 Increase in the hole concentration in $GaAs_{1-x}Bi_x$ with increasing Bi content (x) observed by Pettinari et al. in reference [36]

8 Terahertz Emission from III–V-Bismide Alloys

As mentioned already, terahertz emission is a complex phenomenon influenced by a plethora of factors. Isoelectronic alloying could allow us to tweak many of these factors and alter the terahertz emission properties in semiconductors. In the previous section, we have discussed the characteristic deviation of bismide alloys from the parent III–V system. The material characteristics like bandgap, doping, and mobility have a crucial role in the terahertz emission phenomenon. In the following sections, we shall discuss the terahertz emission mechanisms in the GaAsBi and GaSbBi systems.

9 GaAsBi

Much investigation has been done on THz emission aspects of GaAs [5, 42]. With typical NIR excitation wavelengths and moderate excitation densities (~mJ/cm^2), the primary THz emission mechanism is surface field-assisted transient currents. GaAs being a wide-bandgap semiconductor, the system offers the possibility of considerable band bending and high built-in surface fields. The influence of the photo–Dember effect is minimal in GaAs when photoexcited at wavelengths close to the bandgap. These facts have been verified very well over the last couple of decades, and there is a consensus regarding this among researchers. However, in GaAs, excitation with high-energy photons results in a shift to photo–Dember emission. The reason for this is higher carrier temperature due to higher excess kinetic energy [4]. In addition to transient currents, the nonlinear phenomenon of optical rectification is also prevalent in GaAs [42].

In this section, we shall discuss the terahertz emission emerging out of nonlinear phenomena and transient currents in GaAsBi. One must keep in mind that both these emission phenomena are present in the GaAs system as well.

9.1 Optical Rectification

The terahertz emission from GaAsBi due to 800 nm excitation with moderate fluences shows a very clear indication of OR. An essential characteristic of the NL processes is the strong dependence of THz emission on the relative orientation of the excitation laser polarization and the crystal axes. For instance, in a zinc-blende structure, following relations dictate the dependence of p-polarized THz emission on the azimuthal angle (ϕ) with p-polarized laser excitation, due to bulk OR [43].

$$
\begin{aligned}
E_{p-p}^{\langle 100\rangle} &\approx \cos 2\phi \\
E_{p-p}^{\langle 110\rangle} &\approx \sin\phi + \sin 3\phi \\
E_{p-p}^{\langle 111\rangle} &\approx a + b\cos 3\phi
\end{aligned}
\tag{2}
$$

The surface field-assisted OR has a different set of rules for azimuthal dependence. The studies so far have looked at the epilayers grown on the <100> and <311>B substrates. The GaAsBi epilayers grown on (311)B face has a rather interesting azimuthal dependence [44]. The bare <311>B GaAs substrate and the GaAsBi epilayers show entirely different trends in terahertz emission with azimuthal rotation. With the careful analysis of the second- and third-order susceptibility tensor in zinc-blende crystals, one could, in principle, arrive at the azimuthal dependence for any crystal plane. In doing so, the azimuthal dependence from (311)B GaAs substrate agrees well with that of bulk OR. While the trends in epilayer differed significantly, this could well be explained by considering a combination of bulk as well as surface field-assisted OR [44].

The surface field-assisted OR phenomenon arises due to the presence of a static electric field in the zinc-blende structure. Such a static electric field can be present on the surface of semiconductors, as discussed earlier. In such cases, $\left(\text{say, } E_z^{\text{surf}} \neq 0\right)$ the third-order nonlinearity $\left(\chi_{ijkz}^{\{3\}}\right)$ can contribute to an effective second-order nonlinearity, as expressed below.

$$
\chi_{ijk}^{\{2\}\text{eff}} = \chi_{ijk}^{\{2\}\text{bulk}} + 3\chi_{ijkz}^{\{3\}} E_z^{\text{surf}} \tag{3}
$$

While the (311)B-grown GaAsBi layers show terahertz emission via bulk and surface OR, studies have shown no evidence of surface OR contribution in the case of (100) grown GaAsBi epilayers. Also, in (100) orientation, zinc-blende structures show no azimuthal dependence in the case of surface OR (Fig. 4).

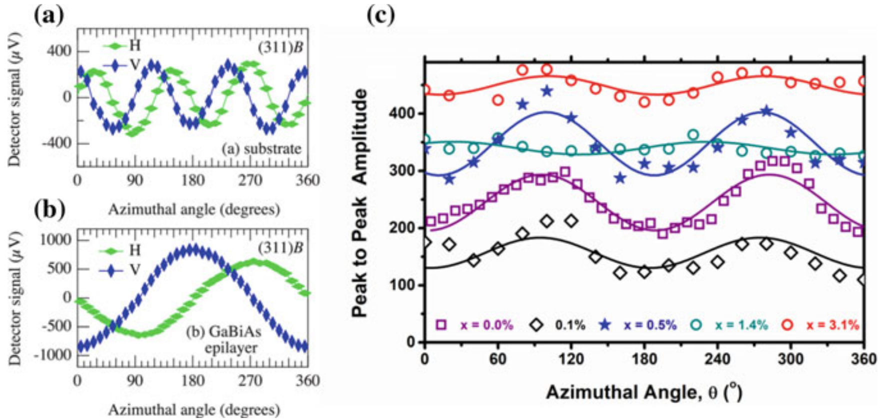

Fig. 4 Azimuthal angle dependence of THz emission from **(a)** GaAs (311)B substrate and **(b)** GaAsBi epilayer reported in reference [44]. **(c)** Similar azimuthal dependence from (100) GaAsBi epilayer reported in reference [45]

Studies have shown that the nonlinear phenomenon gets weaker with increasing Bi content in the alloy [45]. The reason is not entirely apparent yet. The Bi-induced bandgap bowing might also help us partially to explain the reduction in the contribution of OR. With increased optical absorption at lowered bandgap, the electron–hole pair generation process readily consumes the excitation photons. Hence, a lesser number of photons are available for nonlinear processes, which reduces the THz emission via OR. The effect of Bi alloying on the nonlinear susceptibility (nonlinear coefficients) is so far not known.

9.2 Transient Photocurrents

As mentioned earlier, transient currents are the dominant mechanism when it comes to THz emission in GaAs at 800 nm excitation, at low to moderate fluences. Studies show similar behavior in the case of GaAsBi systems too. The transient current could be due to the surface field or photo–Dember effect, depending on several factors. The extent of bismuth concentration itself is one of the most critical factors. At low bismuth content, the GaAsBi system is predominantly a surface field emitter, just like GaAs. Such behavior is easily understandable, considering the high-bandgap semiconductor system. One would see that the polarity of THz signals from *p*- and *n*-doped GaAsBi is opposite to each other. With increasing Bi content, the bandgap of the alloy system linearly decreases. Consider two semiconductors with different bandgaps, which are excited with radiation at the same wavelength (above bandgap excitation). Then, the carriers in the semiconductor with lower bandgap would have higher excess energy (and carrier temperature). Such a situation is very favorable

for creating diffusion current. Hence, decreasing the bandgap by incorporating more and more Bi makes the photo–Dember effect increasingly favorable (Fig. 5).

We reported such a transition happening somewhere between x ~ 0.5% and 1.4% Bi [45]. In the study, all the samples in the set ($0 \leq x \leq 3.1\%$) had inherited p-type doping associated with Bi incorporation. The THz pulses showed opposite polarity between 0.5 and 1.4% due to a crossover in the emission mechanism from

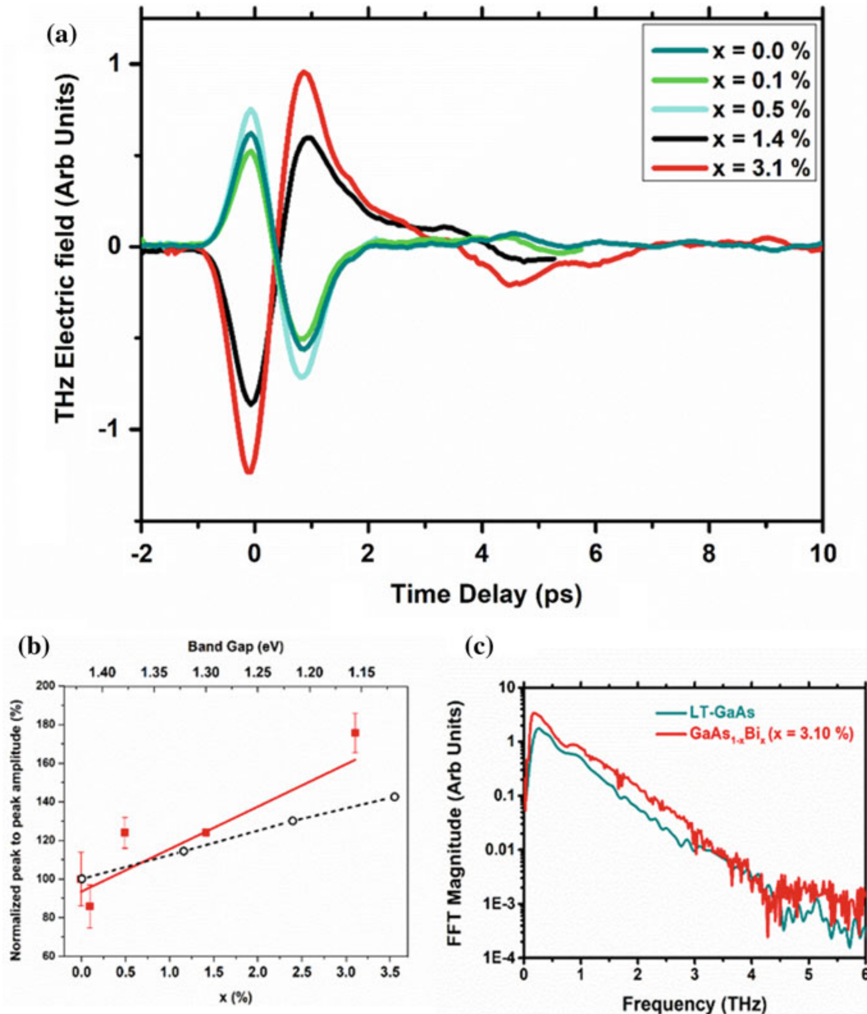

Fig. 5 THz emission characteristics of (100) $GaA_{1-x}Bi_x$ epilayers observed in reference [45]. **(a)** Comparison of THz pulses obtained from epilayers of varying Bi content under similar experimental conditions. One could see the polarity reversal in THz emission between $x \approx 0.5$ and 1.4%. **(b)** Trends in THz emission with varying Bi content and its comparison to the theoretical prediction in reference [46]. **(c)** The broadband emission spectrum from bismide alloys

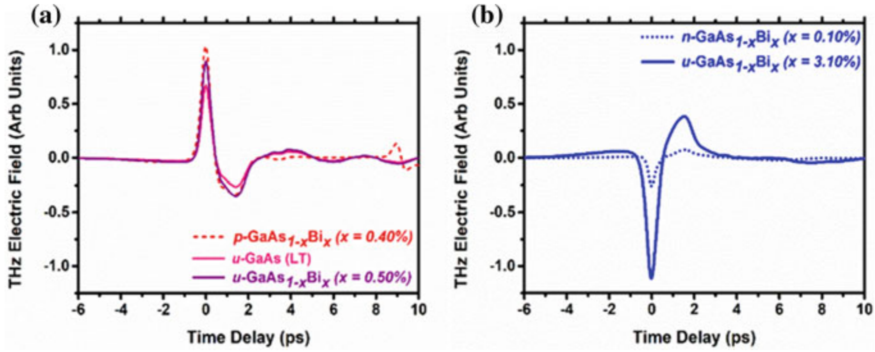

Fig. 6 **(a)**, **(b)** compare the THz pulse polarities of unintentionally doped (u) alloys to the *n*- and *p*-doped GaAsBi alloys. At low Bi concentration, the emission is dominated by drift currents. The claim is supported by the opposite polarity of the THz pulse in *n*- and *p*-type GaAsBi samples

surface field-assisted emission to photo–Dember dominated emission. One could see that with 1.55 eV (800 nm) excitation even at $x \sim 1.4\%$, the carriers would have around twice the excess energy compared to that in GaAs. The *p*-doping density in $GaAs_{1-x}Bi_x$ with increasing x could have a positive impact on the surface field and THz emission. However, in the above study, that effect is seen to be overshadowed by the increase of the photo-Dember effect. In the above study, there is an enhancement in the terahertz emission amplitude with increasing Bi content too. However, the terahertz emission could also face a backlash due to the reduced transport quality by bismuth induced defects [47] (Fig. 6).

The dominance of the photo–Dember effect becomes pronounced in the GaAsBi system with increasing excitation photon energy. But the photo–Dember current does not increase indefinitely with photon energy. The emission efficiency starts to drop once the excess energy of carriers crosses the energy difference between the Γ valley and satellite valley [47]. In such cases, the carriers start to scatter to the higher energy, low-mobility conduction band valleys. This reduces the photo–Dember efficiency. This technique is useful in finding the position of satellite valleys in the new $GaAs_{1-x}Bi_x$ alloys.

9.3 Photoconductive Antennas

GaAs is used extensively for the fabrication of THz photoconductive antenna, making it extremely relevant in THz sciences. Semi-insulating (SI) and low-temperature grown (LT) GaAs substrates are the most used photoconductive materials [48]. LT-GaAs, in particular, is the best material for making high-amplitude, broadband THz PCAs. The LT-GaAs has high resistivity, fast carrier decay, and low dark currents, which makes it ideal for PCA applications. One could also use cheaper SI-GaAs-based THz antennas for spectroscopic applications. If one intends to use a large

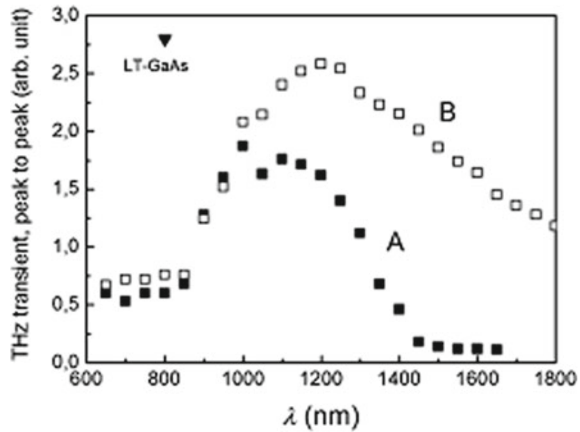

Fig. 7 Detection efficiency of GaAsBi-based PCAs which operate with long wavelength excitation [53]

aperture PCA emitter, SI-GaAs offers results comparable to LT-GaAs or often better [48, 49].

GaAsBi alloys also show great potential in PCA fabrication. The material also shows very fast carrier relaxation and high enough dark resistivity. GaAsBi PCAs operating at 800 nm are well known today [50–52]. But the most attractive prospect of GaAsBi-based PCAs lies in the bandgap tunability of the alloy. The bandgap bowing with Bi incorporation could lead to the usage of fiber lasers emitting in the 1–1.55 μm wavelength range for exciting the PCAs. Fiber lasers are far more compact and cheaper compared to the Ti-sapphire lasers that power GaAs-based PCAs. Arlauskus et al. have already demonstrated $GaAs_{1-x}Bi_x$-based PCAs with $x \sim 6\%$ being able to detect THz pulses even at excitation wavelengths as high as 1.8 μm [53]. Commercial GaAsBi PCAs are available now, which function in all-fiber mode operating at 1.06 μm. A shift to fiber laser-based THz spectroscopy systems could be a key to popularize the THz radiation and revolutionize its industrial applications (Fig. 7).

9.4 GaSbBi

GaSb is a low bandgap material with a bandgap $E_g \approx 0.72$eV. Surface fields do exist in GaSb; however, the strength is meager compared to GaAs due to the low bandgap of GaSb. The THz emission from GaSb due to surface field acceleration is much lower compared to GaAs. GaSb has a high absorption coefficient at typical Ti: Sapphire excitation wavelength ($\lambda \approx 800$nm; $E_{h\nu} \approx 1.55$ eV), and the carriers achieve high excess kinetic energy at such excitation conditions. One might be tempted to predict a stronger diffusion current due to the photo-Dember effect. However, there are more hurdles in GaSb for efficient diffusion currents driven THz emission. The satellite valleys of GaSb are very close to the Γ valley ($E_{\Gamma-L} \approx 0.084$eV and

$E_{\Gamma-X} \approx 0.31\text{eV}$). Excitation with well above bandgap radiation readily scatters the carriers to low mobility satellite valleys reducing the photocurrents and THz emission [7].

We looked at the impact of Bi incorporation on the THz emission. We reported a steady increase in THz emission with increasing Bi content in GaSbBi alloys grown via liquid phase epitaxy [54]. The bare GaSb, as mentioned earlier, is a weak THz emitter, with the emission intensity, which is only about 1/20th of that from LT-GaAs (Fig. 8). However, the emission amplitude from GaSbBi becomes comparable to that from LT-GaAs at a Bi content of ~1.65%. Bismuth incorporation in GaSb gives *p*-nature to the new alloy. As discussed earlier, studies have shown an increase in the *p*-doping density with increasing Bi content [38]. The study attributed the increased strength of the surface field due to increased doping density as the reason for such an emission enhancement. Another work on the GaSb system had revealed such an improvement in THz emission from GaSb due to impurity compensated *n*-doping due to tellurium inclusion [10]. The effect of bandgap lowering should not impact the photo–Dember effect so much at 1.55 eV excitation, as the GaSb system already has a low bandgap and excess carrier energy will not very different in the GaSbBi alloys with different Bi concentrations.

The study of the terahertz radiation pattern reveals the orientation of radiating dipole in the semiconductor system. We did this by rotating the sample with respect to the excitation beam (Fig. 9). The radiation pattern ($A°(\theta_d)$) due to a dipole oriented at an angle X to the normal to the surface, inside the semiconductor is as follows [54].

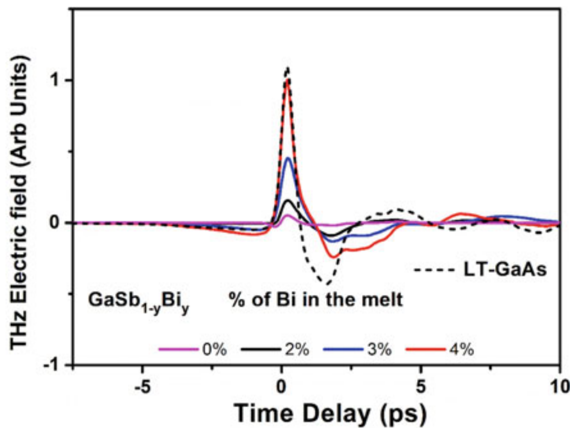

Fig. 8 THz pulses from GaSbBi alloys with varying Bi content and its comparison to LT-GaAs. The anionic Bi content in the alloy increases with increasing Bi content in the growth melt. The highest Bi content, in this case, is 1.65% Bi when grown at 4% Bi in the growth melt. The emission improves around 20-fold between GaSb and $GaS_{1-y}Bi_y$ ($y \approx 1.65\%$)

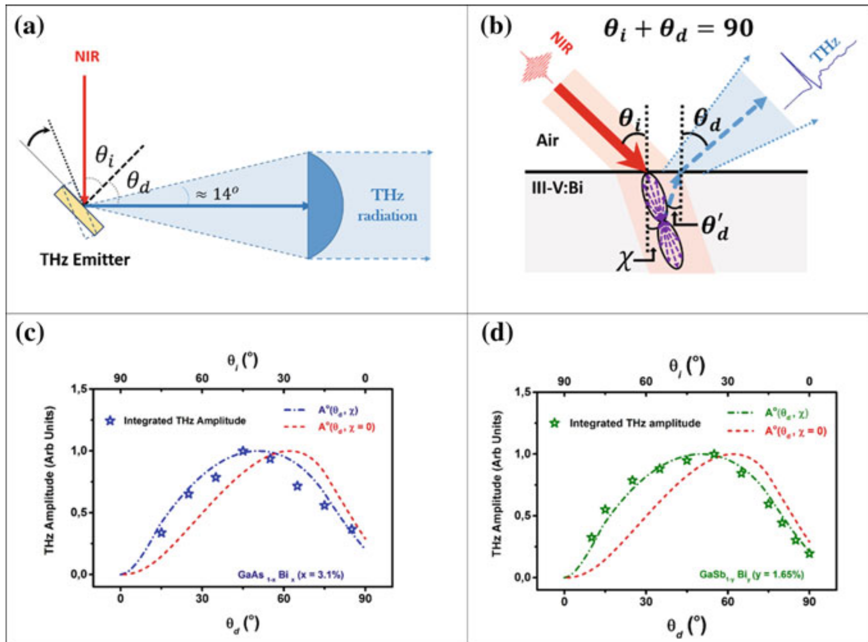

Fig. 9 **(a)** A schematic illustration of the experimental system for studying the dependence of THz emission on incidence/detection angle and, **(b)** the optical alignment of photocarriers in the semiconductor. The (time) integrated amplitude of the experimentally observed THz radiation from **(c)** $GaAs_{1-x}Bi_x$ and **(d)** $GaSb_{1-y}Bi_y$ emitter, along with the simulated pattern (with and without optical orientation) using Eq. 5 (dash-dotted line). Eq. 5 was integrated for $\theta_d \pm 14°$

$$A(\theta_d, \chi) \sim \frac{\cos\theta_d \times \sin\left(\theta'_d + \chi\right)}{\cos\theta'_d + n\cos\theta_d} \tag{4}$$

$$A^\circ(\theta_d, \chi) \propto [1 - R(90 - \theta_d)] \times \sin\theta_d \times A(\theta_d, \chi) \tag{5}$$

Our study on GaSbBi (and on GaAsBi) shows that the photocurrent (dipole) preferentially align along the refracted pump beam inside the III–V: Bi alloys. Such an "optical alignment" of carrier momentum points to the influence of the photo–Dember effect in the system. So far, no influence of optical rectification was observed from either GaSb or GaSbBi systems.

Further studies are required to understand the influence of Bi on the position of satellite valleys in GaSbBi alloys. Such influences could have a strong influence on the THz emission properties in the GaSbBi system.

To sum up, the terahertz emission from GaAsBi and GaSbBi could be enhanced with increasing Bi incorporation with 800 nm excitation. Giant bandgap bowing in GaAsBi leads to increased photocarrier temperature that enhances the photo–Dember effect in GaAsBi. The unintentional *p*-doping due to Bi inclusion strengthens the

surface field and hence the THz emission in GaSbBi. However, the bandgap bowing in GaSbBi and *p*-doping in GaAsBi seems to be of lesser influence in THz emission amplitude. However, the degradation of crystal quality will reduce the transport quality and the emission amplitude in any semiconductor system. It is exceptionally challenging to create good-quality alloys with high Bi content. But, if we succeed in that endeavor, it would be interesting to learn the THz emission phenomenon from high Bi content alloys with excellent crystal quality. The knowledge of THz emission dynamics in bismide alloys is still minimal. Further studies, including excitation spectra dependence, must be done on bismide systems of a wide composition range if we are to have a broader understanding of the subject.

9.5 Application in THz Spectroscopy

The THz emission from the GaSbBi and GaAsBi films is spectrally broad. The useful tail of the emission extends up to ~4.5 THz. The detected bandwidth could be limited because of the low sensitivity of the PCA detector at higher THz frequencies. We had compared the performance of the GaAsBi emitter and a commercially available iPCA in a THz-TDS system. The emission amplitude from GaAsBi or GaSbBi surface is several orders of magnitude lower compared to the iPCA, but its spectral reach surpasses that of a commercially available iPCA. We had used GaSbBi emitter to study the THz response of β BBO crystal and demonstrated that compared to a commercially available interdigitated PCA (iPCA), the frequency limit in which material response is faithfully measured is higher in the case of GaSbBi. Similar performance has also been obtained from GaAsBi. For example, as shown in Fig. 10, we compare the THz transmitted signal through a spin-ladder compound $\mathbf{Sr_{14}Cu_{24}O_{42}}$. This particular compound attenuates the transmission of THz signal in the frequency band from 0.25–1 THz, which results in two peaks (~0.25 THz and ~1 THz) in the

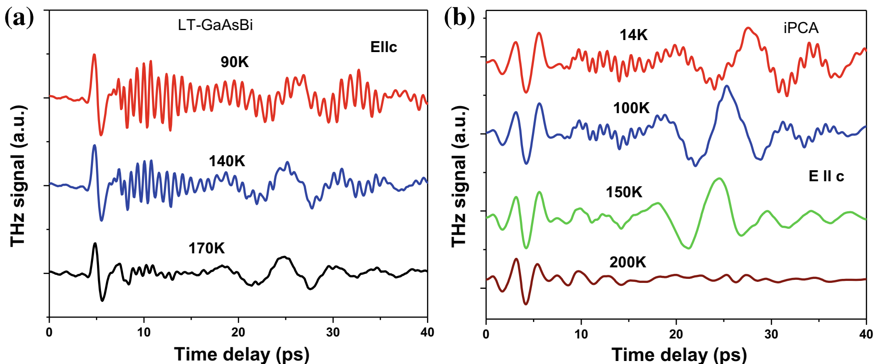

Fig. 10 **a** THz signal generated using an (**a**) GaAsBi emitter and **b** commercially available iPCA after transmitting through a $Sr_{14}Cu_{24}O_{42}$ crystal

transmitted spectra. These two peaks give rise to two kinds of oscillations, (i) a slow oscillation with a period of ~4 ps and (ii) a fast oscillation with a period of ~1 ps. As one can see, the fast oscillations are much more visible in the case of THz generation using GaAsBi compared to iPCA, due to the higher bandwidth of GaAsBi emitter. This demonstrates the feasibility of GaSbBi and GaAsBi alloy emitters for broadband THz-TDS applications.

References

1. R.W. Boyd, *Nonlinear Optics. Nonlinear Optics*. Elsevier Inc. (2008)
2. R.B. Darling, Defect-state occupation, fermi-level pinning, and illumination effects on free semiconductor surfaces. Phys. Rev. B. **43**(5), 4071–4083 (1991)
3. W.H. Brattain, J. Bardeen, Surface properties of germanium. Am. Teleph. Telegr. Co. **32**, 1 (1952)
4. J.N. Heyman, N. Coates, A. Reinhardt, G. Strasser, Diffusion and drift in terahertz emission at GaAs surfaces. Appl. Phys. Lett. **83**(26), 5476–5548 (2003)
5. X.C. Zhang, J. Xu, *Introduction to THz Wave Photonics, Introduction to THz Wave Photonics* (Springer, US, 2010), pp. 1–246
6. A. Arlauskas, A. Krotkus, THz excitation spectra of AIIIBV semiconductors. Semicond. Sci. Technol. **27**, 115015 (2012)
7. P. Gu, M. Tani, S. Kono, K. Sakai, X.C. Zhang, Study of terahertz radiation from InAs and InSb. J. Appl. Phys. **91**(9), 5533–5537 (2002)
8. I. Wilke, R. Ascazubi, H. Lu, W.J. Schaff, Terahertz emission from silicon and magnesium doped indium nitride. Appl. Phys. Lett. **93**(22), 22113 (2008)
9. R. Ascazubi, I. Wilke, K.J. Kim, P. Dutta, Terahertz emission from $Ga_{1-x}In_xSb$. Phys. Rev. B. **74**, 075323 (2006)
10. R. Ascázubi, C. Shneider, I. Wilke, R. Pino, P.S. Dutta, Enhanced terahertz emission from impurity compensated GaSb. Phys. Rev. B—Condens. Matter. Mater. Phys. **72**(4), 045328 (2005)
11. S. Kono, P. Gu, M. Tani, K. Sakai, Temperature dependence of terahertz radiation from *n*-type InSb and *n*-type InAs surfaces. Appl. Phys. B Lasers Opt. **71**(6), 901–904 (2000)
12. R. Adomavičius, A. Urbanowicz, G. Molis, A. Krotkus, E. Šatkovskis, Terahertz emission from p-InAs due to the instantaneous polarization. Appl. Phys. Lett. **85**(13), 2463–2465 (2004)
13. Wang L, Zhang L, Yue L, Liang D, Chen X, Li Y, et al. Novel dilute bismide, epitaxy, physical properties and device application. Crystals [Internet]. 7(3):63 (2017). Available from http://www.mdpi.com/2073-4352/7/3/63
14. R.F. Davis, III–V nitrides for electronic and optoelectronic applications. Proc. IEEE **79**(5), 702–712 (1991)
15. I. Marko, S.J. Sweeney, Progress towards III–V-bismide alloys for near- and mid-infrared laser diodes. IEEE J. Sel. Top. Quantum Electron. **23**(6), 150512 (2017)
16. K. Oe, H. Okamoto, New semiconductor alloy $GaAs_{1-x}Bi_x$ grown by metal organic vapor phase epitaxy. Jpn. J. Appl. Phys. **37**(11), 1283–1285 (1998)
17. Y. Takehara, M. Yoshimoto, W. Huang, J. Saraie, O.E. Kunishige, A. Chayahara et al., Lattice distortion of GaAsBi alloy grown on GaAs by molecular beam epitaxy. Japan. J. Appl. Phys. Part 1 **45**(1A), 67–69 (2006)
18. S. Tixier, M. Adamcyk, T. Tiedje, S. Francoeur, A. Mascarenhas, P. Wei et al., Molecular beam epitaxy growth of $GaAs_{1-x}Bi_x$. Appl. Phys. Lett. **82**(14), 2245–2247 (2003)
19. K.M. Yu, S.V. Novikov, R. Broesler, A.X. Levander, Z. Liliental-Weber, F. Luckert et al., GaNAs alloys over the whole composition range grown on crystalline and amorphous substrates. Phys. Status Solidi. Curr. Top Solid State Phys. **8**(7–8), 2503–2505 (2011)

20. M.P. Polak, P. Scharoch, R. Kudrawiec, First-principles calculations of bismuth induced changes in the band structure of dilute Ga–V–Bi and In–V–Bi alloys: Chemical trends versus experimental data. Semicond Sci Technol. **30**(9), 094001 (2015)
21. M.K. Rajpalke, W.M. Linhart, M. Birkett, K.M. Yu, D.O. Scanlon, J. Buckeridge et al., Growth and properties of GaSbBi alloys. Appl. Phys. Lett. **103**, 142106 (2013)
22. M.P. Polak, P. Scharoch, R. Kudrawiec, J. Kopaczek, M.J. Winiarsky, W.M. Linhart et al., Theoretical and experimental studies of electronic band structure for $GaAs_{1-x}Bi_x$. J. Phys. D Appl. Phys. **47**, 355107 (2014)
23. S. Francoeur, M.-J. Seong, A. Mascarenhas, S. Tixier, M. Adamcyk, T. Tiedje, Band gap of $GaAs_{1-x}Bi_x$, $0 < x < 3.6\%$. Appl. Phys. Lett. **82**, 3874 (2003)
24. Z. Batool, K. Hild, T.J.C. Hosea, X. Lu, T. Tiedje, S.J. Sweeney, The electronic band structure of GaBiAs/GaAs layers: influence of strain and band anti-crossing. J. Appl. Phys. **111**, 113108 (2012)
25. J. Yoshida, T. Kita, O. Wada, K. Oe, Temperature dependence of $GaAs_{1-x}Bi_x$ band gap studied by photoreflectance spectroscopy. Japanese J Appl Physics, Part 1 **42A**(2), 371–374 (2003)
26. K. Alberi, O.D.D. Walukiewicz, K.M.Y. Bertulis, A. Krotkus, Valence band anticrossing in $GaBi_xAs_{1-x}$. Appl. Phys. Lett. **91**, 051909 (2007)
27. D.P. Samajdar, S. Dhar, Estimation of Bi induced changes in the direct E_0 band gap of III–V-Bi alloys and comparison with experimental data. Phys. B **484**, 27–30 (2016)
28. M. Usman, C.A. Broderick, A. Lindsay, E.P. O'Reilly, Tight-binding analysis of the electronic structure of dilute bismide alloys of GaP and GaAs. Phys. Rev. B. **84**, 245202 (2011)
29. K. Alberi, J. Wu, W. Walukiewicz, K.M. Yu, O.D. Dubon, S.P. Watkins et al., Valence-band anticrossing in mismatched III–V semiconductor alloys. Phys. Rev. B. **75**, 045203 (2007)
30. W. Huang, K. Oe, G. Feng, M. Yoshimoto, Molecular-beam epitaxy and characteristics of Ga $N_yAs_{1-x-y}Bi_x$. J Appl Phys. **98**(5), 053505 (2005)
31. X. Lu, D.A. Beaton, R.B. Lewis, T. Tiedje, Y. Zhang, Composition dependence of photoluminescence of $GaAs_{1-x}Bi_x$ alloys. Appl. Phys. Lett. **95**(4), 2007–2010 (2009)
32. A.R. Mohmad, F. Bastiman, C.J. Hunter, R.D. Richards, S.J. Sweeney, J.S. Ng et al., Localization effects and band gap of GaAsBi alloys. Phys. Status Solidi. Basic Res. **251**(6), 1276–1281 (2014)
33. B. Fluegel, S. Francoeur, A. Mascarenhas, S. Tixier, E.C. Young, T. Tiedje, Giant spin-orbit bowing in $GaAs_{1-x}Bi_x$. Phys. Rev. Lett. **97**(6), 11–14 (2006)
34. H.X. Deng, J. Li, S.S. Li, H. Peng, J.B. Xia, L.W. Wang et al., Band crossing in isovalent semiconductor alloys with large size mismatch: First-principles calculations of the electronic structure of Bi and N incorporated GaAs. Phys. Rev. B—Condens. Matter. Mater. Phys. **82**(19), 4–7 (2010)
35. S. Nargelas, K. Jarašiunas, K. Bertulis, V. Pačebutas, Hole diffusivity in GaAsBi alloys measured by a picosecond transient grating technique. Appl. Phys. Lett. **98**(8), 082115 (2011)
36. G. Pettinari, A. Patanè, A. Polimeni, M. Capizzi, X. Lu, T. Tiedje, Bi-induced *p*-type conductivity in nominally undoped Ga(AsBi). Appl. Phys. Lett. **100**(9), 092109 (2012)
37. G. Pettinari, H. Engelkamp, P.C.M. Christianen, J.C. Maan, A. Polimeni, M. Capizzi et al., Compositional evolution of Bi-induced acceptor states in $GaAs_{1-x}Bi_x$ alloy. Phys. Rev. B. **83**, 201201(R) (2011)
38. N. Segercrantz, J. Slotte, I. Makkonen, F. Tuomisto, I.C. Sandall, M.J. Ashwin et al., Hole density and acceptor-type defects in MBE-grown $GaSb_{1-x}Bi_x$. J. Phys. D Appl. Phys. **50**, 295102 (2017)
39. J. Kopaczek, R. Kudrawiec, W. Linhart, M. Rajpalke, T. Jones, M. Ashwin et al., Low- and high-energy photoluminescence from $GaSb_{1-x}Bi_x$ with $0 < x < 0.042$. Appl. Phys. Expr. **7**, 111202 (2014)
40. D.A. Beaton, R.B. Lewis, M. Masnadi-Shirazi, T. Tiedje, Temperature dependence of hole mobility in $GaAs_{1-x}Bi_x$ alloys. J. Appl. Phys. **108**, 083708 (2010)
41. R.N. Kini, A.J. Ptak, B. Fluegel, R. France, R.C. Reedy, A. Mascarenhas, Effect of Bi alloying on the hole transport in the dilute bismide alloy $GaAs_{1-x}Bi_x$. Phys. Rev. B. **83**, 075307 (2011)

42. S.L. Dexheimer, *Terahertz spectroscopy: principles and applications, principles and applications* (CRC Press, Terahertz Spectroscopy, 2017), pp. 1–331
43. M. Reid, I.V. Cravetchi, R. Fedosejevs, Terahertz radiation and second-harmonic generation from InAs: bulk versus surface electric-field-induced contributions. Phys. Rev. B. **72**, 035201 (2005)
44. K. Radhanpura, S. Hargreaves, R.A. Lewis, M. Henini, The role of optical rectification in the generation of terahertz radiation from GaBiAs. Appl. Phys. Lett. **94**, 251115 (2009)
45. C.P. Vaisakh, A. Mascarenhas, R.N. Kini, THz generation mechanisms in the semiconductor alloy, $GaAs_{1-x}Bi_x$. J. Appl. Phys. **118**, 165702 (2015)
46. D.L. Cortie, R.A. Lewis, The importance of scattering, surface potential, and vanguard counter-potential in terahertz emission from gallium arsenide. Appl. Phys. Lett. **100**, 261601 (2012)
47. V. Pačebutas, S. Stanionytė, A. Arlauskas, R. Norkus, R. Butkutė, A. Geižutis et al., Terahertz excitation spectra of GaAsBi alloys. J. Phys. D Appl. Phys. **51**, 474001 (2018)
48. N.M. Burford, M.O. El-Shenawee, Review of terahertz photoconductive antenna technology. Opt. Eng. **56**, 010901 (2017)
49. M. Tani, S. Matsuura, K. Sakai, S. Nakashima, Emission characteristics of photoconductive antennas based on low-temperature-grown GaAs and semi-insulating GaAs. Appl. Opt. **36**(30), 7853 (1997)
50. B. Heshmat, M. Masnadi-Shirazi, R.B. Lewis, J. Zhang, T. Tiedje, R. Gordon et al., Enhanced terahertz bandwidth and power from GaAsBi-based sources. Adv. Opt. Mater. **1**(10), 714–719 (2013)
51. K. Bertulis, A. Krotkus, G. Aleksejenko, V. Pačebutas, R. Adomavičius, G. Molis et al., GaBiAs: a material for optoelectronic terahertz devices. Appl. Phys. Lett. **88**(20), 201112 (2006)
52. V. Pačebutas, A. Bičiūnas, S. Balakauskas, A. Krotkus, G. Andriukaitis, D. Lorenc et al., Terahertz time-domain-spectroscopy system based on femtosecond Yb: fiber laser and GaBiAs photoconducting components. Appl. Phys. Lett. **97**, 031111 (2010)
53. A. Arlauskas, P. Svidovsky, K. Bertulis, R. Adomavičius, A. Krotkus, GaAsBi photoconductive terahertz detector sensitivity at long excitation wavelengths. Appl. Phys. Expr. **5**, 022601 (2012)
54. C.P. Vaisakh, M.K. Bhowal, S. Dhar, R.N. Kini, Enhanced terahertz emission from Bi incorporated GaSb. J. Phys. D Appl. Phys. **51**, 065112 (2018)

Group III—Nitrides and Other Semiconductors for Terahertz Detector

Bijit Choudhuri and Aniruddha Mondal

1 Introduction

Terahertz detector is a type of transducer device which converts the terahertz radiation into the human interpretable signal entity. Basically, terahertz signal refers to the signal staying at a gap between microwave and infrared in electromagnetic radiation spectrum (wavelength range from 1 to 0.01 mm). As terahertz radiation contains 98% of photon emission since the Big Bang, the study of terahertz spectroscopy is gaining an enormous research interest in astronomy and astrophysics [1]. Apart from it, Terahertz spectroscopy also finds its applications in biomedical imaging, biomolecule identification, satellite communication and food product safety analysis to name a few [2–5].

2 Important Figures of Merit

There are some figures of merit which are very important to determine the performance of a terahertz detector.

- Noise-equivalent power (NEP)
- Responsivity
- Response time

B. Choudhuri
Department of Electronics and Communication Engineering,
NIT Silchar, Silchar, Cachar, Assam 788010, India

A. Mondal (✉)
Department of Physics, NIT Durgapur, Mahatma Gandhi Road,
A-Zone, Durgapur, West Bengal 713209, India
e-mail: aniruddhamo@gmail.com

© Springer Nature Singapore Pte Ltd. 2020

A. Biswas et al. (eds.), *Emerging Trends in Terahertz Solid-State Physics and Devices*,
https://doi.org/10.1007/978-981-15-3235-1_12

Noise-equivalent power: The unwanted signal generated due to the random movement of the current carrier is known as noise. The noise contributes to the degradation of information present in a signal. The noise-equivalent power (NEP) of a detector is defined as the amount of power required to generate the same amount of noise in a detector. It is expressed in terms of power per square root of bandwidth ($W/\sqrt{Hz}$).
Responsivity: The responsivity parameter represents the ability of a detector to convert the terahertz radiation into electrical entity (voltage or current). It is defined as the ratio of the generated photocurrent/photovoltage (output) to the incident electromagnetic power (input)

$$R = \frac{I_{\mathrm{Ph}}}{P_{\mathrm{inc}}} (\mathrm{A/W})$$

$$R = \frac{V_{\mathrm{Ph}}}{P_{\mathrm{inc}}} (\mathrm{V/W})$$

where I_{Ph} (V_{Ph}) is the photocurrent (photovoltage) when light is entered into the detector at a given wavelength, and P_{inc} is the incident power,
Response time: Response time can be assumed as the time taken by the system to show a change in the output signal with a change in input radiation. Generally, rise time and fall time are the two terms those specify the speed of the optical detector response. Rise time is the time taken by the signal to reach 90% of its maximum value from 10% of its maximum value. Similarly, the fall time can be defined as the time required by the detector to reach 10% of the maximum value from 90% of the maximum value. These parameters can be measured from the radiation on–off switching characteristics.

3 Various Types of Terahertz Detectors

In 1878, American astronomer Samuel P. Langley demonstrated the first bolometer to measure electromagnetic power using a temperature-dependent electrical resistance [6]. Since then, the bolometers are being used dominantly to measure terahertz radiation. Presently, with the rapid advancement of electronic device industry, the technology is making the shift to the semiconductor-based bolometer development. In the following section, the pioneering research work carried out on semiconductor terahertz detector is elaborated:

Condori Quispe et al. made theoretical analysis and numerical solution of resonant tunnelling diode gated high-electron-mobility transistor for terahertz radiation detection. AlGaN/GaN/AlGaN structure (as shown in Fig. 1) was considered for the development of HEMT device. Maximum stable power gain was observed to be ~48 dB. This high gain was attributed to the gate-to-channel negative differential conductance and 2-D electron gas in HEMT channel region as shown in Fig. 2 [7].

Fig. 1 Schematic of the devices: **a** Cross-sectional view of RTD-gated HEMTs. The black coloured layers represent AlGaN barrier, **b** grating-gate devices with two different filling factors. Filling factor, *f*, is defined as the ratio of the gate length (L_g) to the source-to-drain separation ($S_{S/D}$), **c** top view of the antenna-coupled device. Reproduced from [7], with the permission of AIP Publishing

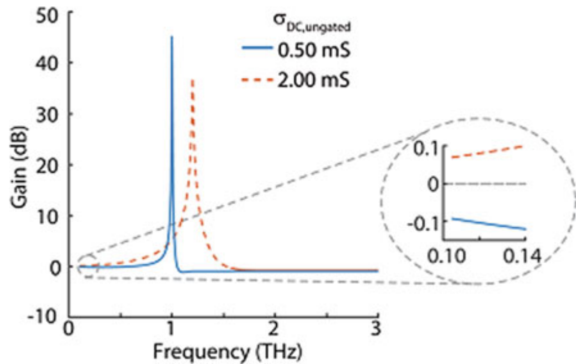

Fig. 2 Gain spectra for configurations exhibiting maximum gain with varying ungated conductivity. Reproduced from [7], with the permission of AIP Publishing

Qin et al. fabricated and investigated the characteristics of a bilayer graphene field-effect transistor (GFET) for the purpose of high-sensitivity terahertz radiation detection. At first, monolayer graphene was deposited by epitaxial growth on a 4H-SiC (0001) wafer under Ar atmosphere and 1550 °C temperature. Subsequently, this layer was annealed at 900 °C under molecular hydrogen atmosphere. UV lithography, e-beam lithography, wet chemical etching and reactive ion etching were used to precisely define the dimension of GFET device. The source–drain contacts also served as terahertz antenna (Fig. 3). The carrier mobility was observed to be 405 cm^2 V^{-1} s^{-1}. The maximum responsivity was 30 V/W at 0.330 THz as shown in Fig. 4. The NEP was 51 pW/$\sqrt{\text{Hz}}$. The overall source–drain resistance was less than 203 Ω which is compatible for developing the high-speed direct/homodyne and heterodyne receivers [8].

Ponomarev et al. demonstrated a hot electron bolometer (HEB) based on tin (Sn) nanothreads array in GaAs FET. The Sn nanothreads were incorporated inside the structure (Fig. 5a). The free electrons from Sn diffused into 2-D electron gas by

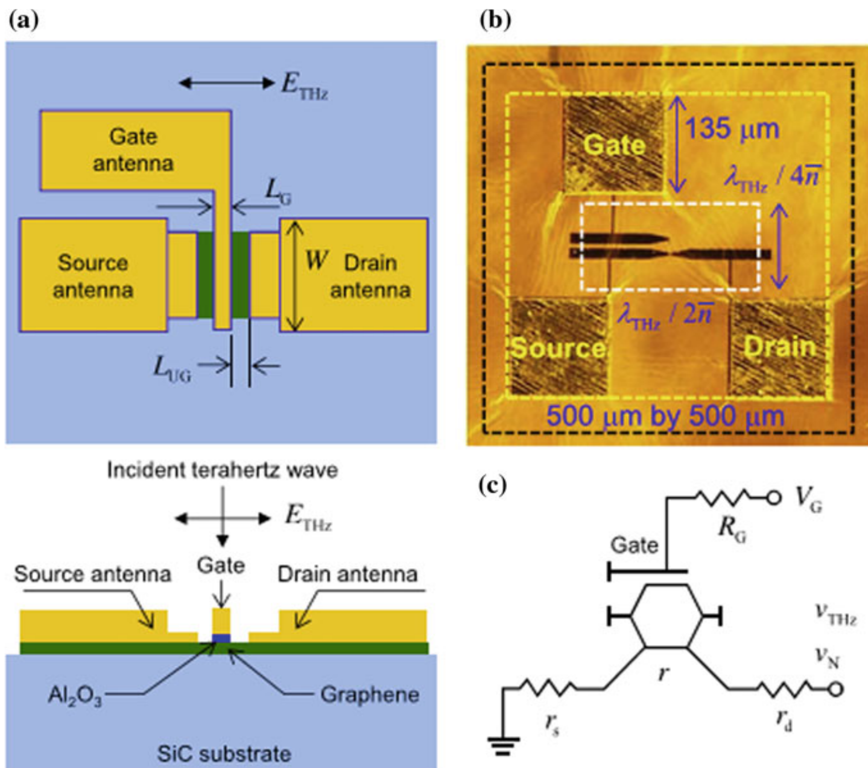

Fig. 3 **a** Sketch of an antenna-coupled GFET terahertz detector, **b** micrograph of the detector, **c** circuit diagram. Reprinted from [8] with permission from Elsevier

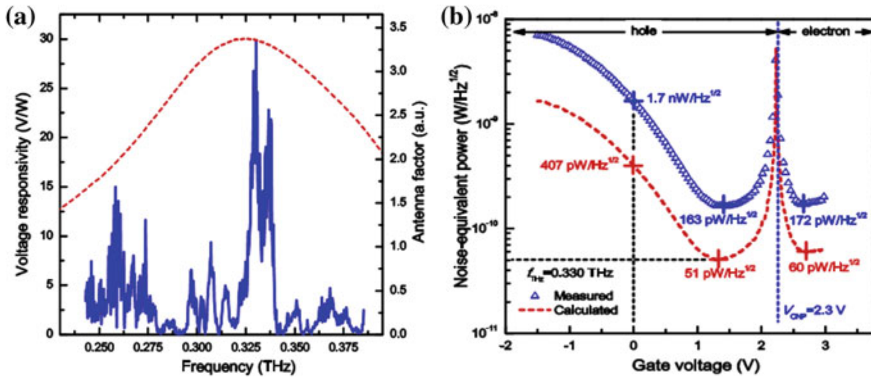

Fig. 4 **a** The voltage responsivity–terahertz frequency characteristics at $V_{\mathrm{G}} = 14$ V, **b** the NEP-gate voltage characteristics at 0.33 THz. Reprinted from [8] with permission from Elsevier

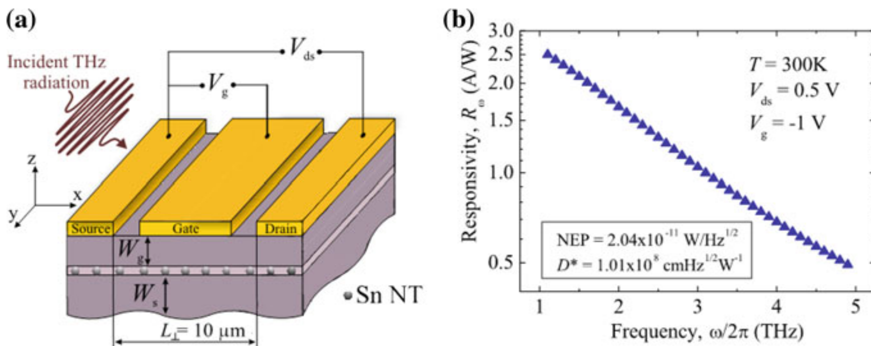

Fig. 5 **a** Schematic of the Sn nanothread incorporated GaAs FET device, **b** Room temperature responsivity–frequency characteristics at $V = -1$ V and $V_{\mathrm{ds}} = 0.5$ V. Reproduced from [9] with permission from IOP Publishing

absorbing energy from the electromagnetic radiation and resulted in superior performance. At 1 THz frequency, the responsivity was 2.51 A/W. The NEP and specific detectivity were calculated to be $20.4\,\mathrm{pW}/\sqrt{\mathrm{Hz}}$ and $1.01 \times 10^{8}\,\mathrm{cm}/\sqrt{\mathrm{Hz}}\,\mathrm{W}^{-1}$ as shown in Fig. 5b. The sensitivity was attributed to the heating of electrons in nanothreads by radiation and subsequent delocalization. The HEB was predicted to exhibit polarization selectivity [9]. The same group also reported the theoretical prediction and fabrication of GaAs FET structure for terahertz detection at very low temperature. In cryogenic temperature (4.2 K), the detector exhibited responsivity and NEP to be 14 A/W and $0.9\,\mathrm{pW}/\sqrt{\mathrm{Hz}}$, respectively, while at room temperature (300 K), the same parameters were observed to be 1.3 A/W and $6.5\,\mathrm{pW}/\sqrt{\mathrm{Hz}}$, respectively [10].

But et al. studied the photoresponse of a silicon metal–oxide–semiconductor field-effect transistor (MOSFET) and InGaAs/GaAs pseudomorphic high-electron-mobility transistor (HEMT). The radiation intensity and frequency were varied from

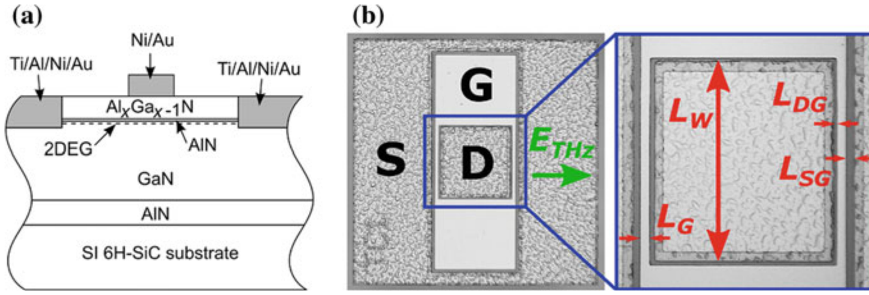

Fig. 6 **a** Schematic of the cross section of GaN–$Al_xGa_{1-x}N$ HEMT for terahertz detection, **b** micrograph of the top view of the device. Reproduced from [12] with permission from Lithuanian Academy of Sciences

0.5 mW/cm^2 up to 500 kW/cm^2 and from 0.13 to 3.3 THz, respectively. The photoresponse was observed to vary linearly with the irradiation intensity followed by a nonlinear and saturated characteristic [11].

Jakštas et al. demonstrated the terahertz sensing by an AlGaN/GaN Schottky diodes HEMT on a semi-insulating SiC substrate. The AlGaN/GaN heterostructures were grown using a metalorganic chemical vapour deposition (MOCVD) method. The Schottky and ohmic contact metallization was carried out by electron beam evaporation. The 2-D schematic and top-view SEM images are shown in Fig. 6. At room temperature, the two-dimensional electron gas (DEG) density and the electron mobility were found to be 8.3 × 10^{12} cm^{-2} and 1.9 × 10^3 cm^2 V^{-1} s^{-1}, respectively. The I_{ON}/I_{OFF} and transconductance were measured to be 70 dB and 165 mS/mm. Under the irradiation of a terahertz source with 11 mW power and 0. THz frequency, the responsivity and the NEP were observed to be 30 mV/W and 26 26 nW/$\sqrt{\text{Hz}}$. The improved performance of the HEMT was attributed to the superior 2-DEG mobility and thermal conductivity of the SiC substrate [12].

Kim et al. demonstrated the terahertz sensing properties of a 65 nm MOSFET both theoretically and experimentally. At 0.3 THz, the device exhibited a responsivity of 27.8 V/W. The noise spectral density (NSD) and NEP were observed to be 9.5 nV/$\sqrt{\text{Hz}}$ and 0.18 nW/$\sqrt{\text{Hz}}$ [13].

Generalov et al. reported the fabrication and sensing of a GHET terahertz detector. The GFET was fabricated by dry transfer of chemical vapour deposition (CVD)-grown graphene on a subsequent atomic layer deposition (ALD) of Al_2O_3 (Fig. 7). The electron and hole mobilities were extracted to be 3100 and 2800 cm^2 V^{-1} s^{-1}, respectively, and the residual carrier concentration was 4.5 × 10^{15} m^{-2}. As shown in Fig. 8, under 0.4 GHz irradiation, the maximum responsivity and minimum NEP were 74 V/W and 130 nW/$\sqrt{\text{Hz}}$. This improvement in performance was attributed to the reduction in residual carrier concentration [14].

Nadar et al. fabricated a heterostructure low barrier diode (HLBD) and investigated its sub-THz radiation sensing properties. The device was grown using gas-source molecular beam epitaxy on 350-μm-thick semi-insulating InP substrates. Figures 9 and 10 show scanning electron micrographs and cross-sectional schematic of the

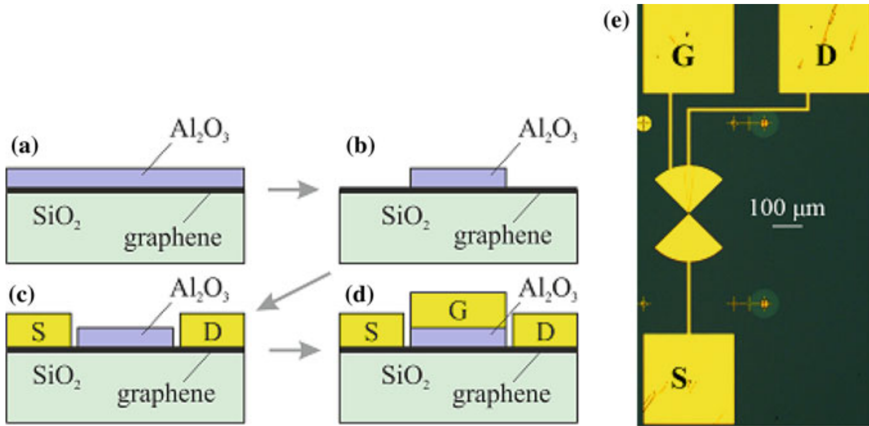

Fig. 7 **a**–**d** Fabrication steps of the GFET device, **e** micrograph of the fabricated GFET detector. © [2020] IEEE. Reprinted, with permission, from [14]

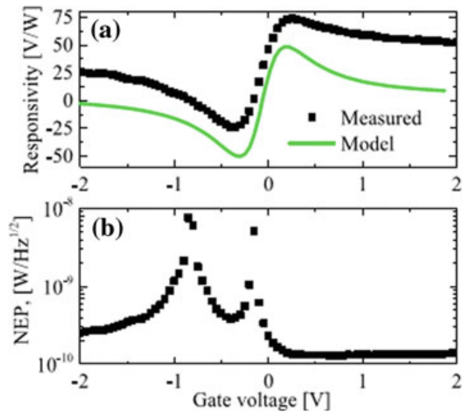

Fig. 8 **a** voltage responsivity and **b** NEP of the GFET detector with $n_0 = 4.5 \times 10^{15}$ m^{-2} at 400 GHz. © [2020] IEEE. Reprinted, with permission, from [14]

device, respectively. Under 175 GHz irradiation, the maximum responsivity and NEP of the detector were 5.2 kV/W and 0.7 pW/$\sqrt{\text{Hz}}$ respectively [15].

Javadi et al. reported that terahertz sensing characteristics of a GaAs HMET detector. The device exhibited a responsivity of 42 and 1.6 V/W under the illumination of 0.271 and 0.632 THz frequency signal, respectively. Under the same irradiations, the recorded NEP values were 135 pW/$\sqrt{\text{Hz}}$ and 1250 pW/$\sqrt{\text{Hz}}$, respectively [16].

Kurita et al. reported the implementation of asymmetric dual-grating gate (ADGG) in an InAlAs/InGaAs/InP HEMT for terahertz radiation detection. Figure 11 shows the schematic and SEM image of the device. The detector exhibited very high responsivities of 2.1 and 0.4 kV/W under 200 and 292 GHz frequency irradiation as shown in Fig. 12. The maximum NEP was calculated to be 0.48 pW/$\sqrt{\text{Hz}}$ under 200 GHz frequency excitation. This improvement in performance was due to the efficient

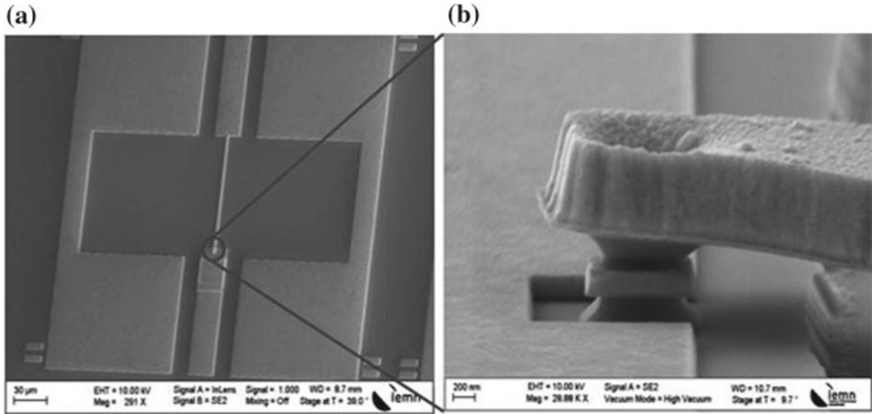

Fig. 9 SEM images of a 0.5 μm^2 heterostructure low barrier diode. © [2020] IEEE. Reprinted, with permission, from [15]

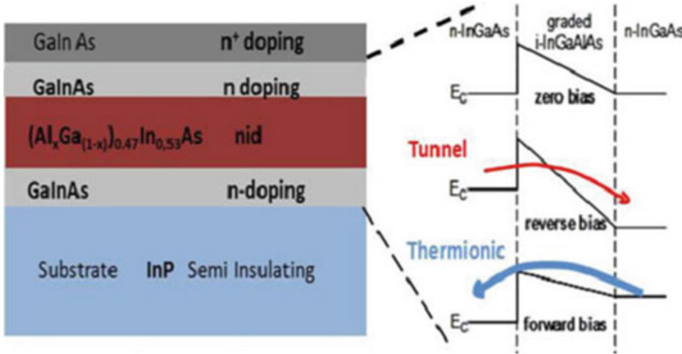

Fig. 10 Cross-sectional schematic of the HLBD heterostructure and its conduction band structure under various bias conditions. © [2020] IEEE. Reprinted, with permission, from [15]

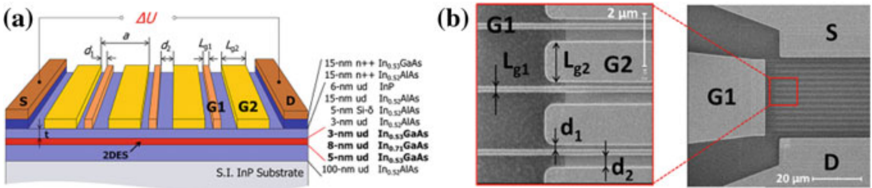

Fig. 11 **a** 3-D schematic view of A-DGG HEMT, **b** top-view SEM images of A-DGG HEMT. Reproduced from [17] with the permission of AIP Publishing

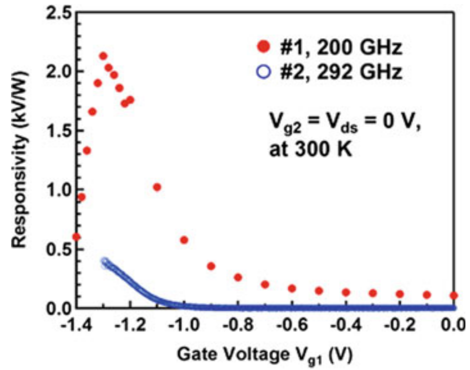

Fig. 12 Room temperature responsivity–voltage characteristic for the device at 200 and 292 GHz. Reproduced from [17] with the permission of AIP Publishing

coupling between the terahertz radiation and the plasmon in the 2DEG channel. Moreover, the DGG structures contributed to a very high photovoltage due to the cascading of multiple depletion regions [17].

Bauer et al. reported the terahertz sensing by GaN HEMT-based detector integrated with a bow-tie antenna. Under 1.18 THz excitation, the detector showed a maximum responsivity of 17 mA/W and a minimum NEP of 155 pW/$\sqrt{\text{Hz}}$ [18].

Hou et al. fabricated a sub-terahertz detector using AlGaN/GaN HEMT with nanoantenna as shown in Fig. 13. The HEMT detector with nanoantenna exhibited a minimum NEP of 0.58 pW/$\sqrt{\text{Hz}}$ as compared to the NEP 1.07 pW/$\sqrt{\text{Hz}}$ for HEMT detector without the nanoantenna. For low value of gate voltage swing, the nanoantenna embedded detector showed a responsivity of 15 kV/W which is nearly 1.8 times enhanced as compared to the responsivity of the device without nanoantenna (Fig. 14) [19].

Guo et al. reported the fabrication of a GFET detector attached with a square spiral antenna and its application in sensing terahertz radiation. A layer of CVD

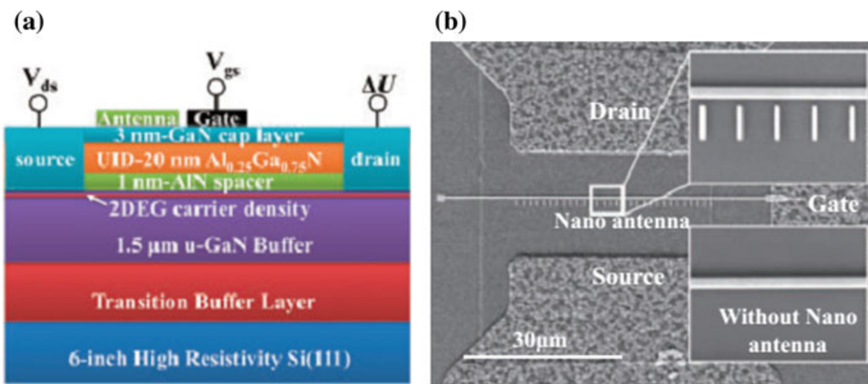

Fig. 13 **a** 2-D schematic view of GaN–AlGaN HEMT, **b** top-view SEM image of GaN-AlGaN HEMT. Adapted from [19]

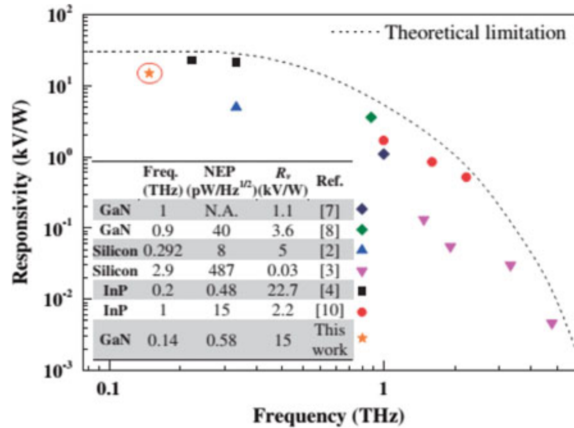

Fig. 14 Responsivity–frequency characteristic for GaN–AlGaN terahertz detecting HEMT. Adapted from [19]

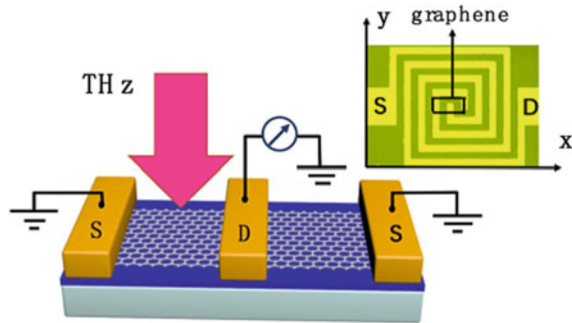

Fig. 15 Schematic of the graphene-based terahertz detector integrated with a square spiral antenna. Reprinted with permission from [20] © The Optical Society

grown monolayer graphene (MLG) was transferred onto a highly intrinsic Si substrate capped with SiO_2 layer. Subsequently, the antenna patterning was carried out by an ultra-violet lithography technique as shown in Fig. 15. The NEP, responsivity and response time for the detector were 0.35 nW/$\sqrt{\text{Hz}}$ 28 V/W and ~9 μs, respectively [20].

Bandurin et al. also fabricated and investigated the terahertz sensing properties of a GFET device. Firstly, bilayer graphene (BLG) was sandwiched between thick layers of hexagonal boron nitride (hBN) using dry-peel technique. This composite was then transferred on a Si–SiO_2 stack followed by antenna definition using photolithography. The device schematics are shown in Fig. 16. The device exhibited a responsivity and NEP of 3 kC/W and 0.2 pW/$\sqrt{\text{Hz}}$, respectively. The lifetime of the plasmon was estimated to be ~0.6 ps [21].

Delgado-Notario et al. reported the implementation of non-resonant strained-Si Schottky gated modulation-doped field-effect transistor (MODFET) detector for sub-THz imaging. Fig. 17 shows the schematic and micrograph of strained-Si quantum well layer, deposited between relaxed $Si_{0.7}Ge_{0.3}$ layers using molecular beam epitaxy (MBE). Platinum was used to form the Schottky contact. Under 300 GHz

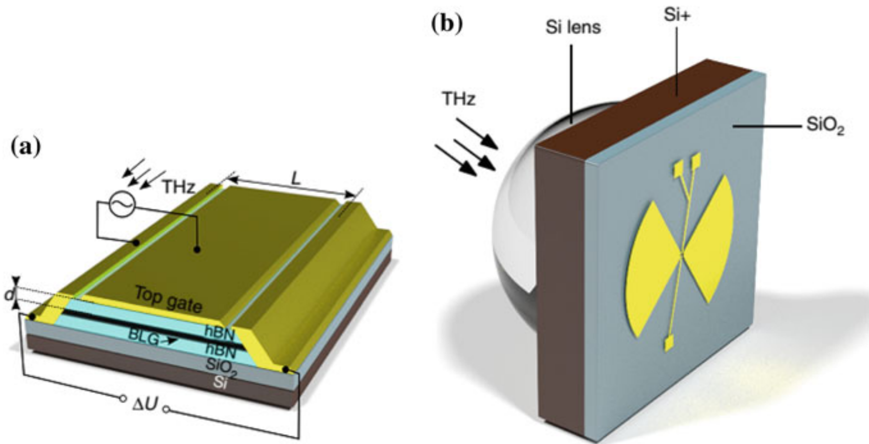

Fig. 16 **a** Schematic of the BLG-hBN FET device, **b** integration of bow-tie antenna and silicon lens to focus terahertz radiation to the detector. Adapted from [21]

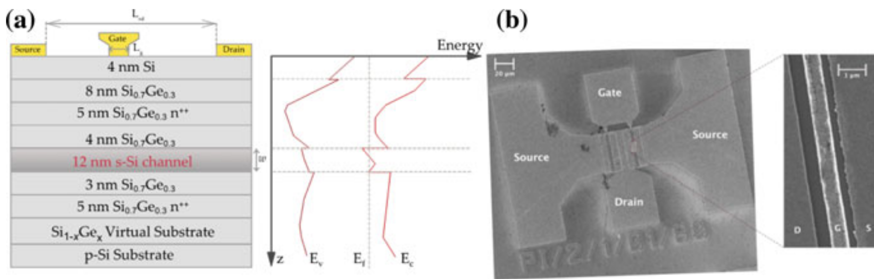

Fig. 17 **a** 2-D schematic view of Si-SiGe MODFET, **b** top-view SEM image of the device. Adapted from [22]

frequency irradiation, the maximum responsivity and minimum NEP were 218 V/W and 70 pW/$\sqrt{\text{Hz}}$, respectively, as shown in Fig. 18 [22].

Hou et al. prepared a GaN HEMT-based terahertz detector and observed its performance up to 200 °C temperature. The 3-D schematic and top-view SEM images are shown in Fig. 19. Under 0.14 THz radiation, the peak responsivity was 15 kV/W and 2.7 kV/W at room temperature and 200 °C, respectively, while under the same environment, the minimum NEP were 0.58 and 9.38 pW/$\sqrt{\text{Hz}}$, respectively (Fig. 20) [23].

Dhar Dwivedi et al. synthesized pine-shaped InN nanostructure array by oblique angle deposition (OAD) method. A high background carrier concentration of 1.8×10^{20} cm^{-3} was observed in the deposited nanostructure. The low-temperature photocurrent measurement under 1078 nm (1.1 eV) illumination revealed the effectiveness of the device as an infrared detector [24]. The same group has also reported the synthesis of InN quantum dot (QD) array by OAD and investigated their application in

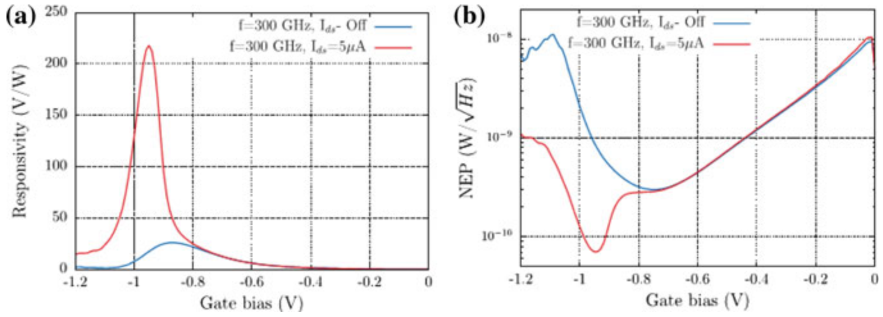

Fig. 18 Figure of merit characteristics of strained-Si MODFET under an excitation of 300 GHz, **a** responsivity vs gate bias characteristics and **b** NEP versus gate bias characteristics. Adapted from [22]

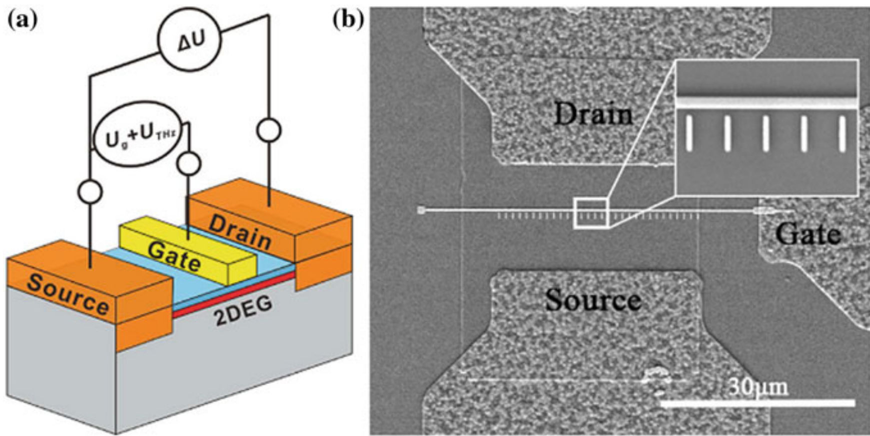

Fig. 19 **a** 3-D schematic view of GaN HEMT terahertz detector, **b** top-view SEM images of the GaN HEMT. Adapted from [23]

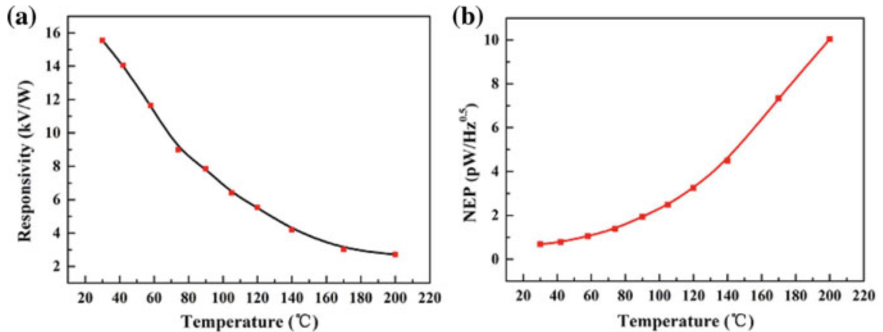

Fig. 20 Variation of figure of merit of the HEMT detector as function of temperature, **a** responsivity–temperature characteristic and **b** NEP–temperature characteristic. Adapted from [23]

infrared detection [25]. The dot diameter was in 25–30 nm range. The photoluminescence (PL) spectra revealed the main bandgap of the device to be 1.08 eV (Fig. 21). A reduction in background carrier concentration in QD (1.8×10^{18} cm^{-3}) was obtained compared to pine-shaped structure (1.8×10^{20} cm^{-3}) by simple tuning in growth parameters. The maximum room temperature and 10 K responsivity were 0.9 and 6 mAW^{-1}. At room temperature under 1080 nm illumination, the specific detectivity and NEP were calculated to be 1.38×10^{10} Jones and 0.2 pW, respectively, while under 10 K temperature environment, the same parameters were elevated to 19.2×10^{10} Jones and 0.15 pW, respectively, as shown in Fig. 22 [25]. They have continued

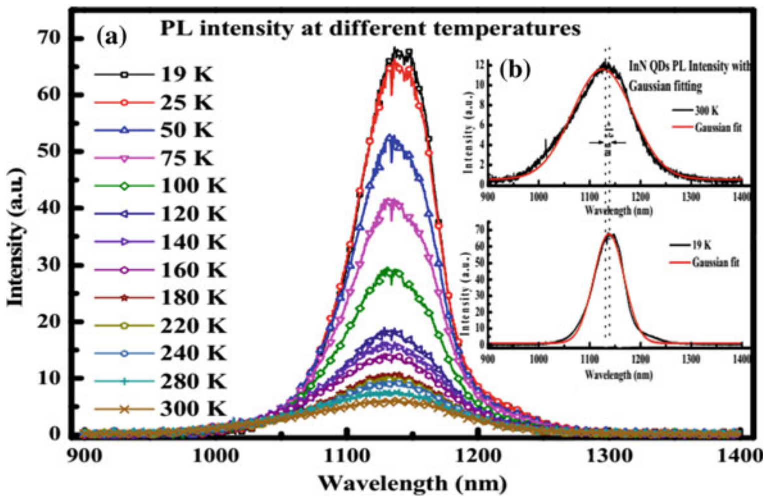

Fig. 21 Photoluminescence (PL) spectra, **a** PL spectrum of InN QDs at different temperatures, **b** Gaussian fit of PL intensity at 19 and 300 K. Reprinted from [25] with permission from Elsevier

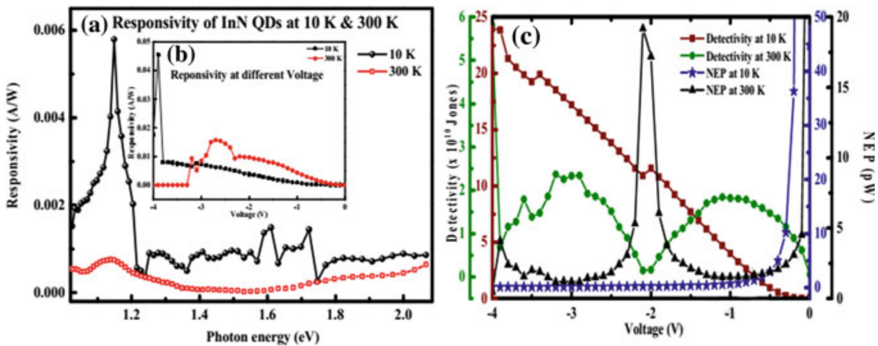

Fig. 22 **a** Responsivity curve of InN QDs device at 10 and 300 K, **b** responsivity curve at different voltage and **c** variation of detectivity and NEP with applied voltage at 10 K. Reprinted from [25] with permission from Elsevier

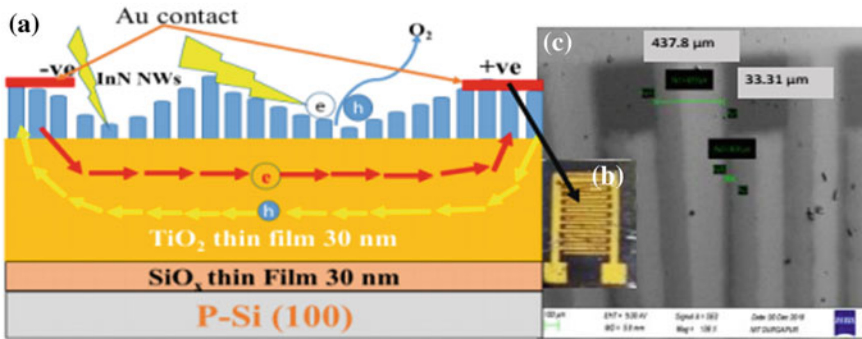

Fig. 23 **a** Cross-sectional diagram of InN NWs/TiO_2 TF device, **b** digital image of M-S-M device and **c** magnified FESEM of M-S-M contact. © [2020] IEEE. Reprinted, with permission, from [26]

their study by growing InN nanowire (NW) assembly on a TiO_2-coated p–Si–SiO_2 stack [26]. Fig. 23 shows the schematic and micrograph image of the prepared device [26]. The maximum bandgap was 1.07 eV as obtained from PL spectra. The detector exhibited very high responsivity of ~250 AW^{-1} due to diffusion and Schottky barrier lowering. The rise and fall time were 0.4 and 0.13 s, respectively, indicating that the detector may be implemented for high-speed switching applications [26].

4 Conclusion

Int this chapter, a brief understanding and ongoing research on terahertz detector has been presented. With the remarkable development in fabrication instruments, a variety of novel material and their transistors are getting employed in the task of efficient photodetection. From the review, it is obvious that most of the conducted researches are focussing on the use of group III-nitride as an active material. Thus, it may be predicted that in the near future, group III-nitride material will be at the heart of some research domain such as terahertz detection, astrophysics and light–matter interaction.

References

1. Sizova et al., THz detectors. Progr. Quant. Electron. **34**, 278–347 (2010)
2. Yang et al., Biomedical applications of terahertz spectroscopy and imaging. Trends Biotechnol. **34**(10), 810–824 (2016)
3. Danciu et al., Terahertz spectroscopy and imaging: a cutting-edge method for diagnosing digestive cancers. Materials **12**(9), 1519 (2019)
4. Saqlain et al., Feasibility analysis of opto-electronic THz earth-satellite links in the low- and mid-latitude regions. Appl Opt **58**(25), 6762–6769 (2019)

5. Afsah-Hejri et al., A comprehensive review on food applications of terahertz spectroscopy and imaging. Compr. Rev. Food Sci. Food Safety **18**, 1563–1621 (2019)
6. S.P. Langley, *"The bolometer," The American Metrological Society* (1880), pp. 1–7
7. Quispe et al., Terahertz amplification in RTD-gated HEMTs with a grating-gate wave coupling topology. Appl. Phys. Lett. **109**, 063111 (2016)
8. Qin et al., Room-temperature, low-impedance and high-sensitivity terahertz direct detector based on bilayer graphene field-effect transistor. Carbon **116**, 760–765 (2017)
9. Ponomarev et al., Lateral terahertz hot-electron bolometer based on an array of Sn nanothreads in GaAs. J. Phys. D: Appl. Phys. **51**, 135101 (2018)
10. Ponomarev et al., Sub-terahertz FET detector with self-assembled Sn-nanothreads. J. Phys. D: Appl. Phys. **53**, 075102 (2020)
11. But et al., Nonlinear photoresponse of field effect transistors terahertz detectors at high irradiation intensities. J. Appl. Phys. **115**, 164514 (2014)
12. Jakštas et al., Development of AlGaN/GaN/SiC high-electron-mobility transistors for THz detection. Lith. J. Phys. **58**, 188–193 (2018)
13. Kim, MOSFET characteristics for terahertz detector application from on-wafer measurement. IEEE Trans. Terahertz Sci. Technol. **5**(6), 1068–1077 (2015)
14. Generalov et al., A 400 GHz graphene FET detector. IEEE Trans. Terahertz Sci. Technol. **7**(5), 614–616 (2017)
15. Nadar et al., High performance heterostructure low barrier diode for sub-THz detection. IEEE Trans. Terahertz Sci. Technol. **7**(6), 780–788 (2017)
16. Javadi et al., Terahertz detection with a low-cost packaged GaAs high-electron-mobility transistor. IEEE Trans. Terahertz Sci. Technol. **9**(1), 27–37 (2019)
17. Kurita et al., Ultrahigh sensitive sub-terahertz detection by InP-based asymmetric dual-grating-gate high-electron-mobility transistors and their broadband characteristics. Appl. Phys. Lett. **104**, 251114 (2014)
18. Bauer et al. High-sensitivity wideband THz detectors based on GaN HEMTs with integrated bow-tie antennas. in *Proceedings of the 10th European Microwave Integrated Circuits Conference* (Paris, France), 7–8 Sept 2015
19. Hou et al., A sub-terahertz broadband detector based on a GaN high-electron-mobility transistor with nanoantennas. Appl. Phys. Express **10**, 014101 (2017)
20. Guo et al., Graphene-based broadband terahertz detector integrated with a square-spiral antenna. Opt. Lett. **43**(8), 1647–1650 (2018)
21. Bandurin et al., Resonant terahertz detection using graphene plasmons. Nat. Commun. **9**(5392), 1–8 (2018)
22. Delgado-Notario et al., Sub-THz imaging using non-resonant HEMT detectors. Sensors **18**, 543 (2018)
23. Hou et al., High temperature terahertz detectors realized by a GaN high electron mobility transistor. Scientific reports **7**(46664), 1–6 (2017)
24. Dhar Dwivedi et al., Pine shaped InN nanostructure growth via vapour transport method by own shadowing and infrared detection. J. Alloy. Compd. **722**, 872–877 (2017)
25. Dhar Dwivedi et al., Oblique angle deposited InN quantum dots array for infrared detection. J. Alloy. Compd. **766**, 297–304 (2018)
26. Dhar Dwivedi et al., InN nanowires based near-infrared broadband optical detector. IEEE Photonics Technol. Lett. **31**(18), 1526–1529 (2019)